Development of a 3D Laser Imaging System and its Application in Studies of Turbulent Flame Structure

Benjamin John Alexander Thorne

Submitted in accordance with the requirements for the degree of Doctor of Philosophy

The University of Leeds
School of Mechanical Engineering

November 2017

Intellectual Property and Publications Statements

The candidate confirms that the work submitted is his own, except where work which has formed part of jointly-authored publications has been included. The contribution of the candidate and the other authors to this work has been explicitly indicated below. The candidate confirms that appropriate credit has been given within the thesis where reference has been made to the work of others.

1) G. Nivarti, B. Thorne, R. S. Cant, M. Lawes and D. Bradley (2017): "Comparisons of Flame Surface Density Measurements with Direct Numerical Simulations of a lean Methane-air Flame in High-intensity Turbulence", 16th International Conference on Numerical Combustion. *The Author of the present thesis provided the experimental data. Other Authors of this publication provided the results of combustion simulations and technical discussions and guidance.*

2) B. Thorne, G. Nivarti, M. Lawes, R. S. Cant and D. Bradley (2018): "Three-dimensional measurements and Direct Numerical Simulations of Flame Surface Density for turbulent premixed lean methane-air flames", Combustion Institute Spring Meeting, Advanced Combustion Methods *The Author of the present thesis contributed the experimental data and presented the work.. Other Authors of this publication provided the results of combustion simulations and technical discussions and guidance.*

To Janet and Keith

With special thanks to Caroline Watson for her encouragement of my interest in Science, for her patience and going the extra light-year

Acknowledgements

As I write this, I of course want to extend my infinite thanks to everyone who's helped me along the way, in one way or another, both before and during my PhD study. Indeed, without them, I may even have chosen a different path entirely. For instance, I might have become a wealthy non-Academic! Therefore, I'm not entirely sure whether I should be grateful or not…

Regardless of the outcome, it's been an enjoyable journey which I wouldn't hope to have been different. So, in no particular order (but of course, Malc comes first!):

Those who helped directly:

- My Supervisor, Malcolm Lawes, not least for giving me the opportunity to study at Leeds and trusting me to work with highly dangerous lasers, but for trying to pass on so much knowledge (with some success), pulling out all the stops to ensure my thesis was completed in time and in conjunction with the combustion group, for funding my last few months at Leeds.

- Derek Bradley for all of his advice, encouragement, scientific suggestions and for his help negotiating the scientific literature.

- My Sponsor, Shell Global Solutions via Roger Cracknell, for funding a good fraction of my research and me as a person, the opportunity to present my work in Warsaw and London, both of which were highly memorable (if mildly terrifying at the time!) and for always taking interest in my work and making helpful suggestions, despite his already heavy workload.

- Brian Leach, for casting his mind back many, many years to provide advice on how the swinging sheet system might have worked in the past and for his electrical genius. And his musical efforts (or at least ensuring an adequate supply of auditory PPE). Mark Batchelor and Paul Banks, for mechanical aid, both in the lab and outside it with my various doomed (and occasionally successful) automotive repair ventures. And for the history lessons.

- My various colleagues/friends and those in transition between the two: Richard, Luke, Myeji, Jeong-Do, Moustafa, George, Aaron, Inna, Jamie, Luis and Ahmed, who made the whole process more enjoyable, and in Richard and Luke's case for giving me such a good introduction to "the bomb", Matlab and mesh processing environments. And not forgetting Girish, of Cambridge, for attempting to educate me about combustion simulations.

- The Mysterious Students who took the time to nominate me for my Postgraduate Teaching Award in 2016, for which I was deeply touched.

Equally importantly, those who helped "behind the scenes":

- John Ayto, for his extended chicken-minding, help moving house and everything else which I struggle to remember.

- Roger and Jutta Davis, for frequently entrusting me with their beautiful home and their cats, Humphrey & Mumpi and for always being so warm and appreciative, whatever their circumstances. The regular trips back to North Norfolk were very much appreciated and enjoyed and made PhD study far less gruelling.

And those who helped to steer me down the path of Science and Engineering:

- Michael, Shirley and Martin Garrard, for the enormous and willing supply of high quality fish and chip oil for conversion into bio-diesel, which ultimately cemented my interest in fuels and combustion.

- Tim Wilkes and Kris Smith of Fakenham Sixth Form, for having faith in me undertaking my A-levels a little early and their help and encouragement throughout. Ian Ponton for his help in the preceding preparations (and not charging any extra for the sheer quantity of black coffee he required during my lessons). And Klaus of Lindchem, for his encouragement of my interest in chemistry.

- Philip Hawes, for encouraging me to study for a PhD, in a round-about sort of way!

Oh, and I almost forgot…

- I also need to thank my immediate family members for their support and encouragement over the years, which took many forms. In particular, my Nan for preventing my financial demise at the end of my first year at Leeds and my Granddad for investing in a good part of my education. And, last but not least, my Mum, for tolerating the permanganate stained PVC windows, singed worktops, dissolved tarmac driveway and everything else associated with accommodating an Aspiring Scientist. And, in more recent years, for producing an endless supply of tea.

- And, to everyone else who has helped in one way or another but hasn't featured here (and there are many:)

Thank-you.

Abstract

The necessity for increasing the efficiency of combustion engines whilst simultaneously reducing the emissions of various pollutants is widely accepted. With reference specifically to premixed spark ignition (SI) engines, the turbulence/flame interaction is of particular relevance as it not only determines the maximum possible burning rate in such an engine, but also if flames are likely to extinguish (quench).

The present study describes a three-dimensional laser imaging technique which has been developed to study turbulent premixed flames in a fan-stirred combustion bomb. This has, for the first time, allowed the full 3D structure of flames developing at engine-like conditions to be analysed without the assumptions required in previous works using 2D flame imaging techniques.

Methane/air mixtures at a starting temperature and pressure of 298K and 0.1 MPa respectively and an equivalence ratio with respect to stoichiometry of 0.6 were centrally ignited using a laser ignition system at various root-mean-square (RMS) turbulence velocities, where for each explosion, a 3D image of the growing flame was captured at various instants in time. The flame images were quantitatively characterised to yield flame surface area, burned gas volume, reaction progress variable and flame surface density.

From the flame surface areas and burned gas volumes, turbulent burning velocities were directly measured from surface area ratios and compared with correlations of turbulent burning velocities made previously at Leeds using 2D flame imaging techniques. This tested the assumption that flame structure observed with 2D imaging techniques gave a good representation of the overall 3D flame structure. An excellent agreement was found between the datasets, indicating that such assumptions were valid under the conditions employed in the present work.

The surface area ratio data obtained in the present work were also compared with the predictions of direct numerical simulation (DNS) studies conducted at Cambridge University, where it was found that the experimentally derived results typically exhibited slightly higher flame surface area ratios. This was attributed to the combustion chamber geometry in the DNS study and differences in mixture properties between the two studies, with more work at similar starting conditions required to elucidate the exact cause of the differences.

Reaction progress variable was calculated for the 2D laser sheet images obtained in the present work and their 3D counterparts. Although a good agreement was seen where the central laser sheet image in a 3D reconstruction was analysed, disparities were observed when laser sheet images at a fixed position in the combustion bomb was used at high root mean square turbulence velocities. This indicates that the use of fixed position laser sheet imaging techniques, such as particle image velocimetry, are of limited use for highly turbulent flame analysis.

Contents

Intellectual Property and Publications Statements i

Acknowledgements ..... **Error! Bookmark not defined.**

Abstract vi

Contents viii

List of Figures xi

List of Tables xix

Nomenclature xx

Chapter 1 - Introduction 1

1.1 Foreword 1

1.2 Background 1

1.3 Thesis Outline 2

1.4 Laminar Burning 3

1.4.1 Laminar Flame Radius, Flame Speed and Burning Velocities 3

1.4.2 Flame Stretch and Stretch Effects 6

1.4.3 Laminar Flame Thickness 8

1.4.4 Laminar Flame Instabilities 9

1.5 Turbulent Burning 11

1.5.1 Flame Radius and Turbulent Burning Velocity Definition 11

1.5.2 Reaction Progress Variable 13

1.5.3 Flame Surface Density 14

1.5.4 Measurement of Turbulent Burning Velocity from Pressure Traces 15

1.5.5 Evolution of the Effective Root Mean Square Turbulence Velocity 16

1.5.6 Calculation of u_t from the Correlation of Turbulent Burning Velocity Measurements 18

1.6 Direct Numerical Simulation Description 21

Chapter 2 - Experimental Apparatus and Technique 24

2.1 Introduction 24

2.2 Combustion Vessel and Ancillary Systems 25

2.2.1 Auxiliary Systems 27

2.3 Swinging-Sheet 3D Laser Imaging System 35

2.3.1 Laser and Sheet-Forming Optics Description 35

2.3.2 Control and Synchronisation System 50

2.4 Experimental technique 56
Chapter 3 -Data Processing Techniques 59
3.1 Introduction 59
3.2 Processing of 2D Laser-sheet Mie Scattering Images 59
3.3 Assembly of 2D sheets into 3D reconstructions 63
3.3.1 Initial 3D matrix preparation and sheet equation generation 63
3.3.2 Sheet Interpolation and Surface Mesh Generation 65
3.3.3 Surface smoothing 68
3.4 Analysis of reconstructed flame surfaces 70
3.4.1 Flame Surface Area 70
3.4.2 Burned Gas Volume 71
3.4.3 Determination of the Reaction Progress Variable for 2D and 3D Images 72
3.4.4 Determination of Flame Surface Density 73
3.5 Schlieren image processing 74
3.5.1 Determination of schlieren flame radius 74
3.5.2 Determination of S_s and L_b 76
3.5.3 Determination of utv from Turbulent Flame Schlieren Images ..... **Error! Bookmark not defined.**
Chapter 4 – Results 79
4.1 Introduction 79
4.2 Laminar Burning Results 79
4.3 Turbulent Burning 83
4.3.1 2D Laser Sheet Images 83
4.3.2 3D Flame Reconstructions 89
Chapter 5 – Discussion 110
5.1 Introduction 110
5.2 Analysis of Flame Surface Areas, Volumes and Surface Area Ratio Measurements 111
5.2.1 Analysis of 3D Flame Surface Areas 111
5.2.2 Surface Area Ratio Measurements 120
5.3 Comparison of Reaction Progress Variable Profiles for 2D/3D Images 131
5.3.1 Comparison of 3D Reconstructions and the Central Sheet Image 132
5.3.2 Comparison of Fixed Position 2D Images with 3D Reconstructions 138
5.4 Analysis of Flame Surface Density Measurements 144

5.4.1 Analysis of Flame Surface Density Profiles 144
5.4.2 Comparison with Harker et al. (2012) 146
5.4.3 Comparison with Nivarti and Cant (2017) 152
5.4.4 Comparison with Bradley et al. (2009) 154
5.5 Effect of Seeding Particles on the Laminar Burning Velocity 157
Chapter 6 – Conclusions and Recommendations for Future Work 159
6.1 Conclusions 159
6.2 Recommendations for future work 162
Chapter 7 References 164
Bibliography 170
Appendix I – Matlab Image Processing Codes 173

List of Figures

Figure 1.1 Schlieren image for ϕ = 1.0 2,2,4-trimethyl pentane/air mixture at 87^{o}C initial temperature and 0.1 MPa initial pressure, reproduced from Mumby (2016) 5

Figure 1.2 Species concentration and temperature gradient across the flame front as computed for a one dimensional, adiabatic flame developing through a stoichiometric methane-air mixture at 0.1 MPa and 300K, reproduced from Gillespie et al. (2000) 8

Figure 1.3 Schlieren image of a cellular stoichiometric iso-octane air mixture at 0.5 MPa initial pressure and 87^{o}C initial temperature, reproduced from Mumby (2016).....10

Figure 1.4 Reference radii and associated unburned and burned gas masses for a 2D laser sheet Mie scattering image, reproduced from Bradley et al. (2003).....12

Figure 1.5 A cross section of part of the 3D flame surface showing the burned and unburned region along with a spherical shell of inner and outer radii R_1 and R_2, respectively 13

Figure 1.6 Development of u'_k/u' with increasing flame radius at various Reynolds numbers, reproduced from Bradley et al. (2009).....17

Figure 1.7 Variation in U with K, as presented by Bradley et al (2013) 20

Figure 1.8 Variation of burning velocity ratio with normalised RMS turbulence intensity, reproduced from Nivarti and Cant (2017) 22

Figure 2.1 Leeds MKII fan-stirred bomb, reproduced from Tripathi (2012) 26

Figure 2.2 Spark plug tip and holder, image from Mumby (2016).....29

Figure 2.3 Laser ignition system.....31

Figure 2.4 Schlieren imaging system used in the present study 33

Figure 2.5 Simplified schematic of the swinging-sheet optical setup 37

Figure 2.6 Detailed vertical view of the swinging-sheet arrangement 38

Figure 2.7 Shaping of the laser beam to a small waist at the bomb centre.....40

Figure 2.8 Details of the beam waist at the bomb centre.....42

Figure 2.9 Expansion of the laser beam into a sheet.....44

Figure 2.10 Divergence of successive laser sheets 48

Figure 2.11 Mirror geometric offset 49

Figure 2.12 Schematic of all components in the synchronisation system 52

Figure 2.13 Image (left) and schematic of the connections at the SL800 laser controller to afford interlocked triggering 54

Figure 2.14 Signals involved in triggering the experiment 55

Figure 3.1 Raw, mid-sweep laser sheet image of a methane/air flame at 298K, 0.1 MPa and φ = 0.6 at 24.2 ms from ignition, u' = 0.25 m/s 60

Figure 3.2 Result of edge detection and binarisation on a greyscale image of a low-turbulence flame 61

Figure 3.3 Laser sheet image shown in Fig. 3.2 after edge detection, background cleaning and inversion 62

Figure 3.4 Trajectory of laser sheets through the bomb and insertion of the sheets into a discretised grid 64

Figure 3.5 View of a slice through assembled sheets in the y-axis 65

Figure 3.6 View of a slice through assembled sheets in the y-axis after interpolation 66

Figure 3.7 Triangulated surface mesh plotted over a laser spark influenced laminar 3D reconstruction 67

Figure 3.8 Methane/air flame at 298K, 0.1 MPa, u' = 0.25 m/s and φ = 0.6 at 35.8 ms from ignition. The unsmoothed reconstruction is on the left 68

Figure 3.9 Figure 3.9 Methane/air flame at 298K, 0.1 MPa, u' = 0.75 m/s and φ = 0.6 at 12.6 ms from ignition. The unsmoothed reconstruction is on the left. 69

Figure 3.10 Methane/air flame at 298K, 0.1 MPa, u' = 1.25 m/s and φ = 0.6 at 18.4 ms from ignition. The unsmoothed reconstruction is on the left 69

Figure 3.11 Notation for calculation of polar coordinates (adapted from The Mathworks, 2017) 73

Figure 3.12 Schlieren image processing stages, reproduced from Mumby (2016) 75

Figure 3.13 a) radius versus time, b) stretched flame speed versus radius and c) stretched flame speed versus stretch rate, all for iso-octane air at 0.1 MPa and 360K, reproduced from Mumby 2016 77

Figure 4.1 A typical graph of the variation of stretched laminar flame speed with flame radius, for methane/air at 298K, 0.1 MPa and φ = 0.6, laminar 80

Figure 4.2 A typical graph of the variation of stretched laminar flame speed with stretch rate, for methane/air at 298K, 0.1 MPa and φ = 0.6, laminar. 81

Figure 4.3 Schlieren images of a growing laser-ignited flame, from Bradley et al. (2004) 82

Figure 4.4 3D reconstructions of a growing laminar methane/air flame in the present work .82

Figure 4.5 Full series of laser sheet images for a methane/air flame at u' = 0.25 m/s, 24.2 ms from ignition. 84

Figure 4.6 Enlarged view of Image 8 from Fig. 4.5 85

Figure 4.7 Image from Fig. 4.5 displaying an isolated region of unburned mixture 85

Figure 4.8 Laser sheet images of flames at (a) u' = 0.25 m/s, (b) u' = 0.75 m/s and (c) u' = 1.25 m/s.....87

Figure 4.9 Flame developing at typically quenching levels of turbulence 88

Figure 4.10 Growth of a turbulent flame over time with constant axis scaling, methane/air at 0.1 MPa, 298K and φ = 0.6, u' = 0.25 m/s 90

Figure 4.11 Growth of a turbulent flame over time with constant axis scaling, methane/air at 0.1 MPa , 298K and φ = 0.6, u' = 0.5 m/s 91

Figure 4.12 Growth of a turbulent flame over time with constant axis scaling, methane/air at 0.1 MPa, 298K and φ = 0.6, u' = 0.75 m/s 92

Figure 4.13 Growth of a turbulent flame over time with constant axis scaling, methane/air at 0.1 MPa, 298K and φ = 0.6, u' = 1.0 m/s 93

Figure 4.14 Single 3D reconstruction with u' = 1.0 m/s, 12.6 ms from ignition, various viewing angles as displayed in Meshlab.....94

Figure 4.15 Growth of a turbulent flame over time with constant axis scaling, methane/air at 0.1 MPa, 298K and φ = 0.6, u' = 1.25 m/s 96

Figure 4.16 Single 3D reconstruction with u' = 1.25 m/s, 24.2 ms from ignition, various viewing angle.....97

Figure 4.17 Variation of the surface area ratio and u_t/u_l with time from ignition for methane/air at 298K, 0.1 MPa, u' = 0.25 m/s and φ = 0.6. Crosses represent A/a. 98

Figure 4.18 Variation of the surface area ratio and u_t/u_l with time from ignition for methane/air at 298K, 0.1 MPa, u' = 0.75 m/s and φ = 0.6. Crosses represent A/a. 99

Figure 4.19 Variation of the surface area ratio and u_t/u_l with time from ignition for methane/air at 298K, 0.1 MPa, u' = 1.25 m/s and φ = 0.6. Crosses represent A/a. 99

Figure 4.20 Extrapolation of A/a to u'_k/u' = 0.6, methane/air at 298K, 0.1 MPa and φ = 0.6, u' = 0.25 m/s 100

Figure 4.21 Extrapolation of A/a to u'_k/u' = 0.6, methane/air at 298K, 0.1 MPa and φ = 0.6, u' = 0.75 m/s 101

Figure 4.22 Extrapolation of A/a to u'_k/u' = 0.6, methane/air at 298K, 0.1 MPa and φ = 0.6, u' = 1.25 m/s 101

Figure 4.23 Increase in surface area ratio with flame radius during growth for methane/air at 298K, 0.1 MPa, φ = 0.6 and a variety of u' for the initial and repeat experiment at each condition 103

Figure 4.24 Reaction progress variable as a function of radius for methane/air at 298K, 0.1 MPa, φ = 0.6 and u' = 0.25 m/s 105

Figure 4.25 Reaction progress variable as a function of radius for methane/air at 298K, 0.1 MPa, φ = 0.6 and u' = 0.75 m/s 105

Figure 4.26 Reaction progress variable as a function of radius for methane/air at 298K, 0.1 MPa, φ = 0.6 and u' = 1.25 m/s 106

Figure 4.27 Turbulent flame brush thickness as a function of flame radius for methane/air at 298K, 0.1 MPa, φ = 0.6 and a variety of u' for the initial and repeat experiment. 107

Figure 4.28 Flame surface density as a function of radius for methane/air at 298K, 0.1 MPa, φ = 0.6 and u' = 0.25 m/s 108

Figure 4.29 Flame surface density as a function of radius for methane/air at 298K, 0.1 MPa, φ = 0.6 and u' = 0.75 m/s 109

Figure 4.30 Flame surface density as a function of radius for methane/air at 298K, 0.1 MPa, φ = 0.6 and u' = 1.25 m/s 109

Figure 5.1 Variation of smoothed and unsmoothed flame surface area with laser sheet spacing; methane/air at 298K, 0.1 MPa, φ = 0.6 and u' = 0.25 m/s. t = 12.6 ms. Crosses represent the unsmoothed reconstruction.....112

Figure 5.2 Methane/air flame reconstruction at 12.6 ms after ignition with every second and third sheet image removed 113

Figure 5.3 Variation of smoothed and unsmoothed flame surface area with laser sheet spacing; methane/air at 298K, 0.1 MPa, φ = 0.6 and u' = 0.75 m/s. t = 12.6 ms. Crosses represent the unsmoothed reconstruction. 114

Figure 5.4 Variation of smoothed and unsmoothed flame surface area with laser sheet spacing; methane/air at 298K, 0.1 MPa, φ = 0.6 and u' = 1.25 m/s. t = 12.6 ms. Crosses represent the unsmoothed reconstruction. 115

Figure 5.5 Variation in flame surface area with time from ignition for smoothed/unsmoothed reconstructions at various u' values 117

Figure 5.6 Variation in flame volume with time from ignition for smoothed/unsmoothed reconstructions at various u' values 119

Figure 5.7 Variation of surface area ratio with normalised RMS turbulence intensity 120

Figure 5.8 Comparison of experimentally derived A/a ratios with those from the DNS of Nivarti and Cant (2017) 122

Figure 5.9 Destruction of flame surface area at regions of negative curvature 123

Figure 5.10 Isosurfaces of the leading and trailing edges of flames at low and high turbulence, reproduced from Nivarti and Cant (2017) 124

Figure 5.11 Variation of experimentally obtained A/a with calculated u_t/u_l 126

Figure 5.12 Variation in the probability of burning with Karlovitz number, reproduced from Bagdanavicius et al. (2015) 128

Figure 5.13 Variation in calculated u_t/u_l and A/a corrected for stretch effects with u'/u_l 129

Figure 5.14 Variation of U with K at Ma_{sr} = 1. Reproduced from Bradley et al. (2011). Open symbols are for schlieren results, solid symbols represent pressure measurements 130

Figure 5.15 Variation of c with radius for a central 2D laser sheet image and reconstruction of a methane/air flame at 298K, 0.1 MPa, φ = 0.6 and u' = 0.25 m/s. t = 1 ms 133

Figure 5.16 Variation of c with radius for a central 2D laser sheet image and reconstruction of a methane/air flame at 298K, 0.1 MPa, φ = 0.6 and u' = 0.25 m/s. t = 12.6 ms 133

Figure 5.17 Variation of *c* with radius for a central 2D laser sheet image and reconstruction of a methane/air flame at 298K, 0.1 MPa, φ = 0.6 and *u'* = 0.25 m/s. *t* = 30 ms.....134

Figure 5.18 Variation of *c* with radius for a central 2D laser sheet image and reconstruction of a methane/air flame at 298K, 0.1 MPa, φ = 0.6 and *u'* = 0.75 m/s. *t* = 1 ms.....135

Figure 5.19 Variation of *c* with radius for a central 2D laser sheet image and reconstruction of a methane/air flame at 298K, 0.1 MPa, φ = 0.6 and *u'* = 0.75 m/s. *t* = 6.8 ms.....135

Figure 5.20 Variation of *c* with radius for a central 2D laser sheet image and reconstruction of a methane/air flame at 298K, 0.1 MPa, φ = 0.6 and *u'* = 0.25 m/s. *t* = 18.4 ms.....136

Figure 5.21 Variation of *c* with radius for a central 2D laser sheet image and reconstruction of a methane/air flame at 298K, 0.1 MPa, φ = 0.6 and *u'* = 1.25 m/s. *t* = 1 ms.....137

Figure 5.22 Variation of *c* with radius for a central 2D laser sheet image and reconstruction of a methane/air flame at 298K, 0.1 MPa, φ = 0.6 and *u'* = 1.25 m/s. *t* = 6.8 ms.....137

Figure 5.23 Variation of *c* with radius for a central 2D laser sheet image and reconstruction of a methane/air flame at 298K, 0.1 MPa, φ = 0.6 and *u'* = 1.25 m/s. *t* = 12.6 ms.....138

Figure 5.24 Comparison between *c* v's radius profiles for 2D and 3D flame images for methane/air at 298K, 0.1 MPa, φ = 0.6 and *u'* = 0.25 m/s at various instances after ignition 139

Figure 5.25 Comparison between *c* v's radius profiles for 2D and 3D flame images for methane/air at 298K, 0.1 MPa, φ = 0.6 and *u'* = 0.75 m/s, *t* = 1 ms.....140

Figure 5.26 Comparison between *c* v's radius profiles for 2D and 3D flame images for methane/air at 298K, 0.1 MPa, φ = 0.6 and *u'* = 0.75 m/s, *t* = 6.8 ms.....141

Figure 5.27 Comparison between *c* v's radius profiles for 2D and 3D flame images for methane/air at 298K, 0.1 MPa, φ = 0.6 and *u'* = 0.75 m/s, *t* = 12.6 ms.....142

Figure 5.28 Comparison between *c* v's radius profiles for 2D and 3D flame images for methane/air at 298K, 0.1 MPa, φ = 0.6 and *u'* = 1.25 m/s, *t* = 12.6 ms.....142

Figure 5.29 Comparison between *c* v's radius profiles for 2D and 3D flame images for methane/air at 298K, 0.1 MPa, φ = 0.6 and *u'* = 1.25 m/s, *t* = 18.4 ms.....143

Figure 5.30 Comparison between *c* v's radius profiles for 2D and 3D flame images for methane/air at 298K, 0.1 MPa, φ = 0.6 and *u'* = 1.25 m/s, *t* = 24.2 ms.....143

Figure 5.31 Flame surface density as a function of reaction progress variable for methane/air at 298K, 0.1 MPa, φ = 0.6 and u' = 1.25 m/s 145

Figure 5.32 Reconstructions of the flame analysed in Fig. 5.31, at t = 6.8 ms (left) and t = 12.6 ms (right), scaled to enhance the flame surface structure 145

Figure 5.33 Flame surface density as a function of reaction progress variable for methane/air at 298K, 0.1 MPa, φ = 0.6 and u' = 0.25 m/s, various times from ignition 146

Figure 5.34 Flame surface density as a function of radius, methane/air at 298K, 0.1 MPa and φ = 0.6, u'/u_l = 4.2 147

Figure 5.35 Flame surface density variation with normalised radius, reproduced from Harker et al. (2012); φ = 0.7, u'/u_l = 2.35 148

Figure 5.36 Normalised flame surface density as a function of reaction progress variable for methane/air at 298K, 0.1 MPa, φ = 0.6 and u' = 0.25 m/s, u'/u_l = 4.2, various times from ignition 149

Figure 5.37 Normalised flame surface density as a function of reaction progress variable for methane/air at 298K, 0.1 MPa, φ = 0.6 and u' = 0.75 m/s, u'/u_l = 12.7, various times from ignition 150

Figure 5.38 Normalised flame surface density as a function of reaction progress variable for methane/air at 298K, 0.1 MPa, φ = 0.6 and u' = 1.25 m/s, u'/u_l = 21.2, various times from ignition 150

Figure 5.39 Normalised flame surface density plots reproduced from Harker et al. (2012); (a) φ = 0.7, u'/u_l = 2.35, (b) φ = 1.0, u'/u_l = 1.11 151

Figure 5.40 Flame surface density as a function of c, methane/air at 298K, 0.1 MPa and φ = 0.6, various u'/u_l 153

Figure 5.41 Flame surface density profiles from DNS at various u'/S_L, reproduced from Nivarti and Cant (2017) 153

Figure 5.42 Variation of flame surface density with n for methane/air at 298K, 0.1 MPa and φ = 0.6, u'/u_l = 4.2 155

Figure 5.43 Variation of flame surface density with n for methane/air at 298K, 0.1 MPa and φ = 0.6, u'/u_l = 12.7 155

Figure 5.44 Flame surface density variation with normalised radius for propane/air at 300K, solid line φ = 1, broken line φ = 0.8 for (a) 0.1 MPa, u'/u_l = 3.57 (b) 0.1 MPa, u'/u_l = 10.7, (c) 0.5 MPa, u'/u_l = 5.88. Reproduced from Bradley et al. (2009) 156

List of Tables

Table 2.1 Optical design for beam contraction towards the bomb centre 45

Table 2.2 Optical design for sheet formation and calculation of the minimum beam waist ...46

Table 4.1 Burning parameters obtained for methane/air at 298K, 0.1 MPa and φ = 0.6.....81

Nomenclature

A	Flame area
A_i	Area of equivalent spherical flame
A_T	Wrinkled flame area
A_L	Laminar flame area
A_m	Centre of flat to mirror
a_i	Laser sheet offset
α	Flame stretch
α_s	Stretch rate due to strain
α_c	Stretch rate due to curvature
c	Reaction progress variable
c_p	Mixture specific heat
D_s	Sphere diameter
D_{ij}	Mass diffusion
d_i	Initial beam diameter
d_b	Expanded beam diameter
d_f	Focal diameter
δ_l	Flame thickness
δ_i	Distance between beam entry and exit of area of interest
ρ	Mixture density
ρ_b	Burned gas density
ρ_u	Unburned gas density
ε	Energy dissipation per unit mass
f	Focal length
f_k	Face 'k'

f_1, f_2	Frequency lmits
df	Change in frequency
γ_i	Sheet angle
$\overline{K}_\eta$	Dimensionless wave number
K	Karlovitz stretch factor
k	Thermal conductivity of mixture
K_c	Stretch factor associated with curvature
k_H	Mean curvature
k_G	Gaussian curvature
k_1, k_2	Principle curvature operators
L	Integral length scale
L_b	Burned gas Markstein length
Le	Lewis number
L_c	Markstein length associated with curvature
L_s	Markstein length associated with strain
λ	Taylor length scale
λ_{sc}	Positive scale factor
λ_w	Wavelength of light
M^2	Beam quality factor
Ma	Markstein number
N	Fan speed
N_s	Number of samples recorded
n_v	Number of vertices
n_f	Number of faces
n_s	Number of sheets
η	Kolmogorov length scale

ω	Frequency of rotating mirror
R_u	Cold front radius
R_{eq}	Equivalent radius
R_i	Radius of equivalent spherical flame
R_L	Turbulent Reynolds number
S_s	Unstretched laminar flame speed
S	Flame speed factor
S_i	Distance of sheet 'i' from centre line
S_{iso}	Flame isosurface
$S(f)$	Spectral coefficient
$\bar{S}$	Dimensionless energy
Σ	Flame surface density
T	Instantaneous temperature
T_{ad}	Adiabatic flame temperature
T_0	Unburned gas temperature
t_s	Time for 1 sweep
t_b	Time between sweeps
τ_L	Integral time scale
τ_λ	Taylor timescale
τ_η	Kolmogorov timescale
θ_b	Beam divergence
θ_m	Angle of mirror
u_l	Unstretched laminar burning velocity
u_n	Stretched laminar burning velocity
u_t	Turbulent burning velocity
$\bar{u}, \bar{v}, \bar{w}$	Mean velocities

u'	RMS velocity
μ_{sc}	Negative scale factor
ν	Kinematic viscosity
v_i, v_j	Vertex i, j
v_{1k}, v_{2k}, v_{3k}	Vertices of face 'k'
v_g	Gas velocity in front of flame
V_{rms}	RMS velocity vector
Y_F	Fuel mass fraction
Y_{F0}	Mass fraction of fresh reactants
$Y_{F\infty}$	Mass fraction of burned products
x_m	Mirror face length
ζ	Co-ordinate normal to brush
$\zeta_{0.5}$	Value of ζ at c = 0.5
Z	Distance between mirror centreline and vessel

Abbreviations

AI	After Ignition
DNS	Direct Numerical Simulation
FSD	Flame Surface Density
LIF	Laser Induced Fluorescence
$MKII$	Leeds Fan Stirred Combustion Vessel
MRI	Magnetic Resonance Imaging
PIV	Particle Image Velocimetry
$PLIF$	Planar Laser Induced Fluorescence
RPV	Reaction progress variable

Chapter 1 - Introduction

1.1 Foreword

The problems of carbon dioxide emissions with relevance to climate change (Ortiz et al. 2011, Shukman 2013 and Gupta 2009, p70), the effects of combustion related vehicular emissions on health (Wenger et al. 2009) and rising fossil fuel consumption (Rand and Dell 2008) are well described in the literature and will not be repeated here. Thus, combustion is not only a rewarding area for study but also very relevant in the context of a more sustainable future.

1.2 Background

Previous studies of turbulent combustion, e.g. Bradley et al. (2009, 2011 and 2013) and Bagdanavicius et al. (2015) have employed two-dimensional imaging techniques such as schlieren imaging (Section 2.3) and 2D laser sheet imaging to study turbulent flame structure. These studies relied on the assumption that the flame surface detail witnessed was representative of the overall three-dimensional flame structure. Other works employed 3D imaging techniques. For example, Yip et al. (1988) presented the 3D imaging of a gas jet using a multiple laser sheet imaging technique, with a dye laser as the laser light source. Hult et al. (2002) applied a similar technique employing a neodymium yttrium-aluminium garnet (Nd:YAG) laser to study flames stabilised on a burner, whilst Nygren et al. (2002) investigated combustion in a homogeneous charge compression ignition (HCCI) engine using a similar setup, with laser-induced fluorescence employed to reveal chemical species as an indicator of extent of combustion. More recently, Upton et al. (2011) studied burner flames using computed tomography (CT) with 12 individual detectors equispaced around the flame.

Harker et al. (2012) present a study of flames developing in the Leeds MKII fan-stirred combustion vessel (hereafter referred to as “the bomb” or “the combustion vessel”) using a multiple laser sheet imaging technique. An Oxford Lasers LS20-50 copper vapour laser, pulsed at a repetition frequency of 18 kHz, was used to provide pulses of laser light which were shaped into sheets using a number of lenses. The resulting laser sheets were swept through the bomb by reflection off a rotating octagonal mirror.

This allowed a number of “sweeps” through a flame during its development. However, due to the small sheet height of 50 mm and the finite time required within and between each sweep,

only flames developing at low turbulence and in the early stages of growth could be imaged. The resolution of 0.7 mm per pixel in all directions allowed structures of the integral and Taylor length scales of turbulence (20 mm and 3 mm, respectively) to be resolved, but not the Kolmogorov scale (0.15 mm).

In the present study, the system described by Harker et al. (2012) has been significantly developed as described in full in Section 2.3. A Laser Lines Nd:YAG laser supplying laser light at a repetition frequency of 49 kHz and a pulse energy of 2 mJ has been employed to generate thin laser sheets at a height of approximately 83 mm in the centre of the bomb, as described in Section 2.4. The use of a 16-sided rotating mirror running at 10 Hz allowed a time interval between sweeps of 5.8 ms and an intra-sweep time of 1.4 ms. For the first time, this has enabled a fully temporally resolved 3D study of turbulent flame structure at engine-like conditions.

1.3 Thesis Outline

This thesis is split into six individual chapters; the first chapter presents the motivation for study and the relevant theory. The second chapter describes the experimental setup and its operation, including a description of the bomb, which was used for all experiments conducted in this study. The design of the optical layout which was used to generate the laser sheets is also described, along with the laser ignition system and the synchronisation setup used to ensure that all of the individual sub-systems were actuated at the appropriate time with respect to each other.

The third chapter describes the data processing techniques used to generate the 3D reconstructions from the 2D laser sheets and to quantify the flame surface structure. This yielded flame surface areas (where the flame surface is represented by an "isosurface" corresponding to a particular extent of reaction in the reaction zone), volumes, reaction progress variable and flame surface density. The majority of the data processing was carried out in Matlab using codes written by the present Author, though Meshlab and Meshmixer were used to effect surface smoothing of the reconstructions and allow 3D printing, respectively.

The fourth chapter presents the results obtained in the study and an analysis of these results is given in Chapter 5, along with a comparison of these with the literature. Chapter 6 presents a summary of the present study along with recommendations for future work.

1.4 Laminar Burning

This section addresses aspects of combustion in its simplest, laminar form, in the absence of turbulence and is further broken down into several subsections; Section 1.4.1 describes definitions of the flame radius and the flame speeds and burning velocities derived from these. Section 1.4.2 explores flame stretch effects, Section 1.4.3 the laminar flame thickness and Section 1.4.4 laminar flame instabilities.

1.4.1 Laminar Flame Radius, Flame Speed and Burning Velocities

Combustion is employed as a method of releasing chemical energy for conversion to mechanical (and sometimes ultimately electrical) energy in a variety of applications, including gas turbines, reciprocating internal combustion engines and commercial boilers. Depending on the fuel to be used in the application, the fuel and air can either be mixed at the molecular level in advance of ignition, in the case of "premixed" combustion (Turns 2006, p7), or can be locally mixed in the form of dispersed droplets/particles immediately prior to combustion ("non-premixed" combustion). Premixed combustion can thus be characterised by an adiabatic combustion temperature and burning velocity (Dixon-Lewis 1990), whereas these are less applicable to non-premixed combustion. Employers of the former are, for example, gasoline engines and gas turbines, whilst the latter is employed in furnaces, Diesel and Jet engines.

Upon ignition, a premixed charge of gaseous fuel and air will burn at a localised thin flame front, with this front progressing through the mixture at the stretched flame speed (where stretch effects are described in Section 1.4.2), S_n, represented as follows (Gillespie et al. 2000)

$$S_n = \frac{dR_u}{dt} \tag{1.1}$$

Where R_u is the radius of the isotherm 5K above the temperature of the unburned reactants (Bradley et al. 1996), which may be obtained from schlieren (see Section 2.2) images using the following relation (Gillespie et al. 2000)

$$R_u = R_{sch} + 1.95\delta_l \left(\frac{\rho_u}{\rho_b} \right)^{0.5} \tag{1.2}$$

Here, R_{sch} is the schlieren radius, δ_l is the laminar flame thickness as described in Section 1.4.3, ρ_u is the density of the unburned reactant mixture and ρ_b is the burned gas density at the adiabatic flame temperature. The flame speed is composed of the consumption burning velocity of unburned reactants, u_n, and the gas expansion velocity, v_g, in accordance with the following relation (Gillespie et al. 2000)

$$S_n = v_g + u_n \tag{1.3}$$

Where the mass burning velocity relative to the unburned reactants, u_n, is defined as

$$u_n = \frac{1}{\rho_u} \left(\frac{\dot{m}_e}{A} \right) \tag{1.4}$$

Here, ρ_u is the density of the unburned reactant mixture, A is the flame surface area and m_e is the mass rate of entrainment of reactants into the flame front.

By the use of schlieren photography, described in Section 2.2, applied to developing laminar flames, it is thus possible to obtain values for S_n. A schlieren image for a developing flame kernel is shown in Fig.1.1, where the visible flame "surface" is a result of light refraction due to the density gradient brought about by the inherent temperature gradient in this region.

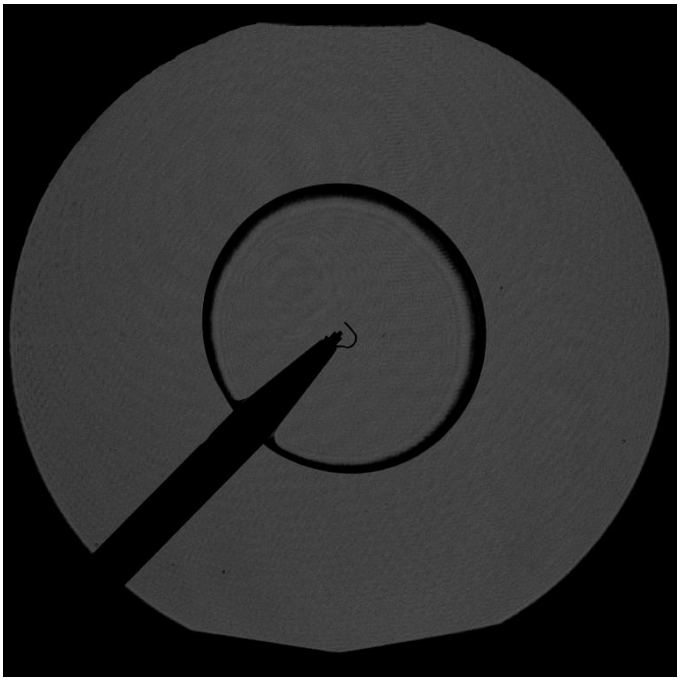

Figure 1.1 Schlieren image for ϕ = 1.0 2,2,4-trimethyl pentane/air mixture at 87^{o}C initial temperature and 0.1 MPa initial pressure, reproduced from Mumby (2016)

By plotting S_n against the flame stretch rate, α (descried in Section 1.4.2), and extrapolating the resulting curve to zero stretch, the unstretched flame speed, S_s, may be obtained as the intercept. From this, the unstretched laminar burning velocity may be deduced using the following expression (Bradley et al. 1998)

$$u_l = S_s \frac{\rho_b}{\rho_u} \tag{1.5}$$

This parameter represents a theoretical burning velocity as stretch exists in all real flames. It allows for a comparison of the fundamental burning rates of mixtures at given initial conditions in the absence of stretch effects, as well as a means to predict the turbulent burning rate of a mixture based on the properties of the turbulent flow. This is discussed further in Section 1.5.6.

1.4.2 Flame Stretch and Stretch Effects

As a flame develops, its surface experiences a stretching effect due to the effects of curvature and aerodynamic strain. Flame stretch is represented mathematically by

$$\alpha = \frac{1}{A}\frac{dA}{dt} \tag{1.6}$$

Where A is the instantaneous flame surface area and *dA/dt* represents a change in flame surface area over time *dt*. From experimental burning rate data obtained from schlieren imaging, α may be obtained from the following (Bradley et al. 1998)

$$\alpha = \frac{1}{4\pi R_u^2}\frac{d4\pi R_u^2}{dt} = \frac{2}{R_u}\frac{dR_u}{dt} = \frac{2}{R_u}S_n \tag{1.7}$$

The two components of flame stretch were defined by Bradley et al. (1998) as

$$\alpha_c = \frac{2u_n}{R_u} \tag{1.8}$$

$$a_s = \frac{2u_g}{R_u} \tag{1.9}$$

Here, α_c and α_s are flame stretch due to curvature and aerodynamic strain, respectively, whilst u_g is the gas velocity due to expansion at radius R_u. Thus, the total stretch rate, α, is given by

$$\alpha = \alpha_c + \alpha_s \tag{1.10}$$

Flame stretch can either increase or decrease the local burning velocity, where this effect is quantified by the Markstein number of the mixture. This is expressed as

$$u_l - u_n = L_c\alpha_c + L_s\alpha_s \quad (1.11)$$

Where L_c and L_s are the Markstein lengths related to curvature and strain, respectively. However, due to the finite flame thickness as described in Section 1.4.3, the burning velocities may be described in terms of the consumption of cold products in the form of u_n or the generation of burned gas as $u_{nr,}$ with this effect lessening as the flame radius increases with respect to the laminar flame thickness. Thus, Eq. 1.11 takes the form

$$u_l - u_{nr} = L_{cr}\alpha_c + L_{sr}\alpha_s \quad (1.12)$$

where

$$L_{sr} = \frac{1}{\rho_u/\rho_b - 1}\left(L_b - L_s\right) \quad (1.13)$$

and

$$L_{cr} = \frac{1}{\rho_u/\rho_b - 1}\left(L_b - L_c\right) \quad (1.14)$$

The dimensionless Markstein numbers may be obtained by dividing the Markstein lengths by the laminar flame thickness, δ_l as

$$Ma_{sr} = \frac{L_{sr}}{\delta_l} \quad (1.15)$$

Where this parameter is employed in the turbulent burning velocity correlations described in Section 1.5.6.

Alternatively, the effect of stretch on the flame surface may be quantified by the Lewis number. This parameter is directly related to the Markstein number, has been employed by e.g. Chakraborty and Cant (2011) and is defined as the ratio of thermal to mass diffusivity, calculated as follows

$$Le = \frac{k}{\rho_u c_p D_{ij}} \tag{1.16}$$

Where k is the thermal conductivity, c_p is the specific heat capacity and D_{ij} is the mass diffusion. Where $Le < 1$, mass diffusivity dominates which leads to an increased concentration of reactants in the reaction zone, which increases the heat release rate and thus wrinkling of curved regions. Where $Le > 1$, correspondingly less heat release occurs which leads to less formation of surface wrinkling.

1.4.3 Laminar Flame Thickness

Rather than existing as a binary step between reactants and fully burned products, the flame front exists as a continuous transition as illustrated in Fig. 1.2 (Gillespie et al. 2000).

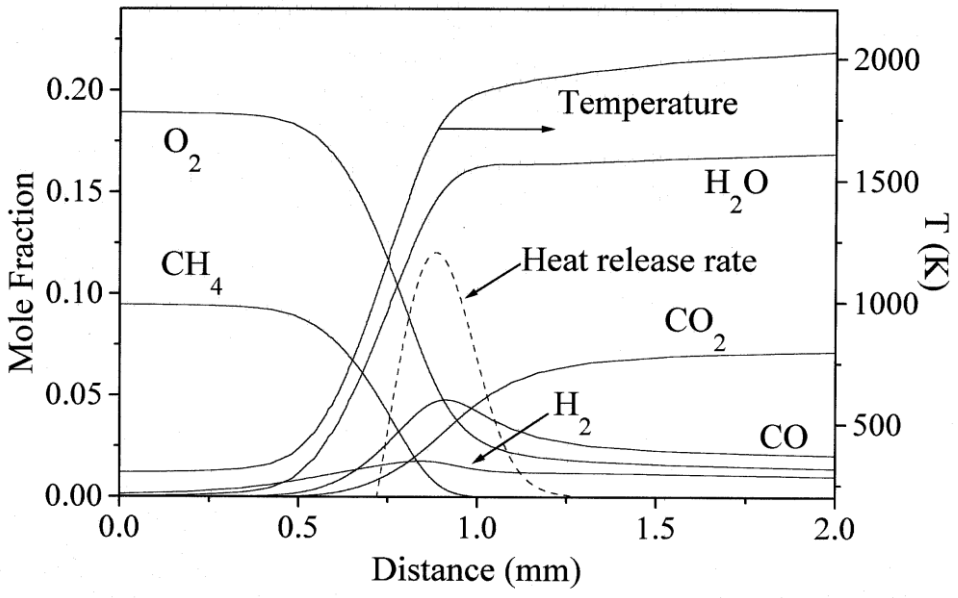

Figure 1.2 Species concentration and temperature gradient across the flame front as computed for a one dimensional, adiabatic flame developing through a stoichiometric methane-air mixture at 0.1 MPa and 300K, reproduced from Gillespie et al. (2000)

This figure shows a gradual transition over several mm where the definition of thickness is subjective. Alternatively, the flame thickness may defined for the initial mixture as a characteristic length. In the present work, a hydrodynamic definition is employed as follows:

$$\delta_l = \frac{\nu}{u_l} \tag{1.17}$$

Where ν is the kinematic viscosity of the unburned mixture. As stated in Section 1.4.2, the laminar flame thickness is important as it underpins the definition of the flame radius used to calculate burning velocities. For example, schlieren imaging relies on the temperature and thus density gradient to visualise a flame edge. If species concentrations are used, this will yield a slightly different radius as may be seen in Fig. 1.2.

1.4.4 Laminar Flame Instabilities

Immediately after ignition, a flame is highly stretched due to the relatively low flame surface area and the boost from residual spark energy. This high level of stretch serves to smooth out any wrinkling of the flame surface but, at a critical radius, the flame stretch will no longer be sufficient to stabilise the flame structure (Gillespie et al. 2000). At this point, the flame surface begins to cross-crack (Bradley and Harper, 1994), leading to a fully cellular flame structure (Bradley et al. 2000). This leads to an increase in the surface area of the flame and thus the burning rate. The transition to cellularity may be quantified by the critical Peclet number, as (Gu et al. 2000)

$$Pe_{cl} = \frac{r_{cl}}{\delta_l} \tag{1.18}$$

Where r_{cl} is the radius at which the cellular flame structure becomes apparent which increases with increasing Ma_{sr}. This instability is also relevant to turbulent burning, as discussed in Section 1.5.6. Figure 1.3 shows a schlieren photograph of a cellular flame, where the normally smooth flame surface has become highly structured.

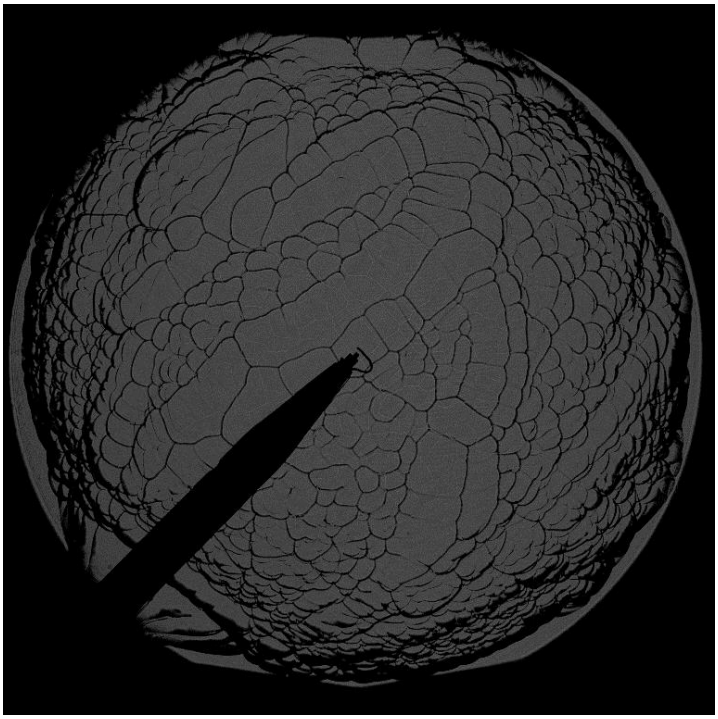

Figure 1.3 Schlieren image of a cellular stoichiometric iso-octane air mixture at 0.5 MPa initial pressure and 87^{o}C initial temperature, reproduced from Mumby (2016)

1.5 Turbulent Burning

This section presents the turbulent combustion theory relevant to this study and is split into several subsections. Section 1.5.1 addresses the definitions of turbulent flame radius and burning velocities employed in this study, including the derivation of turbulent burning velocities from schlieren images. Section 1.5.2 introduces the reaction progress variable, c, and Section 1.5.3 introduces the flame surface density, Σ. Section 1.5.4 describes the method for obtaining turbulent burning velocities from pressure traces and Section 1.5.5 describes the effects of increasing flame radius on the extent of the turbulence spectrum by which a flame is affected. Finally, Section 1.5.6 describes the correlations developed at Leeds to calculate the turbulent burning velocity of a mixture based on the properties of the unreacted mixture.

1.5.1 Flame Radius and Turbulent Burning Velocity Definition

Bradley et al. (2003) have defined a number of reference flame radii for 2D laser sheet Mie scattering images, as shown in Fig. 1.4. These images are generated by laser light scattered by seed particles in the flow, where dark patches indicate that the particles have evaporated or burned due to high temperatures from i.e. combustion. When analysing such images, it was assumed that the turbulent flow field was isotropic at any radius, reaction zone and laser sheet thicknesses were neglected, the extent of reaction was binary i.e. unreacted or fully burned and the unburned and burned gas densities, ρ_u and ρ_b were for the cold reactants and the products at the adiabatic flame temperature, respectively. These assumptions have also been applied in the present work and the resulting definitions extended into the third dimension for use with 3D reconstruction obtained from multiple 2D sheet images.

In Fig. 1.4, R_r represents the root radius, i.e. the smallest spherical radius at which unburned mixture is encountered, R_t is the tip radius, indicating the smallest radius beyond which the gas is fully unburned and the reference radius, R_j, describing a chosen radius between these two extremities, typically where the volume of burned gas outside this radius is equal to the volume of unburned gas within it, where in this case this radius may also be termed R_v. Various masses are also defined, where m_u is the mass of unburned gas outside of the sphere of radius R_t, m_{uo} is the mass of unburned gas in the spherical shell contained between radii R_j and R_t, m_{bo} is the mass of burned gas outside of the sphere of radius R_j, m_{ui} is the mass of unburned gas within a sphere of radius R_J, and m_{bi} is the mass of burned gas within a sphere of radius R_j.

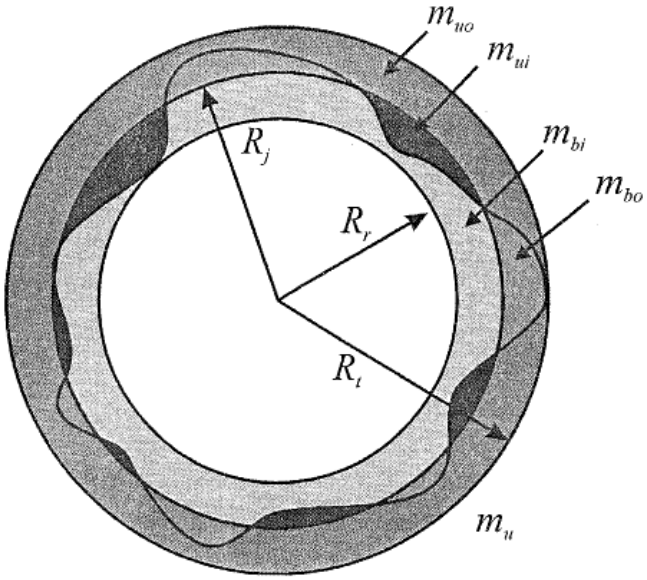

Figure 1.4 Reference radii and associated unburned and burned gas masses for a 2D laser sheet Mie scattering image, reproduced from Bradley et al. (2003)

To allow comparison of 2D laser sheet images with schlieren images, Bradley et al. (2003) arrived at the following relationship based on the analysis of 37 propane/air explosions

$$R_v = \left(\frac{1}{1.11}\right) R_{sch} - 2.1 \tag{1.19}$$

Where R_{sch} is the radius obtained from a schlieren images. The above is stated by the Authors to hold true where $2 \le R_v \le 40$ mm. From the radius R_v, the turbulent burning velocity with reference to consumption of cold reactants may be defined as follows

$$u_{tv} = \frac{\rho_b}{\rho_u} \frac{dR_v}{dt} \tag{1.20}$$

In the present work, 1.19 and 1.20 have been used to calculate turbulent burning velocities from schlieren images for comparison with those obtained from the 3D imaging technique described in Section 2.3.

1.5.2 Reaction Progress Variable

Whereas some Authors (Bray et al. (2005), Nivarti and Cant (2017)), define the reaction progress variable as the extent of reaction across the reaction zone, the Mie scattering images captured in the present study show a binary transition from reactants to products as either unburned reactants or fully burned products. Thus, an alternative definition of the reaction progress variable for turbulent flames is required in the present work. Harker et al. (2012) define the reaction progress variable at a given radius as the proportion of burned gas by volume within an annulus between two similar radii, R_1 and R_2, where the radius in the turbulent flame brush where c = 0.5 is equal to the radius R_v presented by Bradley et al. (2003). A similar approach for the calculation of c is adopted in the present study, with the relevant radii illustrated in Fig. 1.5. This figure shows a cross section through part of a 3D flame along with a spherical shell of inner radius R_1 and an outer radius R_2. The flame surface area within the annulus between R_1 and R_2, the cross section of which is represented by the dashed lines, is denoted as A_j.

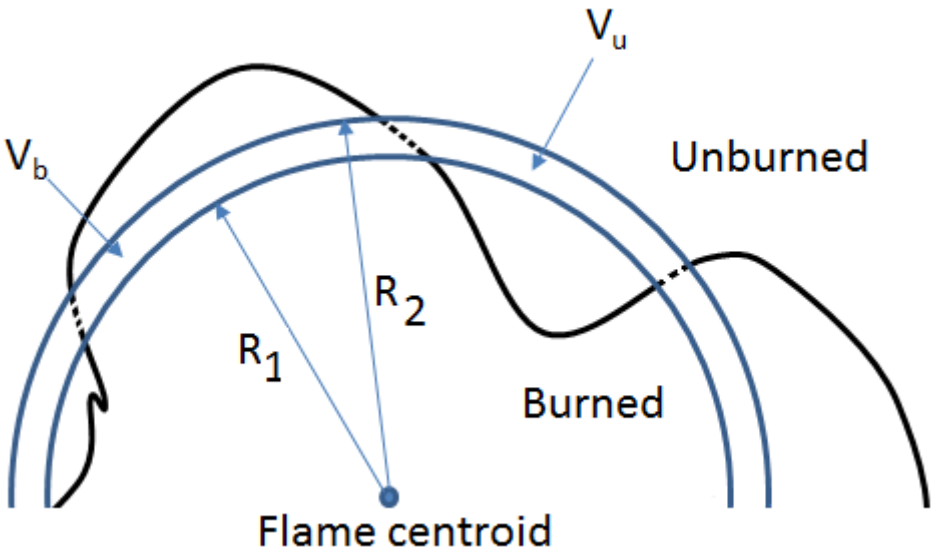

Figure 1.5 A cross section of part of the 3D flame surface showing the burned and unburned region along with a spherical shell of inner and outer radii R_1 and R_2, respectively

The value of c at a radius $\frac{R_1 + R_2}{2}$ is defined as

$$c_{\frac{R_1+R_2}{2}} = \sum_{R_1}^{R_2} \frac{V_b}{V_b + V_u} \tag{1.21}$$

Where V_b and V_u are the volume of burned gas and unburned gas respectively, contained between the radii R_1 and R_2.

1.5.3 Flame Surface Density

The flame surface density, Σ, defined as the flame surface area per unit volume of flame, is a useful parameter for assessing the extent of wrinkling of a flame surface and is also used as a basis for simulation studies of combustion such as those of Hult et al. (2007), Chakraborty and Cant (2013) and Nivarti and Cant (2017). It is however, difficult to measure from 2D laser sheet images, requiring painstaking diagnostics (Bradley et al. 2009). In the present study, it is calculated for 3D reconstructions using a similar algorithm to that employed for measuring c.

The value of Σ at a radius of $\frac{(R_1 + R_2)}{2}$ is defined as

$$\Sigma_{\frac{(R_1+R_2)}{2}} = \frac{\sum_{r_1}^{r_2} A_j}{\frac{4\pi\left(R_2^3 - R_1^3\right)}{3}} \tag{1.22}$$

Where $\sum A_j$ is the summation of A_j previously defined. The thickness of the spherical shell ($R_2 - R_1$) employed here was 1 mm, chosen so as to minimise noise without significantly compromising the resolution. Both values of c and Σ thus determined were recorded as a function of radius.

1.5.4 Measurement of Turbulent Burning Velocity from Pressure Traces

Bradley et al. (2011) present a method for the determination of the mass turbulent burning velocity, u_{tm}, from pressure trace measurements. Based on the assumption that the pressure rise in the bomb due to combustion is proportional to the mass of fuel/air mixture consumed, the following applies

$$m_b = \left(m_u + m_b\right)\left(\frac{p - p_0}{p_f - p_0}\right) \tag{1.23}$$

Here, m_u and m_b are the masses of unburned and burned gas, p_0 and p_f are the initial and final pressure and p is the pressure at any instant in time. By further derivation, the radius r_m, the radius of an equivalent sphere where the mass of burned gas outside is equal to the mass of unburned gas inside, may be calculated as

$$r_m = R\left\{1 - \left(\frac{p_0}{p}\right)^{1/\gamma_u}\left[\frac{p_f - p}{p_f - p_0}\right]\right\}^{1/3} \tag{1.24}$$

Where R is the spherical bomb radius obtained from its measured volume and γ_u is the ratio of specific heats for the unburned mixture. This ultimately leads to the following expression to calculate u_{tm}

$$u_{tm} = \frac{R\left(\frac{p_0}{p}\right)^{1/\gamma_u}\frac{dp}{dt}}{3\left(p_f - p_0\right)\left\{1 - \left(\frac{p_0}{p}\right)^{1/\gamma_u}\left(\frac{p_f - p}{p_f - p_0}\right)\right\}^{2/3}} \tag{1.25}$$

1.5.5 Evolution of the Effective Root Mean Square Turbulence Velocity

A flame developing under turbulent conditions will initially be smooth, possessing a laminar-like appearance and will not be exposed to the full spectrum of turbulence present; whilst the flame is in its early stages, only the smallest turbulence wavelengths will affect the surface structure, whilst larger wavelengths will merely deflect it (Aleiferis et al. 2004). As the flame grows, it will become susceptible to the full range of turbulence scales present and the effective root mean square (RMS) turbulence intensity acting on the flame, u'_k, will approach the RMS turbulence intensity present in the vessel, u' (Bradley et al. 2009). As a consequence, the turbulent burning velocity, turbulent flame brush thickness and mass burning rate approach their fully developed values (Abdel-Gayed et al. 1987); in the latter case, where the flame thickness is smaller than the smallest scale of turbulence present, the turbulence acts to wrinkle the flame front, increasing its surface area and thus the burning rate (Halter et al. 2009).

Based on the original study by Abdel-Gayed (1987), Bradley et al. (2009) express the evolution of u'_k/u' as follows:

$$\frac{u'_k}{u'} = \left[\frac{15^{0.5}}{R_\lambda} \int_{\bar{k}_{\eta k}}^{\bar{k}_{\eta G}} S\left(\bar{k}_\eta\right) d\bar{k}_\eta \right]^{1/2} \tag{1.26}$$

Where $\bar{S}\left(\bar{k}_\eta\right)$ is the non-dimensional power spectral density function, and is expressed in terms of $\bar{k}_\eta$, a dimensionless wavenumber obtained from the wavenumber multiplied by η, the Kolmogorov distance scale. The limits $\bar{k}_{\eta G}$ and $\bar{k}_{\eta k}$ represent the smallest and largest possible wavelengths. From the numerical integration of Eq. 1.26, between the limits:

$$\bar{k}_{\eta k} = \left(\frac{32\pi}{15^{0.25} n} \right) R_\lambda^{-1.5} \tag{1.27}$$

And:

$$\bar{k}_{\eta G} = \frac{2\pi\eta}{l_G} \tag{1.28}$$

where n is the number of integral length scales, R_λ is the Reynolds number based on the Taylor scale and l_g is the Gibson scale, Bradley et al. (2009) present a plot of u'_k/u' against n, shown in Fig. 1.6. This figure shows that the greatest increase in u'_k occurs between ignition and when the flame has reached a radius four times the size of the integral length scale of turbulence. Thereafter, there is a diminishing return where there is an asymptotic increase towards $u'_k = u'$. This figure has been directly used in the present work to determine u'_k/u' using the method described in Section 4.2.

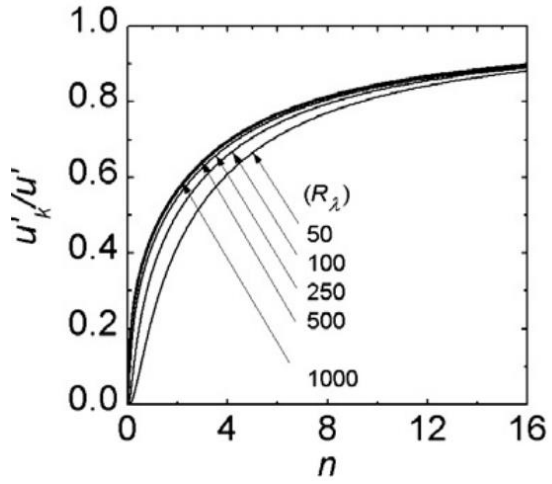

Figure 1.6 Development of u'_k/u' with increasing flame radius at various Reynolds numbers, reproduced from Bradley et al. (2009)

1.5.6 Calculation of u_t from the Correlation of Turbulent Burning Velocity Measurements

Based on correlations of experimentally obtained turbulent burning velocities of ethanol/air mixtures between equivalence ratios of 0.7 and 1.5 at 0.1 to 1.2 MPa starting pressure and an earlier study (Bradley et al. 2009) utilising propane/air mixtures, Bradley et al. (2011) present an expression to obtain turbulent burning velocities of mixtures based on their strain rate Markstein number, Ma_{sr}, laminar burning velocity, u_l, the integral length scale of turbulence, l, the kinematic viscosity, v and the root mean square (RMS) turbulence velocity, u'. Schlieren imaging and pressure trace recording were employed to yield u_{tv} and u_{tm} where these are related as follows

$$\frac{u_{tm}}{u_{tv}} = \left(\frac{r_v}{r_m} \right)^2 \tag{1.29}$$

A further contributory factor is the Karlovitz number, K, which is the ratio of chemical to eddy lifetimes and a descriptor of the wrinkling effect of turbulence on a flame surface. This is defined as

$$K = \left(\frac{u'}{\lambda} \right) \left(\frac{\delta_l}{u_l} \right) \tag{1.30}$$

Where u'/λ is the root mean square strain rate. If $R_\lambda = 4R_l^{0.5}$ and given that $\delta_l = v/u_l$, this then becomes

$$K = 0.25 \left(\frac{u'}{u_l} \right)^2 R_l^{-0.5} \tag{1.31}$$

Where R_l is the Reynolds number based on the integral length scale. From the correlations and based on the above parameters, the turbulent burning expression takes the following form

$$U = A_m \alpha K^{\beta} = \frac{u_{tm}}{u'_k} \quad \text{for } K \geq 0.05 \tag{1.32}$$

Where A_m is a constant relating to the surface from which the turbulent burning velocity is defined and takes a value of unity here. The constants α and β are expressed in terms of Ma_{sr} as follows

$$\alpha = 0.0227(30 - Ma_{sr}) \quad (1.33)$$

$$\beta = 0.01(Ma_{sr} - 30) \quad (1.34)$$

These constants are applicable for positive values of Ma_{sr}, with different numerical values for sub-unity Ma_{sr}. These are not presented here as only positive Ma_{sr} have been employed in the present work. Thus, using the relations given in Eq. 1.30 to 1.34, values of u_{tv}/u_l were obtained for each u' value used in this study. To obtain generality, the values were calculated in each case for $u'_k/u' = 0.6$ as discussed in Section 4.3.

Using these correlations, a plot illustrating the variation of U with K was generated by Bradley et al. (2013) as shown in Fig. 1.7, for a number of Ma_{sr} and seven different fuels at a variety of equivalence ratios. Zone A illustrates the region where the effects of cellular flame enhancement and turbulent wrinkling are coupled, leading to high values of U. Zone B represents burning in the absence of instabilities. In this zone, mixtures with more negative Ma_{sr} show much greater burning rates. The broken regions represent the results of calculations where experimental validation has not been carried out. The dotted curve represents the boundary where the probability of an initial flame kernel propagating falls to 0.8, where the K value corresponding to this is denoted $K_{0.8}$. Beyond this lies Zone C, where the observed flame front starts to become les coherent, making measurements of u_t less reliable. This zone also indicates increasing quenching, with this beginning at lower values of K for positive Ma_{sr}.

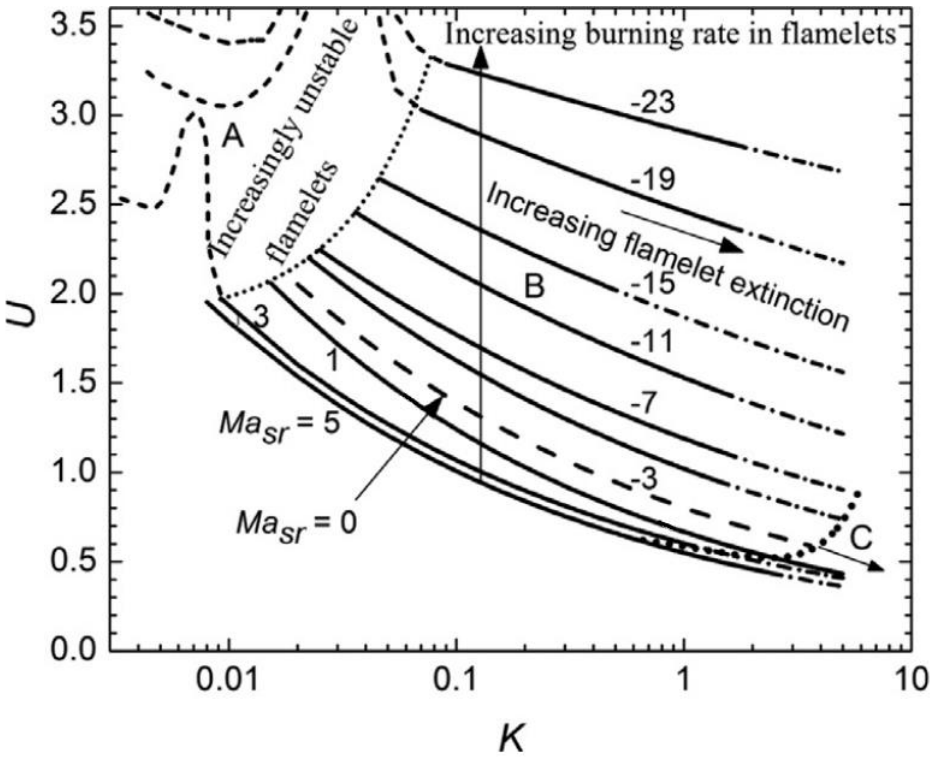

Figure 1.7 Variation in *U* with *K*, as presented by Bradley et al (2013)

1.6 Direct Numerical Simulation Description

Nivarti and Cant (2017) presented a direct numerical simulation (DNS) study of turbulent premixed combustion of a methane/air mixture in a rectangular inflow/outflow duct at 0.1 MPa pressure and with a unity Lewis number. A single step (chemistry) Arrhenius expression was used to model the reaction rate as

$$\dot{\omega}_F = B\rho(1-c)e^{-E_a/(RT)} \tag{1.35}$$

Where B is the pre-exponential factor, ρ is a density, E_a is the activation energy, R is the universal gas constant and T is the temperature of the cold reactants (300K). The laminar flame speed, s_L, was constant at 0.39 m/s with a laminar flame thickness of 0.36 mm. The reaction progress variable, c, is defined as

$$c \equiv \frac{(Y_u - Y)}{(Y_u - Y_b)} \tag{1.36}$$

Here, Y_u is the fuel mass fraction in the unburned gas, Y_b is the fuel mass fraction in the burned gas and Y is the fuel mass fraction at a given point in the reaction zone. Note that the definition of c used by these Authors is different to that employed in the present study as defined in Section 1.5.2.

The turbulent burning velocity, s_T, takes the form of the global transformation rate of reactants to products across the turbulent flame brush defined as

$$s_T \equiv \frac{1}{\rho_u Y_{u,F} A_0} \int_V \dot{\omega}_F \, dV \tag{1.37}$$

Where ρ_u is the unburned gas density, $Y_{u,F}$ is the fuel mass fraction in the unreacted mixture, A_0 is the cross-sectional area of the flow and V is the volume of the domain, which physically measured 5 mm x 5 mm x 15 mm and incorporated 288 x 96 x 96 grid points with uniform spacing of 52.3 μm.

The Batchelor-Townsend turbulence spectrum was used as it represents homogeneous, isotropic turbulence in the final period of decay, with an integral length scale of 0.99 mm. Turbulence was forced in the inflow to the domain and decayed towards the outflow.

The surface area of the turbulent reaction zone, A_T was measured by integrating Σ at isovalues of the reaction progress variable, $c = c^*$. The surface area ratio, A_T/A_L, was then obtained from the cross sectional area of the duct, A_L.

These Authors conducted simulations at 5 values of u'/u_l and in each case the calculation of s_T was carried out after 4 eddy turnover times, where the flow kinematics had reached statistical convergence. The results of this are shown in Fig. 1.8

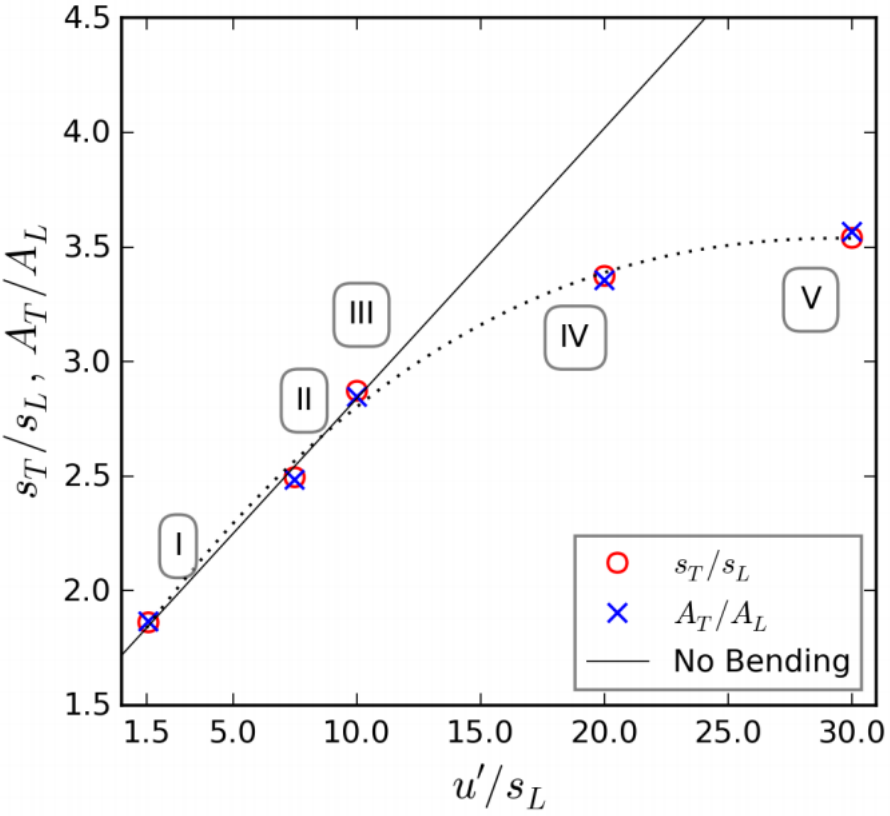

Figure 1.8 Variation of burning velocity ratio with normalised RMS turbulence intensity, reproduced from Nivarti and Cant (2017)

It can be seen in Fig. 1.8 that at low u', a linear increase in this yields a proportional, linear increase in both the surface area and burning. Beyond a u'/s_L value of around 10 in this case, the rate of increase in these ratios can be seen to reduce, termed the "bending effect". These Authors discovered that beyond the onset of bending, the reaction layer was preserved, thus suggesting that quenching was not the reason for the reduction in burning rate.

As the surface area ratio and burning velocity ratios assume nearly identical values, this indicates that an inhibition of the increase in growth of the flame surface is responsible for the bending effect. The Authors found that while the smaller eddies could create curvatures on the flame surface, they could not strain it. Additionally, areas of high curvature showed predominantly negative curvatures, which led to negative stretch rates which tend to decrease the flame surface area. A comparison between these results and the results of the present study is presented in Section 5.3.

Chapter 2 - Experimental Apparatus and Technique

2.1 Introduction

This chapter presents the apparatus and experimental techniques used to study the temporal development of premixed turbulent flames, in three dimensions, in an explosion bomb. Whilst 3D imaging and flow field analyses of burners and gas-jets have been carried out in previous studies (Section 1.2), the Leeds MKII fan-stirred bomb has been utilised in this study to allow the investigation of developing flames at engine-like conditions. To this end, a high-speed 3D laser-sheet imaging technique has been developed by the present Author.

This chapter is divided into several sections. Section 2.2 describes the Leeds MKII fan-stirred combustion vessel (hereafter described as "the bomb") and its ancillary components, including the laser ignition system used to ignite mixtures and the schlieren imaging system used to obtain laminar burning velocities and Markstein lengths for the mixtures employed in this study.

Section 2.3 presents the 3D, high-speed laser-imaging technique (hereafter referred to as the "swinging-sheet" system) including details of the design and development of this system and Section 2.4 describes the experimental techniques, including the thermodynamic properties of the mixtures used and the calculation of the required liquid fuel volumes and gaseous fuel partial pressures.

2.2 Combustion Vessel and Ancillary Systems

The combustion vessel used for all experiments in this study was the Leeds MKII fan-stirred bomb (hereafter referred to as "the bomb"). Shown in Fig. 2.1, this spherical vessel was constructed from SAE316 grade stainless steel and was capable of withstanding the temperatures and pressures generated by explosions from initial temperatures and pressures up to 600K and 1.5 MPa respectively. The internal diameter of this vessel was 380 mm, with a total internal volume of 0.30372 m^3. Optical access was possible from three pairs of orthogonally opposed, 150 mm diameter, 100 mm thick quartz windows. Turbulence was generated by four identical eight-bladed fans, each driven by an 8 kW motor, at speeds continuously variable in the range of 212 – 10,000 rpm (3.3 – 176 Hz). This afforded *u'* values of between 0.25 and 11 m/s with the integral, Taylor and Kolmogorov length scales of 20 mm, 3 mm and 0.15 mm, respectively (Harker et al. 2012).

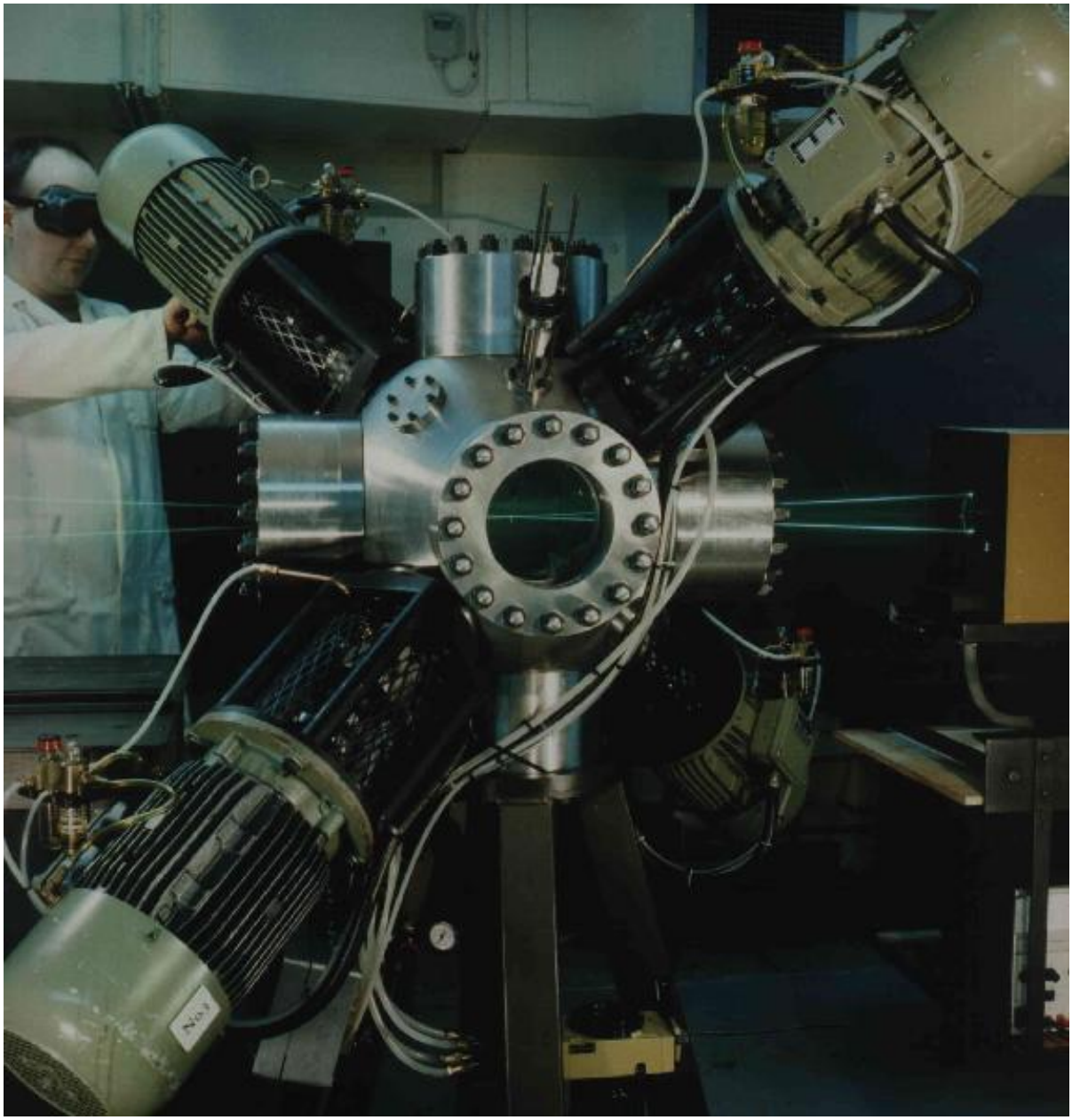

Figure 2.1 Leeds MKII fan-stirred bomb, reproduced from Tripathi (2012)

2.2.1 Auxiliary Systems

Various instruments were used to monitor and control the starting pressure and temperature of mixtures in the bomb, initiate combustion and to track the progress of combustion over time. They are discussed below.

2.2.1.1 Pressure measurement

The pre-combustion absolute pressure in the bomb, during mixture preparation and immediately prior to ignition, was monitored by a Druck PDCR 911 pressure transducer, with a range of 0-1.5 MPa, connected to an LCD display in the protected area of the laboratory. This transducer was calibrated weekly against a mercury barometer also present in the laboratory, with the bomb open to ambient pressure. The transducer was isolated from the rapid pressure rises experienced during combustion by a swage lock ball valve, which was closed immediately prior to triggering an explosion.

The pressure rise during combustion was monitored using a Kistler 701A dynamic pressure transducer, flush-mounted with the inner surface of the vessel. This transducer produced a charge output over a pressure range between 0-25 MPa. This charge output was passed to a Kistler 5007 charge amplifier, which converted the charge to a voltage signal. This voltage signal was supplied to a National Instruments NI6361 DAQ analogue to digital converter (ADC) where it was digitised prior to interpretation by LabVIEW software. For each explosion, a total of 250,000 samples were collected at a frequency of 50 kHz. The sensitivity of the charge amplifier (in Volts output per MPa of pressure input) was set such that 10 Volts output would be produced at a pressure slightly above the expected peak combustion pressure, in order to maximise the signal to noise ratio. For all of the work carried out here, a sensitivity of 0.1 MPa/Volt was employed. Initiation of pressure recording was achieved using the synchronisation and triggering system described in Section 2.2.2.5.

2.2.1.2 Temperature measurement and control

The temperature of the gases within the bomb during mixture preparation and immediately prior to ignition was monitored using a K-type thermocouple (25 μm chrome-alumel wire), sheathed within a 1.5 mm diameter stainless steel tube and located at a distance of 75 mm from the vessel inner wall. The temperature was displayed on the LCD output of a CAL320 PID temperature controller, mounted in the protected area of the laboratory.

Two coiled heater elements, each with a heat output of 2 kW, were mounted on opposite end plates in the bomb. As the heaters were not used in this investigation, full details of the heater control system are not presented here, but are available in Mumby (2016). All experiments in this investigation were carried out at a temperature of 298K to minimise burning rates whilst increasing the Karlovitz number as discussed in Section 4.1. This necessitated very gentle, even heating of the bomb. The electric heater were unsuitable as they produced hot spots and thus a poor distribution of heat in the vessel. Therefore, heating was achieved by combusting stoichiometric methane/air mixtures under turbulent conditions, to ensure an even wall-temperature distribution. Care was taken to ensure removal of all condensed water from the vessel resulting from combustion prior to any experiments.

2.2.1.3 Electronic spark ignition with a spark plug

A conventional spark-ignition system was used only in conjunction with the schlieren system for measuring laminar burning velocities. The ignition unit was a variable ignition energy type, described in Tripathi (2012).

The spark plug, shown in Fig. 2.2, was a miniaturised type developed at the University of Leeds, designed to minimise interference of the turbulent flow. The replaceable spark plug tip insert consisted of an inner wire (the anode), of 1.5 mm diameter, sheathed in a ceramic insulating material. This was contained within an outer stainless steel sleeve, which acted as the cathode. The tip was mounted in a thicker stainless steel outer body, which formed an electrical connection with the cathode of the spark plug tip and was connected to earth. Uncontrolled ignition from residual ignition energy was thus avoided (Kondo et al. 1997). The spark gap, measured by means of feeler blades, was set to 1.25 mm for all experiments.

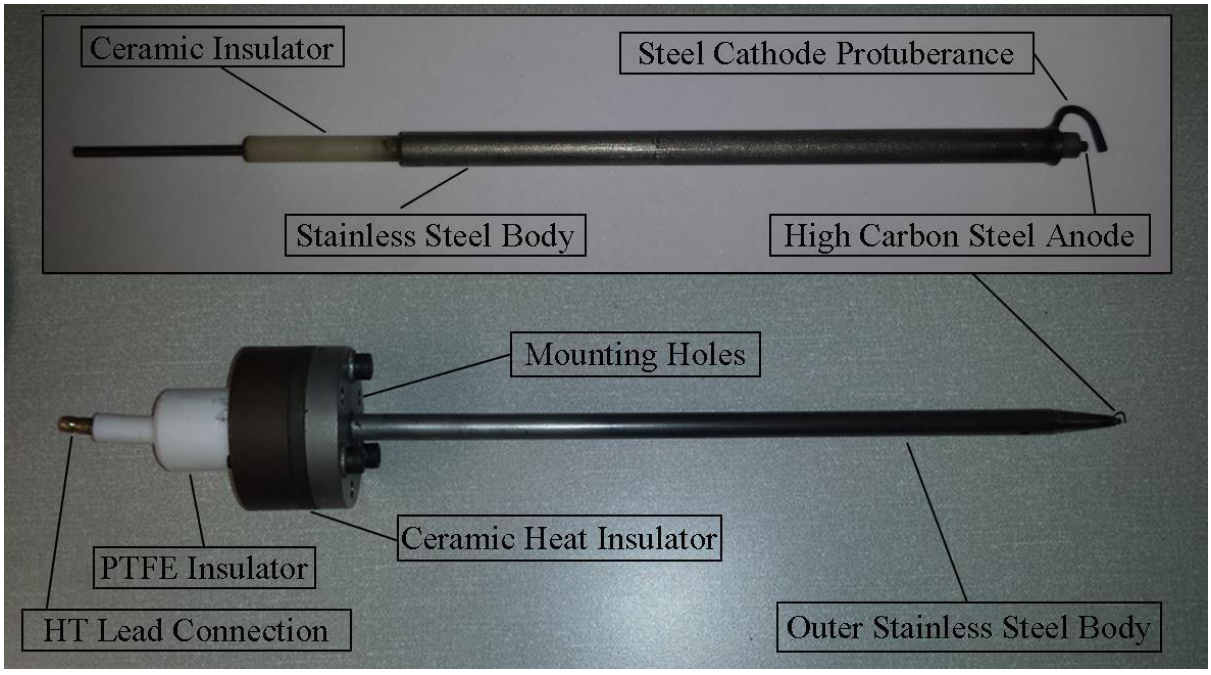

Figure 2.2 Spark plug tip and holder, image from Mumby (2016)

2.2.1.4 Laser Ignition System

The electronic ignition system discussed in Section 2.2.2.3 relied on a spark plug protruding into the centre of the bomb. This arrangement would not only have encumbered the path of the laser sheets (Section 2.3) passing through the bomb, resulting in laser sheets with significant gaps downstream of the spark plug, but would have also disrupted the turbulence flowfield at the centre of the vessel. Therefore, an adapted version of the laser ignition system described by Bradley et al. (2004) was used as the main ignition source in this work.

A Spectron Laser Systems SL800 Nd:YAG laser produced the required laser light, at a frequency of 1064 nm which was invisible to the operator. By frequency-doubling the light to 532 nm, the safety of the system was improved. The pulse repetition rate employed here was fixed at 10 Hz. The pulse energy of the beam was measured using a Spectron Laser Systems laser power meter, which was provided with the laser. This generated a voltage output which could be interpreted by an oscilloscope. The voltage recorded by the oscilloscope was then compared with a look-up table provided by the laser manufacturer, which provided an estimate of the pulse energy at the employed laser light wavelength. The pulse energy measured here was around 200 mJ, which proved sufficient to ignite all mixtures used in this work.

A schematic of the arrangement used in this work is shown in Figure 2.3. The beam vertically exited the laser head and was first reflected by a Thorlabs 25.4 mm diameter 2nd harmonic Nd:YAG mirror. The reflectance of this mirror was quoted by the manufacturer as 98% at a 45^{o} angle of incidence. This mirror was positioned at an angle of 45^{o} with reference to the initial beam trajectory, to produce a horizontal beam path. The beam was then expanded by a 47 mm (f = -50 mm) plano-concave lens. A 145 mm plano-convex lens (f = 1000 mm) was placed downstream of this lens, which began the contraction of the beam. The beam was then focussed to a waist (with diameter d_f) at the centre of the bomb using a 150 mm (f = 450 mm) plano-convex lens. This arrangement was used to produce a tighter focus (i.e. a smaller beam waist over a shorter distance) at the centre of the bomb to avoid unwanted sparks either side of the point of focus. The beam diameters throughout the setup are unknown due to the irregular shape of the beam produced by the laser.

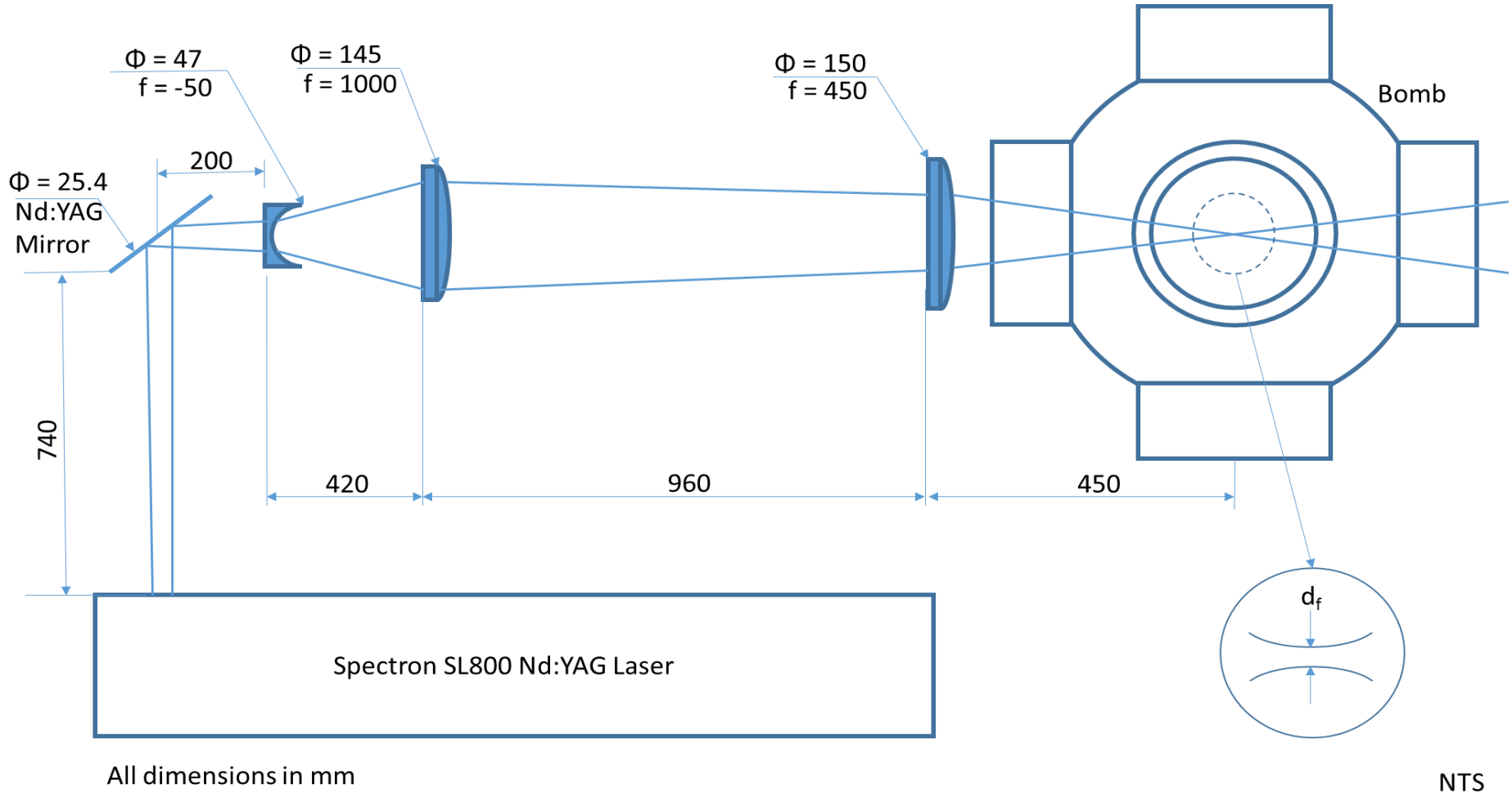

Figure 2.3 Laser ignition system

2.2.1.5 High-speed schlieren photography

High speed schlieren cine photography was employed to track the development of laminar and turbulent flames within the vessel. This technique allows the visual detection of the flame front through the density gradient between the burnt and un-burnt mixtures which cause varying degrees of light refraction. The technique was first used at Leeds by Bradley and Hundy (1971) and has become well established for combustion studies at Leeds (Al-Shahrany et al., 2005; Ormsby, 2005; Tripathi, 2012) and at many other institutes (Broustail et al., 2011; Hu et al., 2009; Jerzembeck et al., 2009).

Figure 2.4 shows a schematic of the schlieren optical configuration. The required light was provided by a 20mW (regulated to 5mW), 635nm LED laser. This was then focused to a point at a pinhole by several plano-convex lenses in series, with an overall focal length of 20 mm. The light then expanded onto a 200 mm (f = 800 mm) plano-convex lens, collimating a 150mm beam through the vessel and its contents prior to focussing of this beam to a point at a 0.5 mm diameter pinhole by another 200 mm (f = 800 mm) plano-convex lens.

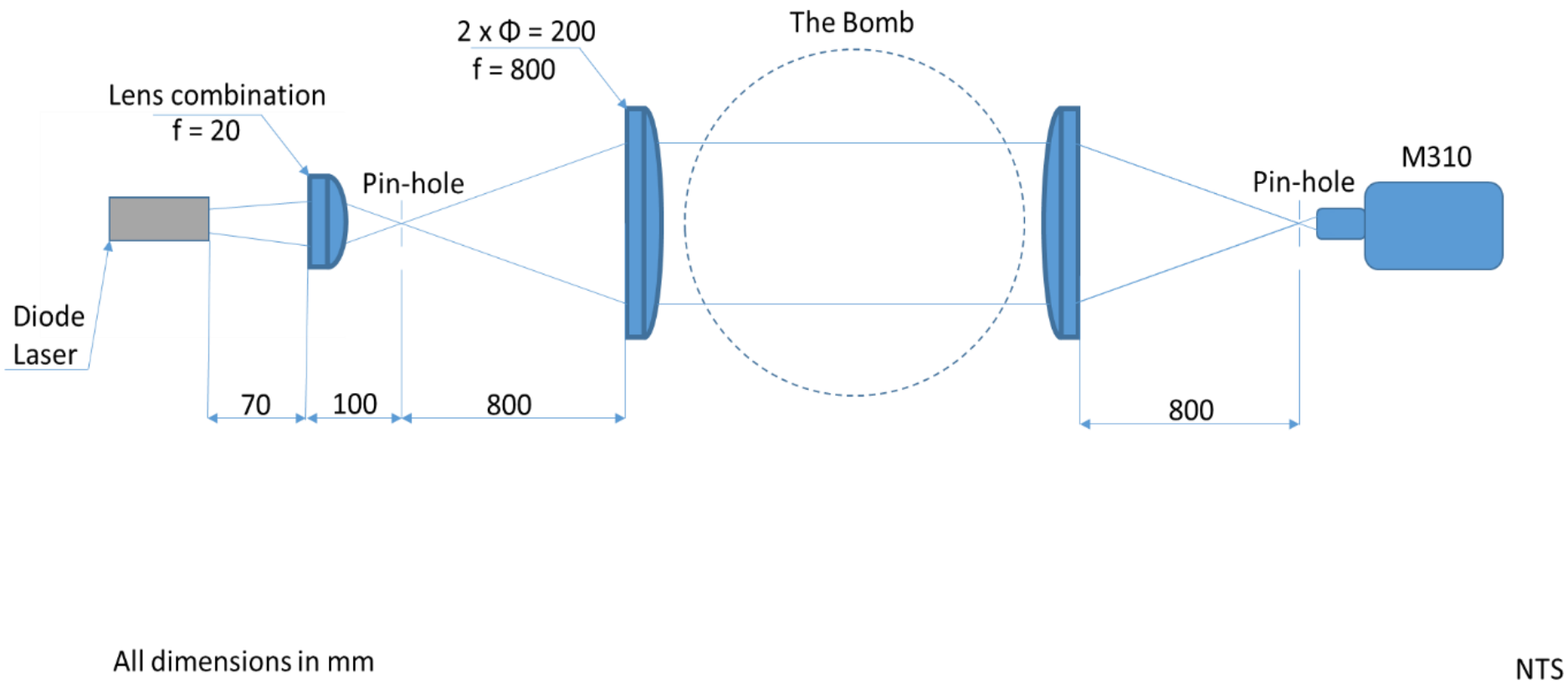

Figure 2.4 Schlieren imaging system used in the present study

A high speed digital Phantom M310 camera, using an 80mm Nikon lens, recorded the resulting image on its internal memory of 512MB. The camera was positioned such that the maximum field of view of 150mm diameter, limited by the vessel windows, took full advantage of the camera resolution of 768 x 768 pixels. This resulted in a recorded square view of 159 x 159mm and thus a pixel size of 0.20708mm/pixel. This resolution was more than sufficient to capture a defined flame edge and detailed flame structure, whilst allowing the ample sampling rate of 5400 frames per second (fps). The exposure time was set to 6μs. Phantom camera software was used to download the resulting ".cine" video file from the camera via an Ethernet cable and allowed the recorded images to be converted to a string of 8-bit ".bmp" images for interpretation by an automated image processing program, as discussed in Section 3.5.

The camera software also featured an 'extreme dynamic range' (EDR) function. This involved a pre-set pixel saturation threshold which, once exceeded, reset the exposure time within the global exposure time of 6μs. This served to slow down pixels which were charging so fast that they would become saturated before the global exposure time expired, thus allowing much better definition of images featuring both low and high intensity light.

At the start and end of each day of experiments, confirmation of the beam collimation and pixel size was carried out. To do this, a 10 mm by 10 mm grid, on a transparent acetate sheet, was placed between the window and the plano-convex optic on one side of the vessel. An image was then recorded and the pixel size determined on the left, right, top, bottom and centre of the image using an image analysis tool developed in MATLAB. This superimposed a computer generated best fit grid of known size and pixel resolution over the image of the acetate grid. This was repeated on the other side of the vessel and the average of both sides taken. If necessary, the collimating lens was adjusted and these steps repeated until the pixel size was equal on both sides of the vessel.

2.3 Swinging-Sheet 3D Laser Imaging System

This section presents the three-dimensional multiple laser sheet imaging technique developed by the present Author. The technique allows for fully time-resolved imaging of developing turbulent premixed flames. Turbulent flame structure is an inherently 3D phenomenon and 2D flame imaging techniques are not able to provide an insight into the third dimension (Section 1.6). Further, computer simulation studies require experimental data for validation (Section 1.6.1) which have previously been unavailable.

Section 2.3.1 describes the imaging laser used in the investigation and the optics used to form the pulsed laser beam into a series of thin sheets. Section 2.3.2 presents the electronic system which allowed the rotating mirror, laser ignition system, camera, imaging laser and the dynamic pressure recording equipment to be synchronised with each other. The effects of the rotating mirror on the paths of the individual laser sheets are discussed in Section 2.3.3 and the characteristics of seed particle generation are given in Section 2.3.4.

2.3.1 Laser and Sheet-Forming Optics Description

The technique developed in the present work used a number of lenses to form a pulsed laser beam into a series of very thin laser light "sheets", which were swept through the bomb using a rotating polygon mirror. Micron-size olive oil droplets, as described in Section 2.3.3 were present in the initial mixture in the bomb, which reflected laser light from the sheets into an imaging camera via a Mie scattering process. Each laser sheet therefore generated a "slice" through a developing flame, where dark regions in the captured images show the presence of burned gas and lighter regions show unburned gas which is visualised by seed particles which have yet to be evaporated.

Shown in Figure 2.5 is a simplified schematic illustrating the shaping of the laser light pulses into successive sheets. A more detailed diagram is given in Figure 2.6 showing a vertical view of the full layout of the optical train and the true path of the laser light into the bomb. Pulsed laser light at a wavelength of 532 nm was generated by a Laser Lines DM60-532DH dual-cavity Nd:YAG laser, where each laser cavity was capable of repetition rates between 5 and 30 kHz. By staggering the pulsing of the two cavities, an overall pulse frequency of 60 kHz was possible with a pulse energy of 1.9 mJ.

As the laser and bomb were not at an equal height, it was necessary to first steer the beam using a periscope, consisting of two 25.4 mm Nd:YAG mirrors angled at 45^{o} with respect to the beam. It was then expanded by a 50.8 mm (f = -100 mm) plano-concave lens to a diameter of approximately 23 mm, prior to focussing it at the centre of the bomb by a 50 mm (f = 250 mm) plano-convex lens. The initial expansion of the beam was necessary to ensure a tight beam focus at the centre of the bomb over the large focal distance.

Two cylindrical lenses, of f = 38.1 and f = 25 mm, were used to vertically expand the laser beam into a thin sheet whilst preserving the horizontal contraction. By using two cylindrical lenses, the beam shaping could be optimised by varying the spacing between the lenses. After shaping the beam, successive pulses were swept through the bomb by reflection off a Lincoln Laser 16-sided polygon mirror, rotating at 10 Hz at the motor shaft. Images were captured using a Phantom M310 camera, using a fixed focal length Nikon Nikkor 50 mm lens, at a resolution of 200*256 pixels and a framing rate of 49 kHz. A faster framing rate would have been possible at a significantly lower resolution, however a higher resolution was favoured for use in the present work.

The pixel size was determined using a similar method to that described in Section 2.2.5, but here the 10 mm by 10 mm acetate grid was attached to an opaque background and was placed in the centre of the combustion vessel. An image was taken and then the grid was moved away from the camera by 75 mm to replicate where the furthest laser sheet from the camera would fall. An image was taken in this position and the grid moved 75 mm closer to the camera than the centre of the bomb and a further image taken. In each case, the image was checked for focus and the camera lens adjusted to obtain good definition, if required. This required a large depth of field, which led to consistent image quality regardless of the location of the sheets in the bomb. The pixel size was then calculated as described in Section 2.2.5 for the image captured with the grid at the centre of the bomb.

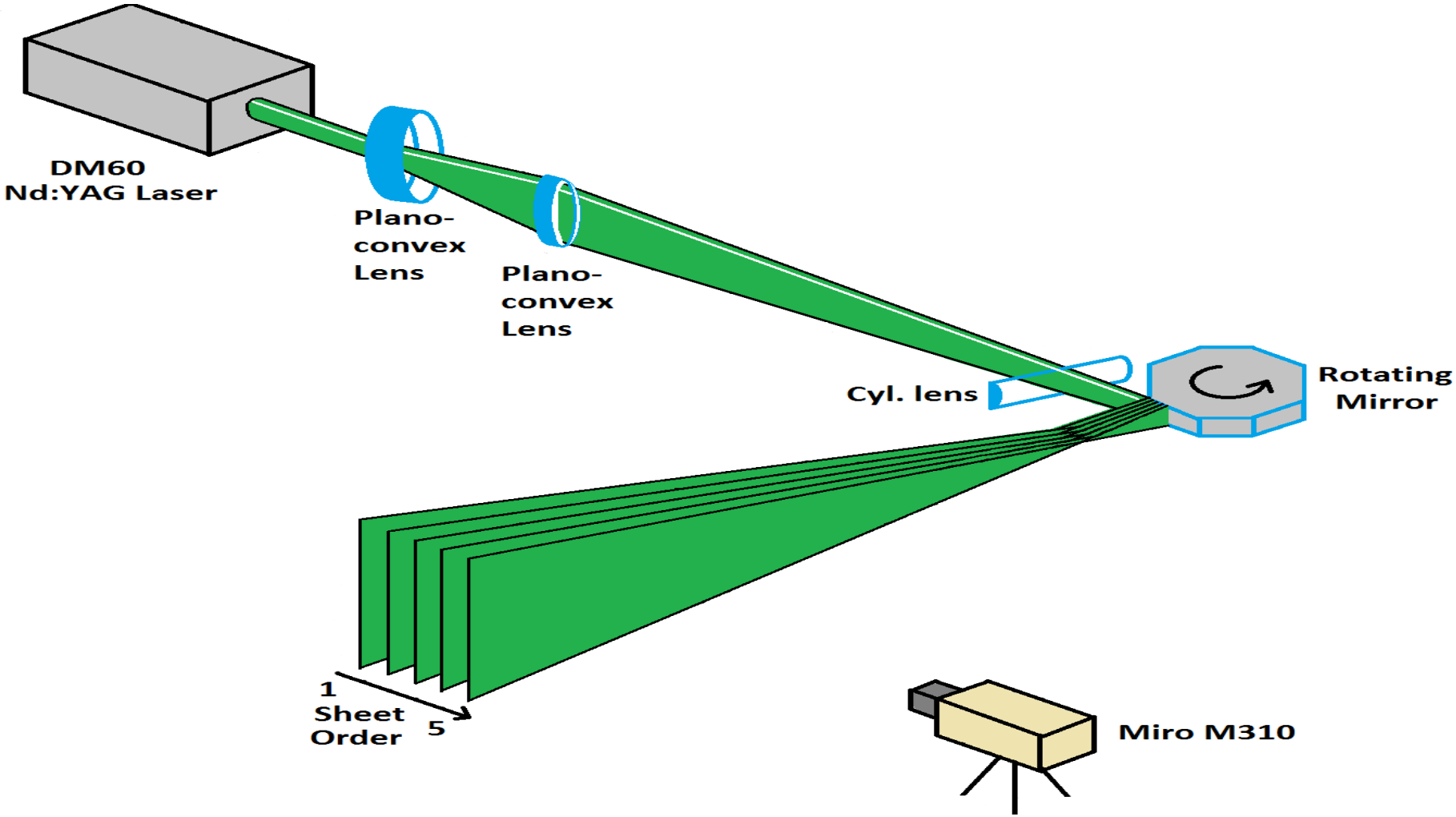

Figure 2.5 Simplified schematic of the swinging-sheet optical setup

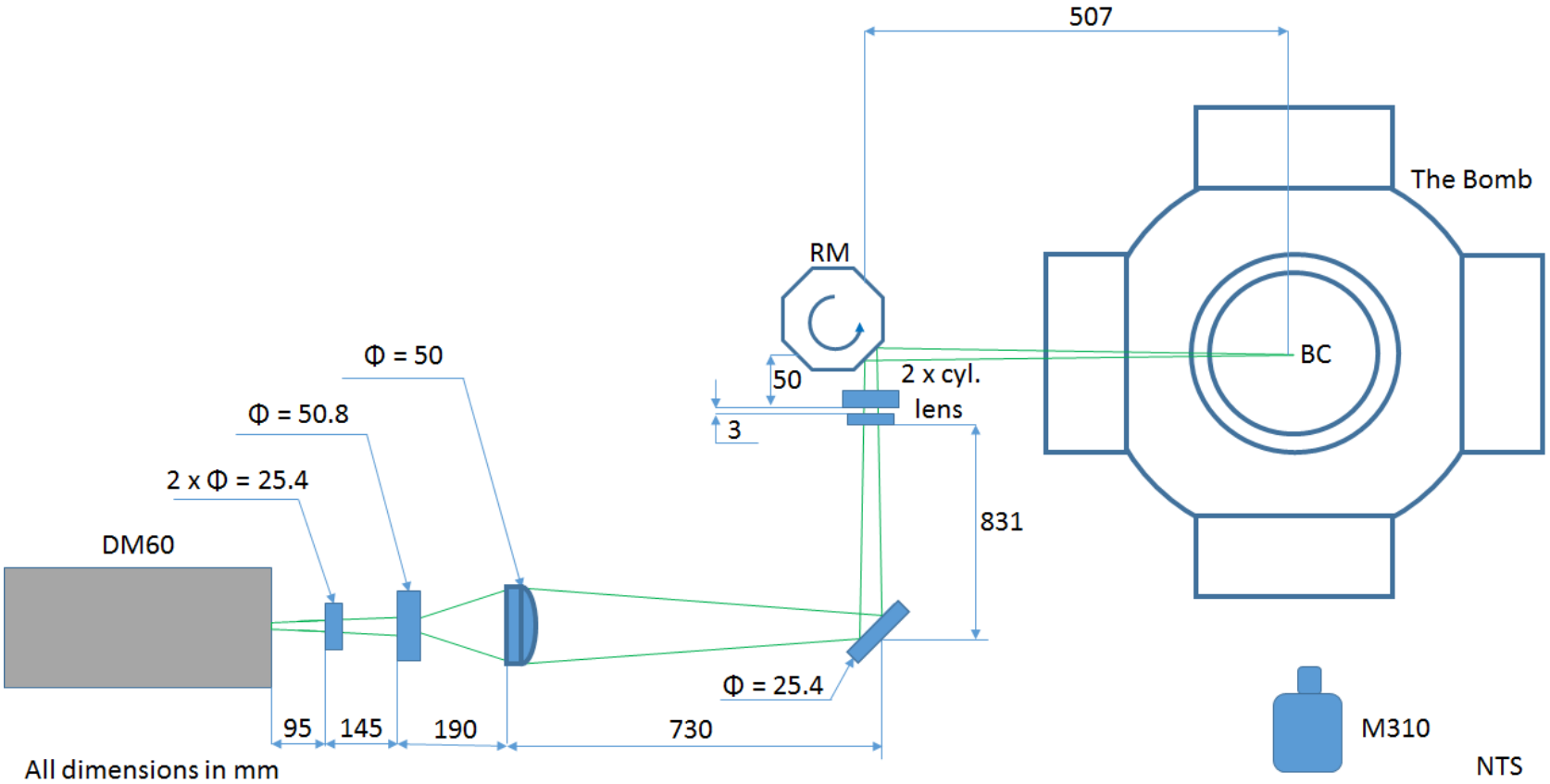

Figure 2.6 Detailed vertical view of the swinging-sheet arrangement

Calculations were performed to determine approximate sizes and focal lengths of the lenses required to optimise the system for maximum sheet height and minimum sheet thickness across the entire region of interest, while ensuring that the laser sheets passed through both bomb windows without impinging on the bomb metal. The latter measure was required to avoid reflections inside and outside of the vessel which would have interfered with the imaging and posed a safety risk, respectively. Using the diameter of the bomb windows and Pythagoras's Theorem, a cubic region in the centre of the bomb of 106 mm in all directions was determined as the maximum size of a cube which would fit through the bomb windows. This was important as it defined the boundaries through which the laser sheets would be required to fit whilst maximising the image size.

Shown in Figure 2.7 is a representation of the initial expansion of the beam by the plano-concave lens (designated Lens L1). The light leaving the laser diverged with a far-field divergence half angle of 44 milliradians and an initial beam diameter of 3.7 mm (Laser Lines, 2016). Using these two statistics, the Tangent rule was used to calculate the distance between the laser head exit and the theoretical point source of light behind it. This distance, plus the distance between the laser head and Lens L1, is designated a_{L1} . The following relation was used to determine the effective focal length of this lens (Hecht 1989, p138)

$$a'_{L1} = \frac{1}{\frac{1}{f_{L1}} - \frac{1}{a_{L1}}} \tag{2.1}$$

Where f_{L1} is the focal length of the lens and a' is the distance between the lens to the focal point. The angle θ_L is the far-field divergence half angle. The beam diameter incident on Lens L1, d_{bL1}, is given by

$$d_b = 2a_{L1}.Tan\theta_L \tag{2.2}$$

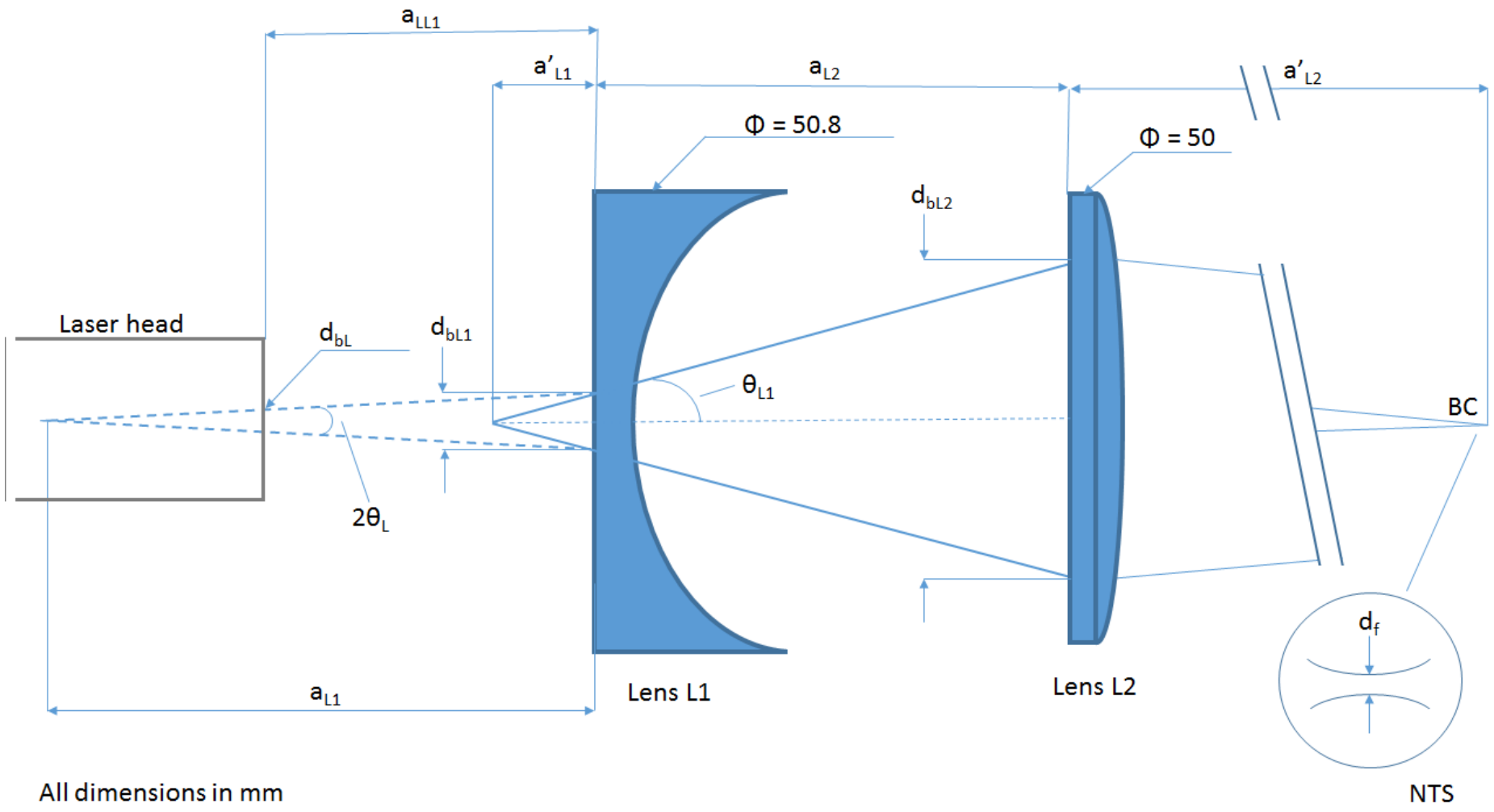

Figure 2.7 Shaping of the laser beam to a small waist at the bomb centre

A similar approach was used to calculate the diameter of the expanded beam incident on the spherical plano-convex lens used to contract the laser light to a point at the centre of the bomb (BC in Fig. 2.7). Figure 2.8 shows an enlarged view of the laser focus. It does not produce an infinitesimal "point", but yields a waist of finite diameter. The minimum beam waist is given by (Steen, 1998)

$$d_f = \frac{4a'_{L2}\lambda M^2}{\pi d_{bL2}} \tag{2.3}$$

Where a'_{L2} is the effective focal length of Lens L2, λ is the wavelength of the laser light, M^2 is the beam quality factor (provided by Laser Lines) and d_f is the minimum beam waist. The value of d_f calculated here was 0.93 mm, as shown in Figure 2.8. The angle of contraction of the beam is given as θ_{L2} in this figure.

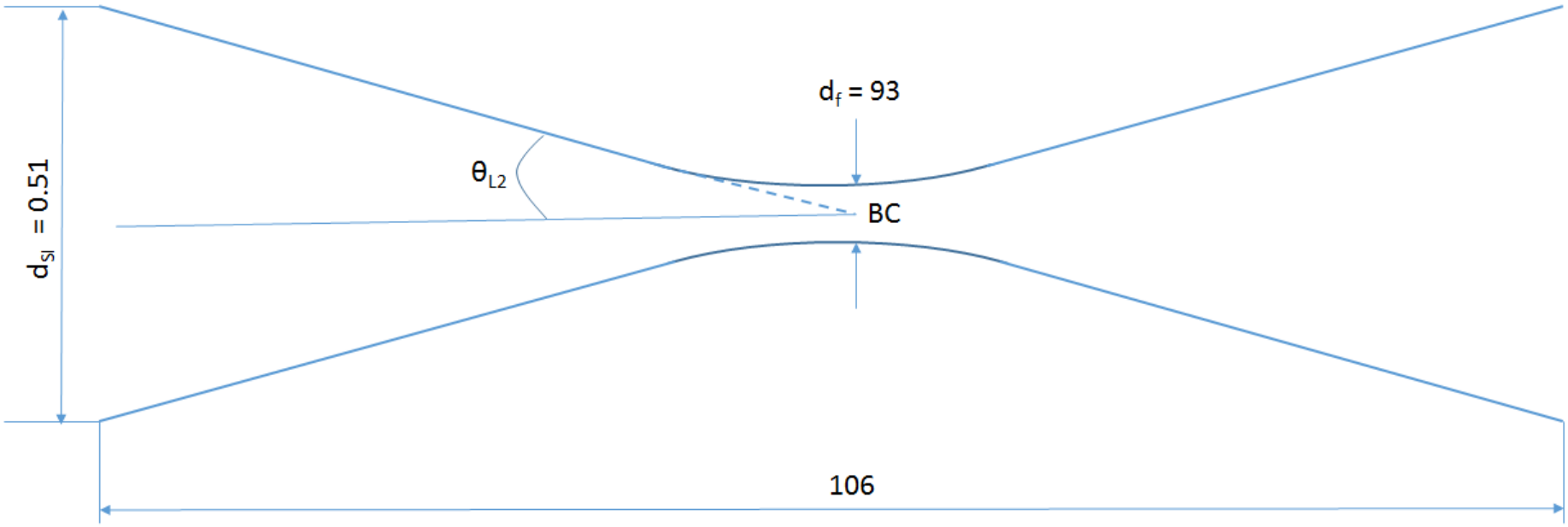

Figure 2.8 Details of the beam waist at the bomb centre

To determine the focal lengths and separation distances of the lenses required to form the converging beam into laser sheets, further calculations were performed. As the formation of the sheets required the use of convex lenses in series, the thin lens equation, below, was used (Hecht 1989, p138) where the thickness of the individual lenses was neglected

$$\frac{1}{F} = \frac{1}{f_1} + \frac{1}{f_2} - \frac{a}{f_1 f_2} \tag{2.4}$$

Here, F is the effective focal length of a system containing two lenses with focal lengths f_1 and f_2 and a is the separation distance between the lenses. This equation was used to calculate the effective focal length of the cylindrical lenses CL1 and CL2 shown in Fig. 2.9. Thus, for the first cylindrical lens, f_1 in Eq. 2.4 takes the value of a'_{L2} in Fig. 2.7. The actual focal length of lens CL1 provides the value for f_2 and a is the separation distance between these lenses, denoted a_{s1} in Fig. 2.9. Once the effective focal length for lens CL1 had been calculated, this parameter could then be obtained for lens CL2. Based on the incumbent diameter of the beam on lens CL2, d_{CL2}, and the focal length f_{CL2}, the divergence angle θ_{CL2} was calculated using the Tangent rule. The sheet height at any given distance from the focal point could then be obtained and for the centre of the bomb is denoted H_s in Fig. 2.9. From this method, it was calculated that the sheet height at the centre of the bomb would be approximately 81 mm, whilst the height entering the 106 mm interrogation region would be 73.4 mm and 88.5 mm at the exit. All of the calculated values are presented in Tables 2.1 and 2.2, which show the sequence of the calculation steps including the required inputs. The minimum beam waist d_f was calculated as 0.51 mm; this is comparable with measurements made of the beam diameter in practice with photographic paper, where a sheet thickness of approximately 0.3 mm was measured.

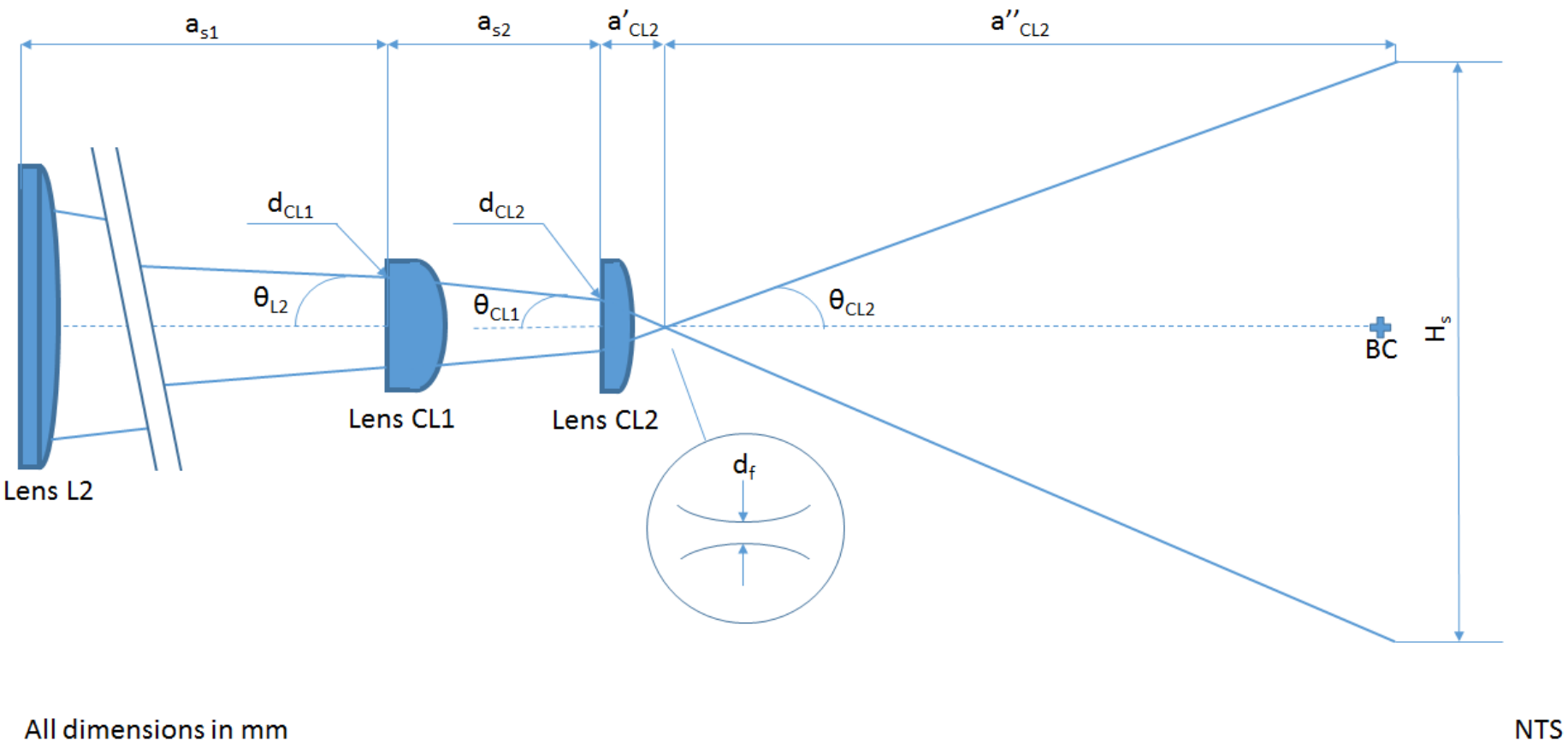

Figure 2.9 Expansion of the laser beam into a sheet

Table 2.1 Optical design for beam contraction towards the bomb centre

Optical Arrangement Design Calculations

Beam Characteristics:

Far-field divergence half angle, θ_L =	0.0044	radians	Laser Lines (2016)
Initial beam diameter, d_{BL} =	0.0037	m	Laser Lines (2016)

Lens L1 Calculations:

Type: Spherical Plano-Concave

Focal length, f_{L1} =	-0.1	m	Thorlabs 2015
Diameter =	0.05	m	
Laser head to Lens 1 distance, a_{LL1} =	0.405	m	
Laser beam focal length, $a_{L1} - a_{LL1}$ =	0.420	m	Point source behind
Focal length on striking Lens L1, a_{L1} =	0.825	m	the laser
Effective focal length (EFL) of Lens L1, a'_{L1} =	-0.0892	m	
Beam diameter entering lens L1, d_{bL1} =	0.00726	m	

Lens L2 Calculations:

Type: Spherical Plano-Convex

Focal length, a'_{L2} =	0.25	m	
Diameter =	0.05	m	
Lens L1 to Lens L2 distance, a_{L2} =	0.19	m	
Beam focal dist. before Lens L2, $a'_{L1} + a_{L2}$ =	0.279	m	
Effective focal length of Lens 2, a'_{L2} =	2.39	m	
Actual measured distance in practice =	2.36	m*	
Beam convergence angle from Lens L2, θ_{L2}	0.00482	radians	

* Note: very small changes in distance between Lenses 1 and 2 (i.e. < 1 mm) have a profound effect on the overall focal length. The discrepancy between actual and calculated focal lengths may be due to measuring errors.

Table 2.2 Optical design for sheet formation and calculation of the minimum beam waist

Optical Arrangement Design Calculations

Sheet thickness calculations:

λ =	5.32E-07	m	Laser Lines (2016)
M^2 =	13		Laser Lines (2016)
Divergence angle from Lens L1, θ_{L1} =	0.0407	radians	
d_b =	0.023	m	Beam dia. Before contraction
d_f =	0.000926	m	Minimum beam waist
	0.9259	mm	
Angle θ_{L2} =	0.00482	radians	
Beam diameter at 53 mm from BC =	0.000510	m	
	0.510	mm	Max. sheet thickness across interrogation region

Sheet Height Calculations

Cylindrical Lens CL1 focal length, f_{cl1} =	0.015	m	Thorlabs (2015)
Lens L2 and CL1 separation (a_{s1}) =	1.916	m	
Effective focal length of CL1, a'_{s2} =	0.077	m	
Cylinder Lens CL2 focal length, f_{cl2} =	0.0381	m	Thorlabs (2015)
Cyl. Lens 1 and Cyl. Lens 2 separation =	0	mm	
Effective focal length of CL2, a'_{CL2} =	0.0255	m	
Actual dist. between CL2 & RM =	0.07	m*	Measured in practice RM = Rotating mirror
Sheet height at rotating mirror =	0.0075	m	
Beam diameter entering CL2, d_{CL2} =	0.00429	m**	
Beam contraction angle from CL2, θ_{CL2} =	0.0839	rad	
Sheet height before centre =	73.4	mm	At start of interrogation region
Sheet height at bomb centre =	81.0	mm	
Sheet height after centre =	88.5	mm	

* Note: the beam was focussed after the mirror to reduce the beam flux on the mirror

** Assumed diameter unchanged by CL1, due to minimal lens spacing

As the rotating mirror turned, it caused each sheet to be reflected at an angle through the bomb, as shown in Fig. 2.10. The angle between successive sheets is equal to the angular rotation of the mirror shaft between them. With the centre sheet passing through the bomb designated as $n = 0$, the angle between this sheet and any other was calculated as

$$\gamma_n = \frac{360.\omega}{f_l} n \tag{2.3}$$

where γ_n is the angle of the nth sheet from the bomb centreline, ω is the angular rotation rate of the mirror shaft in radians/s and f_l is the laser repetition frequency in Hz.

An additional effect of reflection off the rotating mirror is the introduction of geometric offset, as illustrated in Fig. 2.11. This is due to reflection occurring at different points in space for each sheet and is denoted as a_g in Fig. 2.11. In this figure, θ_m is the angle through which the mirror rotates between pulses of laser light, ω is the angular rotation rate of the mirror shaft, A_m is half of the distance between parallel flat faces on the mirror and x_m is the diagonal distance between the centre of the mirror face at the centre of a sweep and after rotation by angle θ_m (illustrated as positions n and $n + 1$ in Fig. 2.10) calculated from

$$x_m = A_m Tan(\theta_m) \tag{2.4}$$

The mirror offset a_g may then be obtained from

$$\frac{a_g}{\sin(\theta_m)} = \frac{x_m}{\sin(45 - \theta_m)} \tag{2.5}$$

Both the sheet divergence and geometric offset were accounted for in the 3D image assembly procedure presented in Section 3.2, where a description is given of how these were implemented into the coding.

A limitation of the present technique is that the 3D image is built up from a sequence of sheets which are recorded at non-zero time separation. Typically, 74 sheets were present in each sweep at the laser repetition frequency of 49 kHz used throughout this work. Thus, the time for one sweep was around 1.5 ms. Increasing the mirror rotation speed would have reduced the duration of, and thus number of sheets in, each sweep. It would thus increase the sheet separation distance, reducing the spatial resolution of the 3D reconstruction. However, it would also reduce the period of time between successive sheets, allowing a greater number of sweeps through a flame and thus capturing more of the flame development. A compromise was sought between these factors, to afford good 3D image resolution whilst minimising flame growth during a sweep and maximising the number of sweeps possible through the flame.

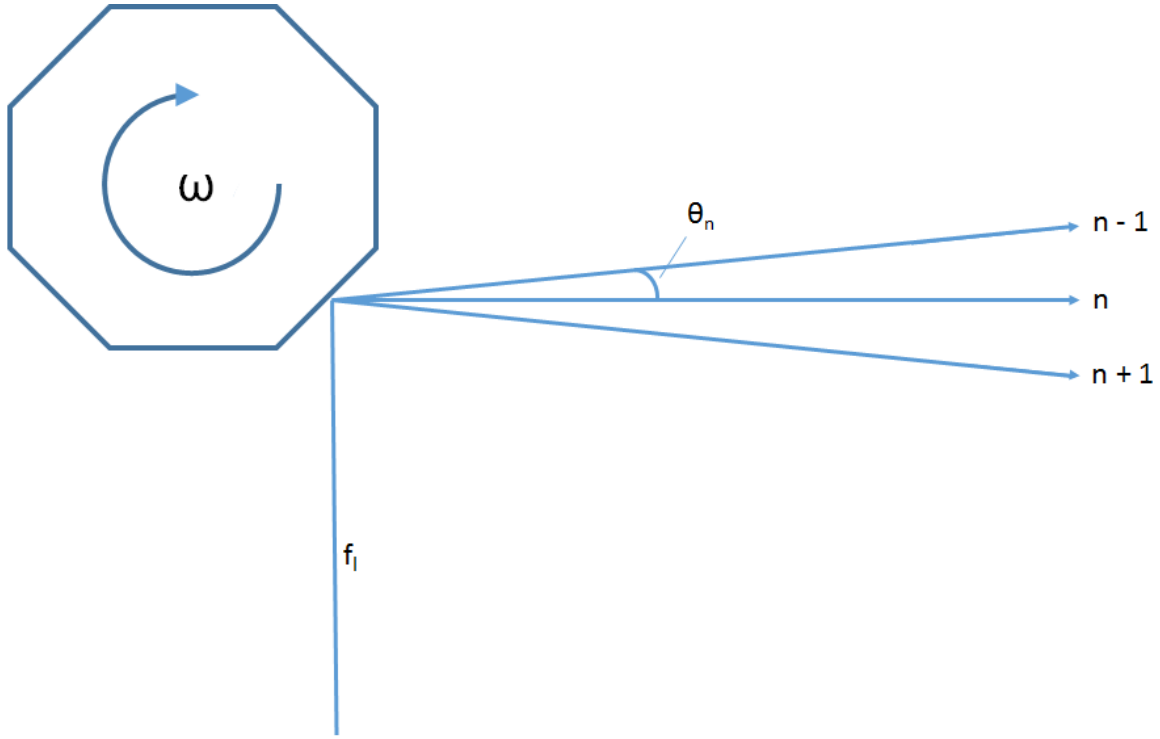

Figure 2.10 Divergence of successive laser sheets

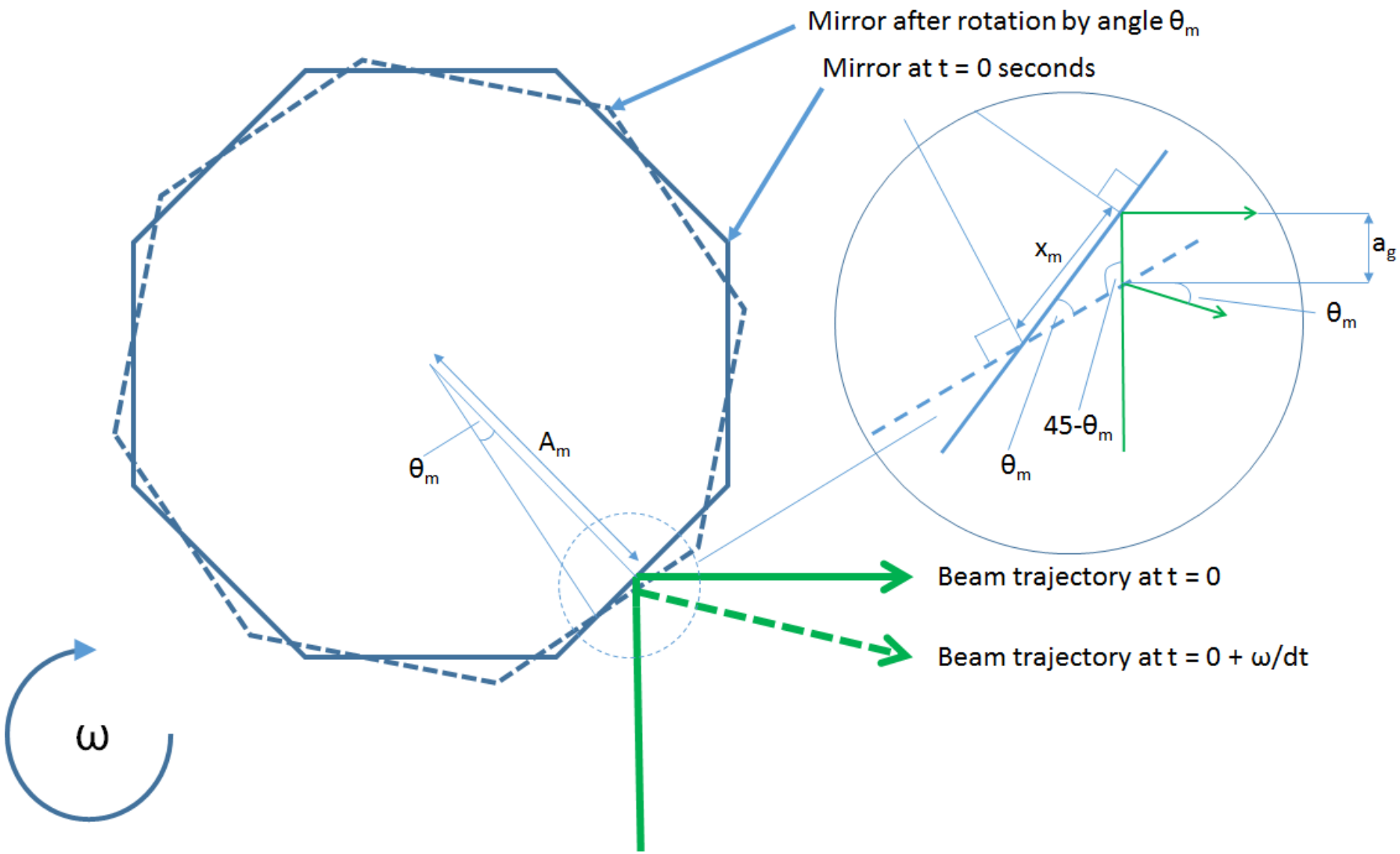

Figure 2.11 Mirror geometric offset

2.3.2 Control and Synchronisation System

In order to obtain fully time-resolved images, it was necessary to synchronise the imaging laser, ignition laser, rotating mirror, camera and triggering system. The rotating mirror acted as the central component of the system as each of the other components were required to be triggered relative to its position. Light from the Nd:YAG imaging laser was received on a given face of the mirror and a continuous wave diode laser was directed at the opposite face. Reflected light from the diode laser was received by a photodiode (PD) detector. The relative positions of the mirror, PD detector and diode laser were set such that the detector received light from the diode laser when the mirror was in the correct position to reflect the first sheet of laser light in a series. By adjusting these components, the trajectory of the first sheet in a sequence could be varied to ensure that the sheet just passed through the far window of the bomb without hitting the window edges.

The signal from the PD detector was amplified before supply to a TGP 110 pulse generator, which generated a gate signal. As the DM60 imaging laser could only emit light whilst the gate was in the "up" position, the width of the sweep of laser sheets and hence the position of the last sheet in the bomb was adjusted by adjusting the gate signal pulse width. The gate signal was sent to the DM60 laser controller, which was set to run at its own internal frequency via a graphical user interface (GUI) on the laboratory P.C.

The laser was operated in "Master/Slave" mode, whereby one laser cavity controlled the other. The delay between pulsing of the Master and Slave cavities was set in the GUI to symmetrically stagger the pulsing of the two cavities and achieve an overall pulse repetition frequency (PRF) of 49 kHz. The synchronising output signal from the Master cavity controller (at 24.5 kHz) was sent to a second TGP 110 pulse generator, which provided an inverted output twice that of the input frequency to produce a negative-going TTL signal. This was supplied to the camera, which recorded an image on each downward pulse it received. Each of the signals described above, and their relationship to each other, is shown in Figure 2.12.

The voltage amplifier also provided a signal to a frequency divider unit designed in-house at Leeds, which converted the received input to a 10 Hz TTL signal by dividing the received signal by a constant value which was entered by the user. Since the rotating mirror rotated at a frequency of 10 Hz at the shaft and was 16-sided, the photodiode detector generated a frequency of 160 Hz, which was divided by 16 at the frequency divider to produce the required 10 Hz. This signal was supplied to the SL800 ignition laser control unit as the external frequency driving signal. Thus, ignition could be triggered only once per full rotation of the mirror.

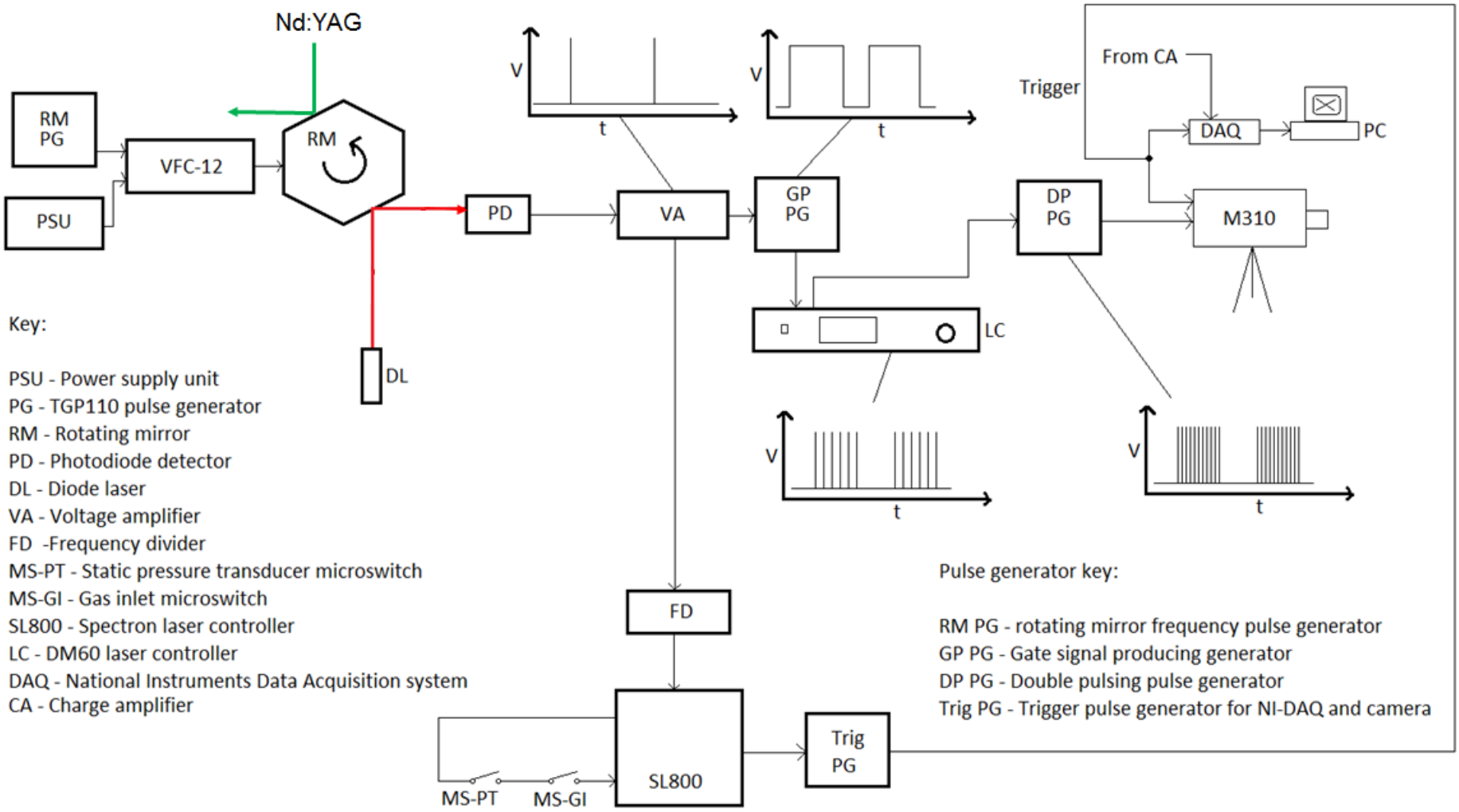

Figure 2.12 Schematic of all components in the synchronisation system

The DM60 laser pulsed synchronously with the rotating mirror, but images and pressure data were only recorded on receipt of a trigger signal from the SL800 laser controller. An image and schematic of the connections required at the laser controller are given in Fig. 2.13.
The circuit for the Q-switch could only be enabled when the microswitches, MS1 and MS2, for the gas inlet supply to the bomb and static pressure transducer had been closed. When the user rotated the Q-switch enabling knob to "normal", the Q-switch activated on receipt of the next pulse from the frequency divider and generated a high energy pulse of laser light and hence a spark. Here, the Q-switch altered the beam time-intensity profile by shutting off one of the mirrors, thereby creating a greater population inversion of high energy molecules in the gain medium. On re-activating the mirror, a large collapse of molecular energy levels occurred, resulting in a large release of light energy in a short time period.

Simultaneously, a 15V CMOS signal was generated at the Q-switch sync. output on the laser controller. This signal was supplied to a further TGP110 pulse generator, which converted this signal to a TTL signal. This was supplied to both the camera and the National Instruments analogue to digital converter (ADC) and initiated the recording of data. Each of these signals is shown in Fig. 2.14. As ignition occurred at frame "0" in the sequence of images, the time after ignition for each image was known.

The triggering system for the schlieren imaging system when using laser ignition was very similar because the SL800 laser controller was used in the same way to generate a 15V CMOS triggering signal. Where spark ignition was employed, the synchronisation system employed by Mumby (2016) was used, excepting that a negative-going CMOS signal was supplied to the high energy ignition unit for triggering rather than a positive-going TTL.

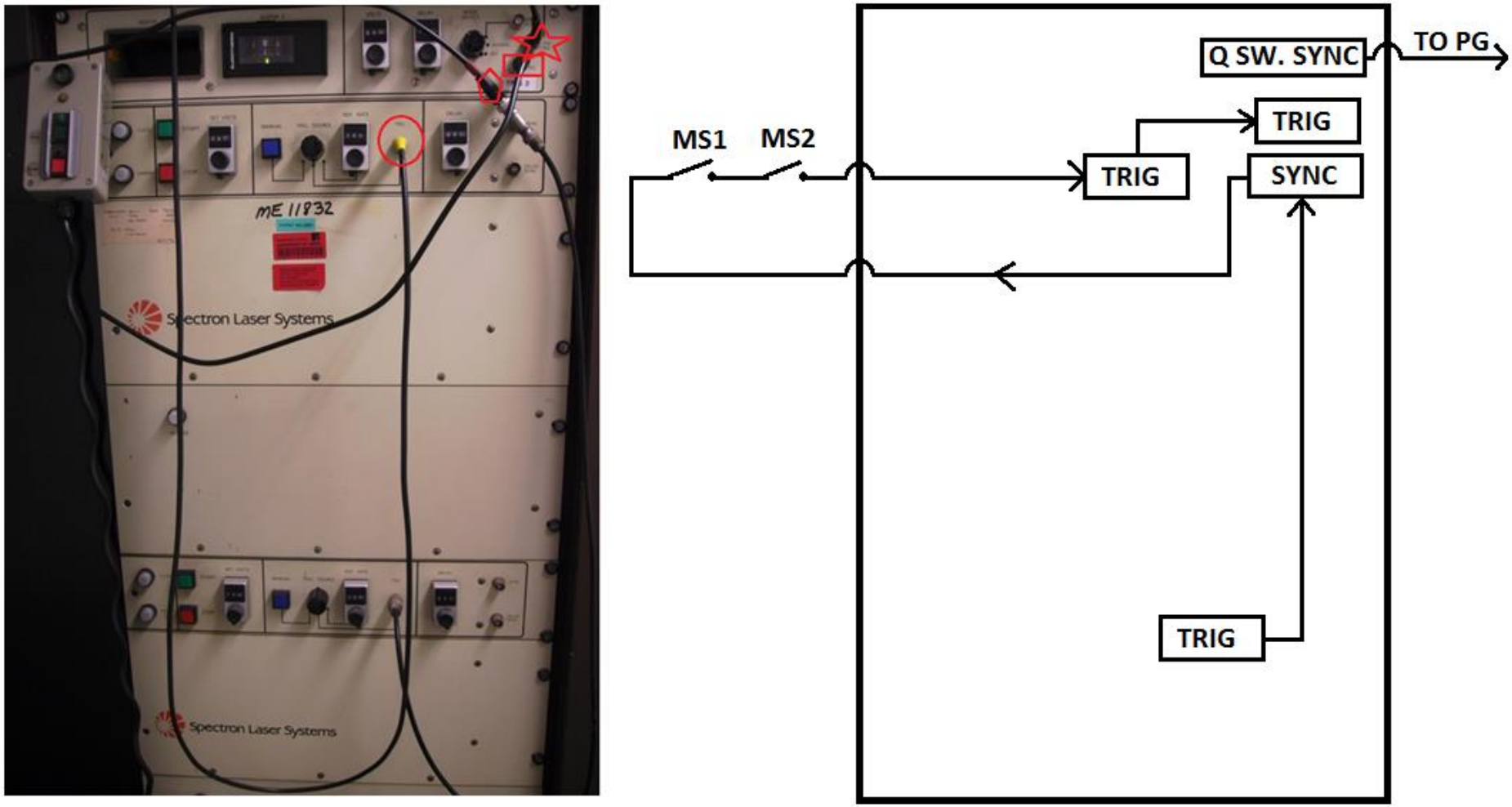

Figure 2.13 Image (left) and schematic of the connections at the SL800 laser controller to afford interlocked triggering

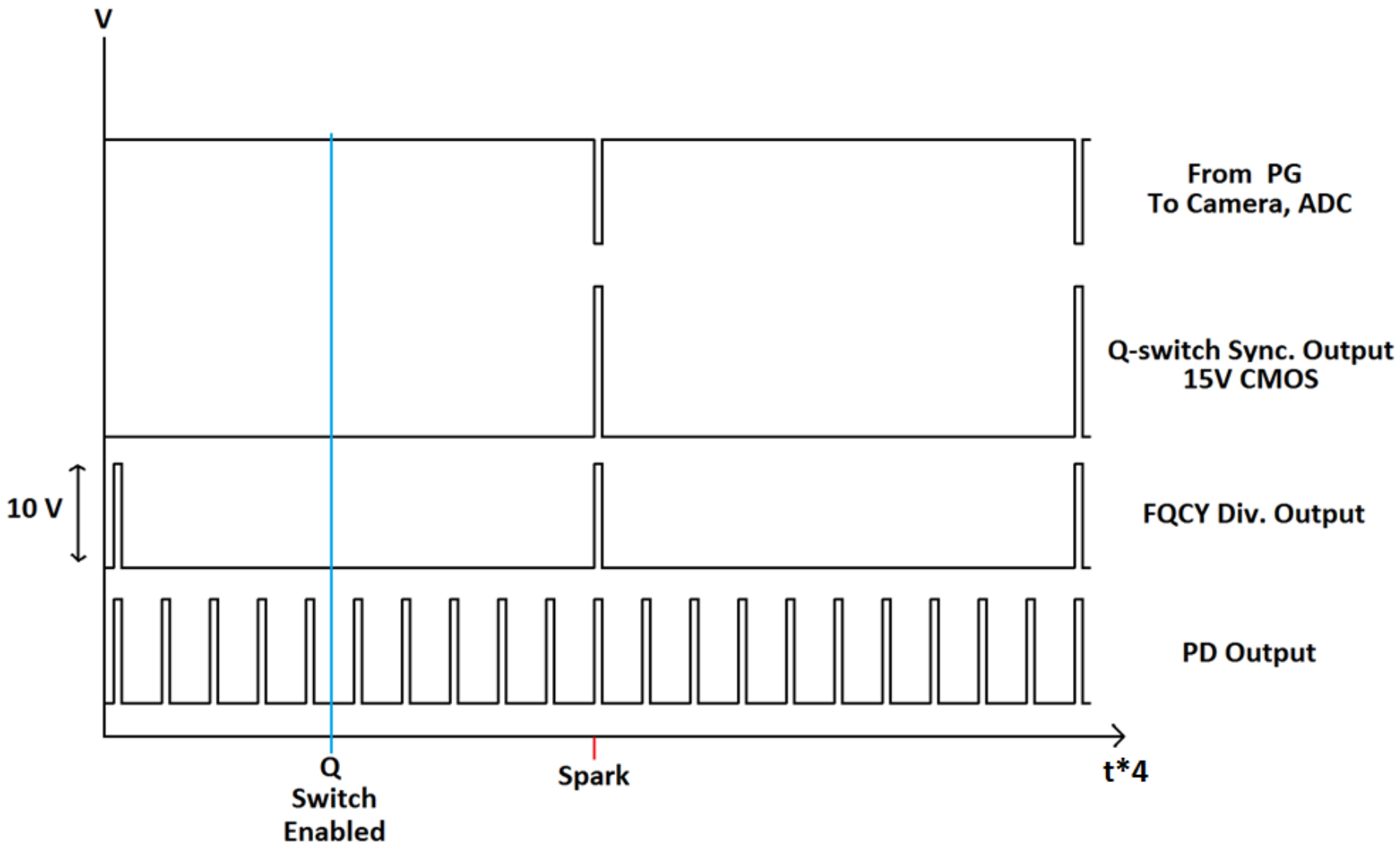

Figure 2.14 Signals involved in triggering the experiment

2.3.3 Seed Particle Generation for Mie Scattering

The multiple laser sheet diagnostic technique employed here relied on Mie scattering to reveal the presence of a flame edge, where laser light scattered off seed particles in the gas mixture in the bomb was detected by the camera. Where the seed particles had burned off due to exposure to high temperatures (i.e. in the pre-heat or reaction zone of a flame), dark regions were visible in the captured images which were taken as being representative of regions of burned gas. It was required that the seed particles reflected enough light to be detected by the camera, whilst also burning rapidly in the presence of a flame and not influencing the burning rate of the mixture. It was also desired that the seed particles remained in suspension for as long as possible. Melling (1997) presented a comparison between a number of different seeding materials for use with flow studies. Harker (PhD Thesis, 2009) trialled a number of seed materials for use with Mie scattering in the presence of combustion and concluded that olive oil provided the best combination of reflectance and entrainment time, in droplet form. This material was thus adopted in the present work.

The olive oil seed particles used in the present work were generated using a PIVTech PIVPart14 seed particle generator. This generator contained three Laskin nozzles, where one of which possessed two orifices ("jets"), another had four jets and the third had eight jets. Each Laskin nozzle was controlled by a separate air supply control valve, so that the seeding rate could be varied as required. The unit required an input pressure of 0.15 MPa and a differential pressure between the inlet and outlet of between 0.05 and 0.07 MPa. Tests conducted by the manufacturer, using di-ethyl hexyl sebacat (DEHS) as the seeding liquid revealed a peak in the particle size distribution at 0.9 μm. However, a study was carried out at the University of Leeds to evaluate the particle size distribution and number concentration of particles output by this device when using olive oil as a seeding material (Kylafis, PhD Thesis 2016). In this work, it was found that the peak in the size distribution of particles occurred at a particle size of around 0.35 μm, with a particle number concentration of around 1×10^5 particles/cm^3.

2.4 Experimental technique

Most previous work at Leeds has used mixtures starting at a temperature and pressure of 360K and 0.5 MPa respectively, as most data in the literature were collected under these conditions. However, in the present work it was required to minimise the burning rate to limit flame growth during imaging. Thus, all experiments in the present study were carried out at 298K and 0.1 MPa at an equivalence ratio, φ, of 0.6 to minimise the laminar burning velocity, u_l. This in turn allowed for high values of the Karlovitz stretch factor, K, to be achieved at low levels of applied RMS turbulence intensity, u'. Accordingly, flames developing at engine-like K values could be studied up to the onset of quenching, without the rapid convection of the flame kernel out of the field of view which otherwise would have occurred if high values of u' had been employed.

A methane/air mixture at an equivalence ratio of 0.6 was employed throughout the present work, where methane was used as it has been widely studied both experimentally and in computational studies and thus data for comparison with the present work are readily available.

After the vessel had been sufficiently warmed, as described in Section 2.4, an initial sealing test was performed, where the vessel was pressurised with dry air to 0.7 MPa and monitored for at least five minutes to ensure minimal leakage. To ensure the vessel was free from any unwanted gaseous residuals from previous experiments, the vessel was vacuumed down to 2.5 x 10^{-3} MPa from atmospheric pressure, filled with dry air to 0.1 MPa, and again vacuumed down to 2.5 x 10^{-3} MPa. This ensured any gaseous residuals were kept to a maximum of 0.06%.

To add the gaseous methane fuel, the relevant needle valve was opened until the required partial pressure of gas had been added to the bomb, as indicated by the digital static pressure gauge. Dry air was then added up to approximately 0.07 MPa, followed by the addition of 0.015 MPa of olive-oil droplet seeded air. This partial pressure of olive-oil seeded air was found to give a good compromise between laser light reflection and clarity of the sheet images furthest from the camera. Higher concentrations led to significant scattering of laser light reflected off the farthest sheets and thus poor flame edge definition. The effects of the seed particles on the burning rate are discussed in Section 5.5.

The vessel was then topped up with dry air to 0.1 MPa whilst ensuring the mixture temperature had stabilised to the desired initial mixture temperature. Throughout mixture preparation, the vessel fans were run at 680 rpm to ensure an even distribution of heat in and homogeneity of the mixture.

Prior to ignition, the fan speed was adjusted to that required (zero for laminar experiments). In each case, once the fans had reached the desired speed after adjustment (as indicated by the digital fan-speed readout in the controlled area), a minimum of 5 seconds was allowed to ensure full decay or development of turbulence prior to ignition. This also allowed sufficient time to arm the triggering system, switch on the ignition laser and allow the pulse energy to stabilise, perform a final brief visual inspection and return to the protected control booth. Ensuring the initial mixture temperature and pressure were as desired, the inlet air supply and static pressure transducer were isolated by remotely closing ball valves and finally, the ignition trigger actuated. After combustion the resulting products were exhausted via a remotely operated exhaust valve, this ensured the vessel was depressurised to a safe level before leaving the protection of the control booth. The fans were then reactivated, the inlet air supply and static pressure transducer isolation valves reopened, and the vessel flushed with dry air for at least one minute to aid the evacuation of combustion products and reduce the transfer of heat from the combustion products to the bomb walls. During this time the acquired data were saved and the LabVIEW and camera software reset. The vacuuming and dry air filling procedure as described above were then repeated to prepare the vessel for the next experiment.

Chapter 3 -Data Processing Techniques

3.1 Introduction

This chapter presents the techniques employed to process the experimental data obtained using the schlieren images, pressure trace measurements and multiple laser-sheet Mie scattering images obtained using the methods described in Chapter 2. The majority of data processing was carried out in Matlab using codes written by the Author; incorporation of other Authors' codes is acknowledged where appropriate. Some further processing was carried out using the Open-Source programs Meshlab and Meshmixer to enable the surface smoothing and 3D printing of reconstructed flames.

Section 3.2 describes the initial processing of 2D laser Mie scattering images, prior to applying the reconstruction technique presented in Section 3.3. Analysis of the reconstructed flames is given in Section 3.4 and the technique employed to process schlieren images is presented in Section 3.5.

3.2 Processing of 2D Laser-sheet Mie Scattering Images

The multiple laser-sheet imaging technique described in Chapter 2 typically yielded 74 greyscale TIFF images per sweep through a developing flame, an example of which is given in Fig. 3.1. Each image consisted of 256 x 200 horizontal/vertical pixels as discussed in Section 2.3.1, resulting in a physical pixel size of 0.417 mm.

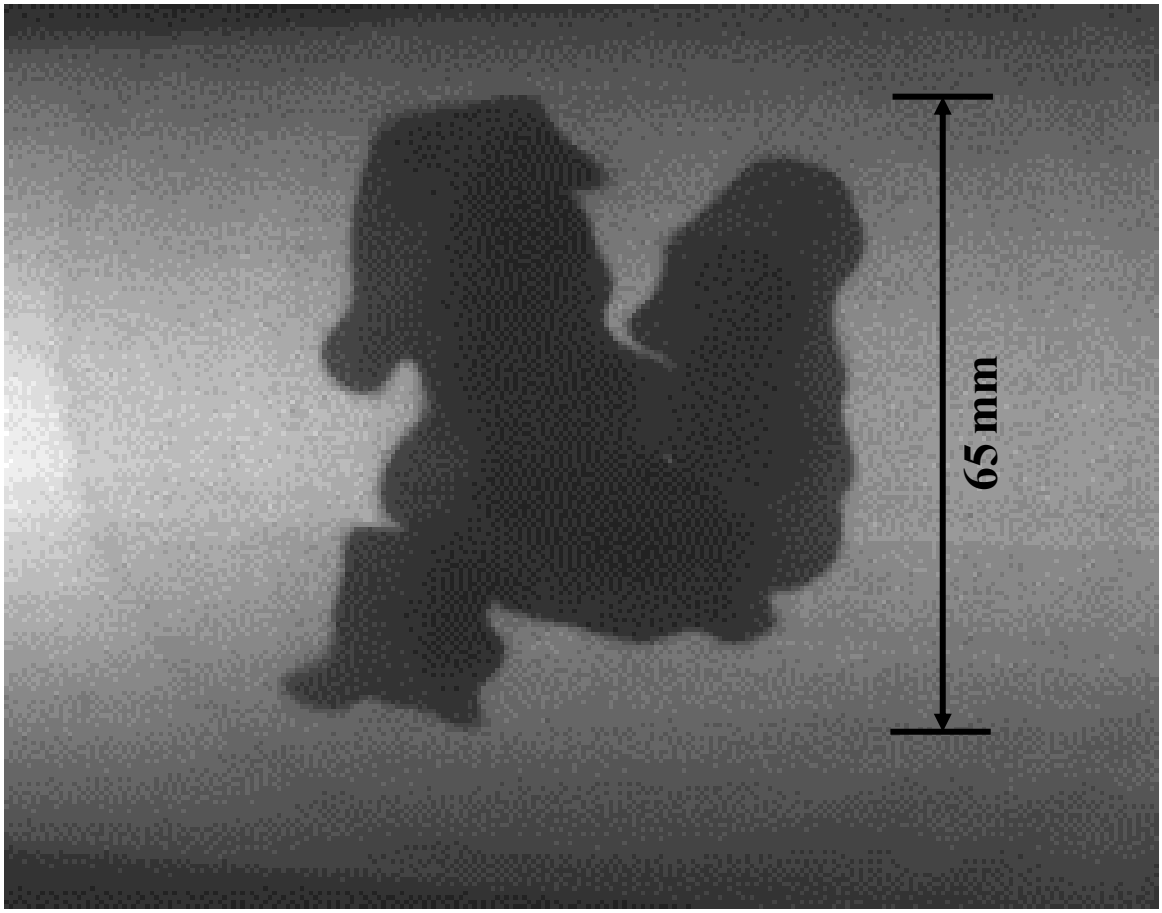

Figure 3.1 Raw, mid-sweep laser sheet image of a methane/air flame at 298K, 0.1 MPa and φ = 0.6 at 24.2 ms from ignition, u' = 0.25 m/s

Figure 3.1 shows a typical raw laser sheet image for a flame at low turbulence, where the dark patch reveals the absence of light-scattering seed particles. The flame edge is mildly wrinkled and well defined. The edges of the laser sheet may be seen at the top and bottom left corners of the image, illustrated by the transition from light to dark and the heating element in the bomb is just visible as the concentric shape in the background. The whole image is approximately 83 mm high and 107 mm wide.

To produce a 3D reconstruction from a sequence of images such as that shown in Fig. 3.1, it was necessary to trace the flame edge or edges. This was achieved using the built-in "log" (Laplacian of Gaussian) edge detection algorithm in Matlab. This gave a good compromise between successful detection of the flame edge and minimal detection of spurious edges caused by differences in intensity in the image background. After application of the edge detection algorithm, which also served to binarise and invert the images, all enclosed areas within the image were filled in using the "imfill" command in Matlab. This resulted in images such as that shown in Fig. 3.2, where white areas represent burned mixture and black areas show unburned mixture. In these binary images, white pixels are assigned a value of unity and black pixels a value of 0.

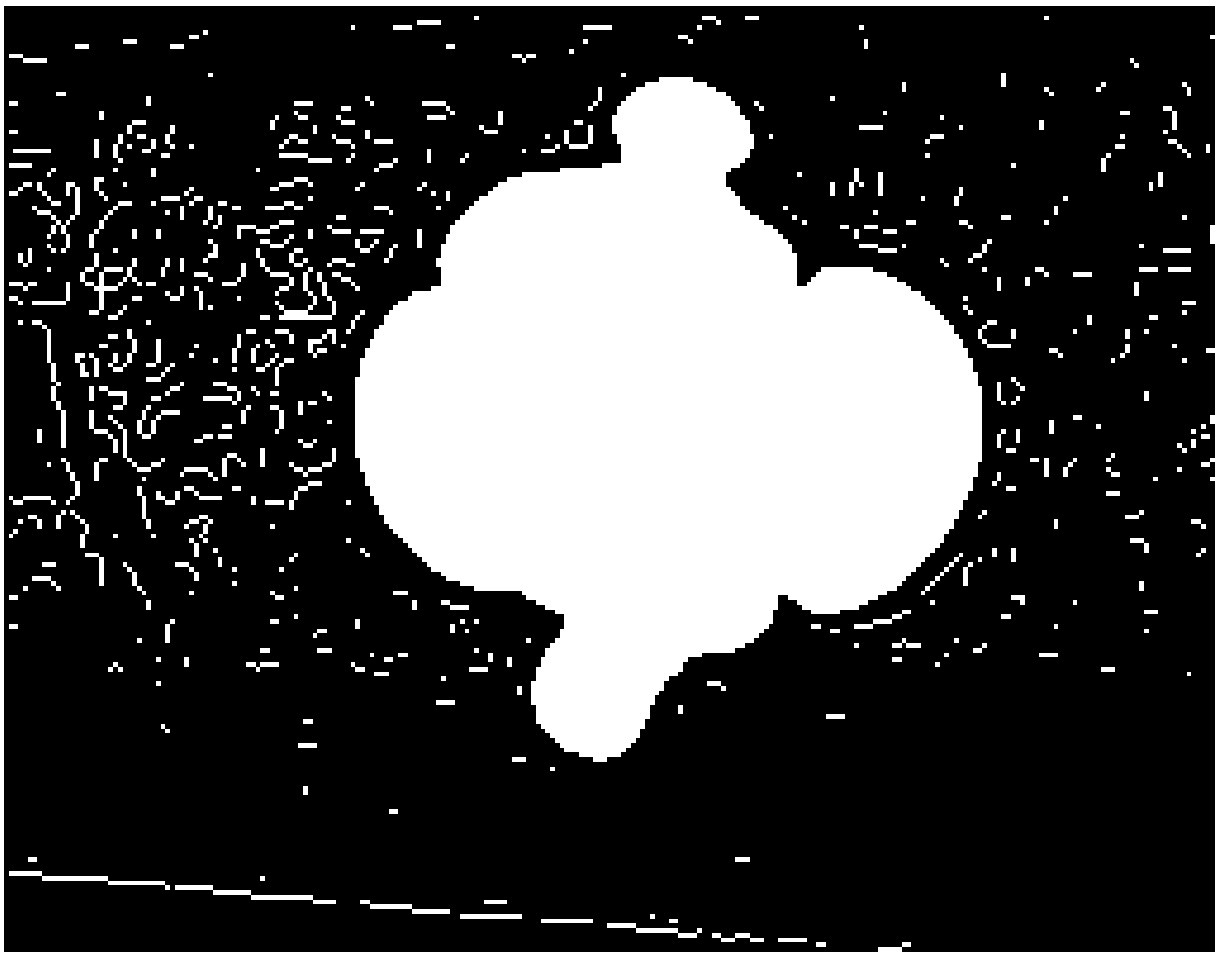

Figure 3.2 Result of edge detection and binarisation on a greyscale image of a low-turbulence flame

The background noise visible in Fig. 3.2 was then removed using two methods in series; the first method looped through each white pixel in the image and determined the sum of the neighbouring cells. If the sum of the neighbouring cells was less than two this indicated that either the pixel was isolated or part of a line and thus its value was changed to zero. This process was then repeated, which removed all thin lines and isolated white pixels in the background whilst leaving the flame edge unchanged. The second method used a built in function in Matlab which examined the number of white pixels in a cluster of white pixels and changed the value of these to zero if the number fell below a certain limit. This limit was selected by the user to ensure that small flame features were not accidentally removed. A complement image was then generated to yield a black flame on a white background as shown in Fig. 3.3.

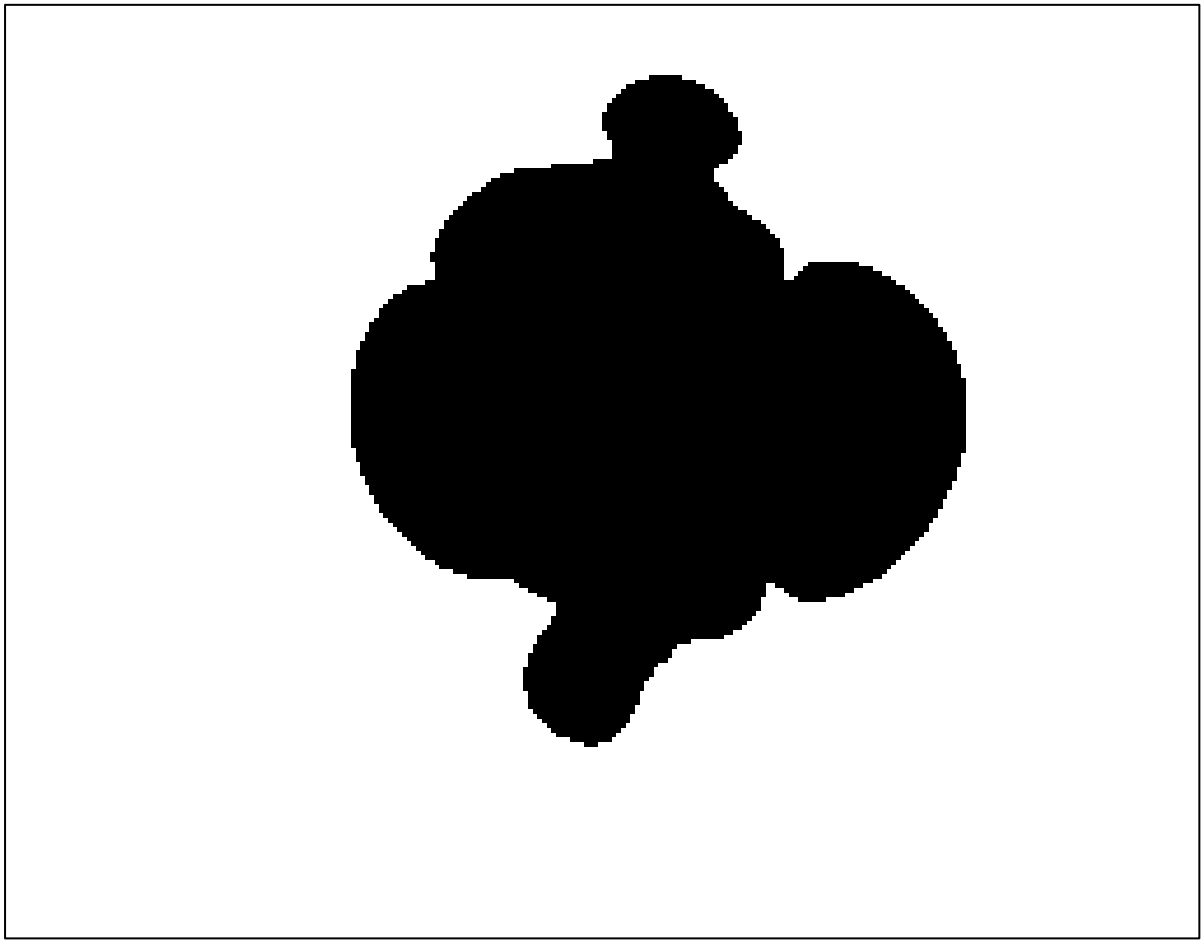

Figure 3.3 Laser sheet image shown in Fig. 3.2 after edge detection, background cleaning and inversion

3.3 Assembly of 2D sheets into 3D reconstructions

After applying the edge detection and binaristion techniques discussed in the previous section, it was necessary to assemble these into a 3D matrix and interpolate between the sheets to yield a solid reconstruction. A triangulated surface mesh was then generated which, when smoothed, yielded a visual representation of the flame surface structure. These steps are discussed in the following sections.

3.3.1 Initial 3D matrix preparation and sheet equation generation

A three-dimensional x, y, z matrix of volume elements (voxels) was first generated in Matlab, with each element in this matrix taking a value of unity (i.e. unburned mixture). For each laser sheet image to be inserted in to the matrix, the geometric offset (a_g) and angle with respect to the centre sheet (θ_m) were calculated as described in Section 2.3.2. These were used to generate a straight line equation of the form z = mx + c for each sheet, where the designations are given in Fig. 3.4. Thus, for any x/y coordinate in the 2D image, the corresponding z coordinate in the third dimension was calculated. Each 2D image was then looped through and the value at each coordinate determined. For each corresponding coordinate in the pre-allocated 3D matrix, the value was changed to match that in the 2D image. Due to the finite resolution in the array, it was necessary to round the calculated z coordinate to the nearest integer value. This led to a slightly stepped appearance of the inserted sheet as can be seen in Fig. 3.4 where this effect has been exaggerated.

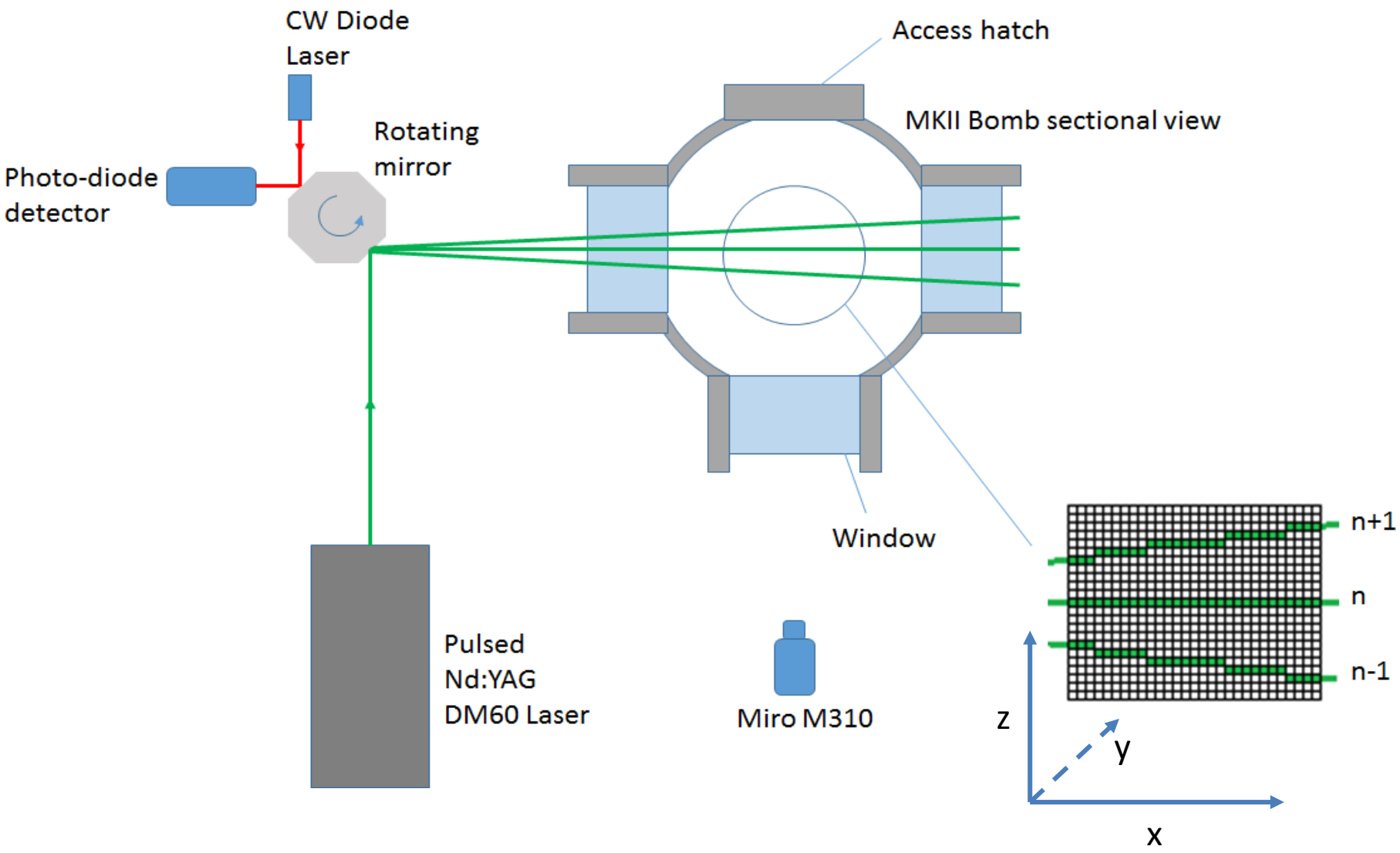

Figure 3.4 Trajectory of laser sheets through the bomb and insertion of the sheets into a discretised grid

3.3.2 Sheet Interpolation and Surface Mesh Generation

As discussed in Section 2.3.1, the selected combination of the mirror rotation rate and the laser pulse repetition frequency introduced a finite spacing between the successive laser sheets. This is shown in Fig. 3.5 as a slice through the assembled array described in the previous section, through the y-axis.

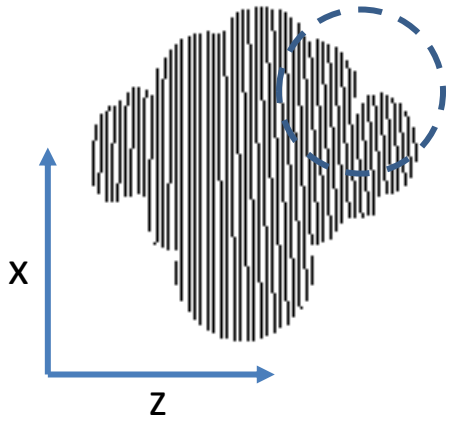

Figure 3.5 View of a slice through assembled sheets in the y-axis

To generate solid reconstructions and allow a surface mesh to be constructed, interpolation was carried out between the sheets. This was accomplished using the built-in "imdilate" function in Matlab. This thickened the sheets slightly, closing the gaps, resulting in an image such as that shown in Fig. 3.5. This method was selected over cubic/linear splining as the sheet spacing was typically only 1-2 pixels, which was insufficient to generate a curved or straight line between the sheets. Additionally, where such algorithms rely on connecting points which are closest together, areas of negative curvature such as that highlighted within the dashed circle in Fig. 3.5 may be completely filled due to incorrect selection of points to be joined. This effect was reduced, though not entirely eliminated, using the dilation technique. It can be seen in Fig. 3.6 that this technique has introduced a serrated edge to the flame image; this was removed using surface smoothing as described in the next section.

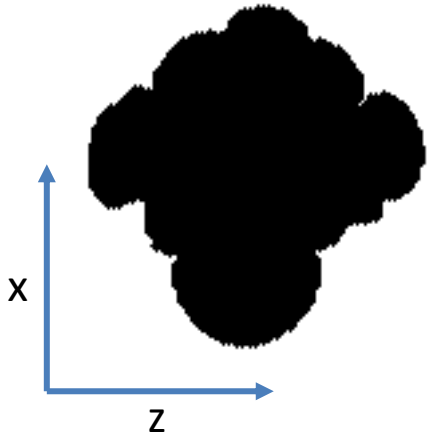

Figure 3.6 View of a slice through assembled sheets in the y-axis after interpolation

After interpolating between the sheets, a triangulated surface mesh was plotted over the reconstruction using the "isosurface" and "patch" commands in Matlab. The isosurface command generated a list of coordinates corresponding to the locations of "isovalues" in the matrix, i.e. points of identical value such as may be observed in isobar lines on meteorological maps. The isovalue was specified by the user, between the bounds of zero and unity, and was arbitrarily chosen in this work as 0.5. The patch command used the list of isovalue coordinates to generate a surface mesh of triangular faces, linked by vertices at the coordinates returned by the isosurface command. An example of the resulting surface mesh is shown in Fig. 3.7, displayed using Meshlab.

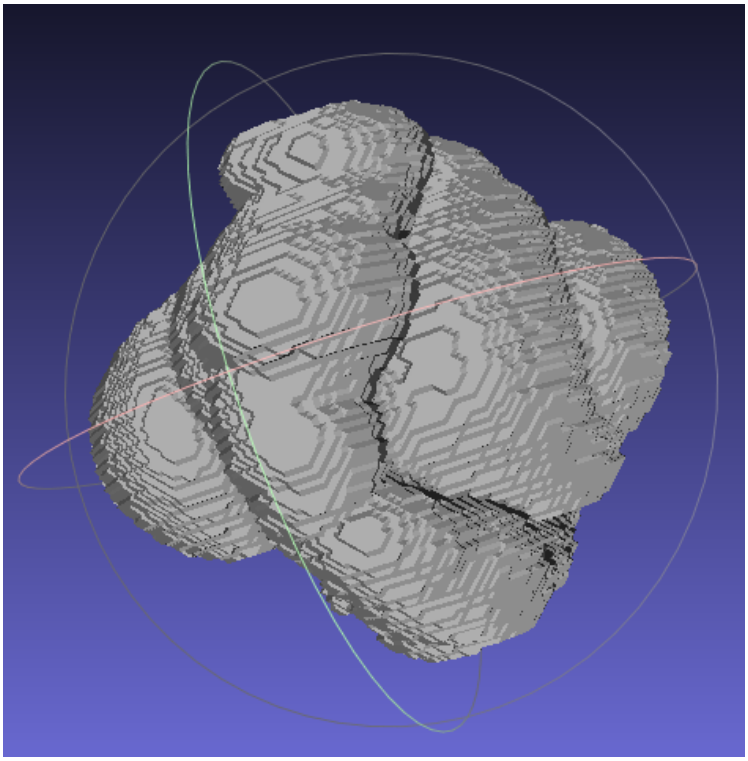

Figure 3.7 Triangulated surface mesh plotted over a laser spark influenced laminar 3D reconstruction

Flat edges and steps are visible in Fig. 3.7, which are an artefact of both the interpolation and surface generation techniques. These were removed using interpolative surface smoothing as discussed in the next section.

3.3.3 Surface smoothing

A smoothing algorithm described by Taubin (1995) was adopted here as it minimised shrink whilst preserving the surface features of the reconstruction. In this approach, the vertices of the triangulated surface are moved, without changing the connectivity of the faces and the processed surface contains exactly the same number of faces and vertices as the original version. Shown in Fig. 3.8 is a comparison between an unsmoothed reconstruction generated by the method described in Section 3.3.1, at the lowest *u'* employed in this study of 0.25 m/s.

Due to the relatively low level of surface wrinkling observed in this figure, the unsmoothed reconstruction shows little in the way of flat edges, though stepping is readily observed. These have been removed by the surface smoothing algorithm, leaving the flame wrinkling visibly intact.

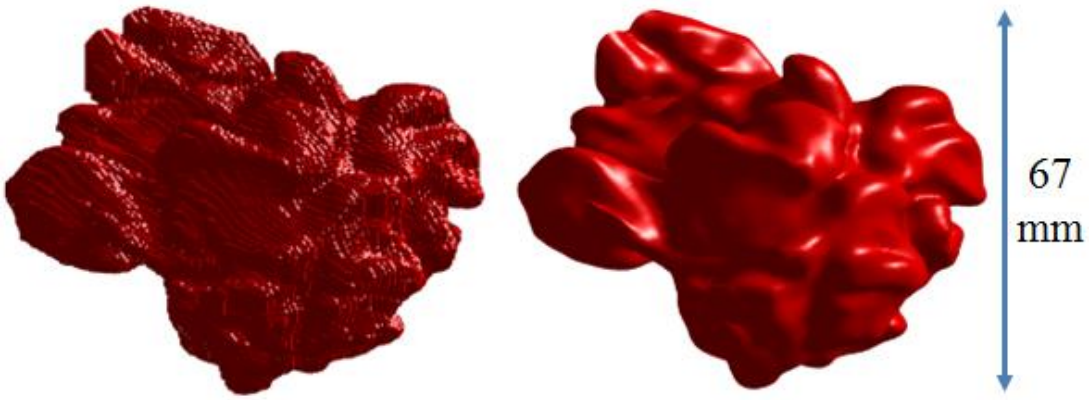

Figure 3.8 Methane/air flame at 298K, 0.1 MPa, u' = 0.25 m/s and φ = 0.6 at 35.8 ms from ignition. The unsmoothed reconstruction is on the left.

The presence of flat edges is visible in Fig. 3.9, due to the higher level of flame surface structure generated by the applied *u'* of 0.75 m/s. In this case, it was more difficult to interpolate between the sheets as some surface detail was lost in the spaces between the laser sheets. Some erosion of the flame extremities can be observed, but appears to be minimal.

Figure 3.9 Figure 3.9 Methane/air flame at 298K, 0.1 MPa, u' = 0.75 m/s and φ = 0.6 at 12.6 ms from ignition. The unsmoothed reconstruction is on the left.

Figure 3.10 shows the smoothed and unsmoothed versions of a reconstruction generated where *u'* = 1.25 m/s, which was the highest u' used in the present work. Flat edges are also visible in this figure, where these appear to be more rounded off in the smoothed version. Again, the overall flame surface structure is preserved during smoothing.

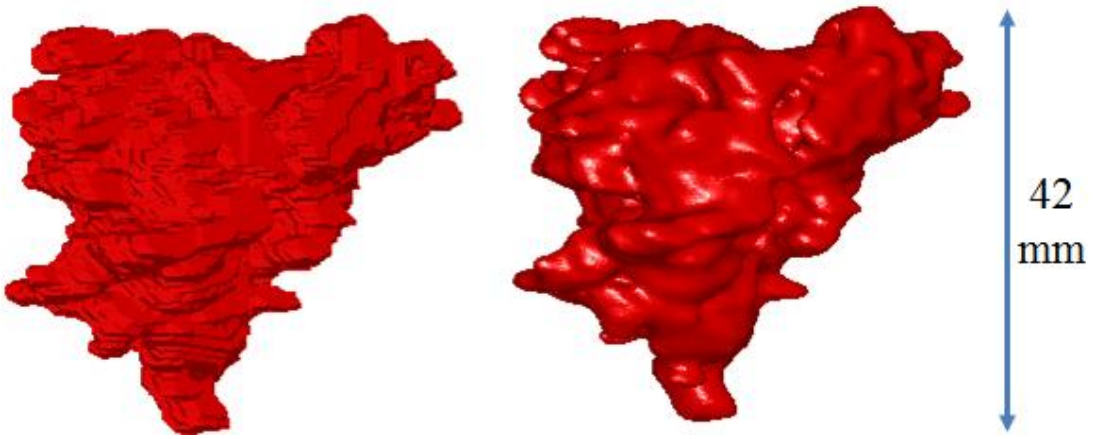

Figure 3.10 Methane/air flame at 298K, 0.1 MPa, u' = 1.25 m/s and φ = 0.6 at 18.4 ms from ignition. The unsmoothed reconstruction is on the left.

A quantitative analysis of the effect of surface smoothing on both flame volume and surface area is presented in Section 5.2.1.

3.4 Analysis of reconstructed flame surfaces

Various parameters have been derived to explore the effect of turbulence on flame surface structure; these included flame surface area, flame volume, reaction progress variable, flame surface density and curvature. The methods for calculating these are presented in the following sub-sections.

3.4.1 Flame Surface Area

Surface areas were obtained by calculating the area of each triangle in the triangulated surface mesh and then summing these to yield the overall area. To do this, the coordinates of the vertices representing the points of each triangle were obtained using an inbuilt function in Matlab and a cross-product calculated, to give the area. This was repeated for each triangle in the reconstruction to give the total surface area.

The area of each individual tringle may be obtained from the following

$$A = \frac{1}{2}\left|\left(v_{ik} \times v_{jk}\right) + \left(v_{jk} \times v_{kk}\right) + \left(v_{kk} \times v_{ik}\right)\right| \tag{3.4.1}$$

Where v_{ik}, v_{jk} and v_{kk} are the vertices of the triangle k. The entire flame surface may then be calculated as the sum of the areas of the individual triangles as

$$A = \sum_{f_{kF}} \left(\frac{1}{2}\left|\left(v_{ik} \times v_{jk}\right) + \left(v_{jk} \times v_{kk}\right) + \left(v_{kk} \times v_{ik}\right)\right| \right) \tag{3.4.2}$$

3.4.2 Burned Gas Volume

The volume of each reconstruction was obtained first by converting the triangulated surface mesh into a solid reconstruction consisting of voxels using a code by Kroon, D. (2016). This code discretises the triangulated surface by splitting and refining each face until the longest edge is smaller than half of a voxel. The voxel is then set beneath the vertex coordinates of the original face to a value of unity.

As the size of each voxel is determined by the resolution of the camera and is thus known, summing the number of the individual voxels and multiplying by the individual voxel volume yields the volume of the reconstruction as per the following

$$V_{tot} = \sum n_v v_{vi} \tag{12}$$

Where V_{tot} is the total flame volume and n_v is the number of voxels. The voxel volume, v_{vi}, is constant throughout this work at 0.072 mm^3.

3.4.3 Determination of the Reaction Progress Variable for 2D and 3D Images

The reaction progress variable, as described in Section 1.5.2, has been calculated here for both 2D laser sheet images and 3D flame reconstructions. A common procedure is used in each case, extended into the third dimension when analysing the 3D reconstructions. The algorithm employed to calculate c was presented in Section 1.5.2. The method for obtaining this parameter using Matlab is as follows

i) Where 2D sheets were to be analysed, the raw, greyscale Mie scattering images were first binarised and the flame edge detected as described in Section 3.2. This yielded images with unburned mixture represented by pixels with a value of unity (represented as white) and burned mixture by pixels of value zero (shown as black)

ii) The coordinates of the centroid of the flame slice or 3D flame were then determined by finding the mean average x, y and z coordinates of all pixels with a value of zero in the binarised image/reconstruction

iii) Initially, both the 2D images and 3D reconstructions existed as Cartesian arrays of picture/volume elements (pixels/voxels), respectively. In each case, the array was converted into polar coordinates with a value of zero or unity at each coordinate. The conversion was carried out using the built in "cart2pol" function in Matlab where the nomenclature for this is shown in Fig. 3.11. For any Cartesian grid point P in the original array, an angle, θ, was calculated with respect to the x-axis along with a radius, ρ. For a 3D grid, based on the calculated value of ρ and the elevation in the z-axis a further radius, r, was calculated. Thus, as the original Cartesian grid consisted of elements of a finite size dependent on the original resolution of the camera, all grid points were described by discrete ρ and r values, where multiple instances of these values could occur

iv) Starting from the centroid, successive shells were created between chosen values of r, e.g. between $R = 1$ and $R = 2$ and the values of the cells lying between these radii determined by looping through the array. The fraction of burned elements out of the total number of burned and unburned elements combined yielded c

3.4.4 Determination of Flame Surface Density

Flame surface density, as defined in Section 1.5.3, has been calculated here for the 3D reconstructions. Much of the approach for obtaining this parameter in Matlab is common to that for obtaining *c*, with an additional step to determine the flame surface area at each radius.

i) The method used to calculate reaction progress variable, described in the previous section, was employed up to and including stage iv.

ii) Within each shell and for each burned element within this shell, the sum of the neighbouring elements was determined. As each element could be treated as possessing physical dimensions equal to those of the pixels in the original images, the surface area of each burned voxel exposed to unburned gas could be calculated

iii) Σ was then found by dividing the total flame surface area within shell by the total volume.

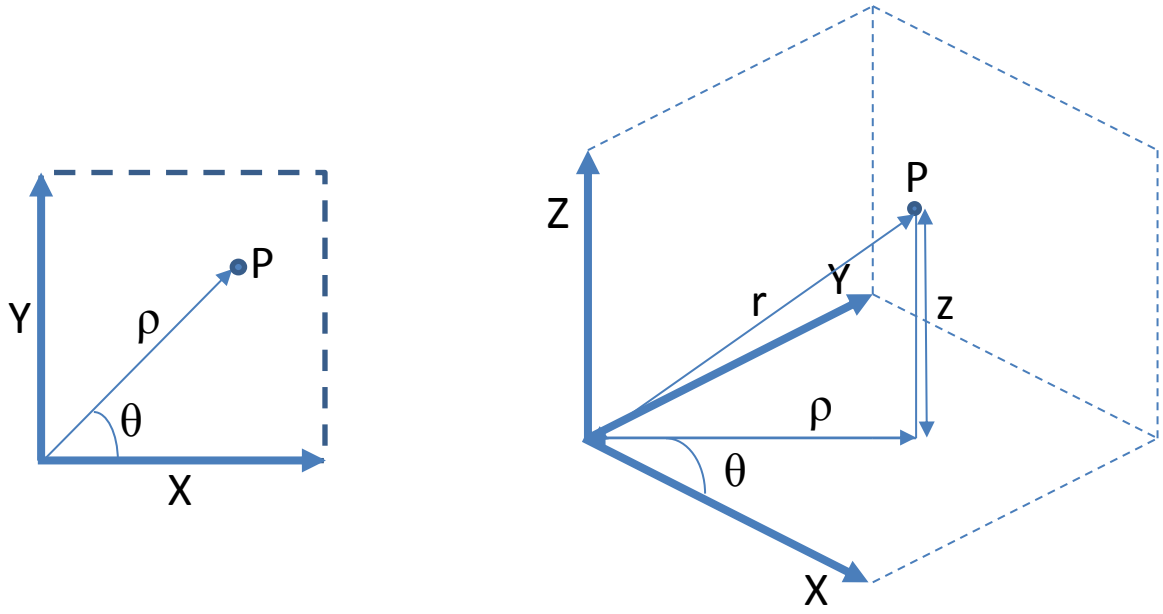

Figure 3.11 Notation for calculation of polar coordinates (adapted from The Mathworks, 2017)

3.5 Schlieren image processing

For the mixtures used in this study, u_l values were obtained from schlieren videos using the setup described in Section 2.2.1. As each video consisted of up to several hundred images, it was required to process several thousand images in total. For this reason, coupled with the empiricism associated with defining a schlieren flame edge and the onset of cellularity, a partially-automated image processing technique was adopted. The software for this was developed by Sharpe (2011) in Matlab.

3.5.1 Determination of schlieren flame radius

Figure 3.12 illustrates the stages involved in processing schlieren images using this software, where Fig. 3.12b shows a cellular flame image to be processed. In the first stage shown by Fig. 3.12.a, the presence of the spark plug and its tip were detected and the region around this masked by a wedge with an internal angle specified by the user (typically 45^o). This was carried out for the first image in the sequence, where no flame was present. The coordinates of the detected spark plug and the bomb window edge were stored by the code and recalled when each further image was processed. The flame edge was then detected using a level-set approach, followed by fitment of a best fit curve shown in Fig. 3.12c. Four radii were measured for this curve and the average obtained to yield a flame radius. This process was repeated for each image in the sequence, with each previous flame front serving as an initial level set starting point. Details of the level set technique are given in Sethian (1999) and Tripathi (2012). The obtained radius for each image was saved to file for further processing.

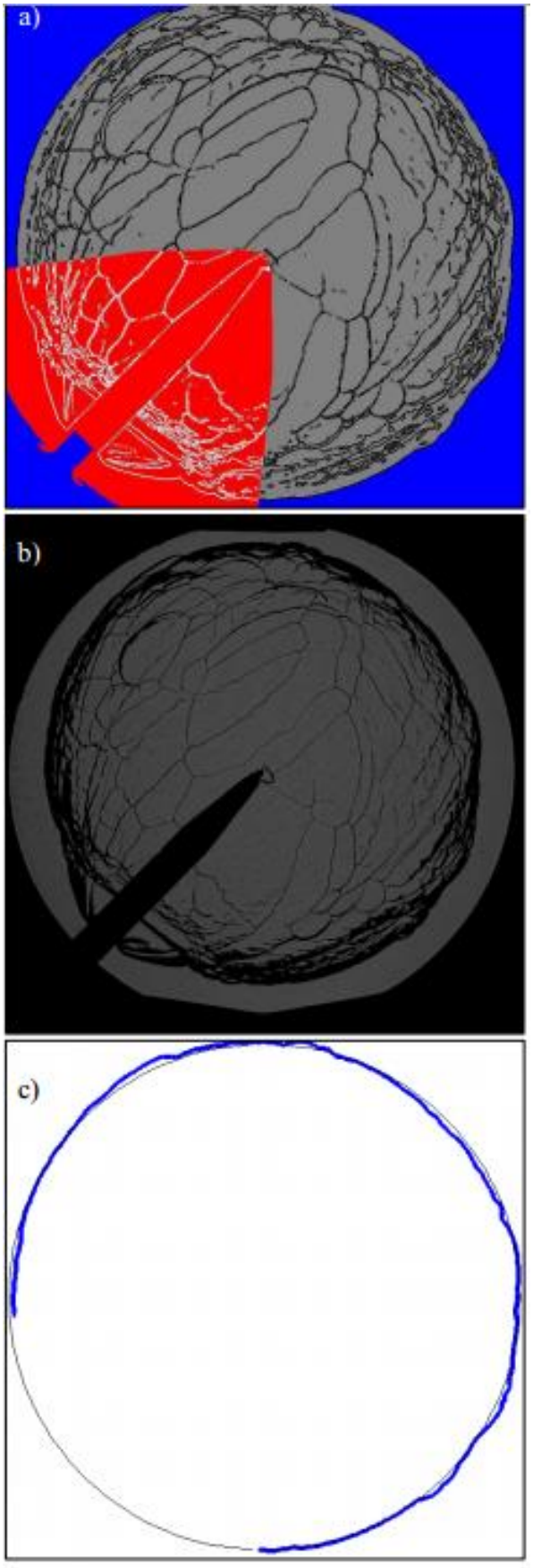

Figure 3.12 Schlieren image processing stages, reproduced from Mumby (2016)

3.5.2 Determination of S_s and L_b

Using the data obtained using the method presented in Section 3.5.2, the stretched flame speed as a function of radius and stretch rate was calculated as described in Section 1.4.1. These calculations were also performed using software developed by Sharpe (2011), which generated plots of radius versus time from ignition, stretched flame speed versus radius and stretched flame speed versus stretch rate. Examples of these plots are shown in Fig. 3.13. Note that Fig. 3.13 (c) shows linear and non-linear curve fits, which is not discussed in the present work as only linear fits have been applied here.

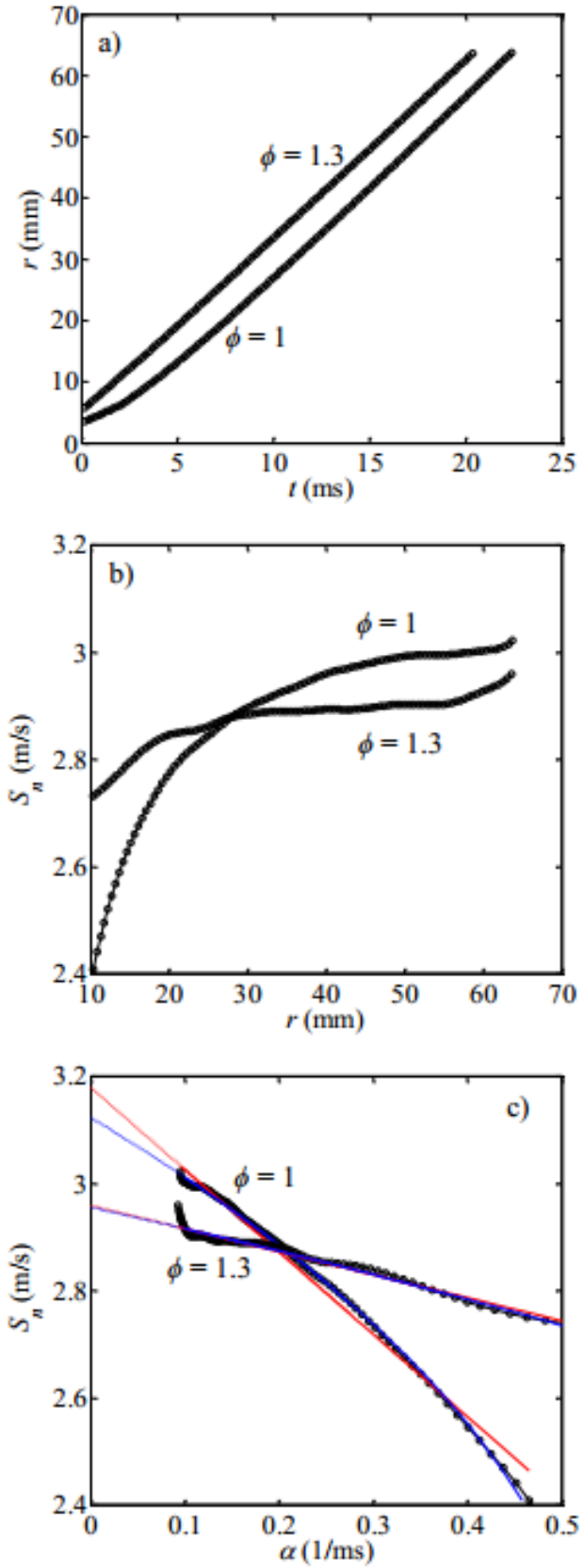

Figure 3.13 a) radius versus time, b) stretched flame speed versus radius and c) stretched flame speed versus stretch rate, all for iso-octane air at 0.1 MPa and 360K, reproduced from Mumby 2016

A linear approach to measuring l_b was automatically applied to the S_n v's α data to deduce S_s via extrapolation to zero stretch rate, with the selected data range overseen at every stage to ensure a realistic fit and application only within the stable regime of the flame growth. The laminar burning velocity, as described in Section 1.4.1, was then obtained as follows

$$u_l = \frac{\rho_b}{\rho_u} S_s \tag{13}$$

Chapter 4 – Results

4.1 Introduction

The 3D laser sheet imaging technique described in Section 2.3 has enabled the study of turbulent flame structure at engine-like conditions, where it also serves as a novel method for the measurement of turbulent burning velocities.

Section 4.2 presents measurements of the laminar flame speed and burning velocity of the mixture employed throughout the present study, using the schlieren imaging technique described in Section 2.2.1. The effects of laser ignition on the structure of laminar flames are also presented in this section. Section 4.3 presents the 2D laser sheet images and 3D reconstructions of flames growing under turbulent conditions along with measurements of the surface area ratio described in Section 1.6, the reaction progress variable described in Section 1.5.2 and flame surface density described in Section 1.5.3.

4.2 Laminar Burning Results

Figure 4.1 shows the variation of stretched flame speed, S_n, with stretch rate α for the mixture employed throughout the present work, where these variables were calculated from schlieren images using the procedure described in Section 1.4.1. At small radii, the flame speed was very high due to boosting of the flame by the high spark energy used to ignite the mixture (Tripathi, 2012). This decayed to a stable value as the flame grows. From the stretched flame speed and flame radius, the stretch rate was calculated using Eq. 1.7 and plotted against S_n in Fig. 4.2. Extrapolating the resulting curve to a theoretical zero stretch rate yielded the unstretched flame speed, S_s. The unstretched laminar burning velocity was calculated from S_s using Eq. 1.5. Figure 4.2 illustrates a positive Markstein number, as it can be seen that the stretched flame speed increases with increasing stretch rate. However, over three experiments, the value of Ma_{sr} was found to be slightly positive at 0.337. Gu et al. (2000) reported a positive Ma_{sr} at φ = 0.6 and a negative value at φ = 0.55. As the equivalence ratio used in the present study was 0.6, it is likely that small experimental errors gave rise to the variation between negative and positive Ma_{sr}.

All laminar burning parameters found in the present study are given in Table 4.1, where Ma_{sr} and S_n are identical in magnitude to 3 decimal places. The values of u_l and Ma_{sr} were used to calculate u_t/u_l using Eqs. 1.31 to 1.34 as described in Section 1.5.5.

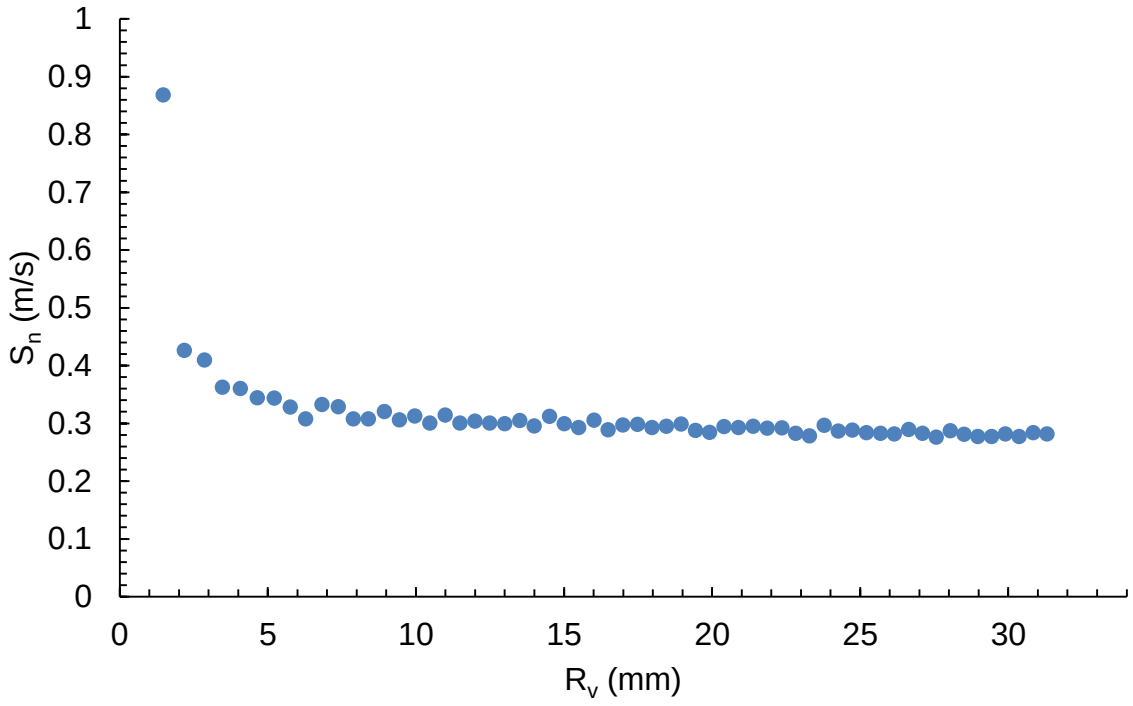

Figure 4.1 A typical graph of the variation of stretched laminar flame speed with flame radius, for methane/air at 298K, 0.1 MPa and φ = 0.6, laminar

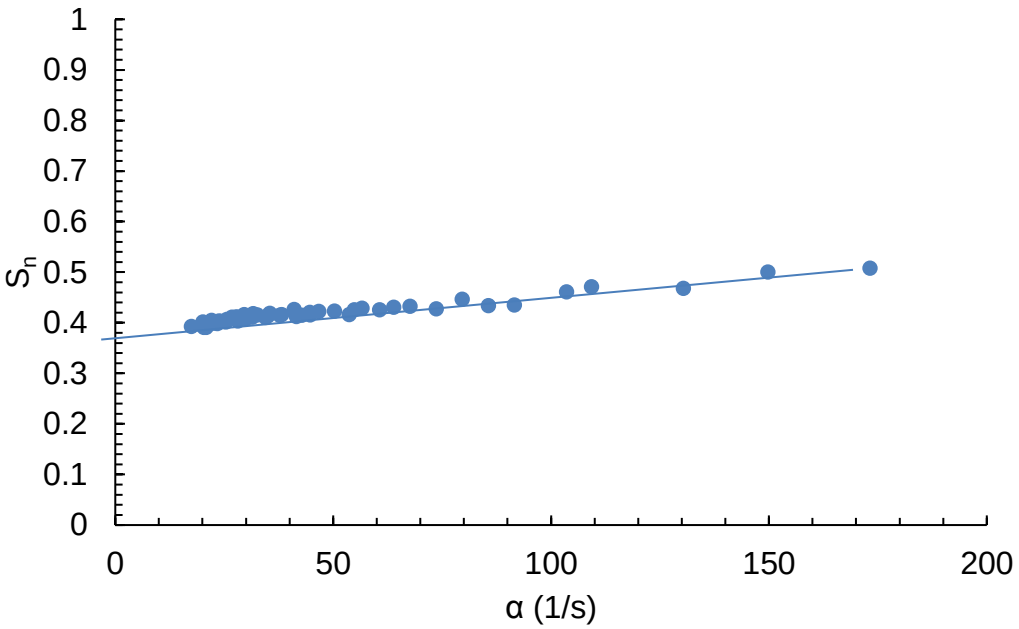

Figure 4.2 A typical graph of the variation of stretched laminar flame speed with stretch rate, for methane/air at 298K, 0.1 MPa and φ = 0.6, laminar.

Table 4.1 Burning parameters obtained for methane/air at 298K, 0.1 MPa and φ = 0.6

Parameter	Value	Units
L =	0.02	m
ν =	2E-05	m^2/s
ρ_b/ρ_u =	0.179	n/a
δ_l =	0.274	mm
S_n =	0.337	m/s
u_l =	0.0591	m/s
Ma_{sr} =	0.337	n/a

The use of laser ignition in the present study gave rise to aspherical flames, where this phenomenon was demonstrated in the schlieren images of Bradley et al. (2004) as shown in Fig. 4.3. For the first time, in the present study 3D images have been captured of such distorted flames, as shown in Fig. 4.4. This figure shows that the flame retains the shape formed during ignition as it grows. This effect is also visible in reconstructions of flames developing at low turbulence, which is discussed in the next section.

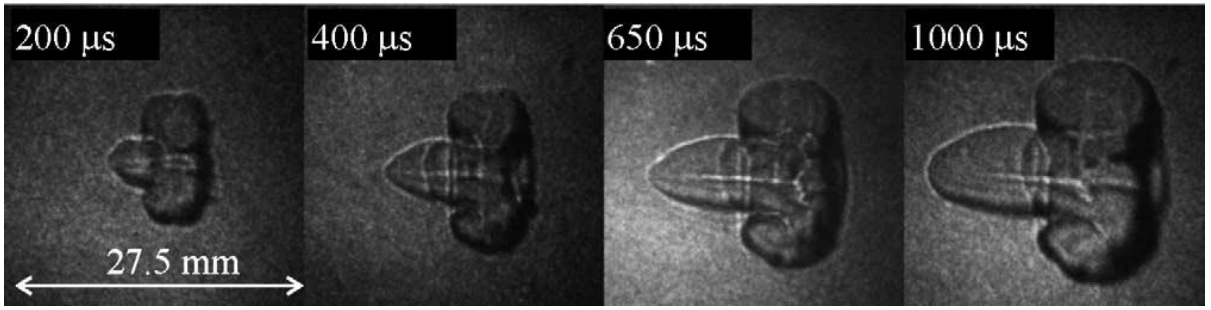

Figure 4.3 Schlieren images of a growing laser-ignited flame, from Bradley et al. (2004)

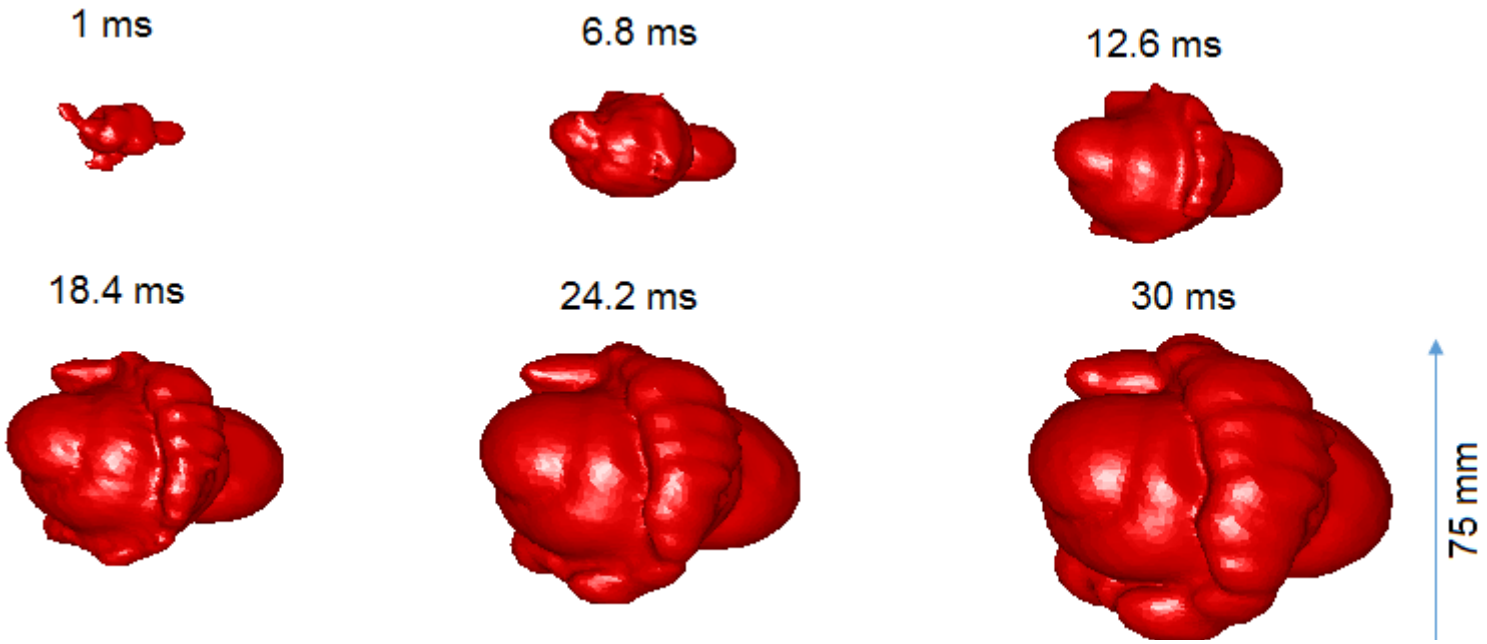

Figure 4.4 3D reconstructions of a growing laminar methane/air flame in the present work

4.3 Turbulent Burning

This section presents a selection of the 2D laser sheet images obtained in the present work for turbulent methane/air flames, along with the reconstructions generated from these. Experiments were conducted using a single methane/air mixture with a starting temperature of 298K, a starting pressure of 0.1 MPa and equivalence ratio, φ, of 0.6. To study the effects of increasing RMS turbulence velocity, *u'*, on turbulent flame structure, discrete *u'* values in increments of 0.25 m/s up to a maximum of 1.25 m/s were employed. This led to Karlovitz numbers (*K*) between 0.25 and 2.85, which corresponded to engine-like conditions of turbulence.

In most cases in the present work, two experiments were conducted at each *u'* value. Although combustion studies typically conduct five or more experiments at each condition due to inherent experimental scatter, this was not feasible in the present work due to the time-consuming nature of data processing. However, as the study of full 3D flame images avoids the necessity of making assumptions about the relationship between 2D flame structure and the extension of this into the third dimension, it is likely that such scatter will have been reduced in the present work.

4.3.1 2D Laser Sheet Images

Figure 4.5 shows a full sweep of laser sheet images for a methane/air flame at low turbulence. Image number 8 in this figure, shown in an enlarged view in Fig. 4.6, shows a seemingly detached section of flame towards the top of the image (circled). On examination of the surrounding sheet images, it is obvious that this section of flame is, in fact, attached to the main body. Thus, a 2D analysis with a fixed sheet position would have incorrectly implied that the flame existed in multiple, fragmented parts.

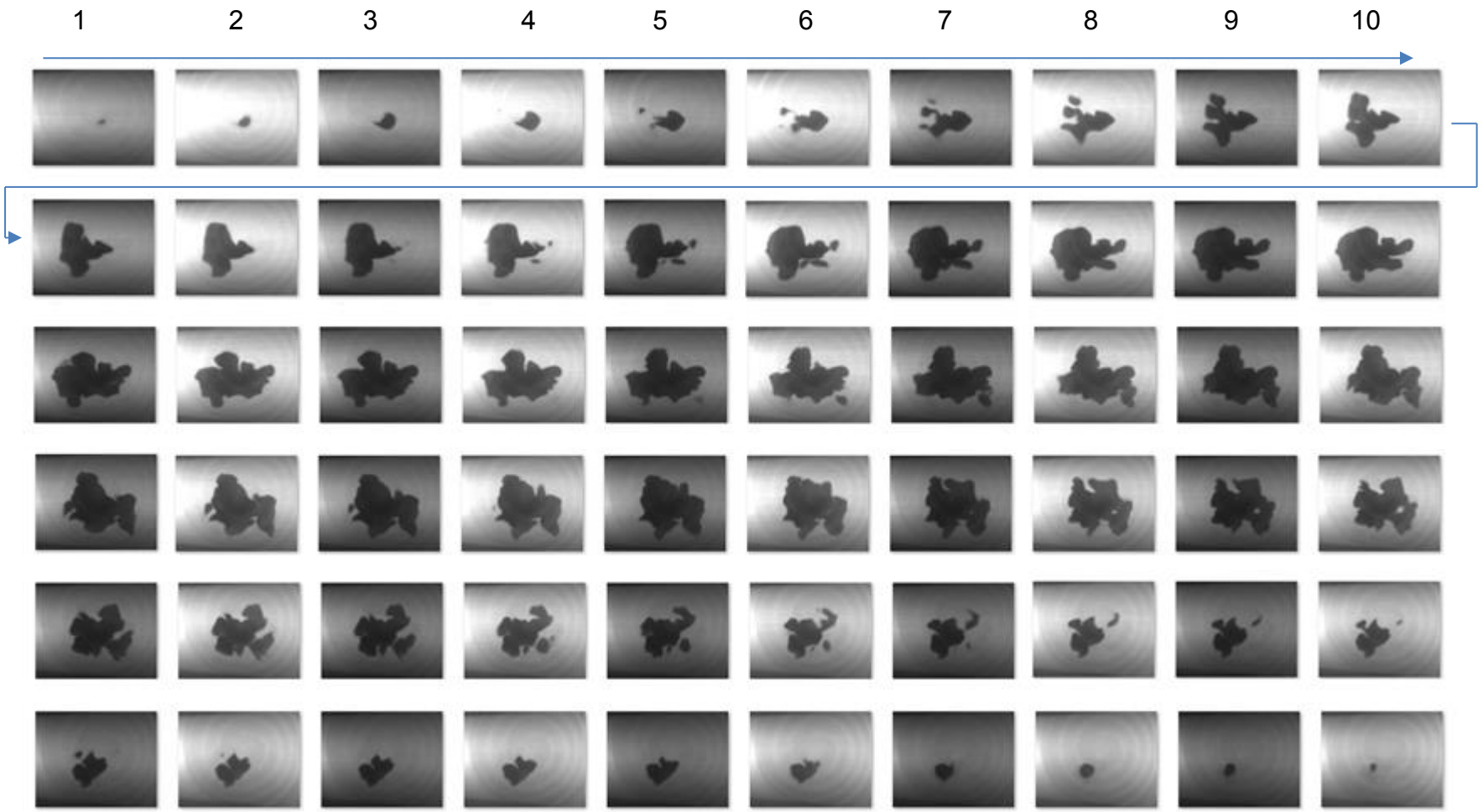

Figure 4.5 Full series of laser sheet images for a methane/air flame at u' = 0.25 m/s, 24.2 ms from ignition.

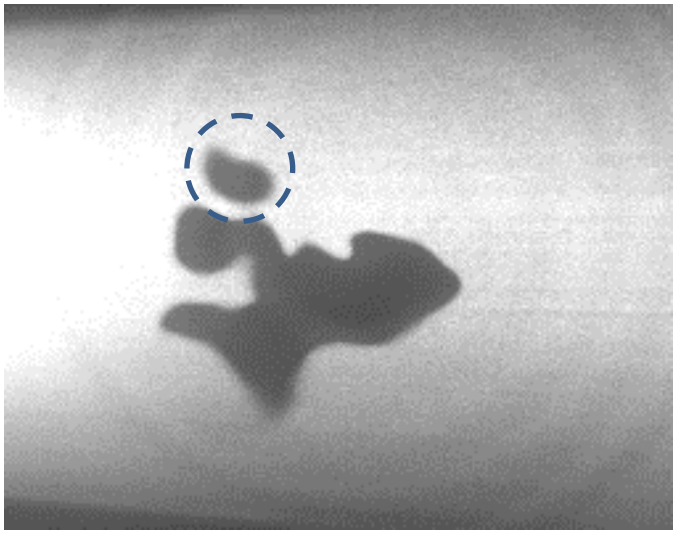

Figure 4.6 Enlarged view of Image 8 from Fig. 4.5

A further single sheet image from Fig. 4.5 is shown in enlarged form in Fig. 4.7, where a small island of unburned mixture is visible. Again, analysis of this single sheet would imply that this region is isolated. On examining the sheet images either side of this, this region is clearly part of a deep wrinkle in the flame surface.

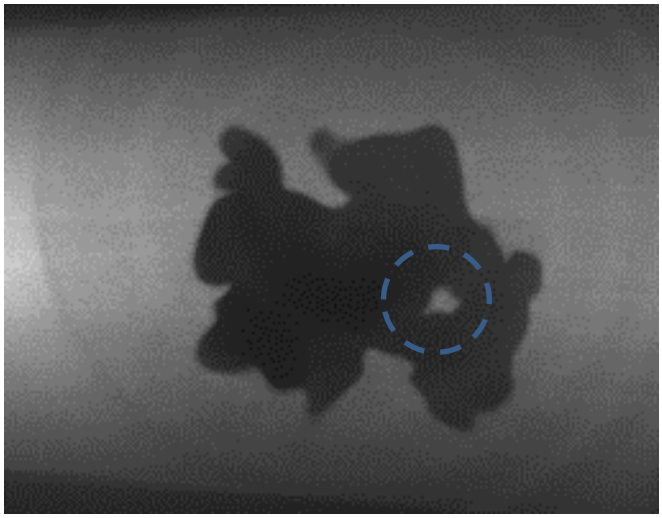

Figure 4.7 Image from Fig. 4.5 displaying an isolated region of unburned mixture

So far, the images examined were captured for flames developing at low *u'* and thus low Karlovitz number, *K*. These images showed a consistent, unambiguous and well-defined flame edge. Thus, application of the edge detection and binarising algorithm described in Section 3.2 led to a reliable representation of the original image. Figure 4.8 shows examples of 2D laser sheet images captured for flames at various *u'*.

At the lowest *u'*, corresponding to K = 0.25, the flame edge is again well defined. At an intermediate K = 1.32, the flame surface is generally intact and well defined, but wispy regions are visible which, although traced by the edge detection algorithm, were manually removed. Such regions resulted from the loss of some of the seed particles from the mixture and in this case was due to clipping the flame edge. In Fig. 4.8 (c), such wispy regions are also present and circled, where the flame was developing at a high K = 2.85, corresponding to the start of the quenching regime illustrated in Fig. 1.8. It appears in this case that the flame edge has been highly stretched by turbulence and has possibly quenched. This gave rise to areas with low seed particle concentrations where hot combustion gases mixed with the unburned mixture.

(a)

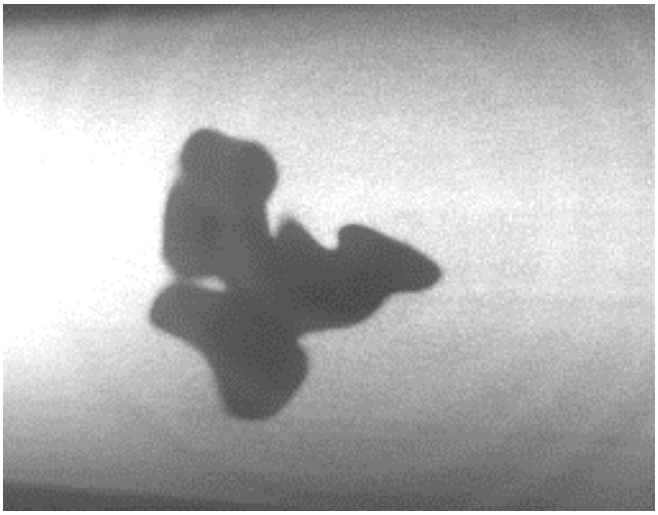

(b)

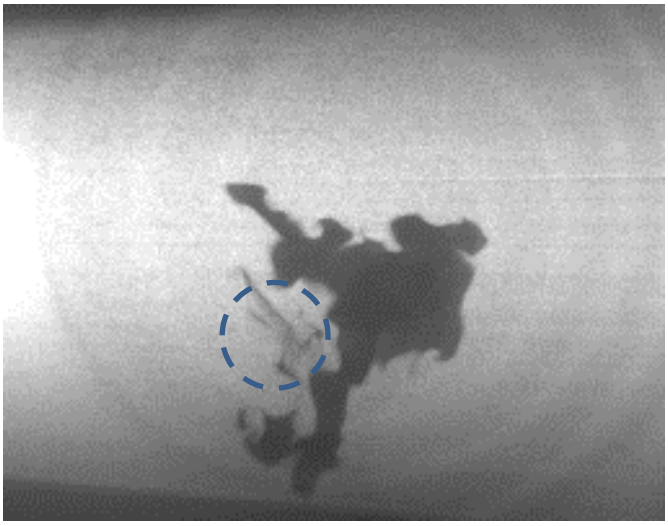

(c)

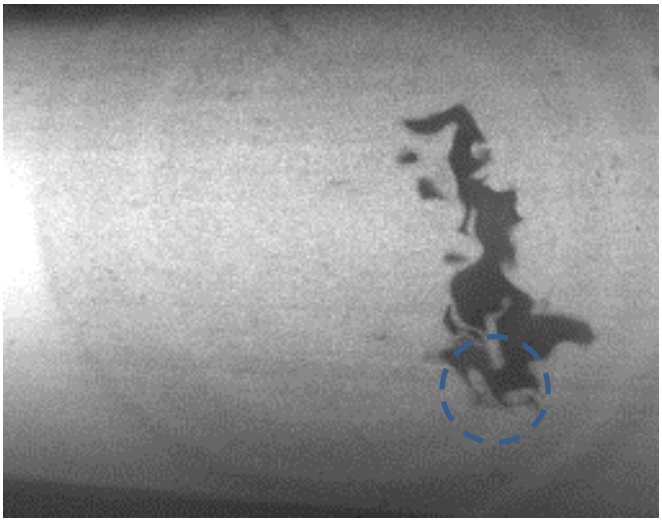

Figure 4.8 Laser sheet images of flames at (a) *u'* = 0.25 m/s, (b) *u'* = 0.75 m/s and (c) *u'* = 1.25 m/s

Figure 4.9 gives an example of a sheet image captured at a *u'* value well into the quenching regime shown in Fig. 1.8, which could not be used to generate a reconstruction as the flame surface was highly distorted by the turbulence and as such, an unambiguous flame edge could not always be defined. Due to the highly distributed nature of the flame, interpolation between the sheets would not have been possible. Such images, in conjunction with particle image velocimetry (PIV) could be used in further studies into the mechanisms behind flame quenching.

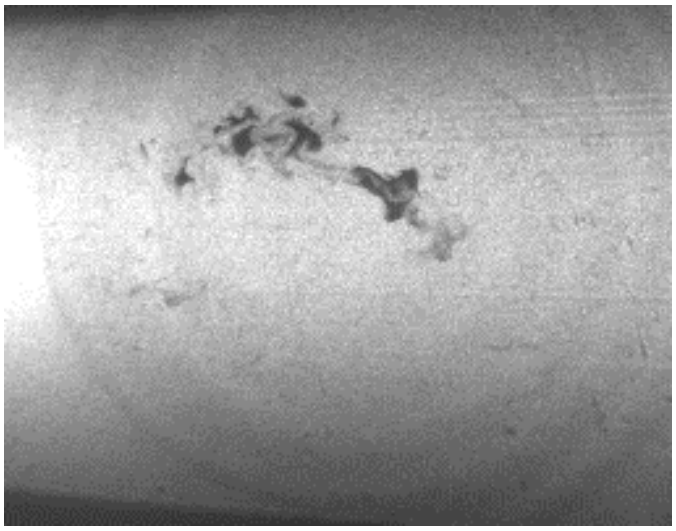

Figure 4.9 Flame developing at typically quenching levels of turbulence

4.3.2 3D Flame Reconstructions

Figures 4.10 to 4.13 show the temporal growth of single flames at each *u'* value employed in the present work. In each case, the flame surface wrinkling increased with time from ignition and thus flame radius due to the flame surface being affected by increasing length scales of turbulence during growth and the effective RMS turbulence velocity, u'_k, increased; in the early stages of flame growth, the larger length scales merely convected the flame (Abdel-Gayed 1987). Figure 4.10 illustrates that at the low level of turbulence applied to this flame, it retained the shape formed during ignition as it grew whilst the surface became more wrinkled. The flame shown in Fig. 4.11 at a higher value of u' did not maintain its initial shape as it grew, with the surface being visibly highly wrinkled. The formation of "fingers" protruding from the flame surface is also noticeable, with an isolated region of flame being visible. The reconstructions shown in Fig. 4.12 exhibit very highly wrinkled surfaces in the later stages of growth.

Figure 4.13 shows an interesting case where, although the flame surface does not appear particularly wrinkled, it is highly distorted and flattened. This becomes even more apparent when the reconstruction is viewed from alternative angles as shown in Fig. 4.14, where the rotated images in this figure were obtained by examining the 3D flame reconstruction in Meshlab.

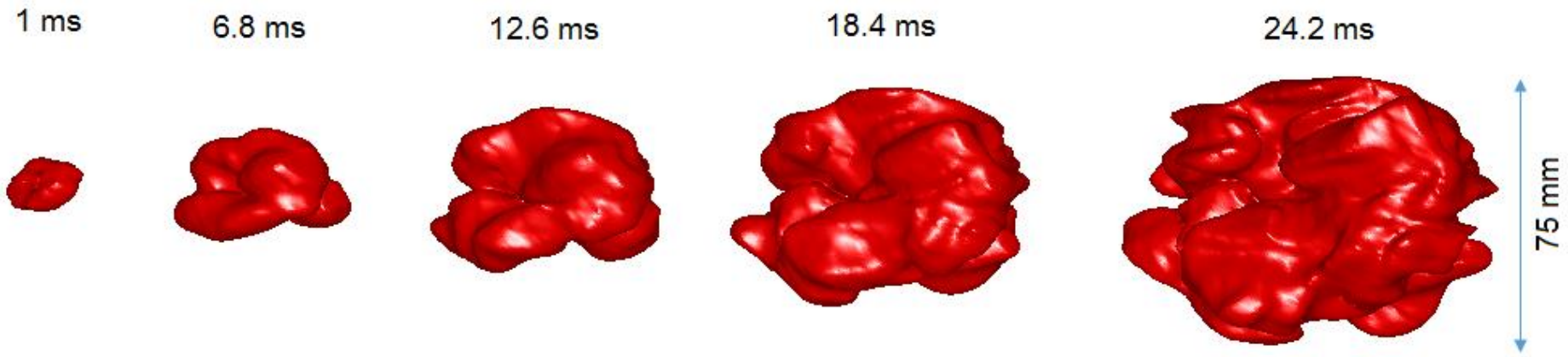

Figure 4.10 Growth of a turbulent flame over time with constant axis scaling, methane/air at 0.1 MPa, 298K and φ = 0.6, u' = 0.25 m/s

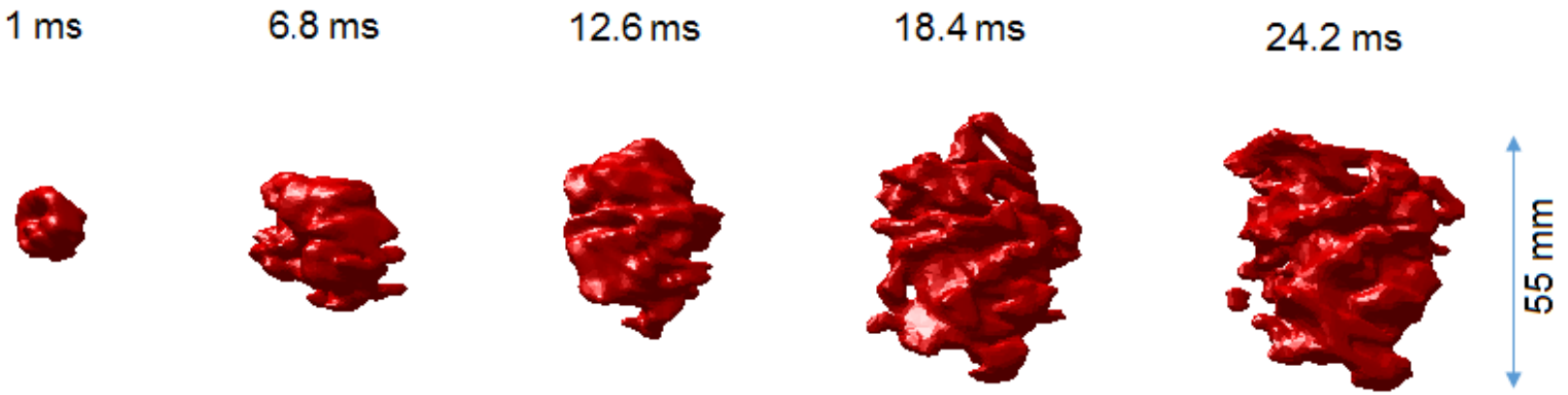

Figure 4.11 Growth of a turbulent flame over time with constant axis scaling, methane/air at 0.1 MPa , 298K and φ = 0.6, u' = 0.5 m/s

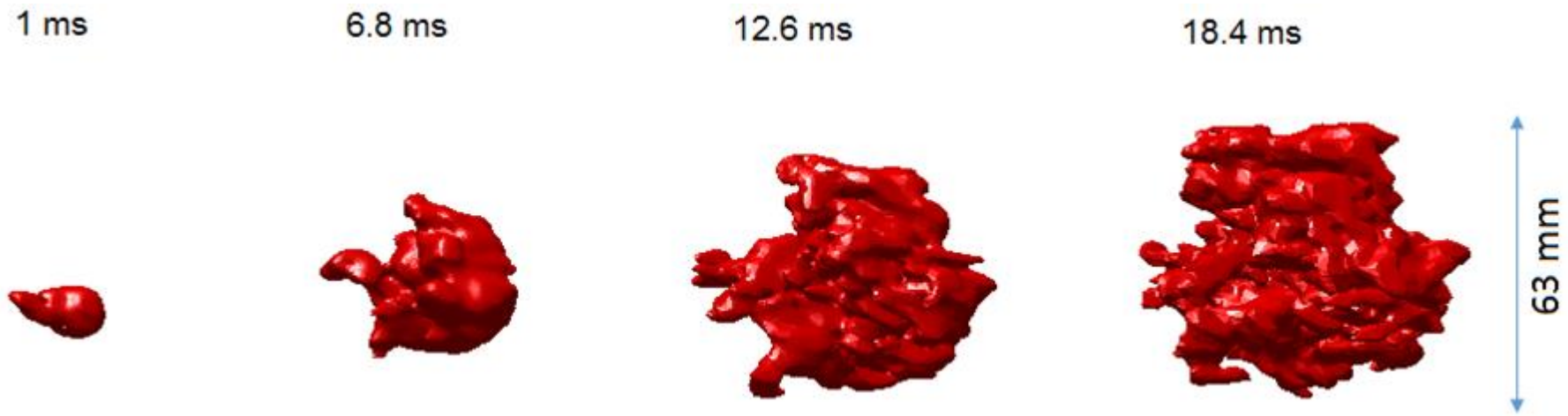

Figure 4.12 Growth of a turbulent flame over time with constant axis scaling, methane/air at 0.1 MPa, 298K and φ = 0.6, u' = 0.75 m/s

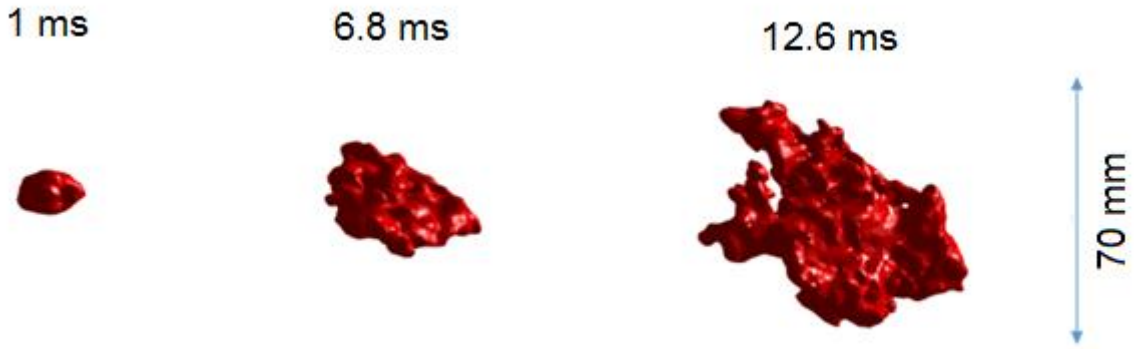

Figure 4.13 Growth of a turbulent flame over time with constant axis scaling, methane/air at 0.1 MPa, 298K and φ = 0.6, u' = 1.0 m/s

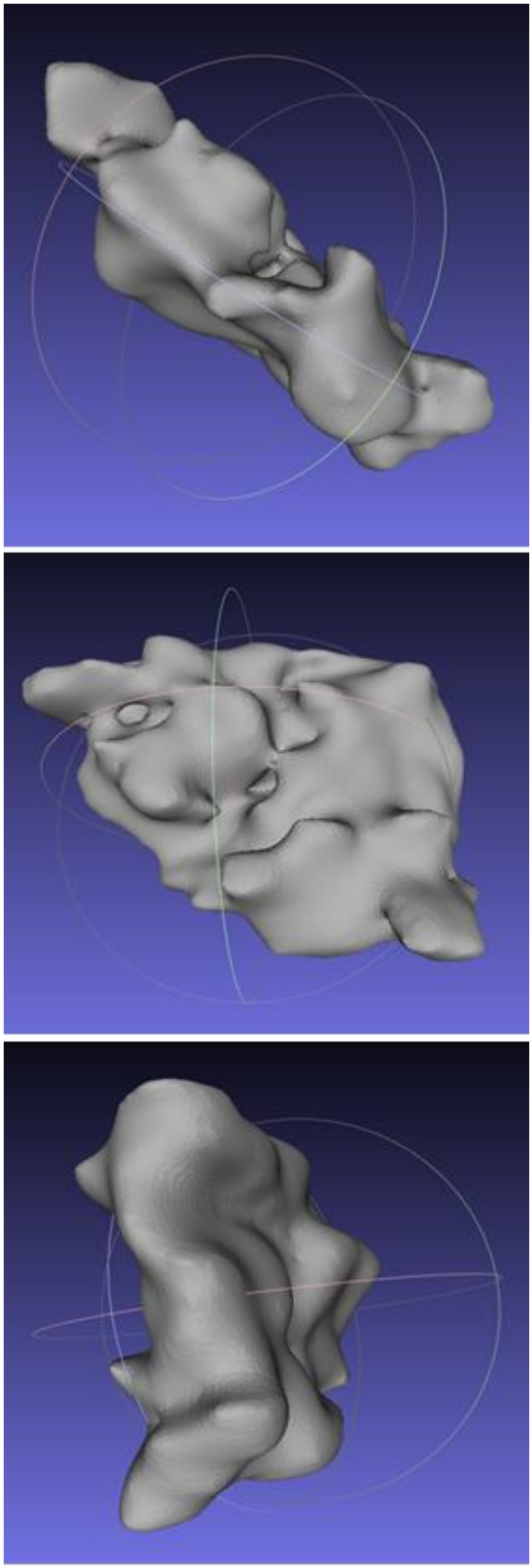

Figure 4.14 Single 3D reconstruction with *u'* = 1.0 m/s, 12.6 ms from ignition, various viewing angles as displayed in Meshlab

This flattening effect is also visible in Fig. 4.15 and the rotated views shown in Fig. 4.16. However, the reconstruction in this case shows a much higher level of wrinkling than that shown in Fig. 4.13 and Fig. 4.14, even though the flame radius was similar in each case. Some similarity may be observed between these figures exhibiting flattening and the 2D high-turbulence image shown in Fig. 4.9, where in each case the flame is longitudinally stretched. In addition to increasing the surface area ratio, A/a, it also frequently led to the flames rapidly extending beyond the field of view, limiting the possible number of sweeps.

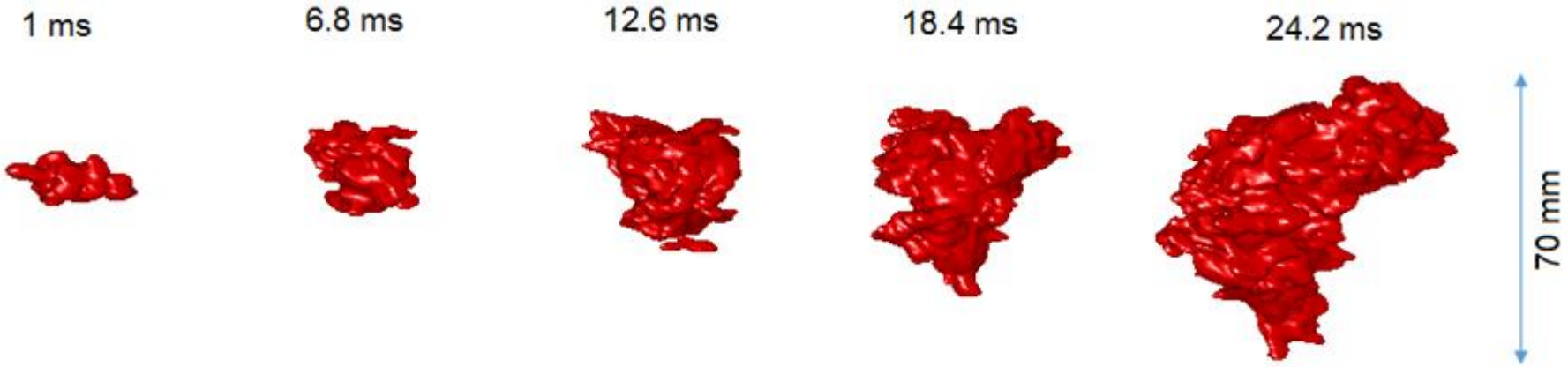

Figure 4.15 Growth of a turbulent flame over time with constant axis scaling, methane/air at 0.1 MPa, 298K and φ = 0.6, u' = 1.25 m/s

+

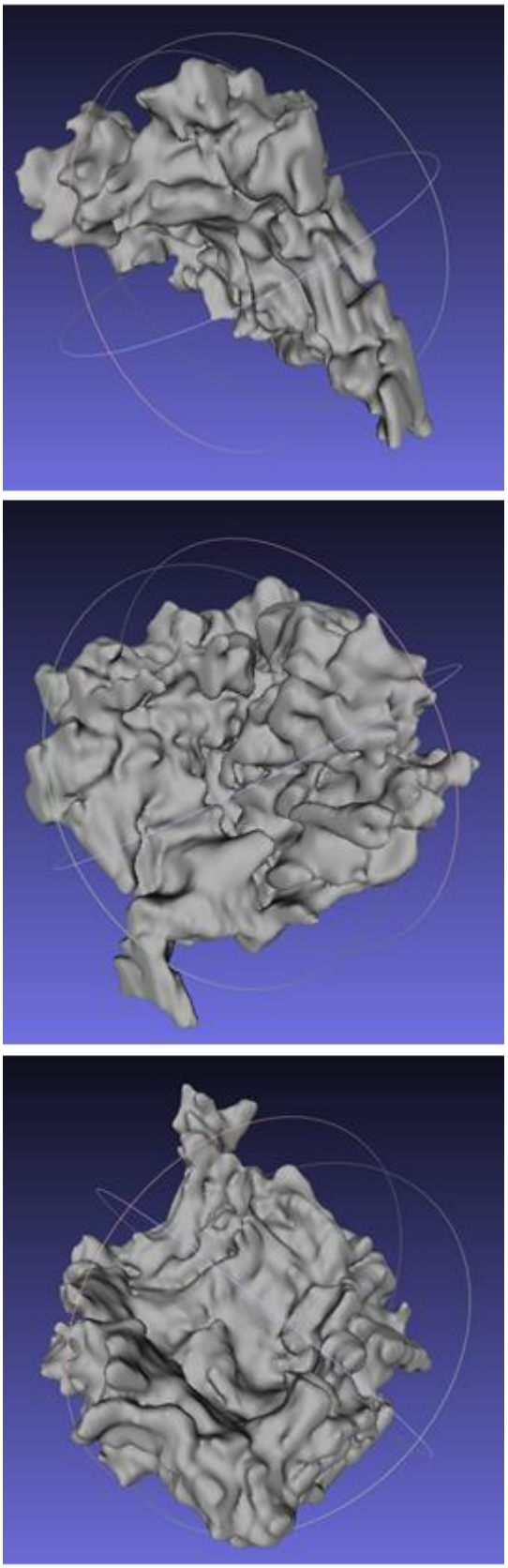

Figure 4.16 Single 3D reconstruction with *u'* = 1.25 m/s, 24.2 ms from ignition, various viewing angle

4.3.2.1 Surface area ratio measurements

For the reconstructions shown in Fig. 4.10 to 4.15, the surface areas and burned gas volumes were obtained as described in Sections 3.4.2 and 3.4.1 respectively. The equivalent spherical surface area, *a*, as defined in Section 1.4.3 was calculated from this volume. The obtained *A/a* values were plotted as a function of time as shown in Fig. 4.17 to 4.19, corresponding to the reconstructions shown in Fig. 4.10, 4.12 and 4.15, which are representative of the full data set and included here as examples. It can be seen in each of these figures that the surface area ratio increases with time from ignition, due to the increase in flame size with time and thus the range of turbulence length scales to which the flame is exposed. This corresponds to an increase in the effective RMS turbulence intensity, u'_k. In each case, the variation of *A/a* with time is slightly non-linear, with the graphs tending towards an asymptote. It could be expected that once the flame had reached a size where all length scales in the bomb could effect wrinkling of the flame surface, subsequent increases in flame size would yield no further increase in surface area ratio.

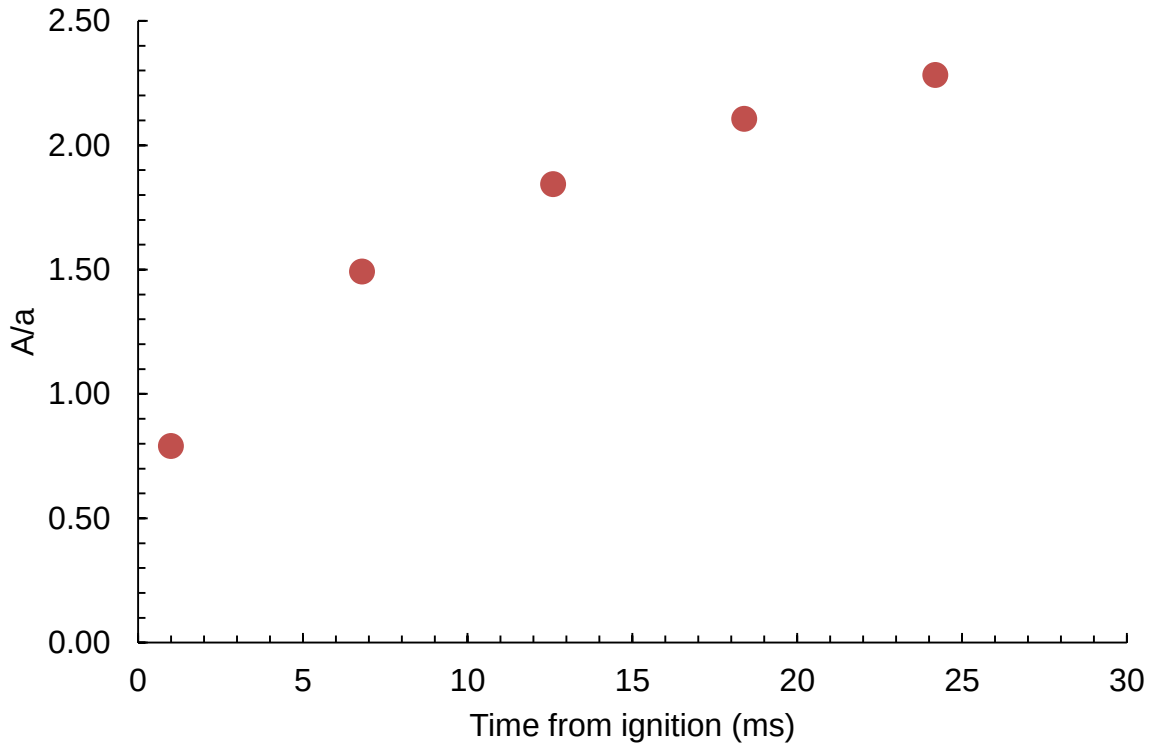

Figure 4.17 Variation of the surface area ratio with time from ignition for methane/air at 298K, 0.1 MPa, u' = 0.25 m/s and φ = 0.6. Crosses represent A/a.

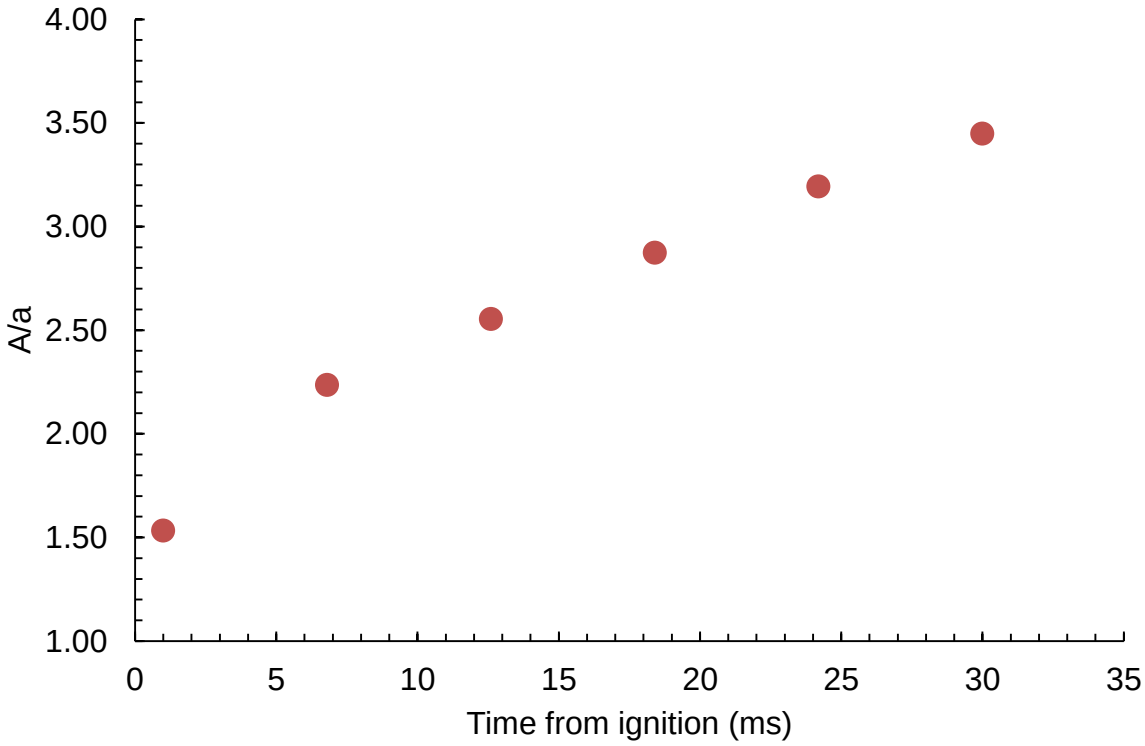

Figure 4.18 Variation of the surface area ratio with time from ignition for methane/air at 298K, 0.1 MPa, *u'* = 0.75 m/s and φ = 0.6. Crosses represent *A/a*.

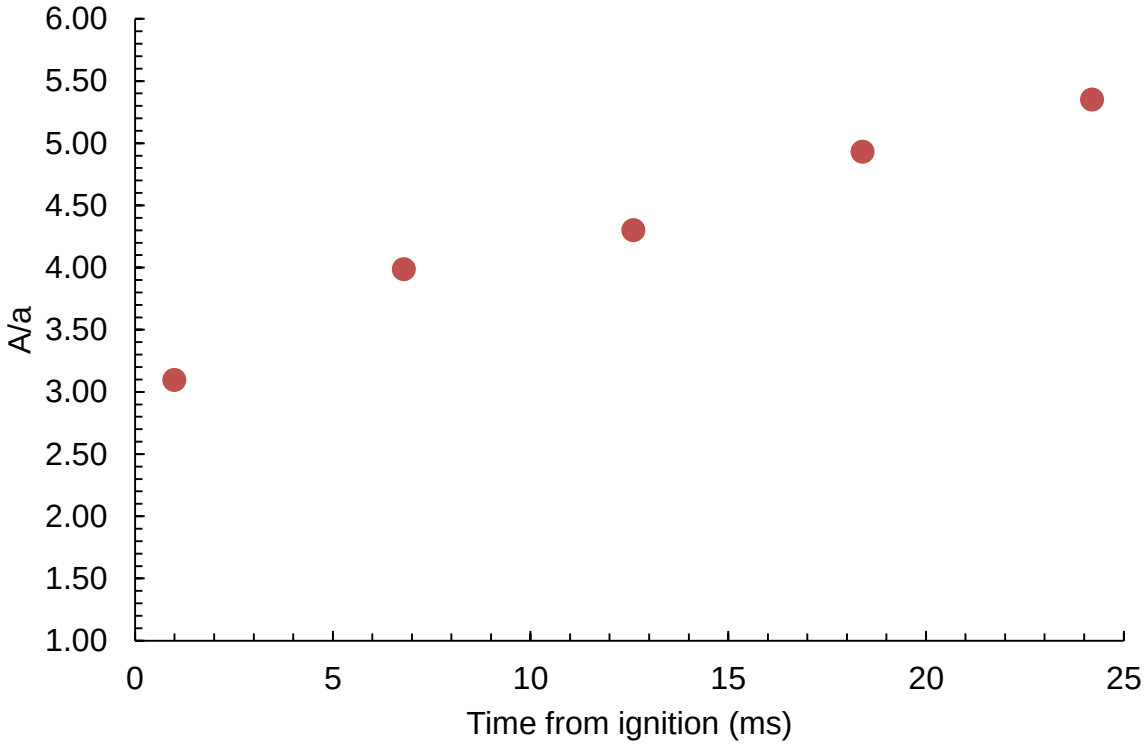

Figure 4.19 Variation of the surface area ratio with time from ignition for methane/air at 298K, 0.1 MPa, *u'* = 1.25 m/s and φ = 0.6. Crosses represent *A/a*.

To obtain generality between the *A/a* results, plots of *A/a* with u'_k/u' were generated and a linear extrapolation performed up to a u'_k/u' value of 0.6. This value was chosen as it was only slightly greater than the maximum value typical of the largest reconstructions (thereby minimising the amount of extrapolation required) and was the minimum value at which Eqs. 1.32 to 1.34 were valid (Bradley 2016). The resulting *A/a* ratios are discussed in Section 5.3.

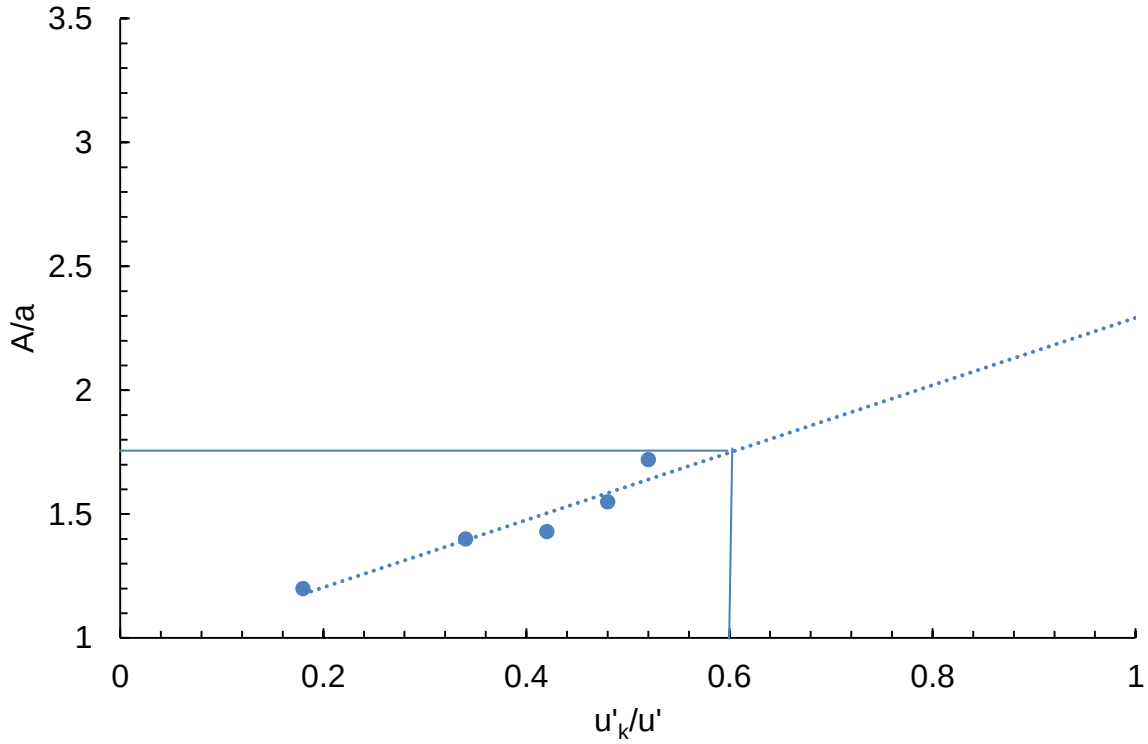

Figure 4.20 Extrapolation of *A/a* to u'_k/u' = 0.6, methane/air at 298K, 0.1 MPa and φ = 0.6, u' = 0.25 m/s

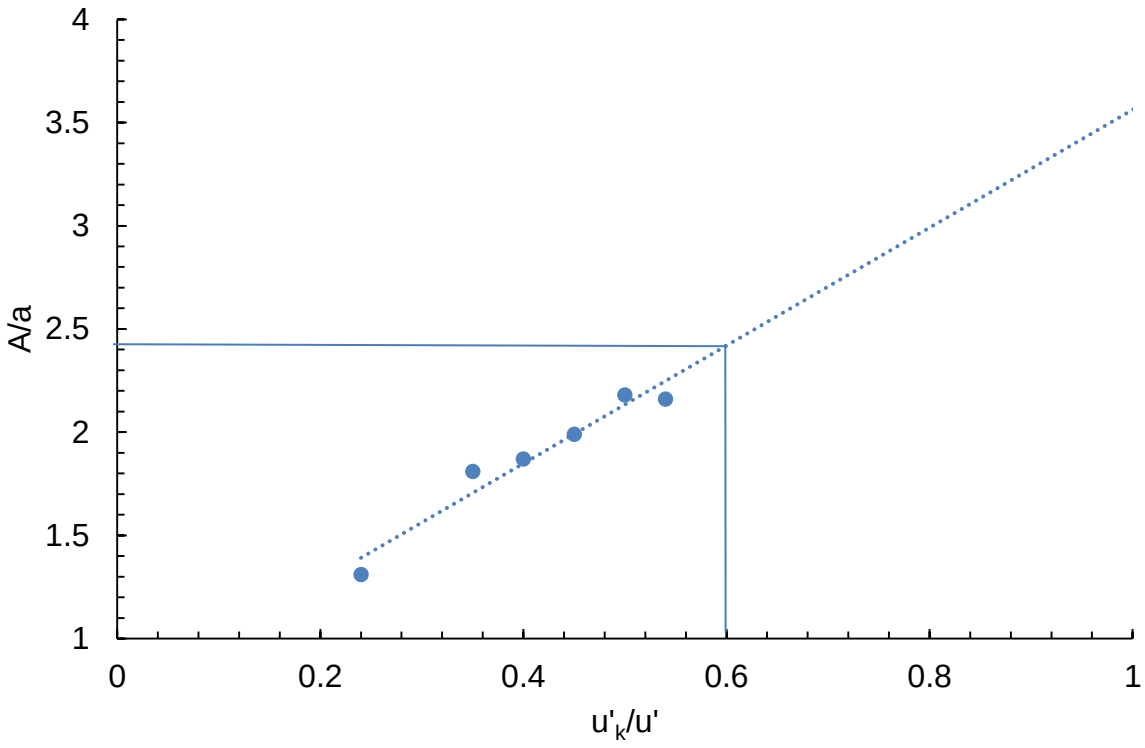

Figure 4.21 Extrapolation of *A/a* to $u'_k/u' = 0.6$, methane/air at 298K, 0.1 MPa and $\varphi = 0.6$, $u' = 0.75$ m/s

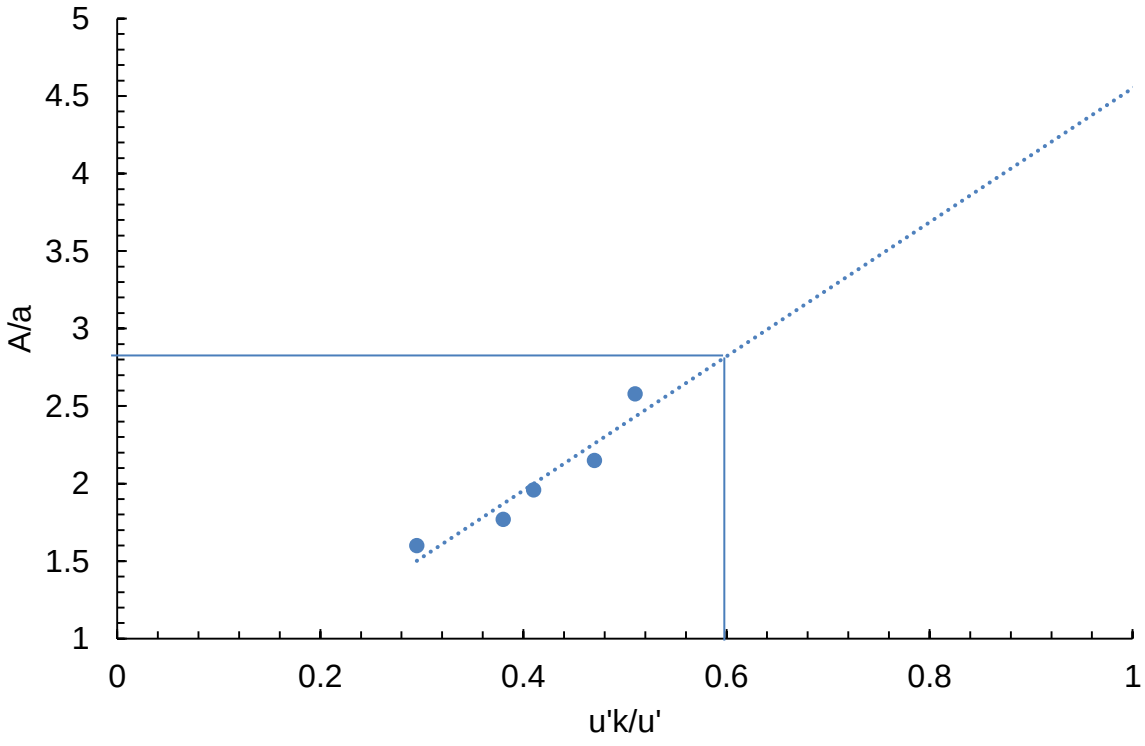

Figure 4.22 Extrapolation of *A/a* to $u'_k/u' = 0.6$, methane/air at 298K, 0.1 MPa and $\varphi = 0.6$, $u' = 1.25$ m/s

Shown in Fig. 4.23 is the variation in *A/a* with flame radius at each *u'* value employed in the present study. Points are connected with straight lines for clarity, where circles represent the first experiment and triangles the repeat. Only one successful experiment was carried out with *u'* = 1.0 m/s due to difficulties in ignition and a propensity for the flame to drift out of the field of view very quickly. These effects were less pronounced at *u'* = 1.25 m/s.

A good correlation is observed between the gradients of the curves and the relevant *u'* values, where higher *u'* values typically lead to a sharper rise in *A/a*. This is only a general trend, as some scatter is evident which is typical for turbulent combustion. Whilst the flames are small, it can be seen that the applied *u'* has a relatively small effect on *A/a* compared to at larger radii, as implied by Abdel-Gayed (1987). Some of the *A/a* values are relatively high immediately after ignition, where distortion of the flame shape due to laser ignition is likely responsible.

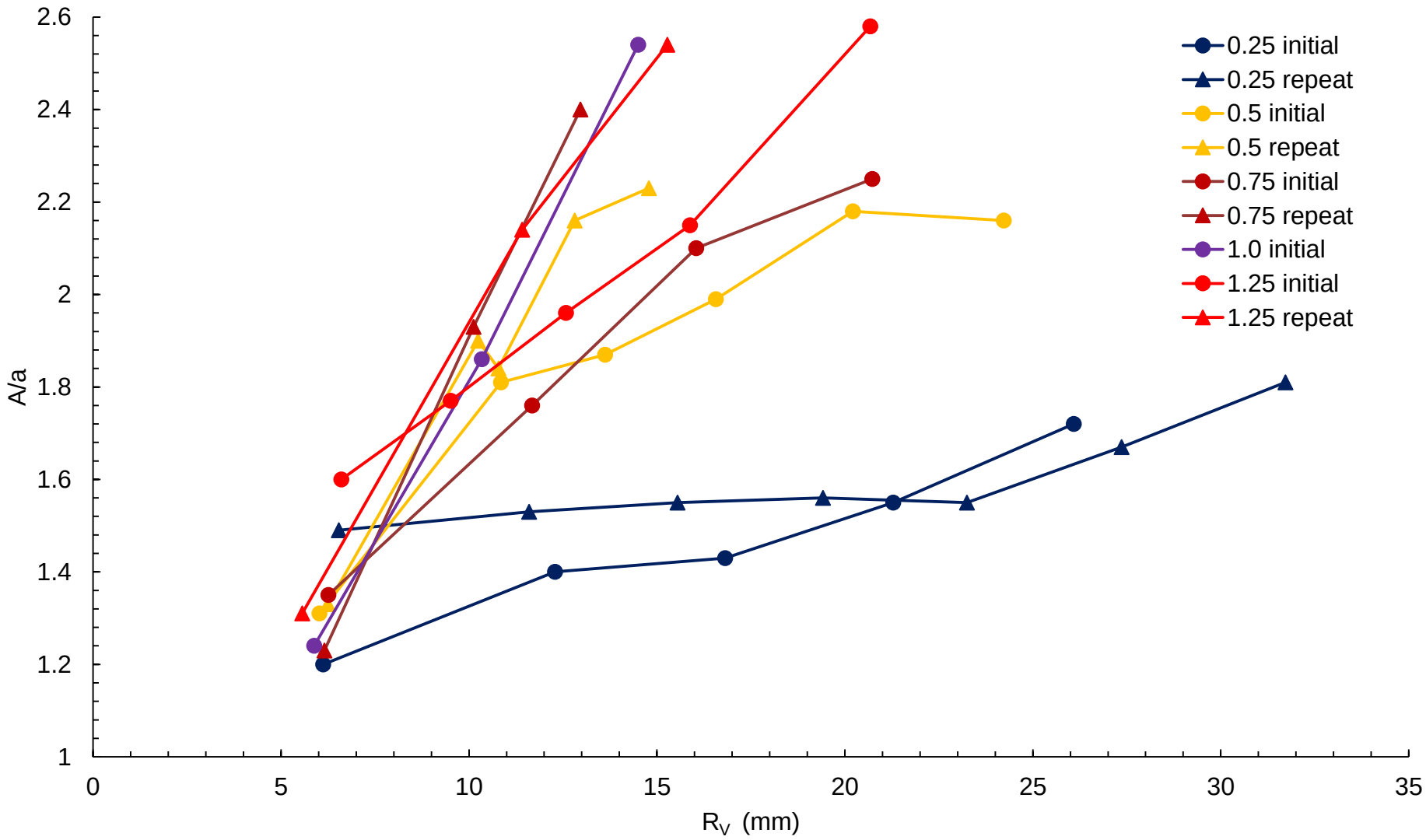

Figure 4.23 Increase in surface area ratio with flame radius during growth for methane/air at 298K, 0.1 MPa, φ = 0.6 and a variety of *u'* for the initial and repeat experiment at each condition

4.3.2.2 Reaction Progress Variable and Turbulent Flame Brush Thickness

This section presents the reaction progress variable, flame surface density and turbulent flame brush thickness results obtained from such images as those shown in Fig. 4.10 to 4.15. The method used for obtaining these parameters from the 3D reconstructions is as described in Section 3.4.

Figure 4.24 shows the variation in reaction progress variable, c, with radius from the centroid of the flame at various instants in time and u' = 0.25 m/s, where the radius is defined in Section 3.4.3. It can be seen that, during the early stages of flame growth up to 6.8 ms from ignition, the reaction progress variable takes a value of less than unity at very small radii. This was caused by the centroid of the flame being located in unreacted mixture due to the flame being hollow or ring-shaped at this stage. As the flame radius increased, the centroid location changed to where fully burned products were present. As the flame grew, the thickness of the flame brush increased, where the flame brush is defined as starting at the smallest radius at which c is less than unity and finishing at the smallest radii where c is greater than zero. This demonstrates that the flame became increasingly wrinkled as it grew.

The profile of the curves shown in Fig. 4.24 to 4.27 become more eccentrically shaped as u' increases, particularly at larger flame radii. Looking at the relevant reconstructions in Section 4.2, it can be seen that the flames not only become highly wrinkled at higher u', but also increasingly distorted. This is reflected in the shapes of the graphs, particularly at longer times after ignition where the flames are most distorted.

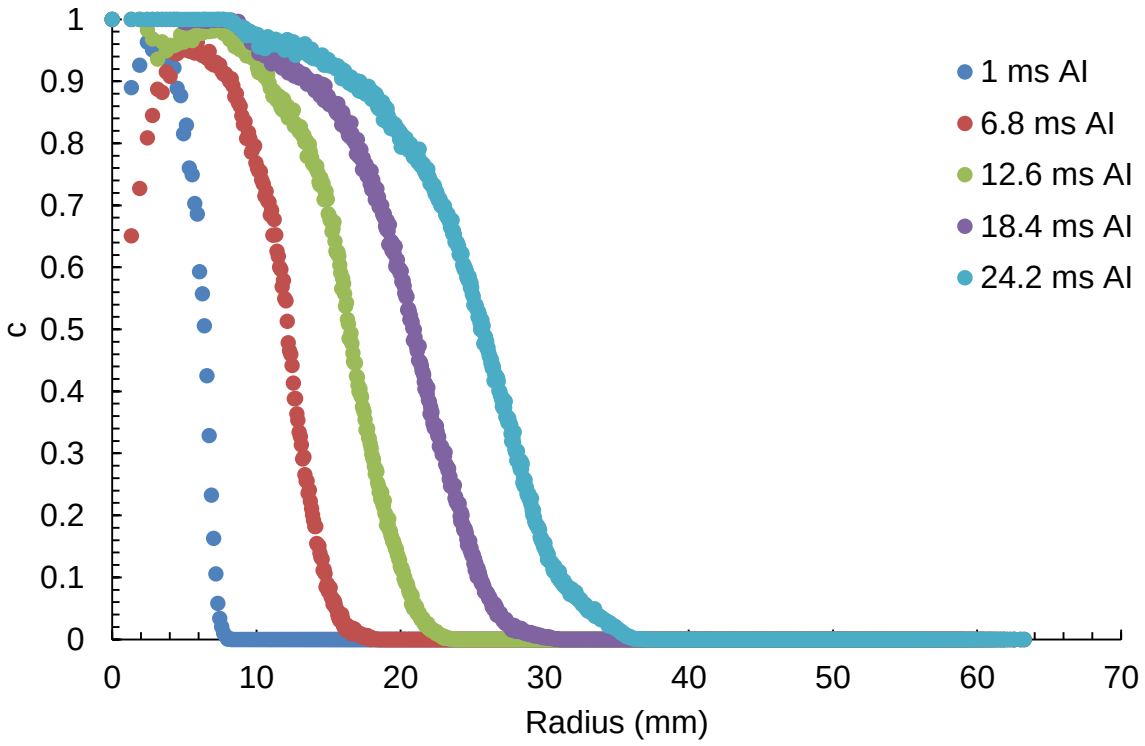

Figure 4.24 Reaction progress variable as a function of radius for methane/air at 298K, 0.1 MPa, φ = 0.6 and u' = 0.25 m/s

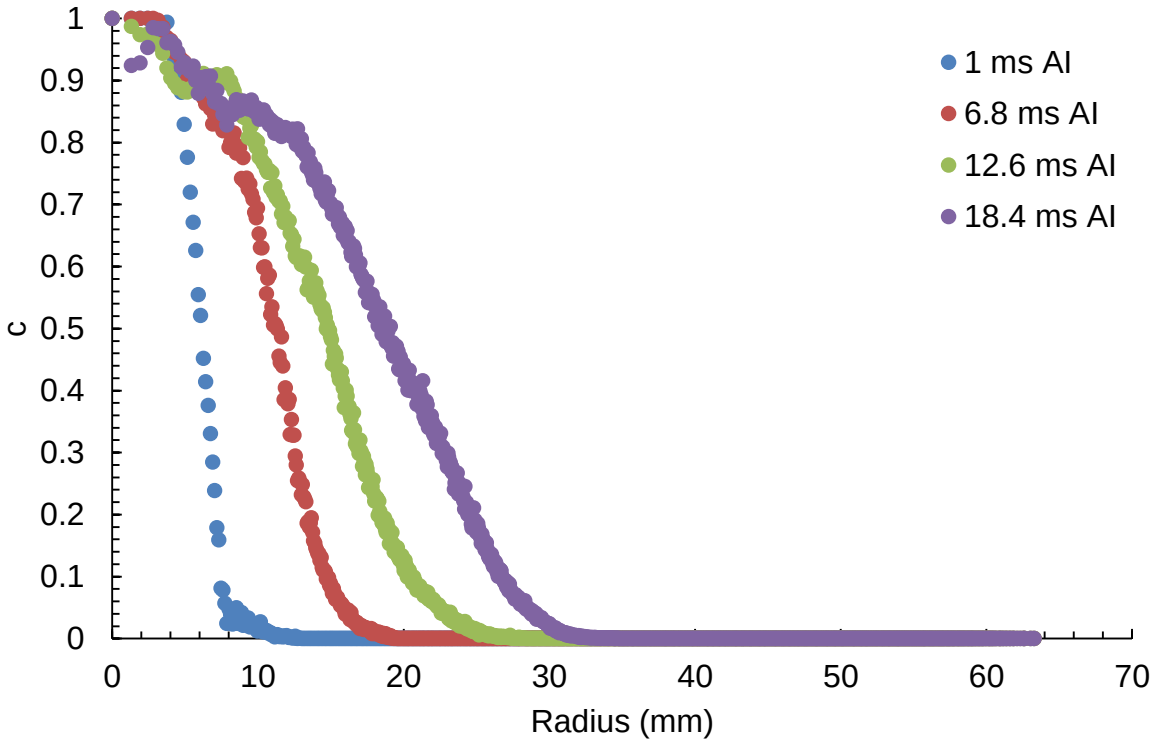

Figure 4.25 Reaction progress variable as a function of radius for methane/air at 298K, 0.1 MPa, φ = 0.6 and u' = 0.75 m/s

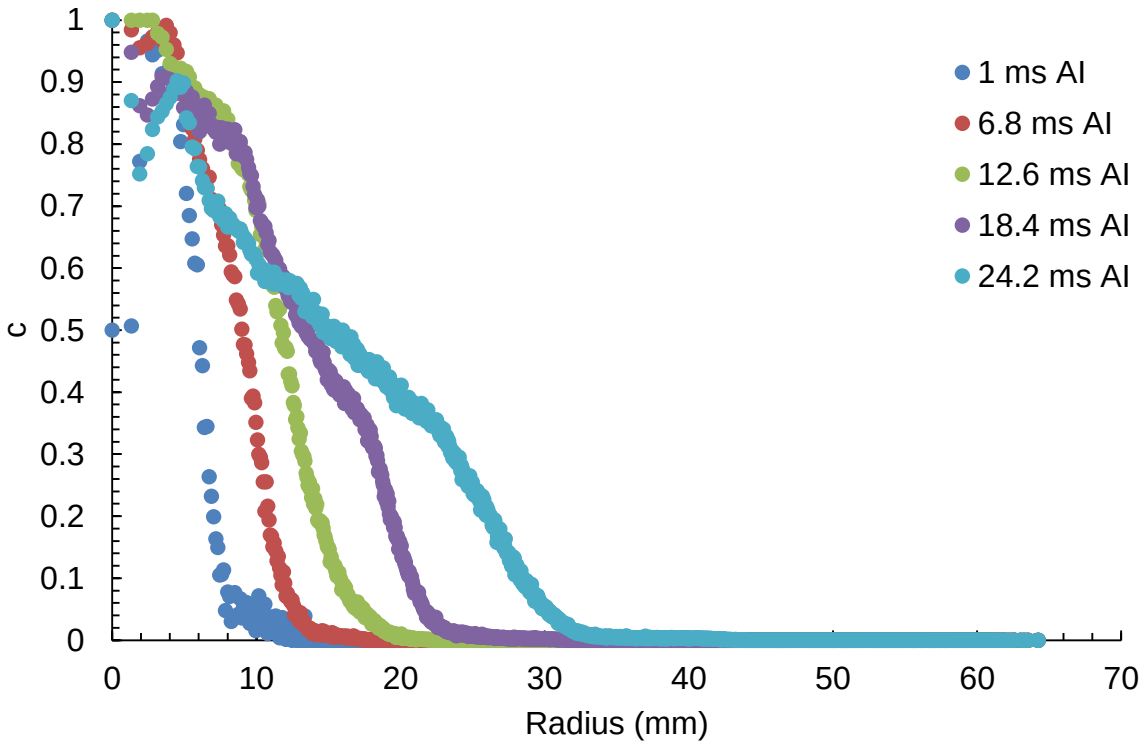

Figure 4.26 Reaction progress variable as a function of radius for methane/air at 298K, 0.1 MPa, φ = 0.6 and u' = 1.25 m/s

Shown in Fig. 4.27 is the variation in turbulent flame brush thickness, defined as δ_t, with flame radius at various u'. The turbulent flame brush thickness was calculated from the c versus radius data and was defined as the distance between the smallest radius where $c < 1$ and the largest radius where $c > 0$.

Here, a good correlation is observed between the δ_t behaviour with radius and the corresponding value of u' where, generally, the higher the value of u' the greater the gradient of the curve. It can, however, be seen that the single experiment conducted at u' = 1 m/s exhibits the steepest gradient of all the curves; experiments proved difficult to conduct at this u' value due to failed ignition/quenching. It is thus possible that a high degree of flame surface distortion was responsible for this, which also manifested in an increased thickness of turbulent flame brush.

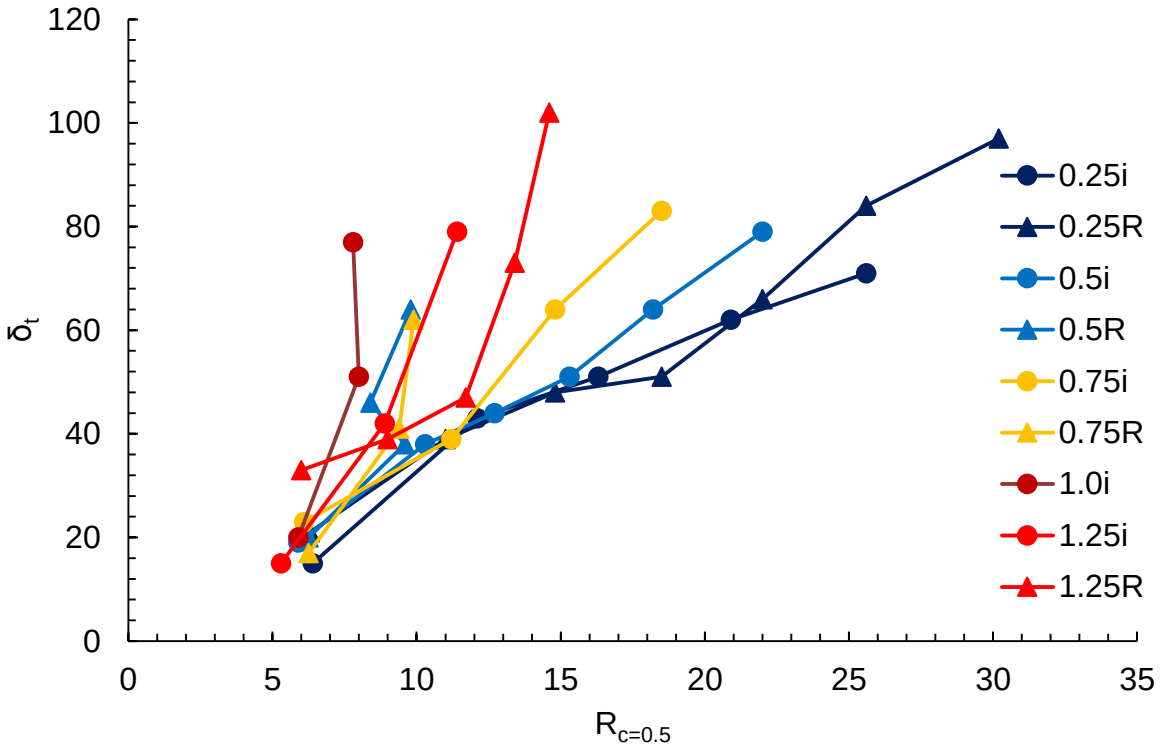

Figure 4.27 Turbulent flame brush thickness as a function of flame radius for methane/air at 298K, 0.1 MPa, φ = 0.6 and a variety of *u'* for the initial and repeat experiment.

4.3.2.3 Flame Surface Density Measurements

Presented in Fig. 4.28 to 4.30 are plots of flame surface density (Σ), calculated as described in Section 3.4.4, against radius from the centroid of the flame as defined in Section 3.4.3. It can be seen in each of these figures that immediately after ignition, each flame exhibits a high peak in Σ with a narrow distribution. This approximates to that of a sphere, where a profile similar to a Dirac Delta Function would be observed as all of the flame surface area is concentrated at a single radius value, with no flame surface area present at any other radius. Due to the laser ignition, however, the flames are not perfectly spherical after ignition, hence there is some width associated with the curve. An additional effect of the laser ignition, which resulted in some flames being "hollow" in the early stages, is a peak in Σ at a high value *c*. This is discussed in Section 5.4.

As the flame grows with increasing time from ignition, the flame surface becomes increasingly wrinkled and the turbulent flame brush thickens. This leads to flame surface being present at an increasing range of radii and hence a wider distribution of Σ, albeit with a similar root radius in each case. At the lower values of u', the peak value of Σ reduces with time from ignition due to departure of the flame shape from sphericity. At the highest u' and 12.6 ms from ignition, the peak in Σ is similar to that observed at 6.8 ms from ignition. The distribution is, however, a little wider. This flame was particularly wrinkled and highly distorted, with an indentation having formed close to the flame centroid. This additionally led to a high peak in Σ with c close to unity, not shown in Fig. 4.27 for clarity, but discussed in Section 5.4.

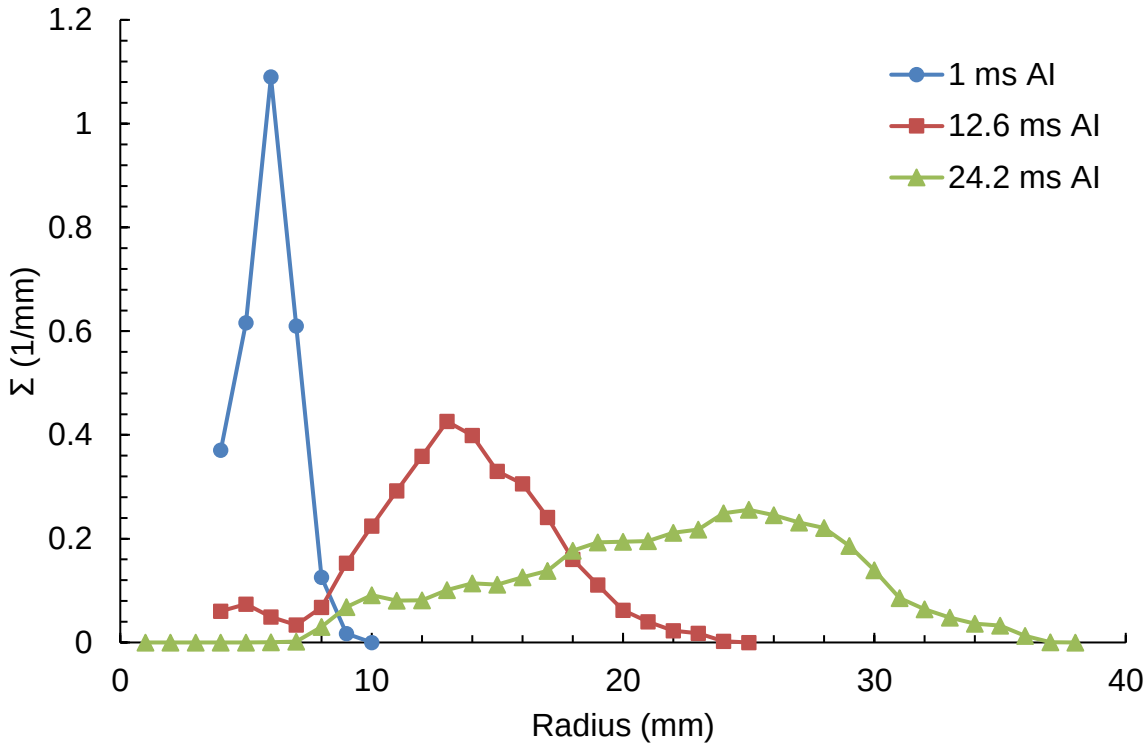

Figure 4.28 Flame surface density as a function of radius for methane/air at 298K, 0.1 MPa, φ = 0.6 and u' = 0.25 m/s

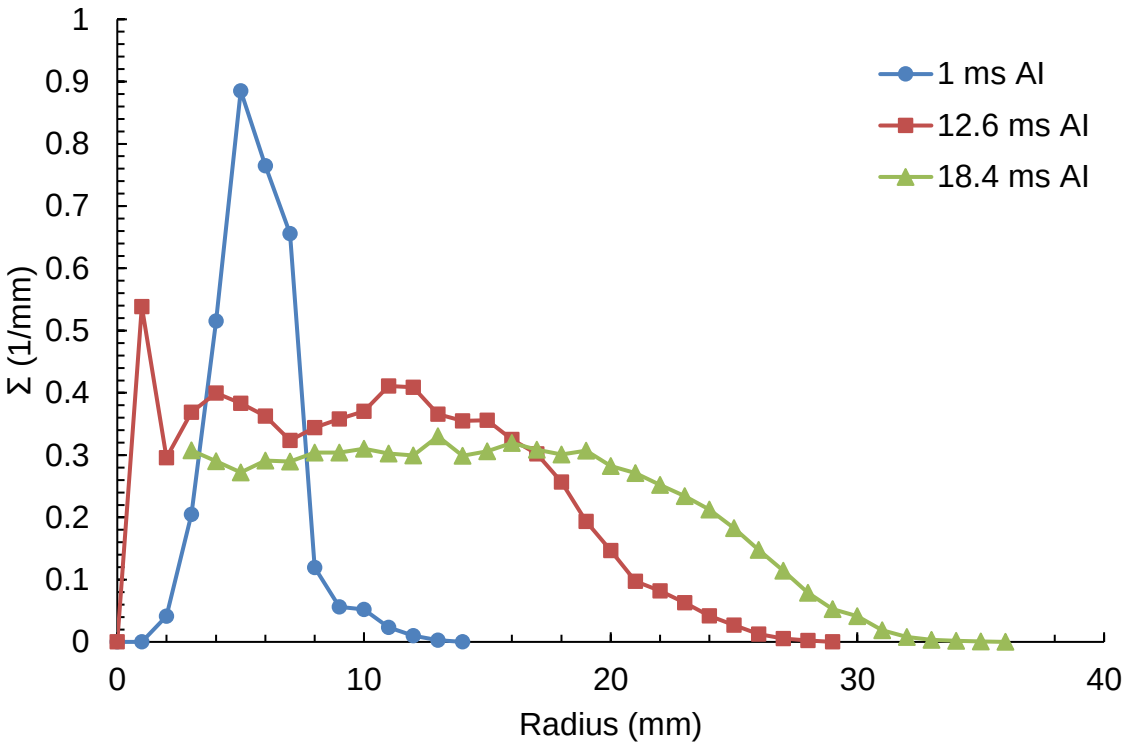

Figure 4.29 Flame surface density as a function of radius for methane/air at 298K, 0.1 MPa, φ = 0.6 and u' = 0.75 m/s

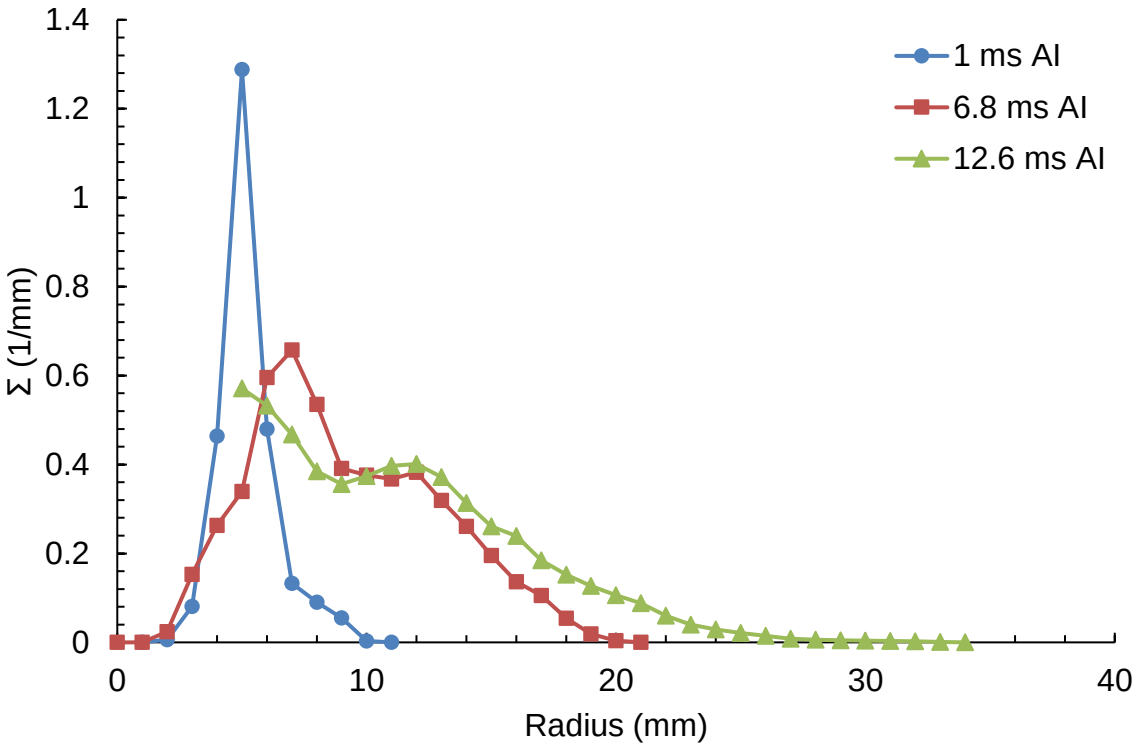

Figure 4.30 Flame surface density as a function of radius for methane/air at 298K, 0.1 MPa, φ = 0.6 and u' = 1.25 m/s

Chapter 5 – Discussion

5.1 Introduction

For the first time, full temporally resolved 3D images have allowed a reliable understanding of turbulent flame structure at engine-like conditions of turbulence. Flame surface areas, reaction progress variable and flame surface density have been measured directly, without the need for the assumptions made when analysing 2D images. The measurements in the present study have been compared with correlations of past 2D-derived data at Leeds to assess the validity of these assumptions. Previously, combustion models such as the direct numerical simulations (DNS) of Nivarti and Cant (2017) described in Section 1.6 have relied on 2D experimental data for validation. Now, it is possible to draw a comparison between the results of such modelling and 3D experimentally derived data captured at similar conditions.

Section 5.2 discusses the 3D flame surface area and area ratio results, where turbulent burning velocities were obtained from the latter. Comparisons are made with the results of burning velocity correlations made by Bradley et al. (2013) and with the direct numerical simulations (DNS) of Nivarti and Cant (2017). Section 5.3 assesses the assumption that the flame structure observed in 2D flame images is representative of the 3D flame structure, by an analysis of reaction progress variable data obtained from 3D images and their 2D counterparts. Section 5.4 explores the flame surface density results obtained in the present work and compares them with data available in the literature. Section 5.5 discusses the effects of the olive oil seed particles on the burning rate of the mixture employed throughout this study.

5.2 Analysis of Flame Surface Areas, Volumes and Surface Area Ratio Measurements

Section 5.2.1 discusses the fidelity of the surface area and burned gas volume measurements obtained in the present work using the 3D laser imaging technique described in Section 2.3. The turbulent burning velocities calculated from the surface area ratios of the 3D reconstructions are discussed in Section 5.2.2 and a comparison made with the surface area ratio measurements of Nivarti and Cant (2017).

5.2.1 Analysis of 3D Flame Surface Areas

The present section addresses the effects of both laser sheet spacing and surface smoothing on the 3D flame surface area measurements obtained in the present work. To enable large flames to be imaged whilst minimising flame growth, the rotating mirror speed was set relative to the laser repetition rate (see section 2.3) so that, at the centre of the vessel, a sheet spacing typically of a single pixel dimension was present. This was slightly larger furthest away from the rotating mirror and slightly smaller closer to it due to the laser sheet divergence described in Section 3.3.1.

5.2.1.1 Effects of Sheet Spacing on Flame Surface Area

To investigate the effect of sheet spacing on the derived flame surface areas, reconstructions were generated with successively increasing sheet spacing, obtained by removing sheets from the series of 2D images used to generate the 3D reconstructions, followed by extrapolation to theoretical zero sheet spacing.

Figure 5.1 shows the effect of sheet spacing on both the smoothed and unsmoothed reconstruction of a methane/air flame at the lowest value of u’ employed in this study, 0.25 m/s. Here, the circles represent surface areas for the smoothed reconstructions and crosses the unsmoothed reconstructions. It is clearly visible that in each case, reducing the sheet spacing reduces the flame surface area, with the unsmoothed reconstructions having a greater surface area than the smoothed versions at each sheet spacing. From the data giving rise to this figure, for the smoothed reconstructions it has been calculated based on linear behaviour that the surface area of a theoretical reconstruction with zero spacing would be 3.8% lower than that for the actual case with a single pixel spacing. The effect of the sheet spacing employed here is thus small.

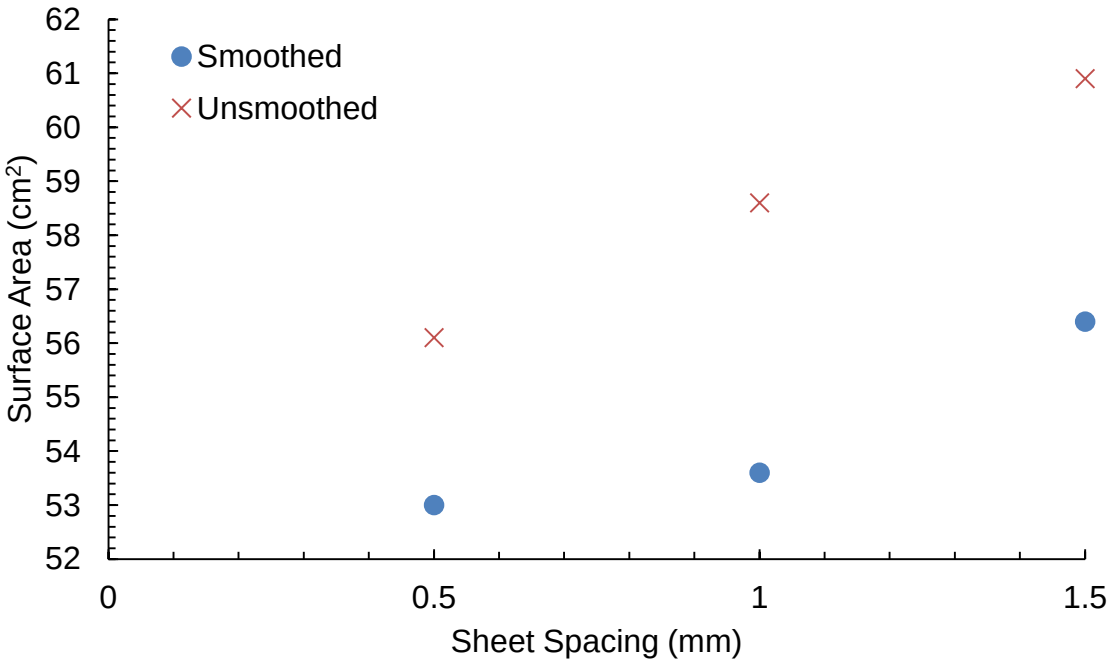

Figure 5.1 Variation of smoothed and unsmoothed flame surface area with laser sheet spacing; methane/air at 298K, 0.1 MPa, φ = 0.6 and u' = 0.25 m/s. t = 12.6 ms. Crosses represent the unsmoothed reconstruction.

It might be expected that increasing the sheet spacing would reduce the flame surface area due to the loss of flame surface detail. However, the reconstruction shown in Fig. 5.2 reveals that removing the intermediate sheets leads to the generation of large flat edges, which increases surface area.

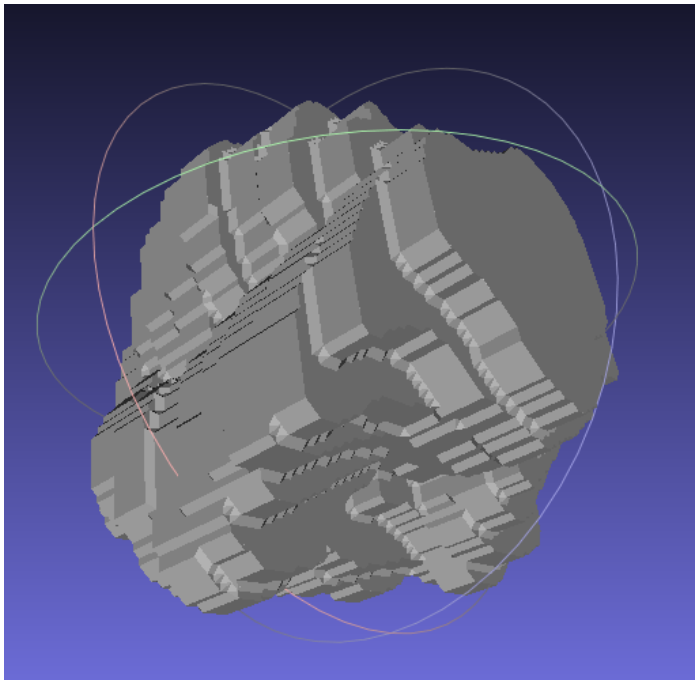

Figure 5.2 Methane/air flame reconstruction at 12.6 ms after ignition with every second and third sheet image removed

Figures 5.3 and 5.4 illustrate the effect of sheet spacing on flame surface area at an intermediate and the highest *u'* values employed in the present work of 0.75 m/s and 1.25 m/s, respectively. These cases show different behaviour to the previous example, as the flame surface decreases here with increasing sheet spacing. Due to the higher applied value of *u'*, these flames visibly exhibit more complex surface structure as may be seen in Figures 4.11 to 4.15. Thus, by removing sheets from the reconstructions and then carrying out interpolation, some surface detail will have been removed. This effect is still very small, where Fig. 5.3 shows only a 2% reduction in flame surface area at the spacing employed in the present work compared to at theoretical zero sheet spacing. In Fig 5.4, for the reconstruction of a flame exposed to a *u'* of 1.25 m/s, the reduction is approximately 1.3% .

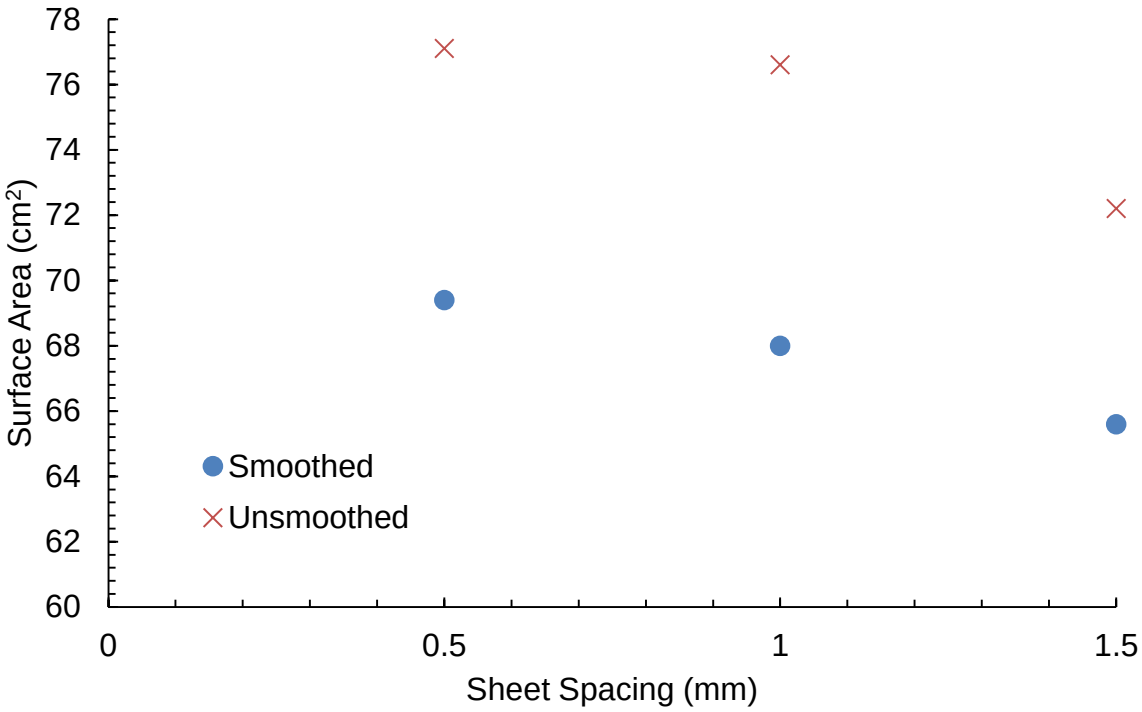

Figure 5.3 Variation of smoothed and unsmoothed flame surface area with laser sheet spacing; methane/air at 298K, 0.1 MPa, φ = 0.6 and u' = 0.75 m/s. t = 12.6 ms. Crosses represent the unsmoothed reconstruction.

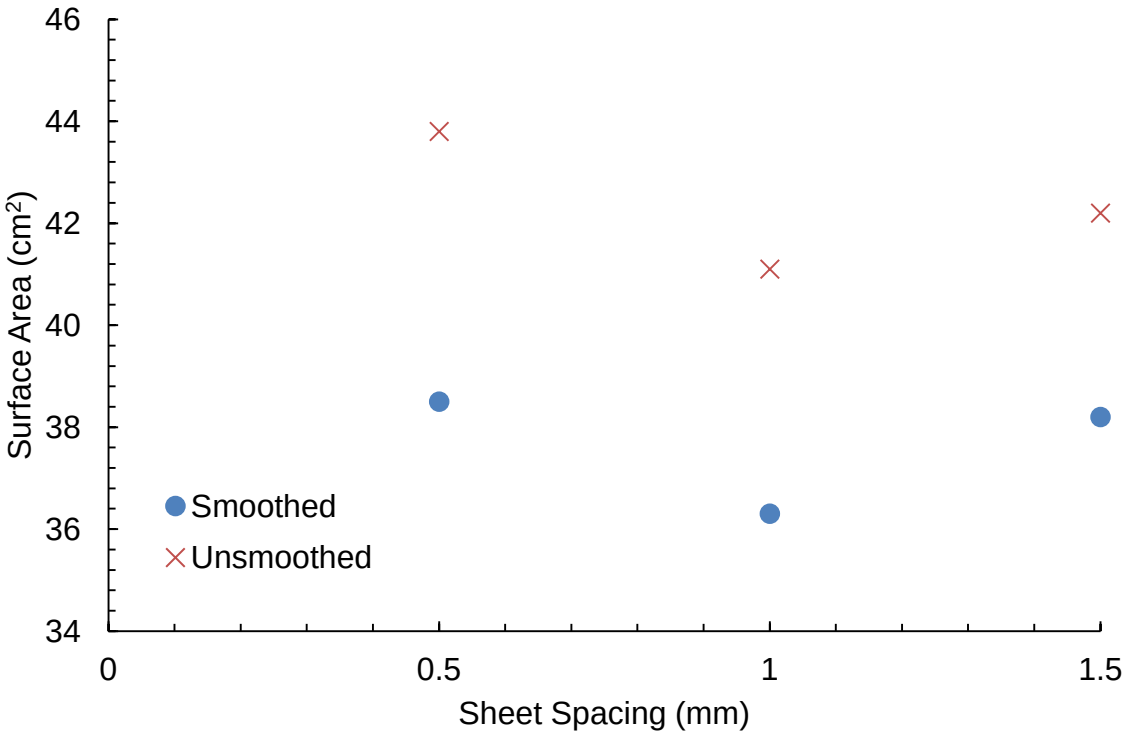

Figure 5.4 Variation of smoothed and unsmoothed flame surface area with laser sheet spacing; methane/air at 298K, 0.1 MPa, φ = 0.6 and u' = 1.25 m/s. t = 12.6 ms. Crosses represent the unsmoothed reconstruction.

Thus, it can be concluded that the surface areas obtained in the present study have not been adversely affected by the sheet spacing employed. The effects of surface smoothing on the surface areas and burned gas volumes are explored in the following sections.

5.2.1.2 Effects of Smoothing on Flame Surface Area and Volume

The surface smoothing algorithm used in this study, described in Section 3.3.3, was employed as it incorporated an expansion term to minimise volume reduction (shrinkage) during smoothing as described in Taubin (1995). To ascertain the effect of this algorithm on both the flame volume and surface area, these parameters were calculated using the methods described in Section 3.4 for the smoothed reconstructions and their unsmoothed counterparts.

Figure 5.5 shows the variation of flame surface area, *A*, with time from ignition for the smoothed and unsmoothed versions of the 3D reconstructions. Straight lines are used to connect the data points to improve visual clarity, where the legend refers to different values of *u'*. This figure indicates an increasing discrepancy in the surface area between the smoothed and unsmoothed reconstructions with increasing time from ignition. For the lowest *u'* of 0.25 m/s, where the largest discrepancies are observed, the reduction in surface area for the smoothed flame with reference to the original unsmoothed version increases from a 7.5% reduction immediately after ignition to a maximum reduction of 23.4% at 24.2 ms from ignition.

Whilst this difference may appear to represent a significant error, part of this effect has been caused by the removal of the square and flat edges from the flame surface and the subsequent joining of sections of the flame with a smooth surface.

For the intermediate value of *u',* the reduction in surface area at the maximum time from ignition (and thus the greatest value of u'_k) is 26.4% whereas for the highest *u'* of 1.25 m/s, the error at this time is 25.4%. As the flame surfaces for the higher u' cases are considerably more complex and wrinkled than at the lowest *u',* with the reduction in surface area being similar in each case this indicates that the surface area reduction is not likely caused by the removal of surface wrinkling and is thus more likely to be caused by the removal of stepping/flat edges. Further, as neither the smoothed or usmoothed reconstructions can necessarily be viewed as true representations of the actual flames, it is difficult to determine the error associated with the application of surface smoothing.

Studying large flames at very high resolution with laser sheet spacing of less than one pixel dimension would minimise the amount of interpolation and surface smoothing required, in addition to minimising the effects of the finest (i.e. pixel-size induced, square) surface details on the overall surface area. Such a study would require the use of a higher resolution camera and higher repetition rate laser.

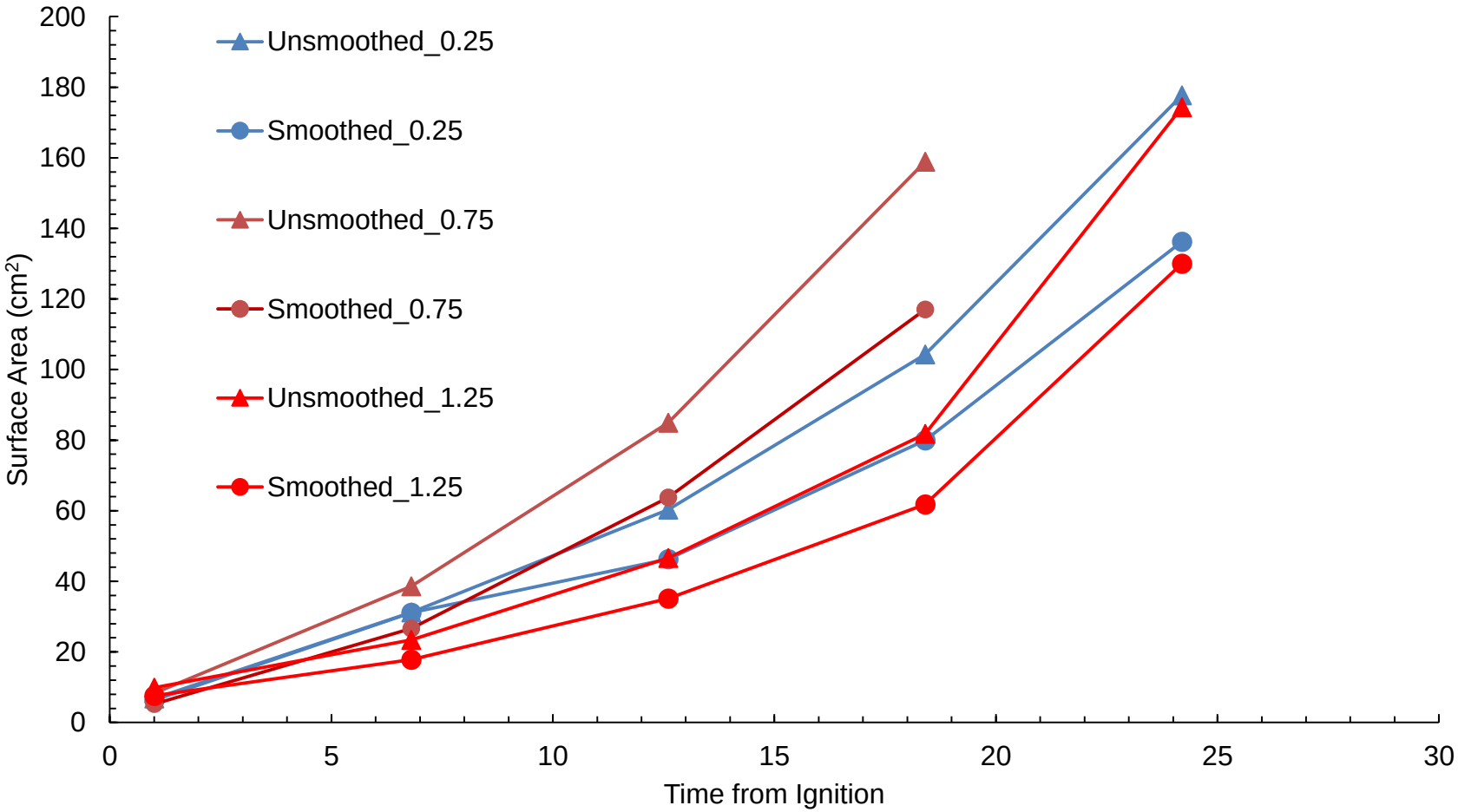

Figure 5.5 Variation in flame surface area with time from ignition for smoothed/unsmoothed reconstructions at various *u'* values

5.2.1.3 Effect of Surface Smoothing on Burned Gas Volumes

Figure 5.6 shows the development of burned gas volume with time from ignition for the lowest, highest and an intermediate value of *u'* used in this study. Points are connected with straight lines to enhance the clarity of the figure and the legend refers to different values of *u'*. Volumes for the smoothed/unsmoothed reconstructions at a given time from ignition and *u'* value are indicated by similar colour points/lines. This figure shows that the difference in volume between the smoothed and unsmoothed versions of the reconstructions is marginal for all *u'* and times from ignition, with the unsmoothed variant typically having a very slightly higher volume. Clearly, the employed surface smoothing technique leads to only very minimal shrinkage.

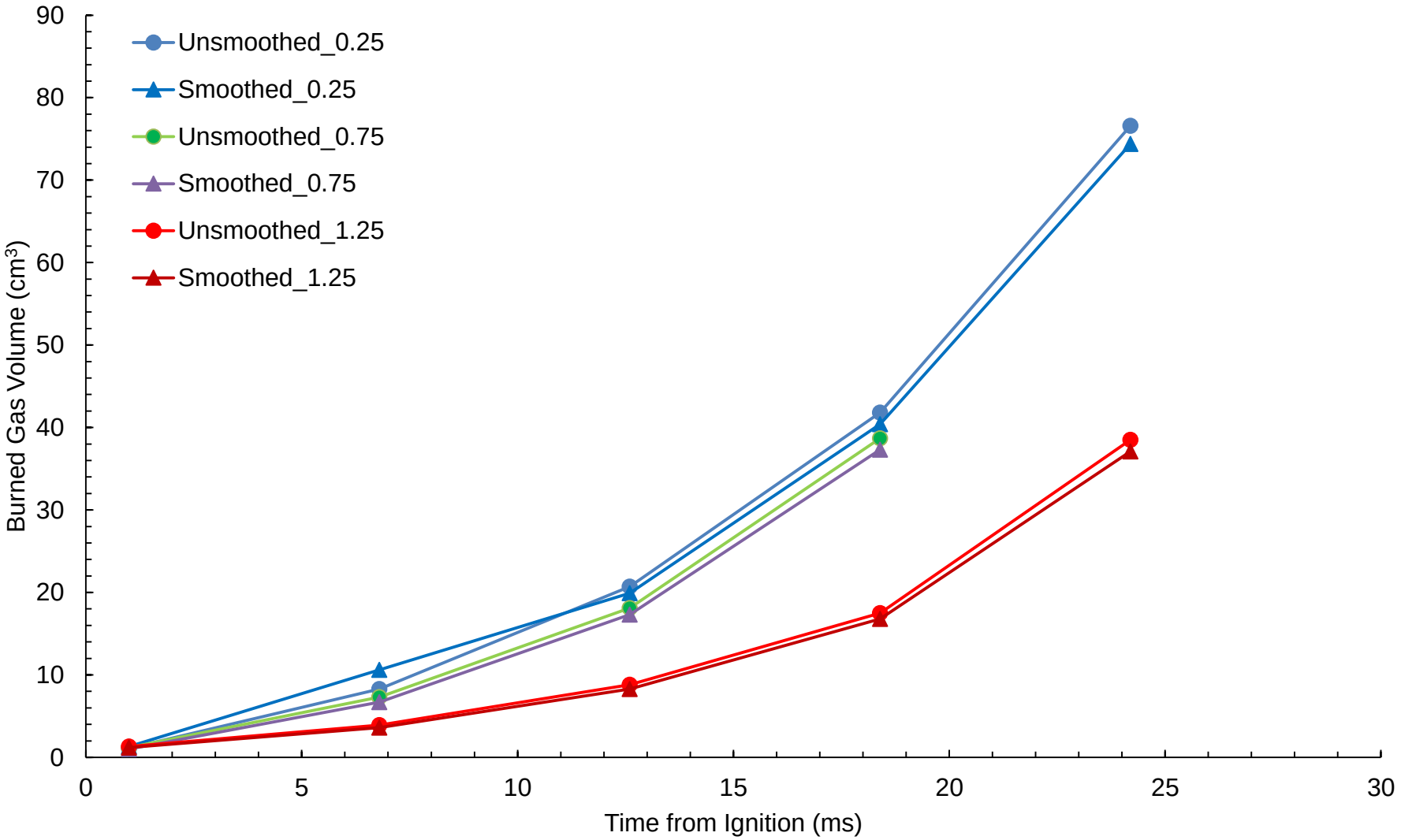

Figure 5.6 Variation in flame volume with time from ignition for smoothed/unsmoothed reconstructions at various *u'* values

5.2.2 Surface Area Ratio Measurements

The 3D multiple laser-sheet imaging technique presented in this study offers a novel method for the determination of turbulent burning velocities through the flame surface area ratio, *A/a*. It was conjectured by Damköhler (1940) that the ratio of the laminar to turbulent burning velocity, u_t/u_l, was equal to the *A/a* ratio, where the wrinkling of the flame surface by turbulence was the sole mechanism for the increase in burning rate. Here, *A* is the wrinkled flame surface area where the surface is defined as an isovalue of the extent of reaction across the reaction zone and *a* is the surface area of the equivalent laminar flame. In the present work, *a* is defined as the surface area of a sphere with the same volume as the burned gas volume of the wrinkled flame. Figure 5.7 shows the increase in *A/a* and thus u_t/u_l with increasing normalised RMS turbulence velocity, where the *A/a* value at each u'/u_l corresponds to a u'_k/u' value of 0.6 as described in Section 4.3.2.1. It clearly illustrates an initial rise in *A/a* with u'/u_l, which begins to tail off beyond u'/u_l = 10 due to the bending effect described in Section 1.6. This indicates that at high *u'/ul*, the turbulence becomes less able to wrinkle the flame surface.

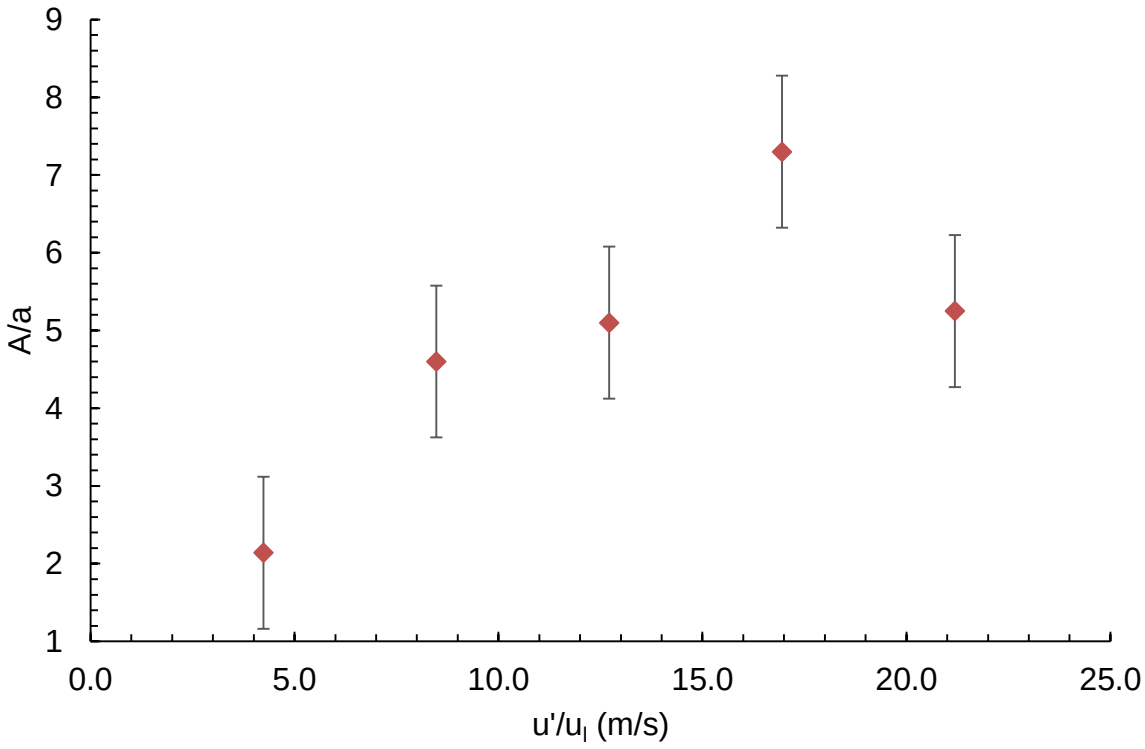

Figure 5.7 Variation of surface area ratio with normalised RMS turbulence intensity

5.2.2.1 Comparison of Experimental Area Ratios with DNS

Previously, 3D data on the surface area of developing turbulent flames at engine-like conditions have not been available for comparison with DNS studies. Nivarti and Cant (2017) developed a DNS method to explore the bending effect and turbulent flame structure and have generated data on the evolution of flame surface area with increasing *u'*, into the bending regime. These Authors express the surface area ratio as A_T/A_L, where A_T is the surface area of the wrinkled flame and A_L is the cross sectional area of the duct. Further details are presented in Section 1.6 in the present work.

A comparison has been made in the present work to relate the surface area ratio predictions of the DNS to experimental data. This is shown in Fig. 5.8. Here, it can be seen that at the lowest applied *u'* agreement between the data sets is excellent. However, as *u'* increases the experimentally derived *A/a* depart significantly from the A_T/A_L predictions of the DNS, with the experimental values being significantly larger. It appears, however, that the onset of "bending" of the surface area ratio occurs at a similar u'/u_l in each case. Nivarti and Cant (2017) propose that the decreasing rate of increase in A_T/A_L after the onset of bending was caused by destruction of the surface wrinkling at regions of high negative curvature i.e. at areas where the flame surface was indented. An illustration of this is presented in Fig. 5.9.

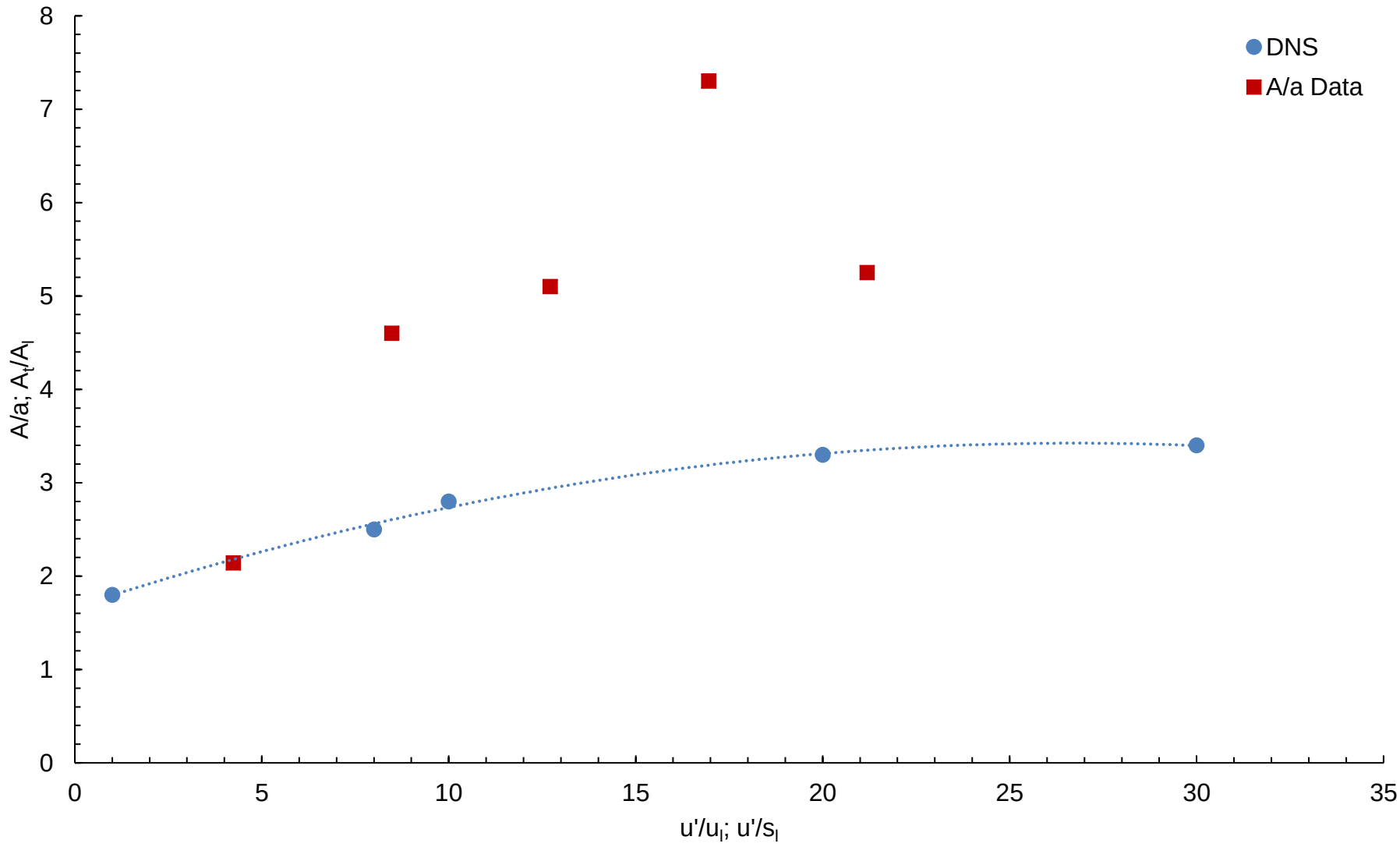

Figure 5.8 Comparison of experimentally derived *A/a* ratios with those from the DNS of Nivarti and Cant (2017)

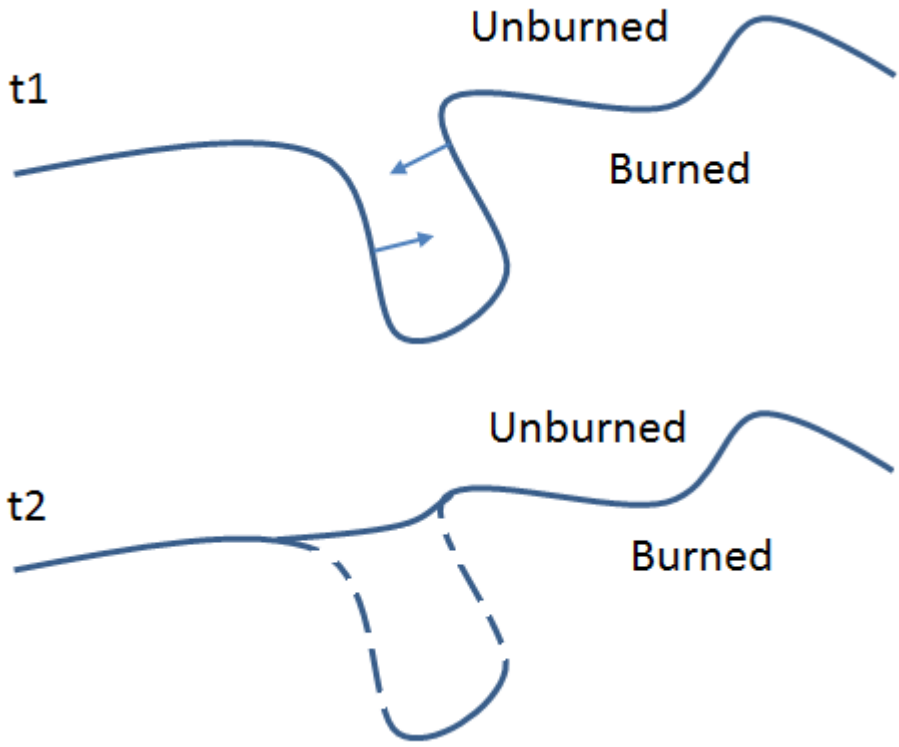

Figure 5.9 Destruction of flame surface area at regions of negative curvature

Flame surface areas were determined in the DNS study by integrating the flame surface density over the isosurface corresponding to a reaction progress variable, c^*, of 0.8, at which the peak reaction rate was found to occur. It is important to note that Nivarti and cant (2017) define the reaction progress variable as the extent of conversion of reactants to products across the reaction zone. In the present study it is defined as described in Section 1.7. It has not been possible in the present work to ascertain the reaction progress variable at the perceived flame edge, but this is likely to lie in the preheat zone for Mie scattering images with olive oil droplets as seed particles due to the low boiling point of olive oil of around 600K (Melling, 1997). In the DNS study, considerable difference was observed in the surface structure between high and low values of c^*, as shown in Fig. 5.10. Hence, if it can be assumed that the highest surface area is observed at the peak c^* value for reaction rate in the DNS study, the flame surface observed in the present study must accordingly be at or below the c^* for peak surface area. It is therefore unlikely that potentially measuring the surface area at different reaction progress variable values has given rise to the observed discrepancy.

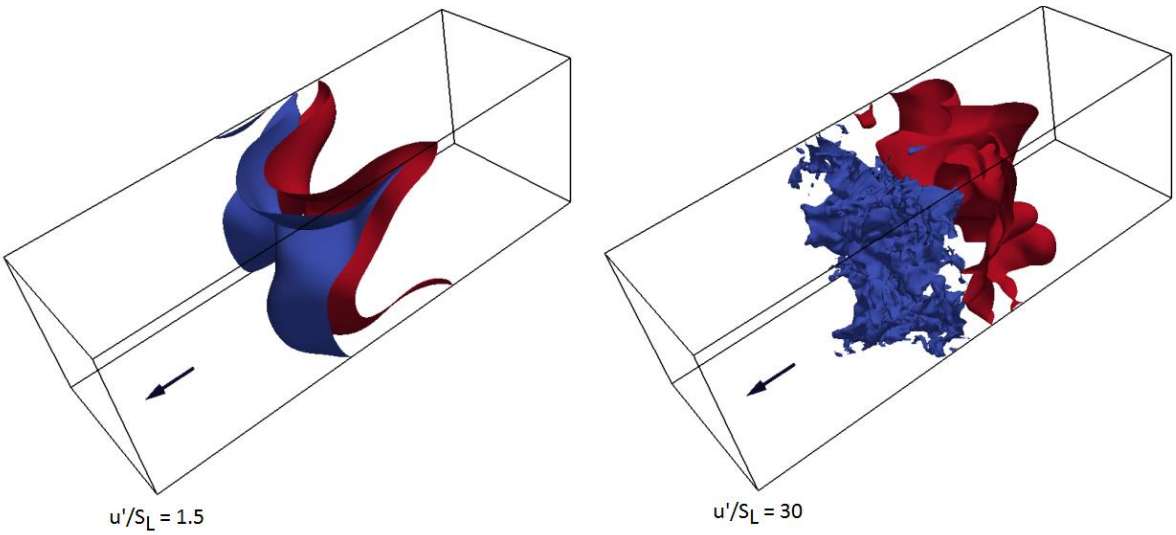

Figure 5.10 Isosurfaces of the leading and trailing edges of flames at low and high turbulence, reproduced from Nivarti and Cant (2017)

In each study, the surface area ratio was defined as the ratio of the surface area of the wrinkled, turbulent flame to that of the flame in laminar form. For DNS, A_L was the cross-sectional area of the inflow/outflow domain in which combustion occurred. As was described in Section 4.3, the flames examined in this study at higher values of *u'* not only become highly wrinkled but also highly distorted, i.e. stretched and flattened. It is possible that for such flames, a very high surface area ratio would have been observed as the wrinkling could occur on both sides of the flattened flames. In the case of DNS, the majority of wrinkling is observed on the leading edge of the flame, with only burned products behind the flame surface. This could have reduced the maximum possible wrinkling. Further, the turbulence applied in the present work was maintained throughout the duration of the explosions. In the DNS, turbulence was initiated at the inflow and then decayed towards the outflow. The decaying of the turbulence may have had led to a reduction in the observed wrinkling and thus surface area, with the *u'* to which the flame was being observed being lower than that originally forced in the inflow.

Additionally, the experimental surface area ratios presented in Fig. 5.8 relate to a u'_k/u' value of 0.6, where a minimal amount of extrapolation has been carried out, where necessary, to achieve this as presented in Section 4.3. For the DNS study, it is not known to what extent the flames were developed. Thus, it may be the case that the surface area ratios presented in the present work are for more developed flames. However, it may be conjectured that with a cross sectional area of the DNS domain of 5 mm and the integral length scale of turbulence being 0.99 mm, the flame would have been more developed than the experimental case with a maximum R_λ of 40 mm and constant L = 20 mm in each case.

At the time of writing, a DNS study is being conducted by Nivarti and Cant to emulate the conditions employed in this study. This should remove any differences in burning behaviour attributable to operation near the flammability limit etc. and will allow a more direct comparison between the DNS and experimental techniques.

5.2.2.2 Comparison of A/a with Prior Leeds Measurements and Correlations

As described in Section 1.5.6, Bradley et al. (2009, 2011 and 2013) correlated measurement of turbulent burning velocities, obtained using schlieren imaging and pressure recording, for a variety of fuels and starting conditions. These Authors generated a relation to allow calculation of u_t based on the strain-rate Markstein number (Ma_{sr}) and laminar burning velocity (u_l) of a mixture at a given Karlovitz stretch factor, K, as given by Eqs. 1.31 to 1.34 in Section 1.5.6. Previously, it was not possible to validate the assumptions made when using these measurement techniques as full 3D data were not available for comparison. In the present study, values of u_t and thus u_t/u_l were calculated based on the characteristics of the methane/air mixture used throughout this work, corresponding to a u'_k/u' value of 0.6 to allow comparison with the A/a ratios. The calculated u_t/u_l and A/a values are shown in Fig. 5.11 for comparison.

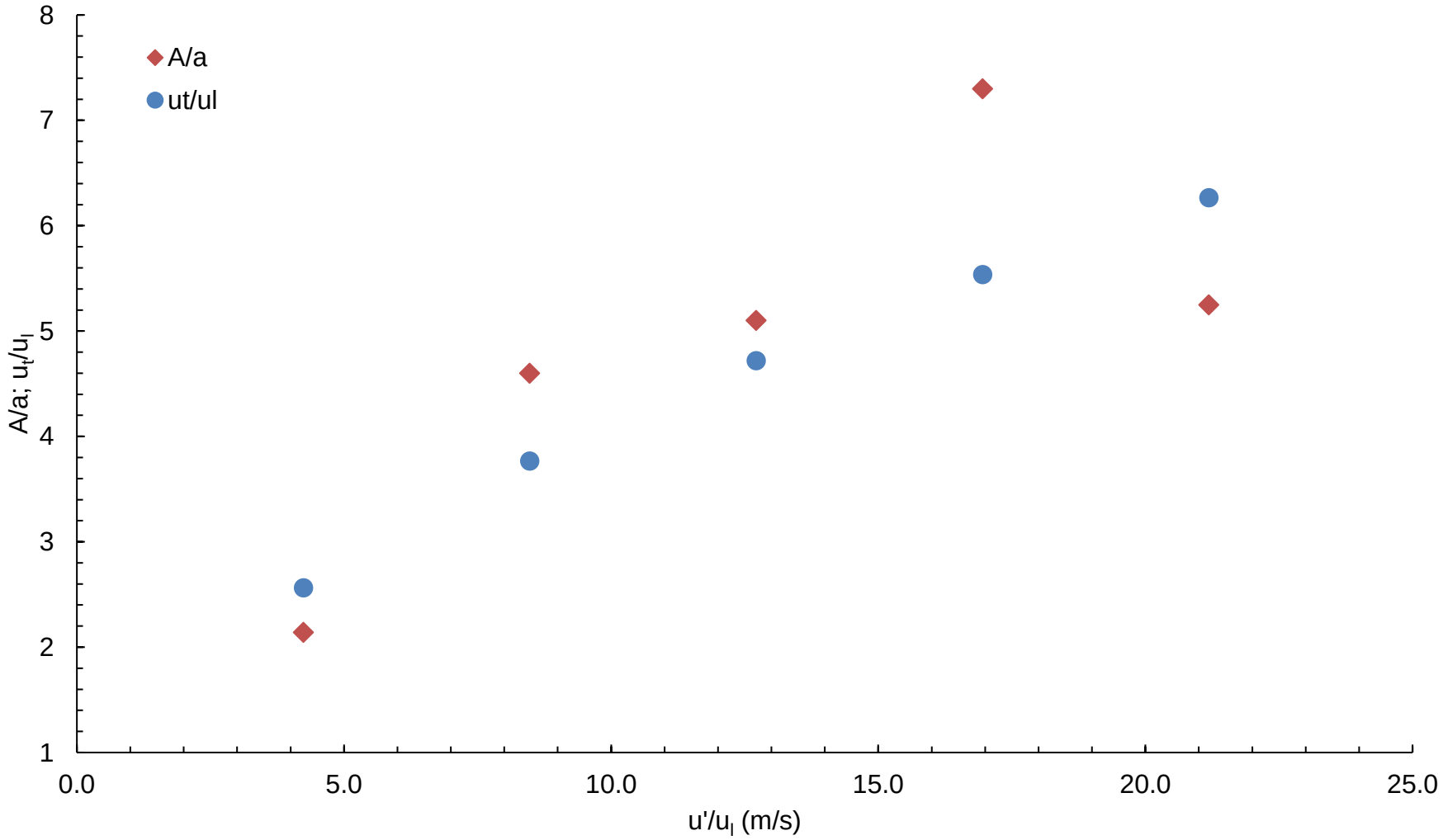

Figure 5.11 Variation of experimentally obtained *A/a* with calculated u_t/u_l

Figure 5.11 shows a very good agreement between the datasets, though some variation is visible within the *A/a* measurements. For the intermediate u'/u_l, the *A/a* values are higher than the calculated u_t/u_l. The hypothesis of Damkoehler (1940) makes the assumption that the local laminar burning velocity at any point on the flame surface is equal to the laminar burning velocity in the absence of turbulent straining. Thus, the increased rate of burning due to turbulence exists solely due to the increased flame surface area for reaction. However, due to stretch rate effects, the local burning velocity will be affected by the turbulent straining of the flame surface as described by Bagdanavicius et al. (2015) where

$$\frac{u_t}{u_l} = \frac{A}{a} P_b^{0.5} \tag{5.1}$$

Here, the probability of burning factor, $P_b^{0.5}$, describes the effect of stretch on the local burning velocity on the flame surface. For mixtures with a positive value of the strain rate Markstein number (Ma_{sr}), the value of $P_b^{0.5}$ decreases with increasing Karlovitz number, *K*, as may be seen in Fig. 5.12. This figure was obtained from correlations of a number of measurements of $\left(P_{bMa}^{0.5}\right)_K$, which is the probability of burning factor expressed as a function of Ma_{sr} and *K*, for the fuels and starting conditions used by Bradley et al. (2011). The dashed line indicates the onset of quenching and the dotted lines are extrapolations of the measured data. For negative Ma_{sr}, $P_b^{0.5}$ increases to above unity with increasing *K*, indicating that turbulent straining increases the local burning rate. Beyond a critical value of *K*, $P_b^{0.5}$ once again decreases, though the mechanism behind this is not fully understood. The value of Ma_{sr} for the mixture employed in this study was found to average +0.3 as presented in Section 4.5, thus indicating a minimal effect of stretch rate on burning rate for this mixture until *K* exceeds approximately 0.5.

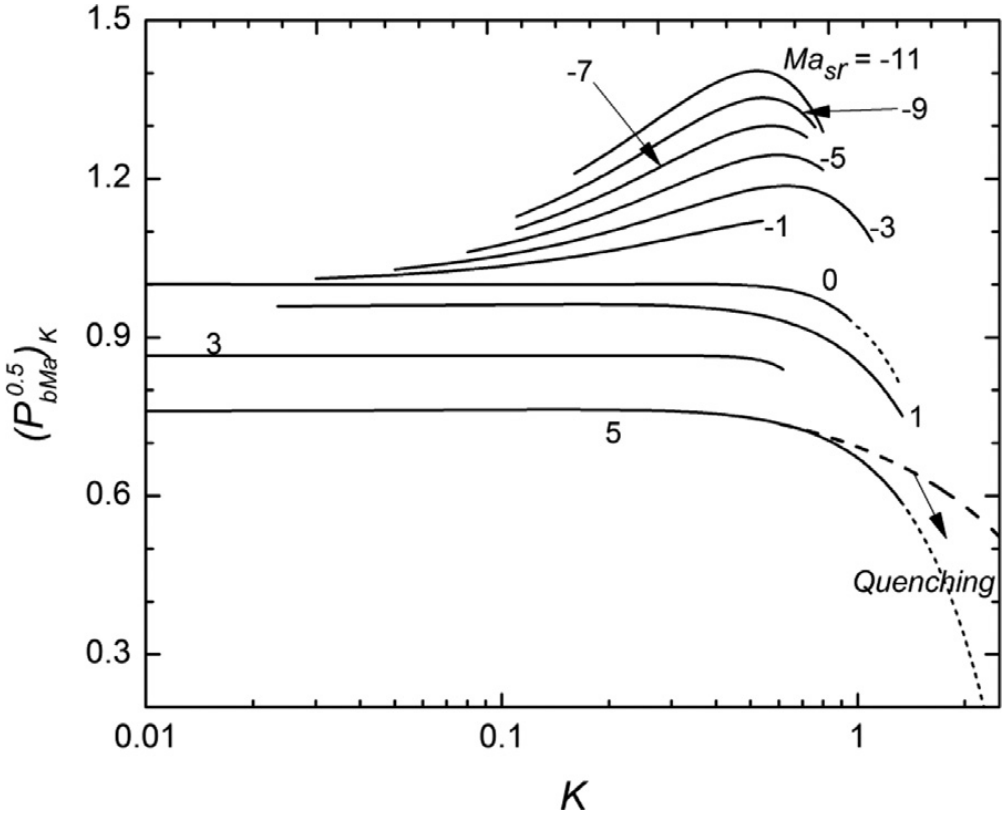

Figure 5.12 Variation in the probability of burning with Karlovitz number, reproduced from Bagdanavicius et al. (2015)

Figure 5.13 shows a comparison between $A/a*P_b^{0.5}$ (circles) and u_t/u_l (squares), where the $P_b^{0.5}$ values were obtained from Fig. 5.12. This figure shows a similar magnitude of deviation between the 3D measurement results and the u_t/u_l values calculated using Eqs. 1.31 to 1.34 until u'/u_l of around 12.5. Thereafter, $A/a*P_b^{0.5}$ rapidly drops away from the u_t/u_l values. It can therefore be concluded that stretch effects are unlikely to have caused the small deviations seen in Fig 5.13. It is possible that the experihmental scatter inherent in turbulent burning velocity measurements is responsible. Such scatter is demonstrated in Fig. 5.14, which shows the variation in both pressure-trace and schlieren measurements of u_t/u'_k with K. As the u_t/u_l values presented in Fig. 5.11 were calculated based on best-fit curves through such data as shown in Fig. 5.13 for datasets obtained using different techniques, the A/a results obtained in the present study are within the bounds of experimental scatter.

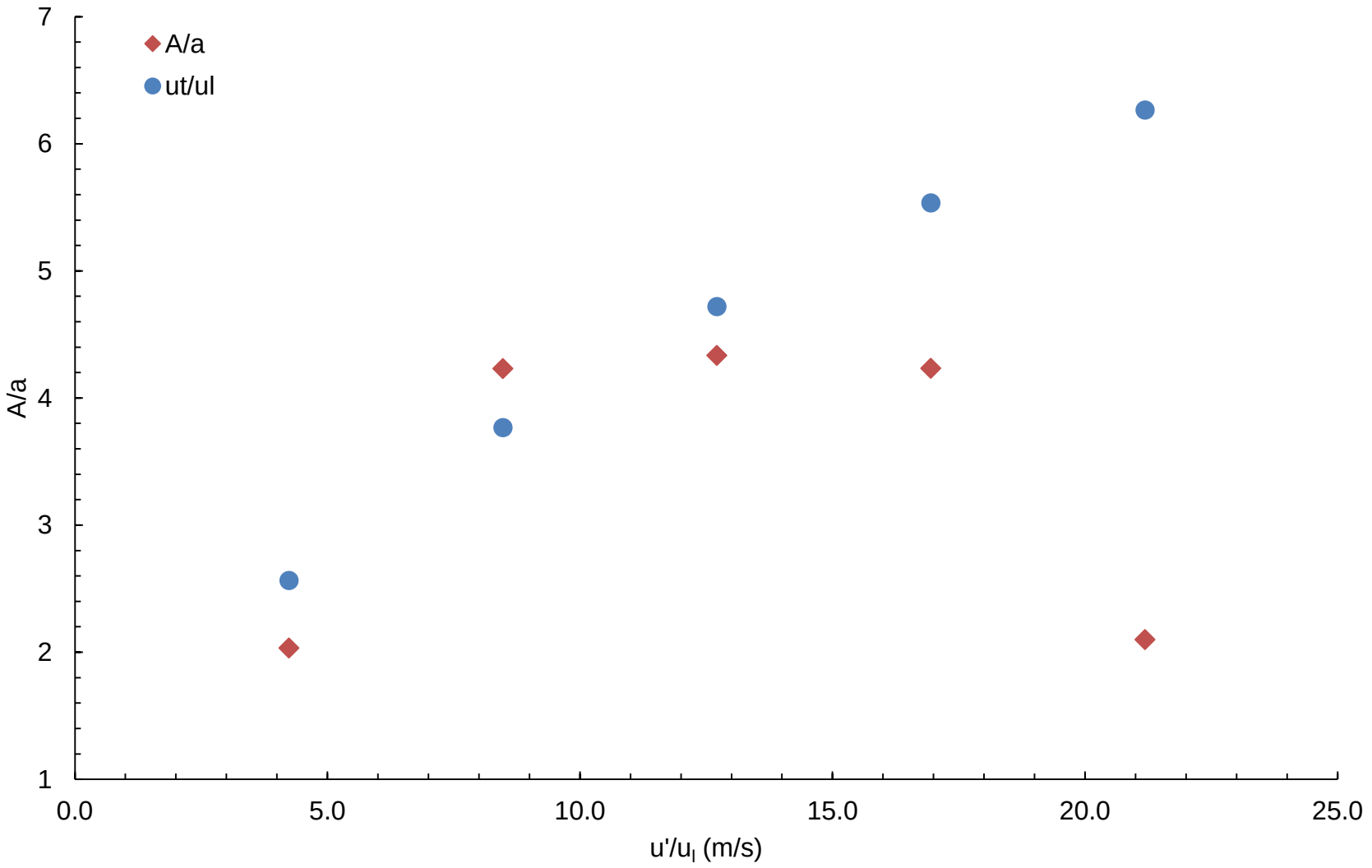

Figure 5.13 Variation in calculated u_t/u_l and *A/a* corrected for stretch effects with u'/u_l

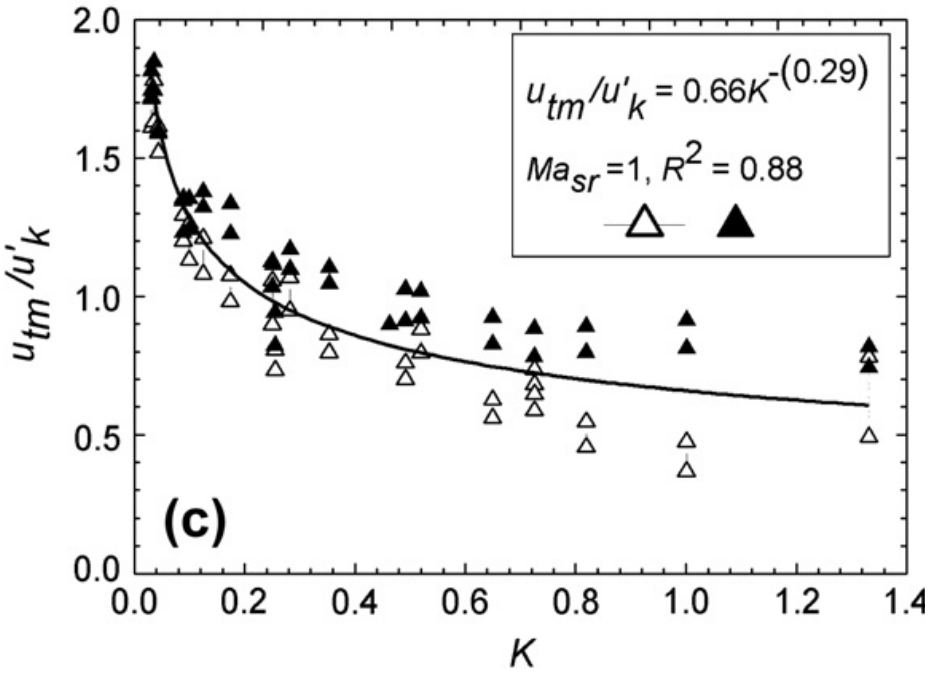

Figure 5.14 Variation of U with K at Ma_{sr} = 1. Reproduced from Bradley et al. (2011). Open symbols are for schlieren results, solid symbols represent pressure measurements

5.3 Comparison of Reaction Progress Variable Profiles for 2D/3D Images

To assess the validity of the assumption that the flame structure observed in two dimensions provides a good representation of the structure in three dimensions (Bradley et al. 2003), reaction progress variable profiles were generated using both 2D sheet images and 3D reconstructions. Reaction progress variable was selected as a suitable flame surface characteristic as it is a good measure of flame surface structure.

With conventional single laser-sheet imaging, it is not known whether the laser sheet is passing through the centre of the flame, or whether it is clipping an edge of it. In the latter case, this leads to an additional term in the velocity vector which cannot be ascertained. This leads to uncertainty when measuring burning velocities by e.g. particle image velocimetry (PIV). Additionally, at higher values of applied *u'*, the flame may convect such that a different region of the flame is being intersected by the laser sheet at each instance where a measurement is taken.

This section is thus split into two sub-sections; the first addresses the assumption of symmetry by examining every laser sheet image in a sequence used to generate a 3D reconstruction, where the sheet image with the largest cross sectional area is processed to reveal the *c* versus radius from centroid profile. Here, it is assumed that the image with the largest cross sectional flame area approximates to the centre of the flame. The second section examines *c* versus radius profiles for laser sheet images at a fixed location (here, traversing the centre of the bomb). This tests the assumption that the flame remains stationary throughout combustion with the laser sheet traversing the centre of the flame.

5.3.1 Comparison of 3D Reconstructions and the Central Sheet Image

For each 3D reconstruction, its constitutive series of binarised 2D sheet images were assessed for cross sectional flame area and the sheet image with the largest cross sectional area was taken to be representative of the series. The reaction progress variable profile of this 2D image and the 3D reconstruction were then determined and plotted on common axes for each instant in time. A selection of these profiles, at the lowest (u' = 0.25 m/s), highest (1.25 m/s) and an intermediate u' (0.75 m/s) used in the present study are presented in the following figures at a selection of times from ignition. This allowed a comparison between profiles at a variety of u' and u'_k values. Throughout the following figures, circles represent 3D derived data and crosses represent 2D derived data.

Figures 5.15 to 5.17 show the reaction progress variable profiles for 2D and 3D images at the lowest u' value of 0.25 m/s at several times from ignition. Figure 5.15 clearly shows a significant difference in c values at small radii, converging near the tip of the flame. This is despite the profiles being of a similar shape. The 2D case illustrates the presence of unreacted mixture at the flame centroid, which is not the case for the 3D reconstruction. Due to the laser ignition, the flames are often highly distorted immediately after ignition and appear broken up in 2D, potentially leading to unreacted mixture being present in the centroids of such images. As the two curves converge at higher radii, this suggests that the greatest extremity of the flame (i.e. the tip radius) was captured in the 2D image.

Figures 5.16 and 5.17 show similar profiles and root and tip radii, with the most developed flame showing the most similarity between the two modes of observation. This suggests that in these cases, the flame structure shows a high degree of symmetry with the centroid 2D sheet giving a good representation of the turbulent flame brush thickness. In this case, the flame being examined was only slightly wrinkled by the low level of applied turbulence.

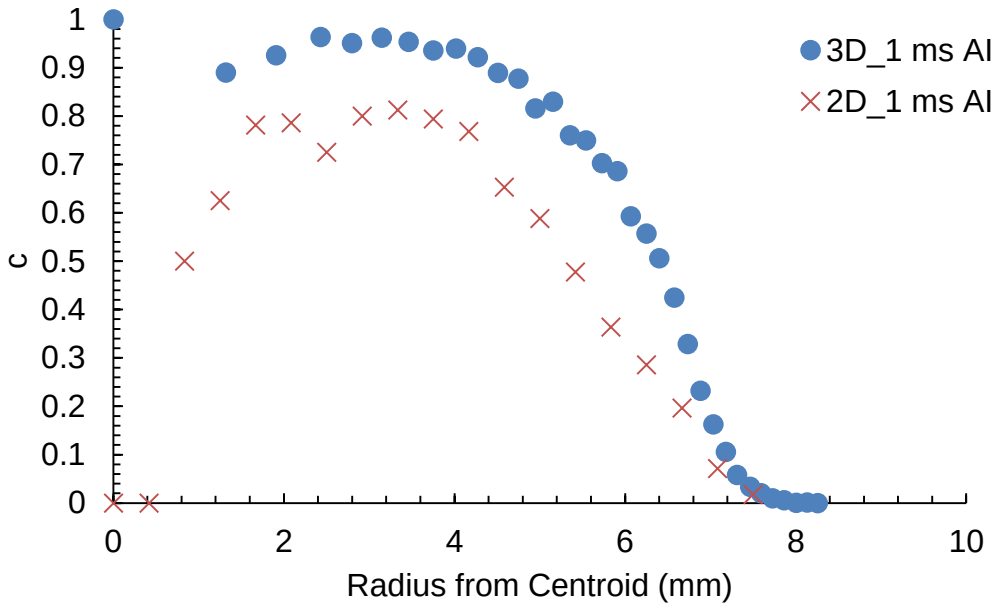

Figure 5.15 Variation of *c* with radius for a central 2D laser sheet image and reconstruction of a methane/air flame at 298K, 0.1 MPa, φ = 0.6 and *u'* = 0.25 m/s. *t* = 1 ms

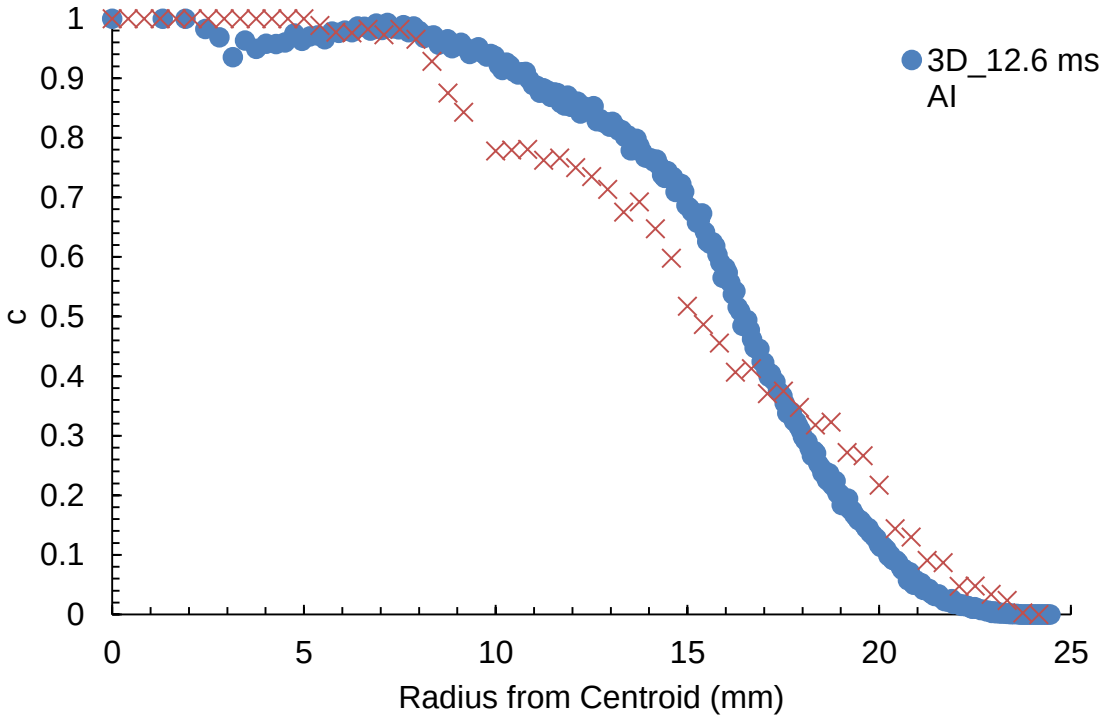

Figure 5.16 Variation of *c* with radius for a central 2D laser sheet image and reconstruction of a methane/air flame at 298K, 0.1 MPa, φ = 0.6 and *u'* = 0.25 m/s. *t* = 12.6 ms

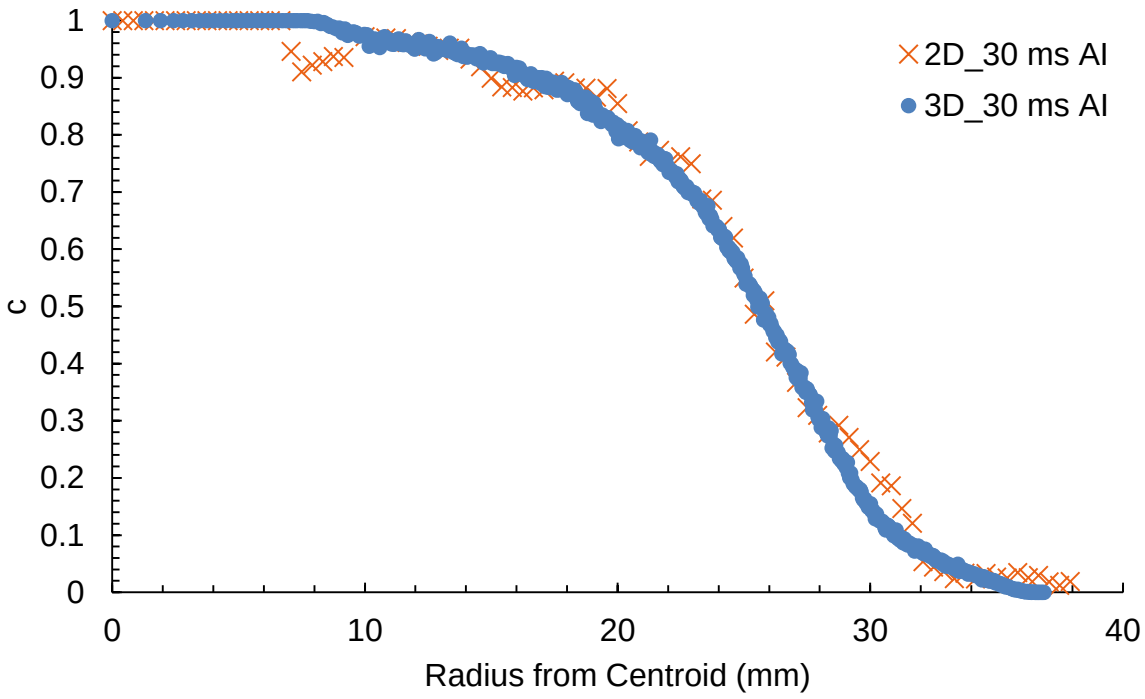

Figure 5.17 Variation of *c* with radius for a central 2D laser sheet image and reconstruction of a methane/air flame at 298K, 0.1 MPa, φ = 0.6 and *u'* = 0.25 m/s. *t* = 30 ms

Figures 5.18 to 5.20 show the c profiles at an intermediate *u'* of 0.5 m/s at a number of times from ignition. Immediately after ignition, the 2D and 3D profiles can again be seen to be different at smaller radii, with the tip radius still being accurately predicted with the 2D imaging. At 6.8 and 18.4 ms after ignition, the root and tip radii are in good agreement, though the profile of the graphs is different. Again, the flame at the longest period of time from ignition shows the best agreement between 3D and 2D imaging.

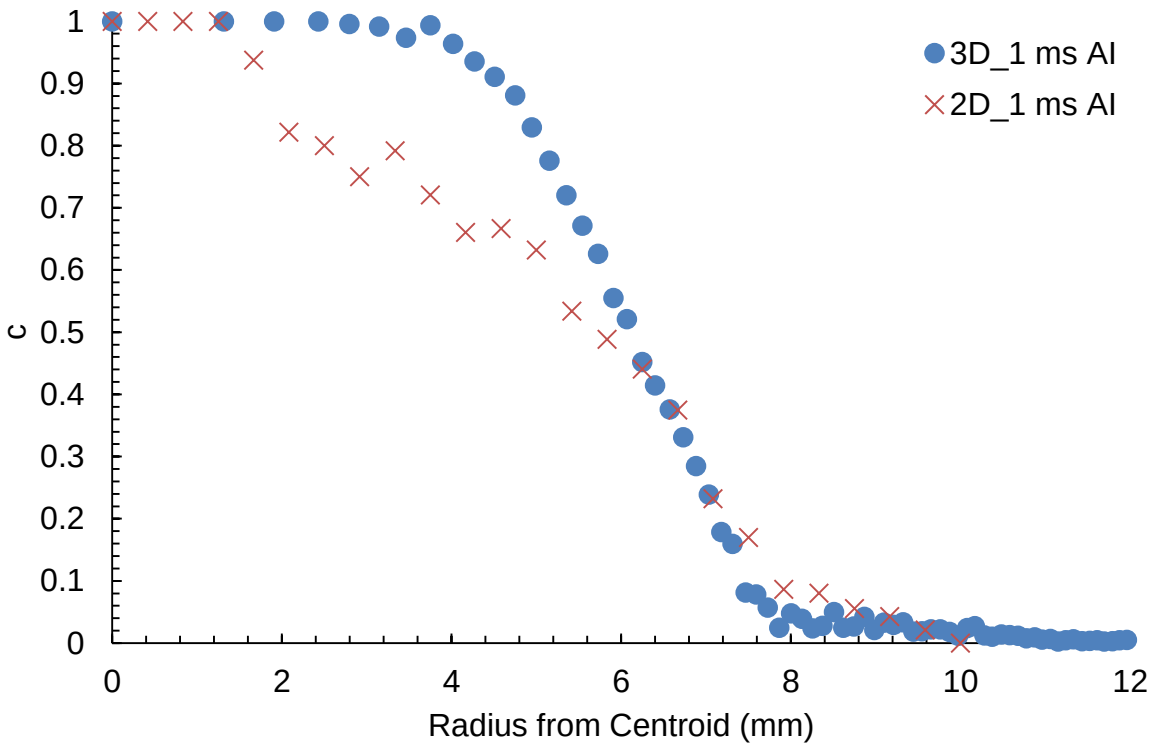

Figure 5.18 Variation of *c* with radius for a central 2D laser sheet image and reconstruction of a methane/air flame at 298K, 0.1 MPa, φ = 0.6 and *u'* = 0.75 m/s. *t* = 1 ms

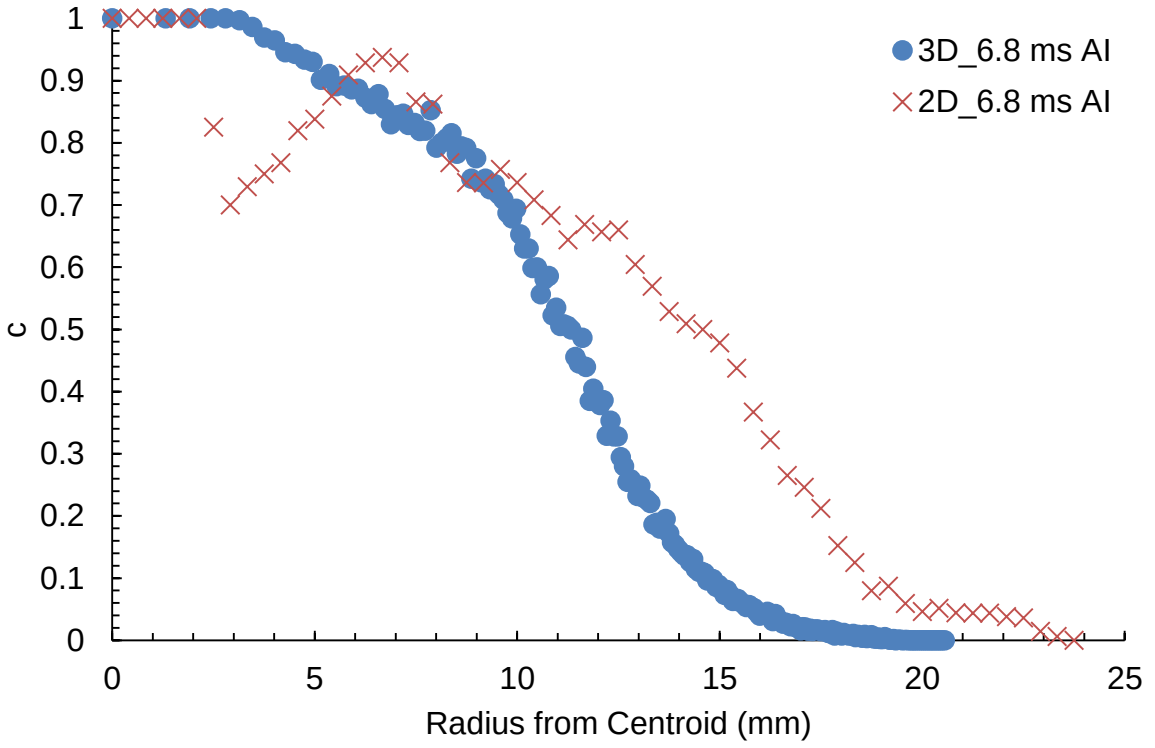

Figure 5.19 Variation of *c* with radius for a central 2D laser sheet image and reconstruction of a methane/air flame at 298K, 0.1 MPa, φ = 0.6 and *u'* = 0.75 m/s. *t* = 6.8 ms

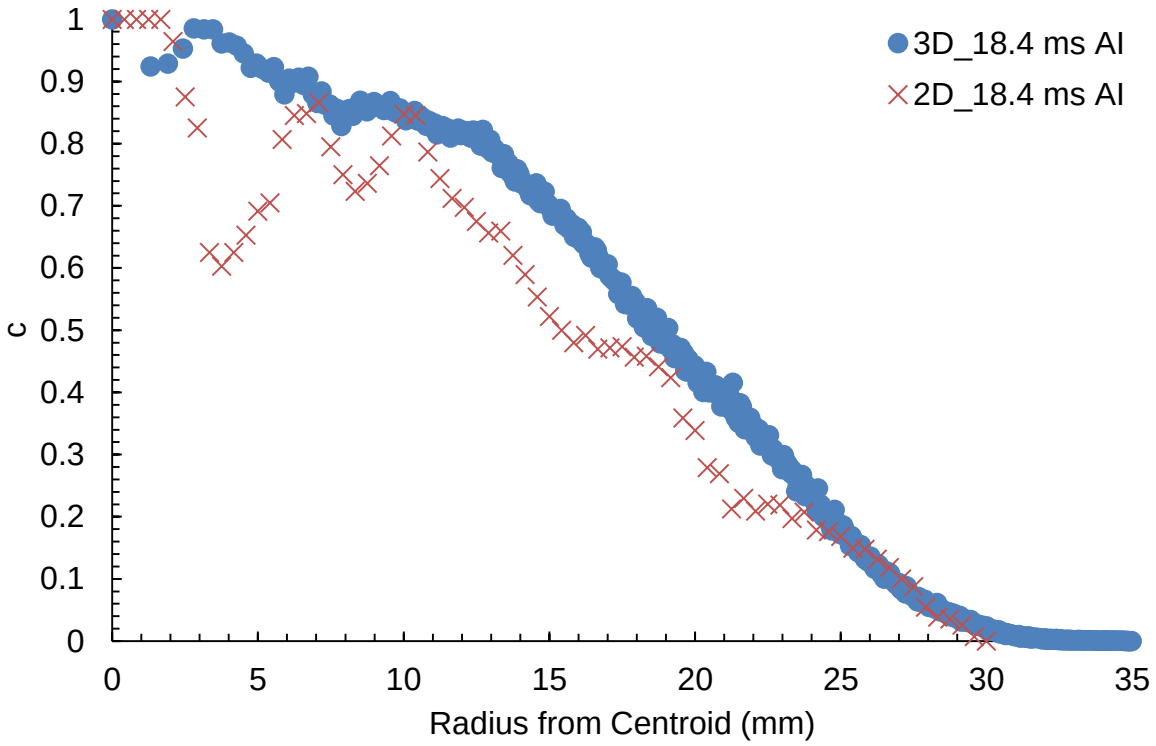

Figure 5.20 Variation of *c* with radius for a central 2D laser sheet image and reconstruction of a methane/air flame at 298K, 0.1 MPa, φ = 0.6 and *u'* = 0.25 m/s. *t* = 18.4 ms

The results of the highest *u'* examined are presented in Figures 5.21 to 5.23. These show very different behaviour to the lower *u'* cases, as the profiles and root and tip radii are very similar immediately after ignition with bigger profile discrepancies at longer time periods from ignition. As the root and tip radii are similar for the 2D/3D images in these cases, extremities of the flame surface are clearly well represented by the 2D images. The differences in profiles suggest that the overall flame structure is less symmetrical at high values of *u'* than at lower values, with the greatest difference at the longest time from ignition suggesting that the flame is becoming highly and more stochastically wrinkled as it is exposed to an increasing fraction of the turbulence spectrum.

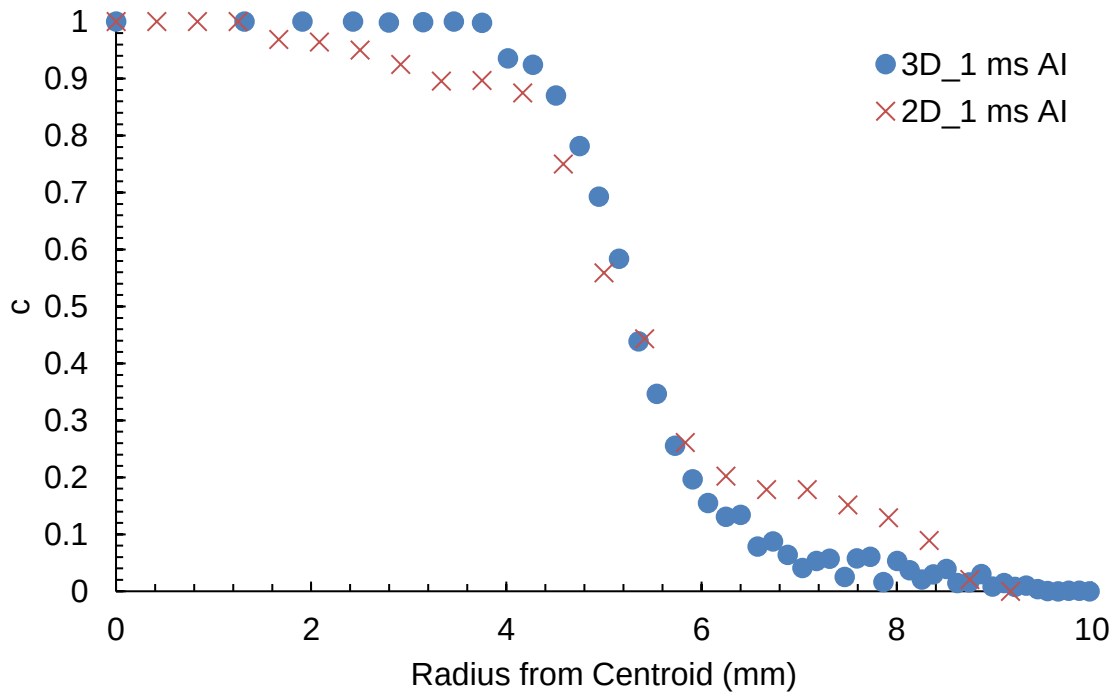

Figure 5.21 Variation of *c* with radius for a central 2D laser sheet image and reconstruction of a methane/air flame at 298K, 0.1 MPa, φ = 0.6 and *u'* = 1.25 m/s. *t* = 1 ms

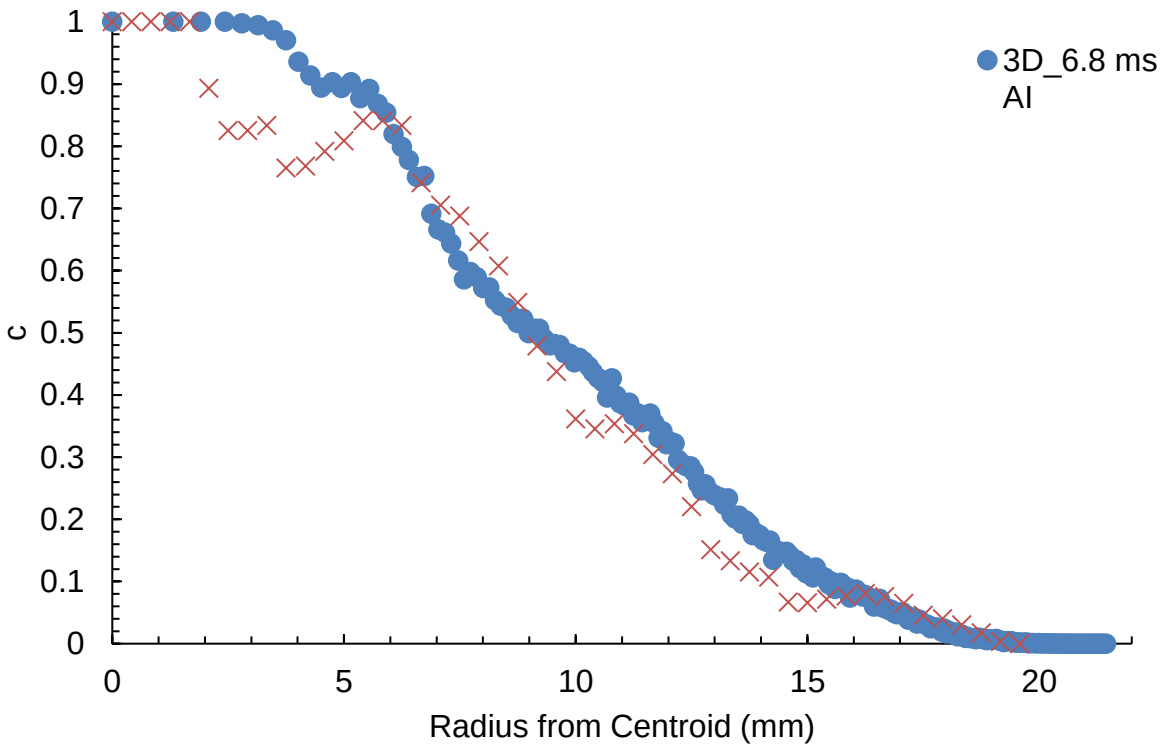

Figure 5.22 Variation of *c* with radius for a central 2D laser sheet image and reconstruction of a methane/air flame at 298K, 0.1 MPa, φ = 0.6 and *u'* = 1.25 m/s. *t* = 6.8 ms

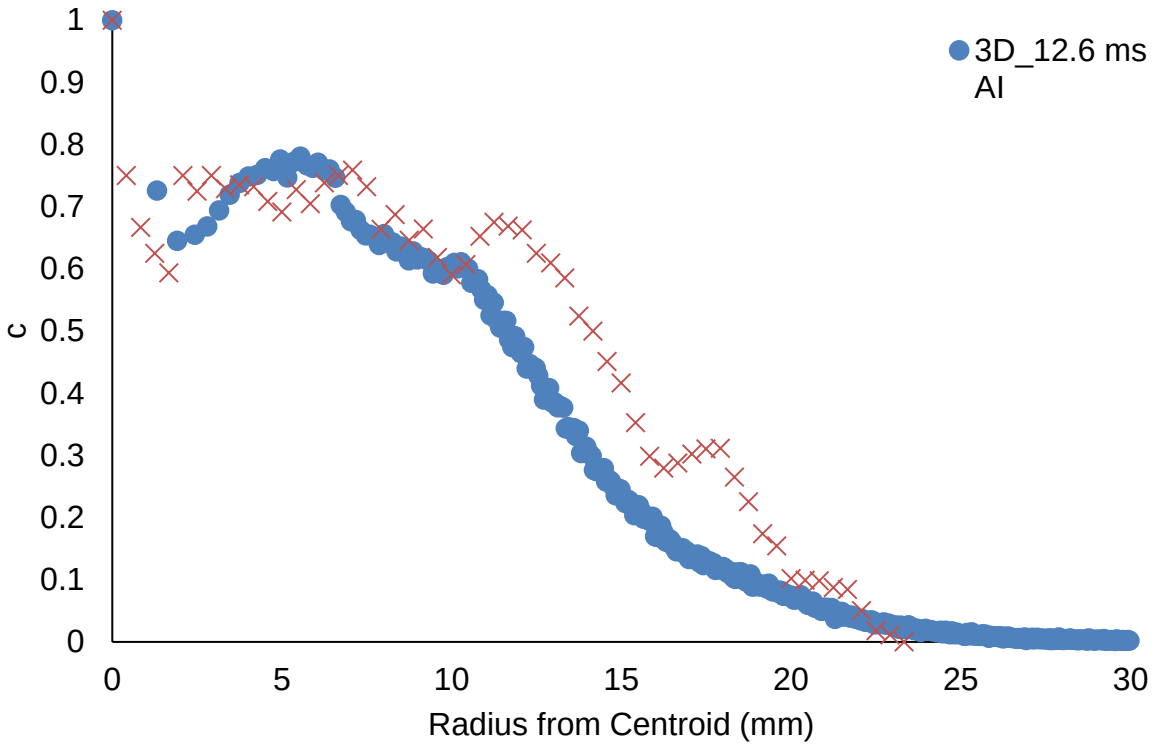

Figure 5.23 Variation of *c* with radius for a central 2D laser sheet image and reconstruction of a methane/air flame at 298K, 0.1 MPa, φ = 0.6 and *u'* = 1.25 m/s. *t* = 12.6 ms

5.3.2 Comparison of Fixed Position 2D Images with 3D Reconstructions

In the previous section, the cases considered generally showed good agreement between the 2D and 3D images, where the 2D images selected for comparison were assumed to be closest to the centre of the flames. The current section addresses limitations arising from using a fixed-position laser sheet in varying turbulence intensity environments. For all figures in the present section, crosses denote 2D results and circles 3D.

Figure 5.24 shows the development of reaction progress variable profiles with radius for both 2D sheet images and their corresponding reconstructions for a single explosion at a number of instants in time. Here, both the profiles and δ_t are visibly similar throughout the development of the flame, with the greatest difference in δ_t occurring immediately after ignition. As the applied *u'* was low, the flame surface exhibited a low level of surface wrinkling and was unlikely convected significantly by the larger length scales of turbulence. It is therefore

probable that the laser sheet sliced the flame close to the centre and that the surface detail gave a good representation of the overall 3D structure.

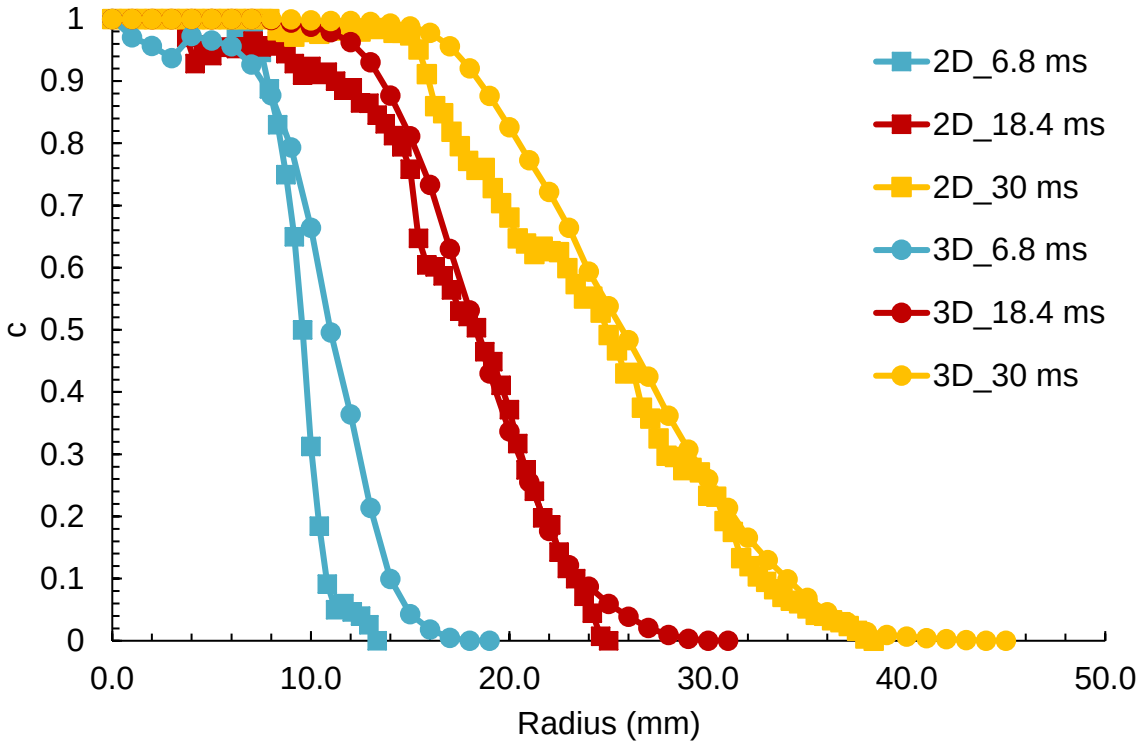

Figure 5.24 Comparison between *c* v's radius profiles for 2D and 3D flame images for methane/air at 298K, 0.1 MPa, φ = 0.6 and *u'* = 0.25 m/s at various instances after ignition

Figures 5.25 to 5.26 show the profiles of c with radius for a flame developing at a *u'* of 0.75 m/s at increasing time from ignition. The profiles at various instants in time are presented in individual graphs for clarity. Immediately after ignition, significant differences may be observed between the 2D and 3D profiles in terms of the flame radius and δ_t. The results obtained from the 2D image show an artificially small flame brush thickness and flame radius, where the latter would have an impact on burning velocity measurements if different portions of the flame were images at each instant in time due to convection.

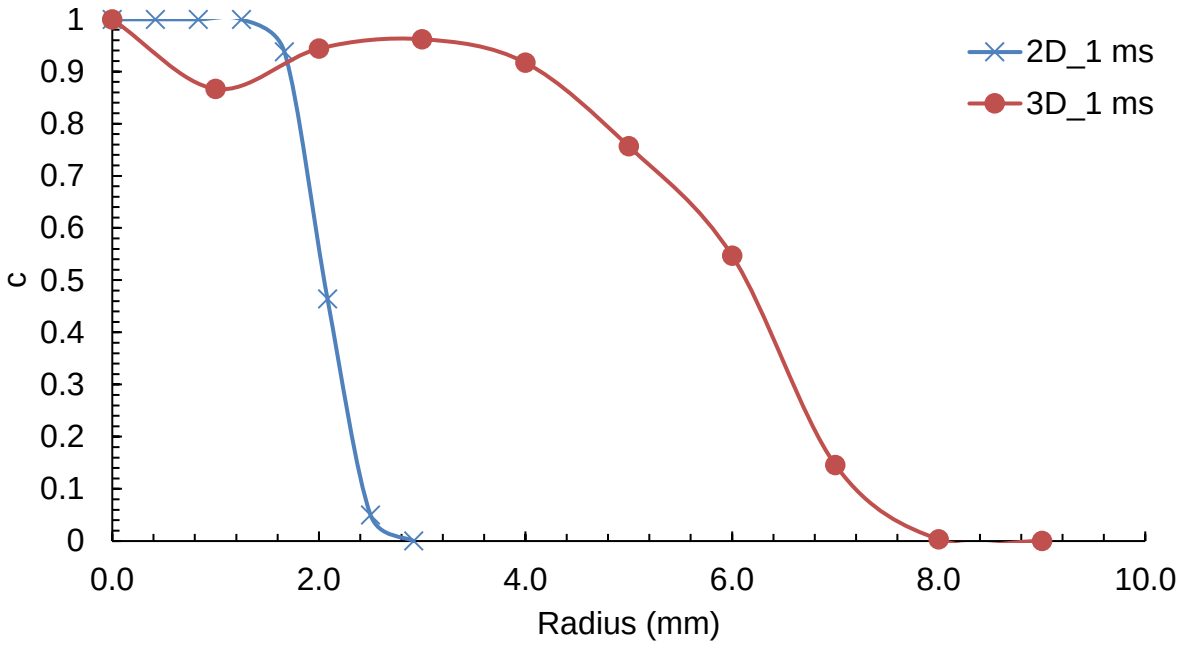

Figure 5.25 Comparison between *c* v's radius profiles for 2D and 3D flame images for methane/air at 298K, 0.1 MPa, φ = 0.6 and u' = 0.75 m/s, t = 1 ms

It can also be observed in Fig. 5.26 that for the 2D case, the centroid of the flame is in unreacted mixture, which is not the case for the 3D reconstruction. The flame brush thicknesses are, however, similar. This implies that the differences between root and tip radii are similar, though the flame structure differs.

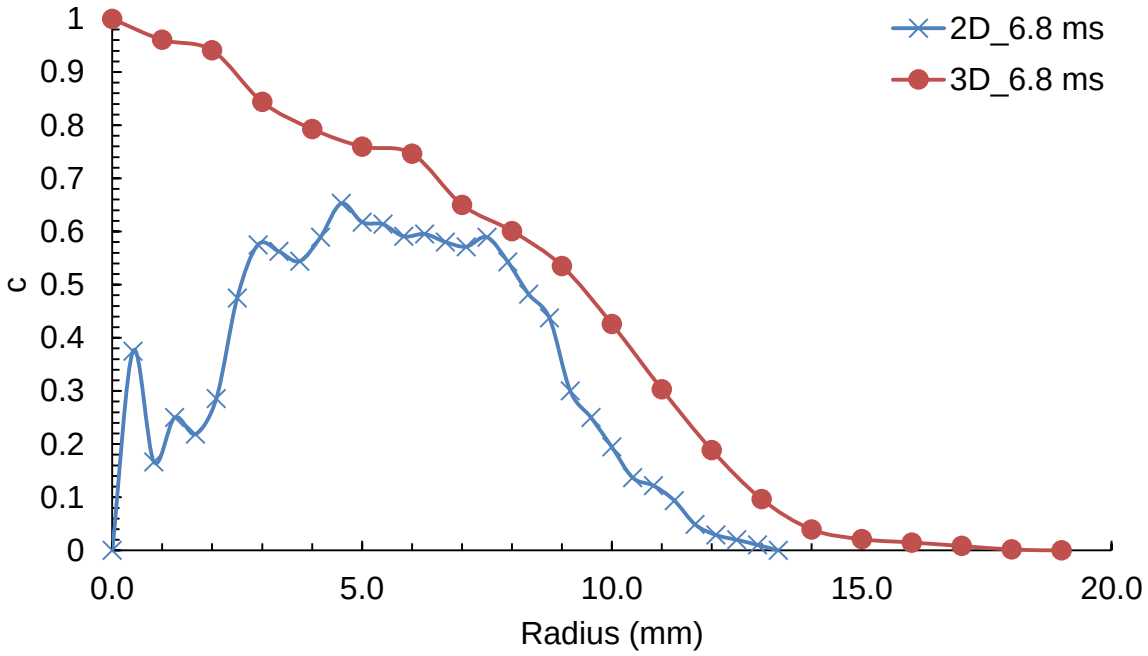

Figure 5.26 Comparison between *c* v's radius profiles for 2D and 3D flame images for methane/air at 298K, 0.1 MPa, φ = 0.6 and *u'* = 0.75 m/s, *t* = 6.8 ms

An even greater level of similarity exists in Fig. 5.27 where δ_t and the curve profiles are similar. Clearly, the 2D technique gives a good representation of 3D flame structure once the flame has started to develop following ignition.

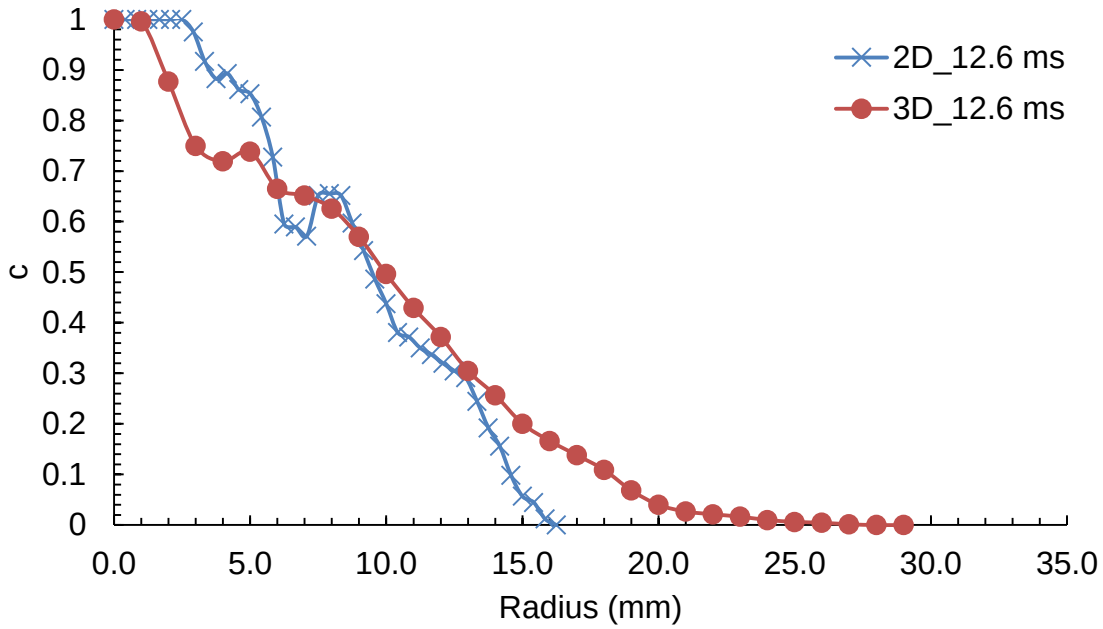

Figure 5.27 Comparison between *c* v's radius profiles for 2D and 3D flame images for methane/air at 298K, 0.1 MPa, φ = 0.6 and *u'* = 0.75 m/s, *t* = 12.6 ms

A similar pattern may be observed in Fig. 5.28 through 5.30 which show the results at the highest *u'*, where the 2D and 3D profiles start to converge at longer time periods after ignition. However, in this case data are presented at greater times from ignition and radii.

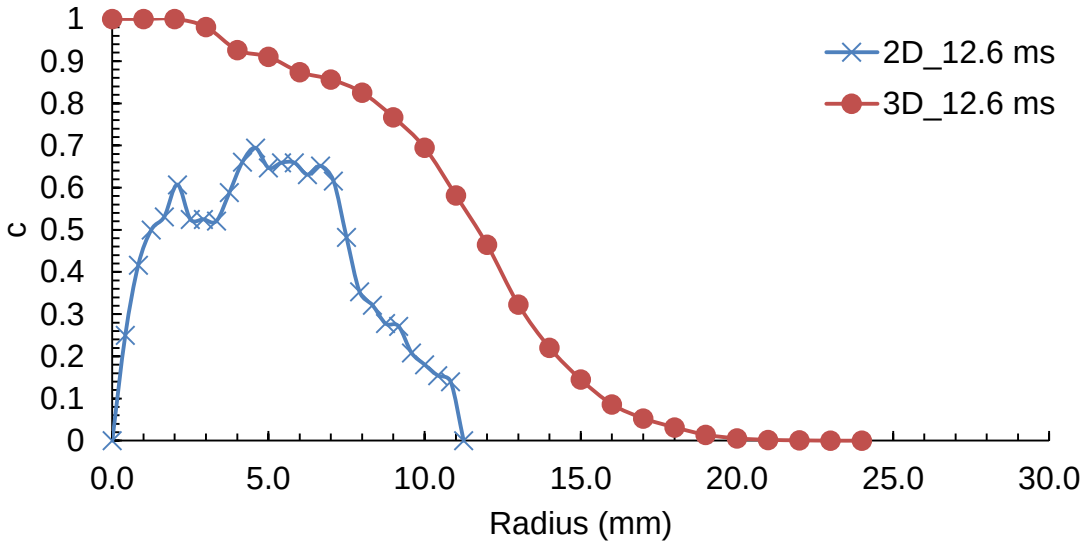

Figure 5.28 Comparison between *c* v's radius profiles for 2D and 3D flame images for methane/air at 298K, 0.1 MPa, φ = 0.6 and *u'* = 1.25 m/s, *t* = 12.6 ms

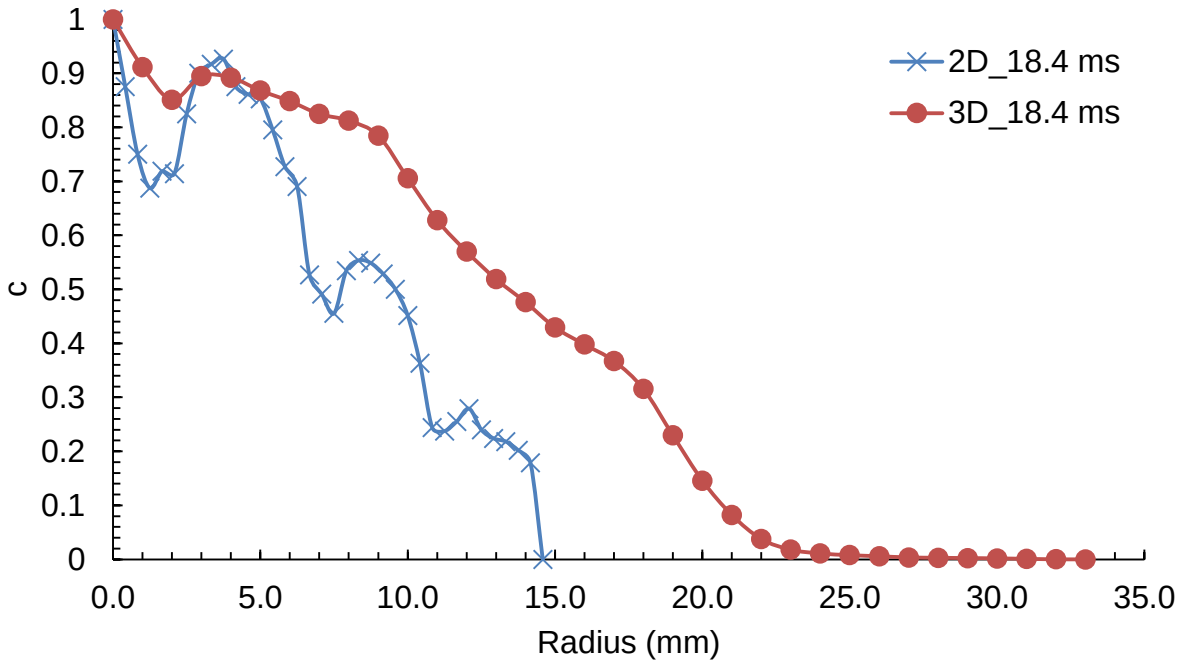

Figure 5.29 Comparison between *c* v's radius profiles for 2D and 3D flame images for methane/air at 298K, 0.1 MPa, φ = 0.6 and *u'* = 1.25 m/s, *t* = 18.4 ms

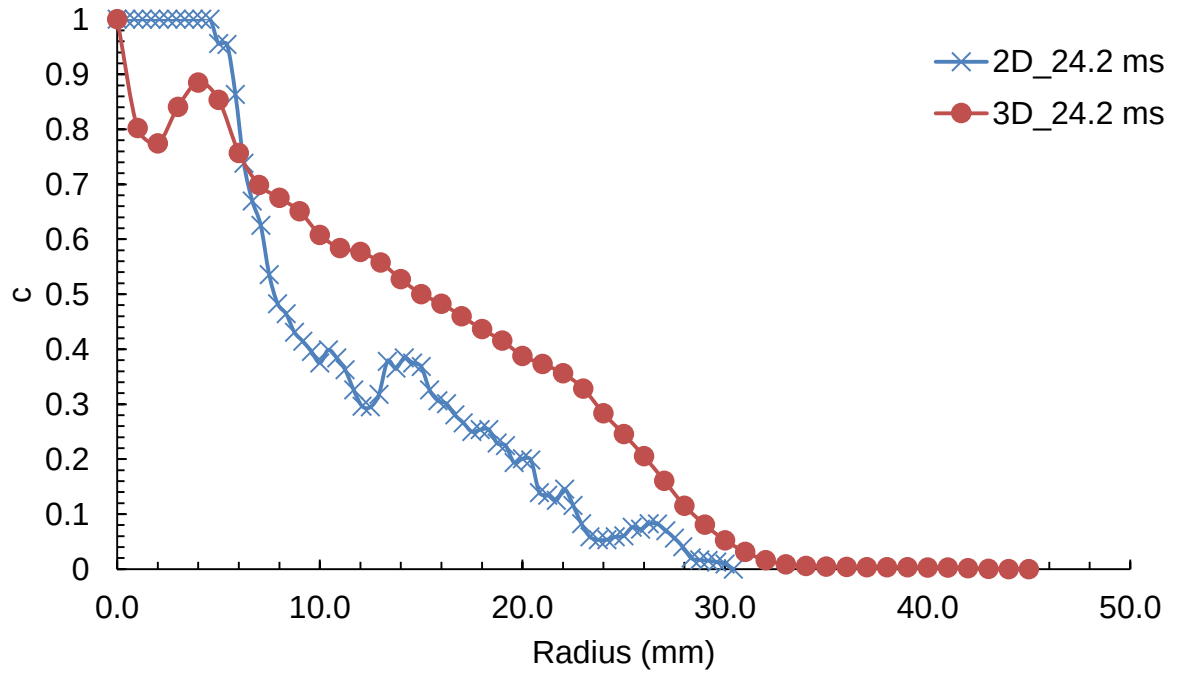

Figure 5.30 Comparison between *c* v's radius profiles for 2D and 3D flame images for methane/air at 298K, 0.1 MPa, φ = 0.6 and *u'* = 1.25 m/s, *t* = 24.2 ms

In conclusion, for a sweep of laser sheet images, selecting that with the largest flame cross sectional area gives a more accurate representation of the flame structure than examining images captured at a fixed point in space. Where the latter is employed, the flame must be reasonably developed before the 2D sheet images start to become representative of the overall 3D flame structure. This is particularly the case at high *u'*. It is therefore suggested that fixed, 2D laser sheet imaging is best employed for flames developing at low *u'*. This calls into question the reliability of particle image velocimetry (PIV) measurements of turbulent burning velocities, where a fixed laser sheet is used to measure velocity vectors around the perceived flame front. In such a case, it is necessary to ensure that the intersecting laser sheet is passing through close to the centre of the flame.

5.4 Analysis of Flame Surface Density Measurements

Flame surface density measurements obtained for the 3D flame reconstructions were presented in Section 4.3.2 as a function of radius from the flame centroid. This section presents a comparison of the obtained Σ profiles with those available in the literature.

5.4.1 Analysis of Flame Surface Density Profiles

Shown in Figure 5.31 is the variation of Σ with c for the highest *u'* used in this work. Here, it can be seen that Σ takes a value of zero at each extreme of c for the two lesser times from ignition. This is because flame surface is not present at the centre of the flame where c takes a value of unity and thus the mixture is fully burned, with no reaction zone present. The similar is true for c of zero, where only unburned mixture is present with a similar absence of reaction zone. The peak value of Σ is observed between c = 0.6 and 0.8. However, for the reconstruction generated at the greatest time from ignition, an uncharacteristically high peak in Σ may be observed at c of around 0.65. On examining the reconstructions of the flame at 6.8 and 12.6 ms from ignition as presented in Fig. 5.32, a very high degree of wrinkling and distortion may be seen for the reconstruction at 12.6 ms from ignition, where the flame surface appears to be close to breaking up. It also appears that the centre of the flame lies in an indented region, with a significant amount of surface structure surrounding this. This is likely the reason for the very high Σ seen at the high value of c. These features are not evident with the reconstruction captured at 6.8 ms from ignition, with the flame surface being considerably less structured.

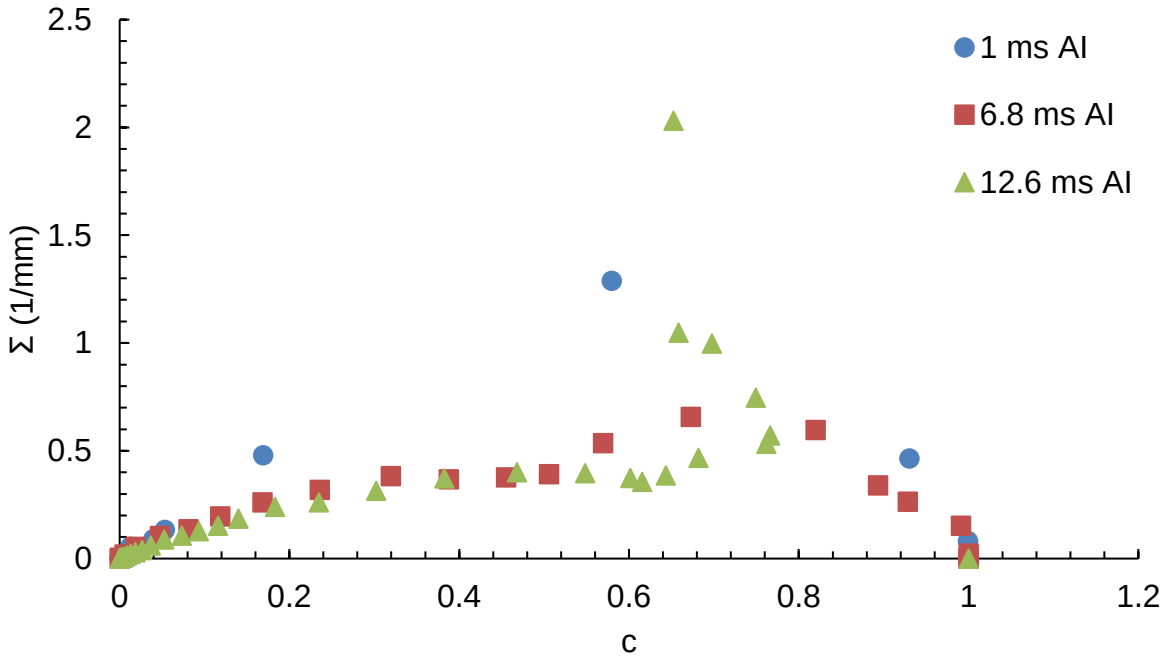

Figure 5.31 Flame surface density as a function of reaction progress variable for methane/air at 298K, 0.1 MPa, φ = 0.6 and u' = 1.25 m/s

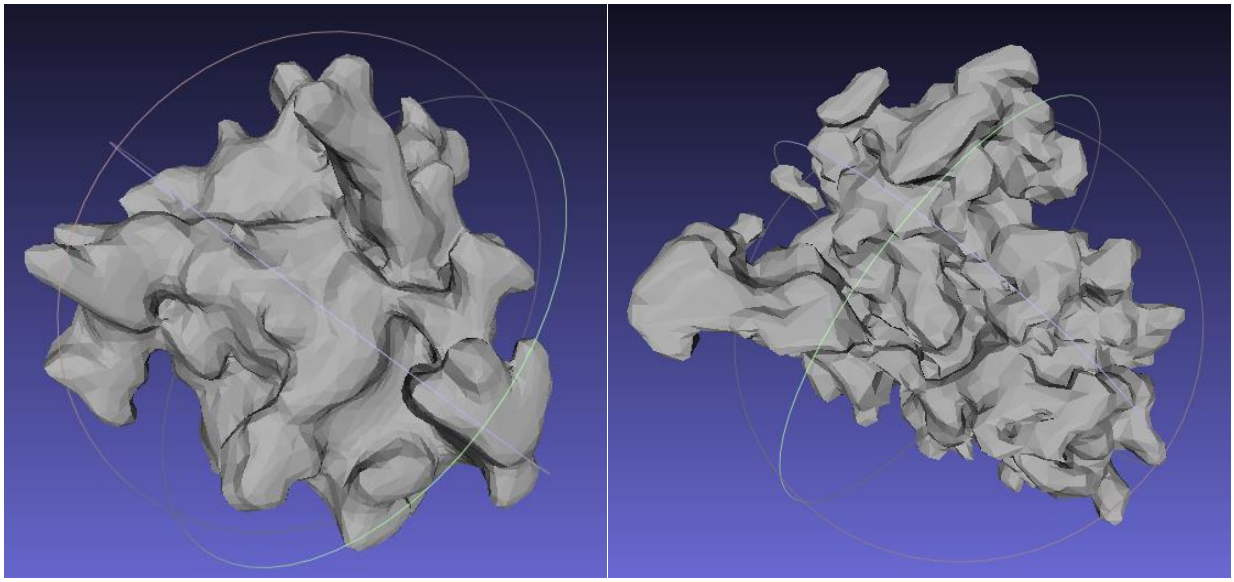

Figure 5.32 Reconstructions of the flame analysed in Fig. 5.31, at t = 6.8 ms (left) and t = 12.6 ms (right), scaled to enhance the flame surface structure

A similar effect also arose from the use of laser ignition where, immediately after ignition, some of the flames possessed recesses towards, or at, their centre. This gave rise to very high Σ values close to the root radius as shown in Fig. 5.33, indicated by a high value of c. Here, once the flame had grown sufficiently to close the gap in its centre, the profiles of Σ regained a more usual shape.

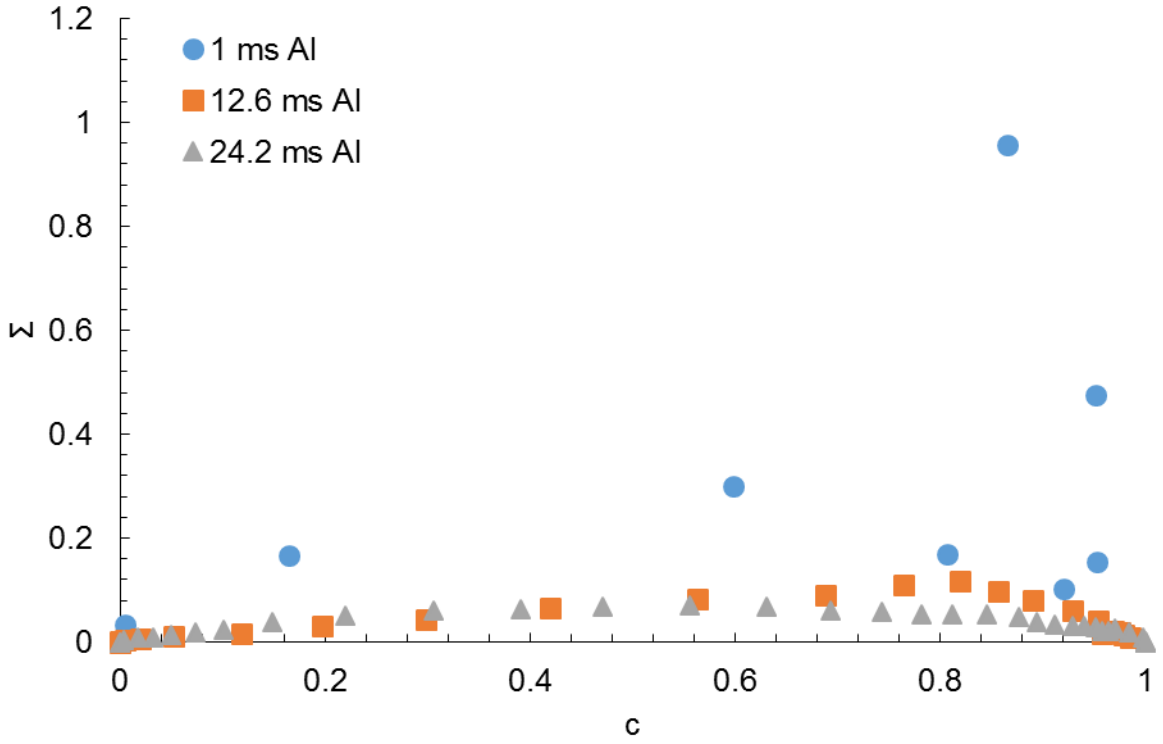

Figure 5.33 Flame surface density as a function of reaction progress variable for methane/air at 298K, 0.1 MPa, φ = 0.6 and u' = 0.25 m/s, various times from ignition

5.4.2 Comparison with Harker et al. (2012)

Shown in Fig. 5.34 and 5.35 are Σ versus radius and normalised radius, obtained in the present work and by Harker et al. (2012), respectively. As the same combustion vessel was used for each study, common r/L values are shown. Here, the highest u'/u_l employed by Harker et al. (2012) is compared with the lowest employed in the present work, of 2.35 and 4.2 respectively. It could be expected therefore that values of Σ calculated in the present work would be higher. However, at a similar time from ignition the flame in the present work is both smaller and possesses a significantly lower maximum flame surface density.

The smaller radius could be expected as the equivalence ratio was lower in the present study (0.6 cf. 0.7), with an associated reduction in laminar burning velocity. Compounding the relatively low values of $\Sigma\delta_l$ obtained in the present work, the values of δ_l in the present work are larger than those found by Harker et al. (2012), as the kinematic viscosity is similar due to the identical starting pressure and temperature but u_l is lower in the present work. From Gu et al. (2000), the u_l for the mixture employed by Harker et al. (2012) would have been 0.205 m/s, making the u' used around 0.5 m/s. Even for greater u' of 0.75 and 1.25 in the present work, such high peak Σ values at similar times from ignition are not observed, as is shown in Fig. 4.36 and 4.37. This suggests lower flame surface areas in the present work (due to the concurrently narrower distributions).

Harker et al. (2012) quote a resolution of 0.7 mm in all directions, whereas for the present work it is approximately 0.4 mm in the x and y directions and 0.8 mm in the z direction. The lower flame surface area observed in the present work is thus not likely due to resolution.

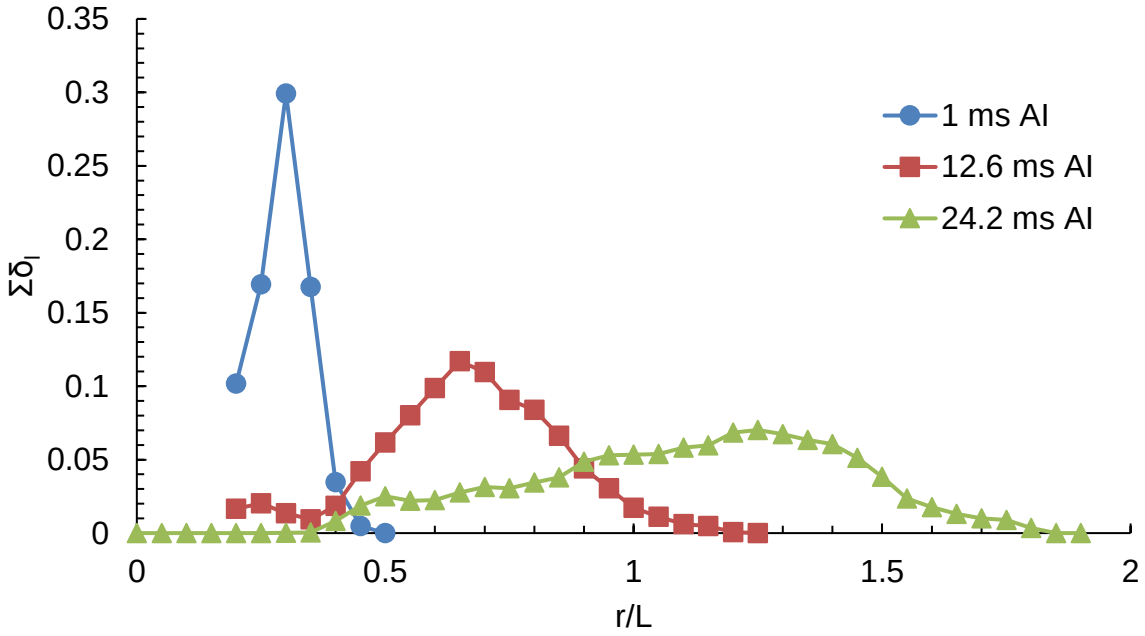

Figure 5.34 Flame surface density as a function of radius, methane/air at 298K, 0.1 MPa and φ = 0.6, u'/u_l = 4.2

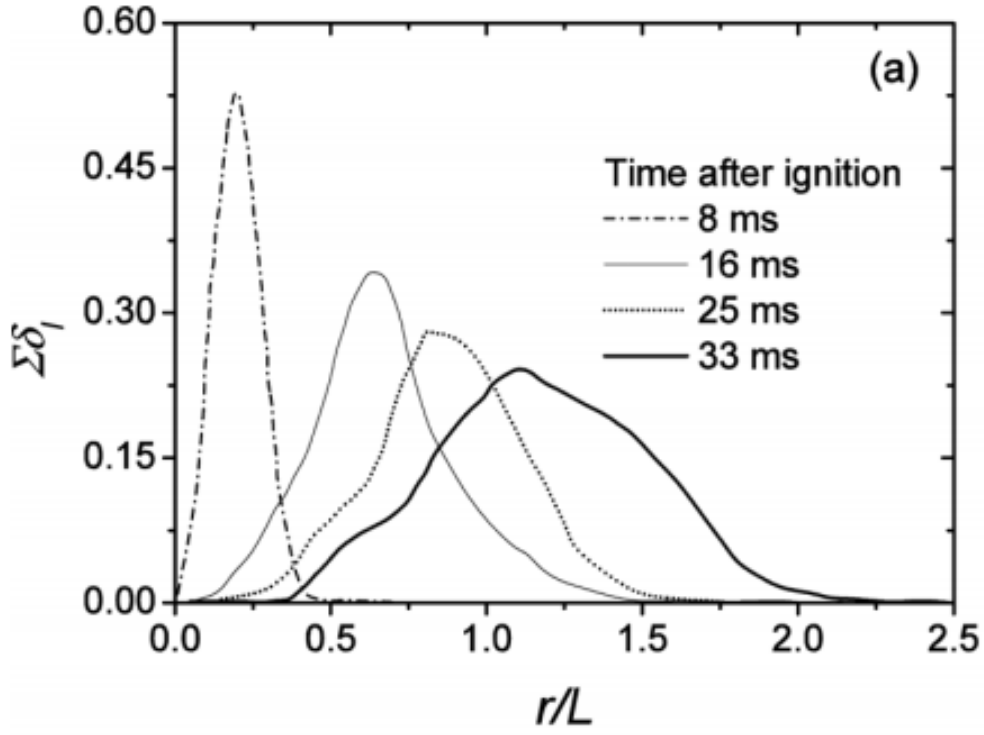

Figure 5.35 Flame surface density variation with normalised radius, reproduced from Harker et al. (2012); $\varphi = 0.7$, $u'/u_l = 2.35$

Presented in Fig. 5.36 to 5.37 are plots of normalised Σ with c generated in the present work. Each of these figures shows a peak in Σ occurring at $c > 0.6$, with the peak value lowering with time from ignition. These curves are not representative of flame surface area as they do not take flame radius into account. Here, the very high peak in Σ in Fig. 5.38 for the curve at 12.6 ms from ignition where c is close to unity has been removed to preserve the clarity of the graph. A similar, but less severe example of this is visible in Fig. 5.37 for the curve at 12.6 ms from ignition. Again, this is caused by indentation and high levels of wrinkling close to the centre of the flame. It can also be seen in these figures that peak Σ increases with u', despite images having being captures at shorter times from ignition at higher u', lowering the applicable u'_k/u' value. This is to be expected as the higher turbulence leads to more flame wrinkling.

Figure 5.36 is most comparable with the results shown in Fig. 5.39 presented by Harker et al. (2012) due to most similar starting conditions. Again, lower Σ values are seen in the present work. Additionally, the c value corresponding to peaks in Σ varies considerably with time from ignition in the present work, from c = 0.6 at 1 ms from ignition, to c = 0.8 at 12.6 ms from ignition, with a somewhat flattened profile at 24.2 ms. This is also evident in Fig. 5.38 and is likely caused by flame distortion. At the low u'/u_l used in Fig. 5.3 (b), the peak in Σ occurs at similar c. In this case, the ratio of chemical to turbulence eddy lifetimes is greater so the flame surface is less affected by the turbulence.

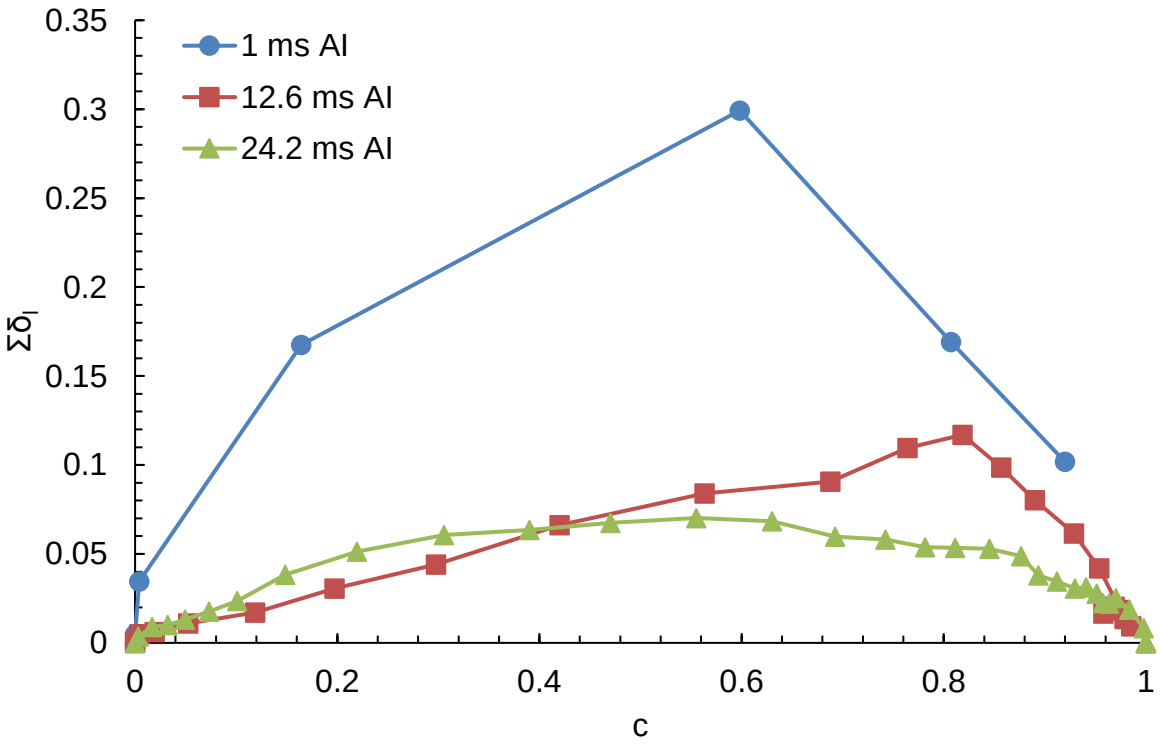

Figure 5.36 Normalised flame surface density as a function of reaction progress variable for methane/air at 298K, 0.1 MPa, φ = 0.6 and u' = 0.25 m/s, u'/u_l = 4.2, various times from ignition

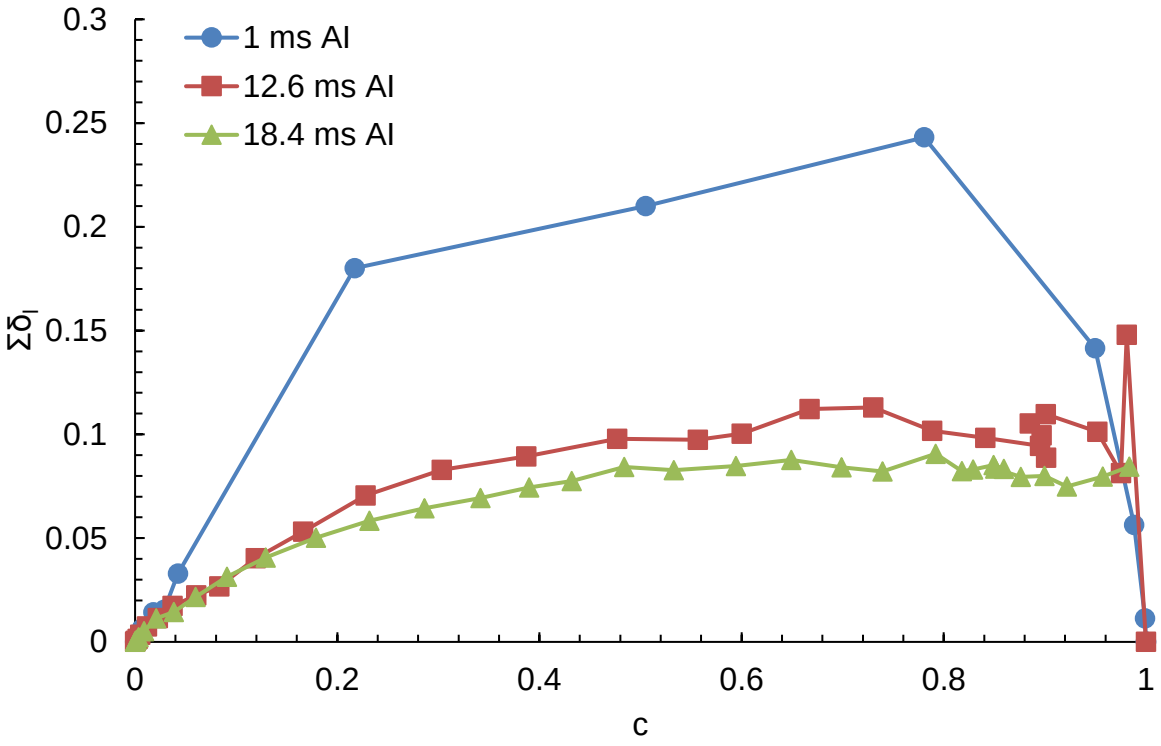

Figure 5.37 Normalised flame surface density as a function of reaction progress variable for methane/air at 298K, 0.1 MPa, φ = 0.6 and u' = 0.75 m/s, u'/u_l = 12.7, various times from ignition

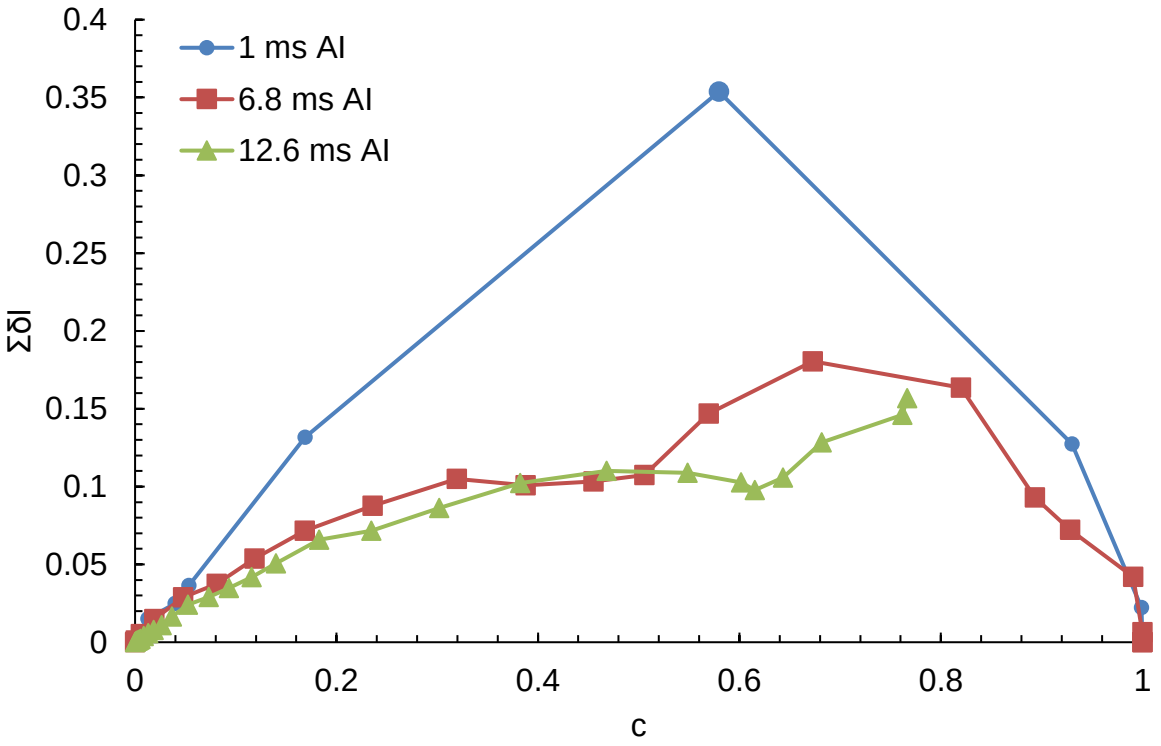

Figure 5.38 Normalised flame surface density as a function of reaction progress variable for methane/air at 298K, 0.1 MPa, φ = 0.6 and u' = 1.25 m/s, u'/u_l = 21.2, various times from ignition

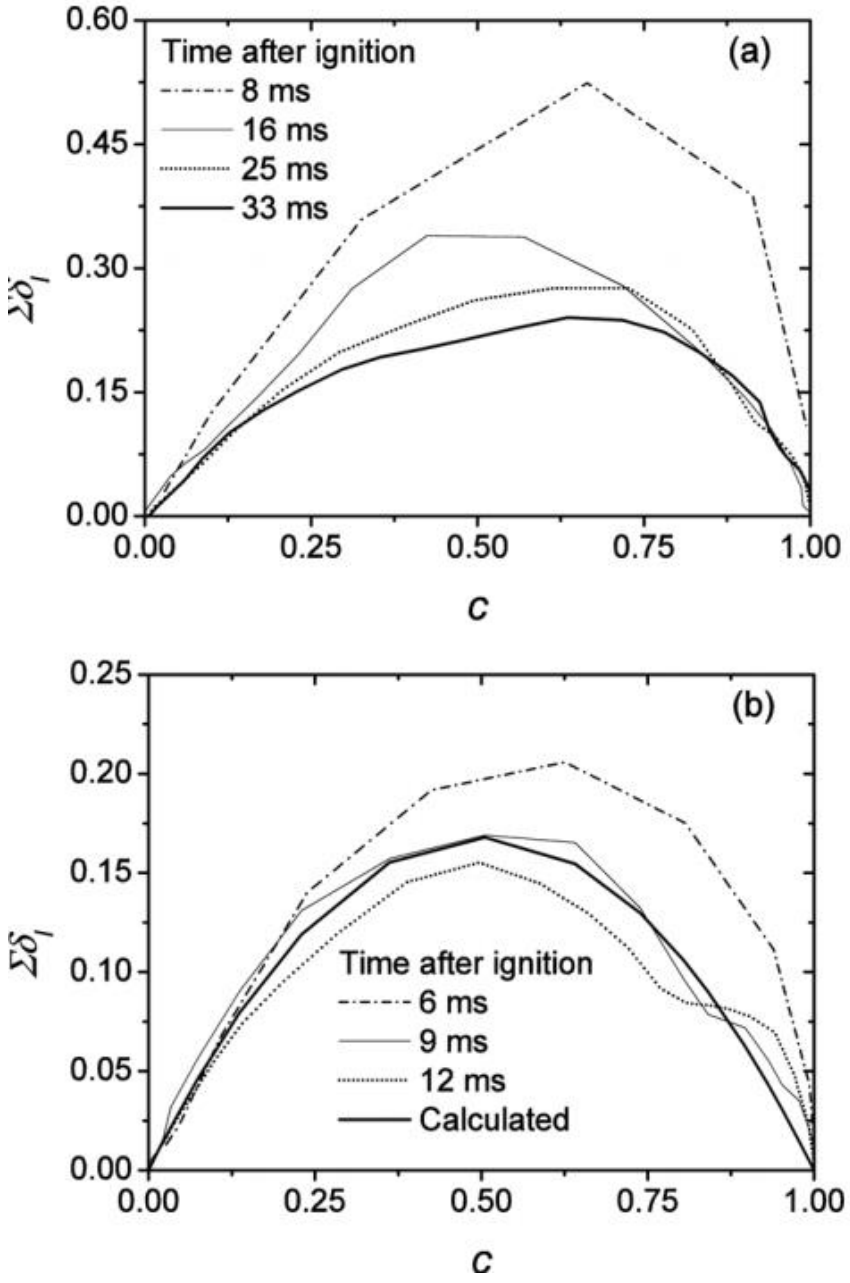

Figure 5.39 Normalised flame surface density plots reproduced from Harker et al. (2012); (a) $\varphi = 0.7$, $u'/u_l = 2.35$, (b) $\varphi = 1.0$, $u'/u_l = 1.11$

5.4.3 Comparison with Nivarti and Cant (2017)

Figure 5.40 presents the flame surface density profiles for each *u'* trialled in this work, where very high Σ at c close to unity has been removed for clarity. The points shown are at the greatest time from ignition in each case. This is to ensure that the curves correspond to the highest u'_k/u' values. This allows a better comparison with the flame surface density results obtained by the DNS of Nivarti and Cant (2017), presented in Fig. 5.41. In this figure, the blue and red curves are for a laminar flame and a parabolic curve fit, respectively. Cases I, III, IV and V represent u'/S_L values of 1.5, 10, 20 and 30, respectively. The units adopted to represent $\Sigma(\bar{c})$ are 1/m, leading to three orders of magnitude greater values than in the present work. Excepting the lowest turbulence case, the flame surface density values shown in this figure are very similar, with little difference between the two highest turbulence cases. It is stated by these Authors that at the onset of bending, increases in the flame surface area ratio begin to level off due to destruction of surface area by negative curvatures. This would have an effect on Σ as it is limited by the same mechanism.

A more consistent difference is apparent in the present work, though direct comparison is difficult as the flames are not fully developed here. It is not clear if the flames of Nivarti and Cant (2017) are fully developed, as discussed in Section 5.2. Additionally, in the present work the maximum *u'* represents the onset of bending. Thus, it could be expected that increases in the relatively low u' employed here would give significant differences in the flame surface area. If higher *u'* were to have been used in the present work, the similarity in Σ observed at the highest u'/S_L observed in Fig. 5.41 may have been observed here also. Difficulty in igniting such mixtures may prevent the exploration of this regime of combustion with the current 3D imaging setup, however, due to limitations in laser-induced spark energy.

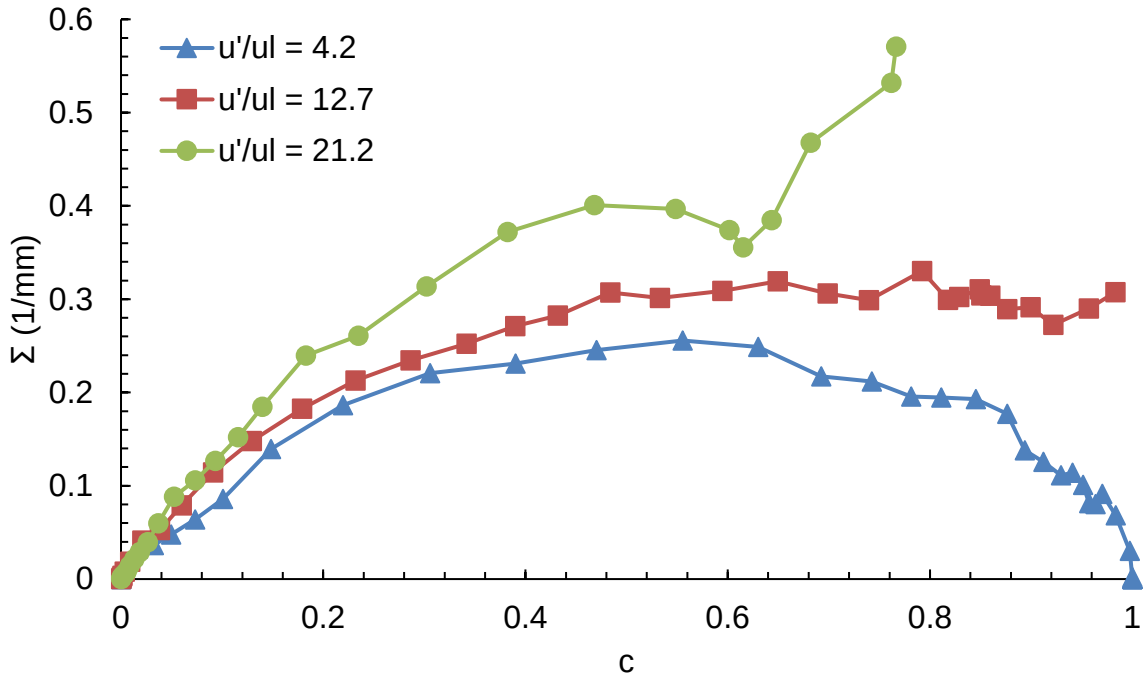

Figure 5.40 Flame surface density as a function of c, methane/air at 298K, 0.1 MPa and φ = 0.6, various u'/u_l

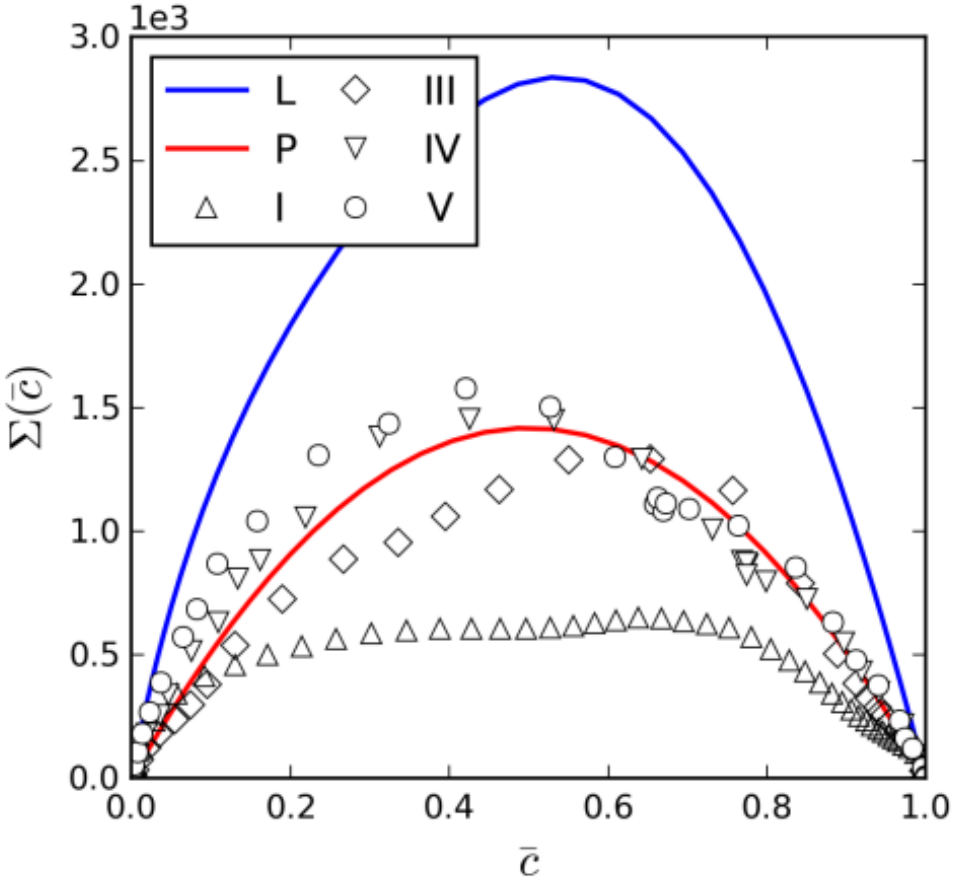

Figure 5.41 Flame surface density profiles from DNS at various u'/S_L, reproduced from Nivarti and Cant (2017)

5.4.4 Comparison with Bradley et al. (2009)

Figures 5.42 and 5.43 show the variation of flame surface density with radius, with the latter expressed as the number of integral length scales, for a low and intermediate u'/u_l of 4.2 and 12.7, respectively. This is to achieve generality with the results presented by Bradley et al. (2009), presented in Fig. 5.44. The latter shows flame surface density results obtained through a 2D laser sheet imaging study of propane/air mixtures, with starting conditions similar to those employed in the present work. The flame surface density was calculated as a function of the reaction progress variable, in line with predictions made by Lipatnikov and Chomiak (2004). Interestingly, in this figure, for the solid lines representing the stoichiometric case both the height and width of the flame surface density peaks increase with increasing u'_k/u' and thus time from ignition. This is also evident to a lesser extent for the lean case in part (a) of this figure, but is not featured in Fig. 5.42 or 5.43, which are at similar conditions to parts (a) and (b) of Fig. 5.44, respectively. However, the obtained values of Σ are slightly lower than those found in the present work for similar u'/u_l, whereas in the previous comparisons the present work revealed generally lower values. Clearly, the results of the present work corroborate the magnitude of Σ obtained using the analysis presented by Bradley et al. (2009), though the behaviour with increasing u'_k/u' is less consistent. Carrying out further experiments at the exact conditions employed by these Authors would provide a useful comparison.

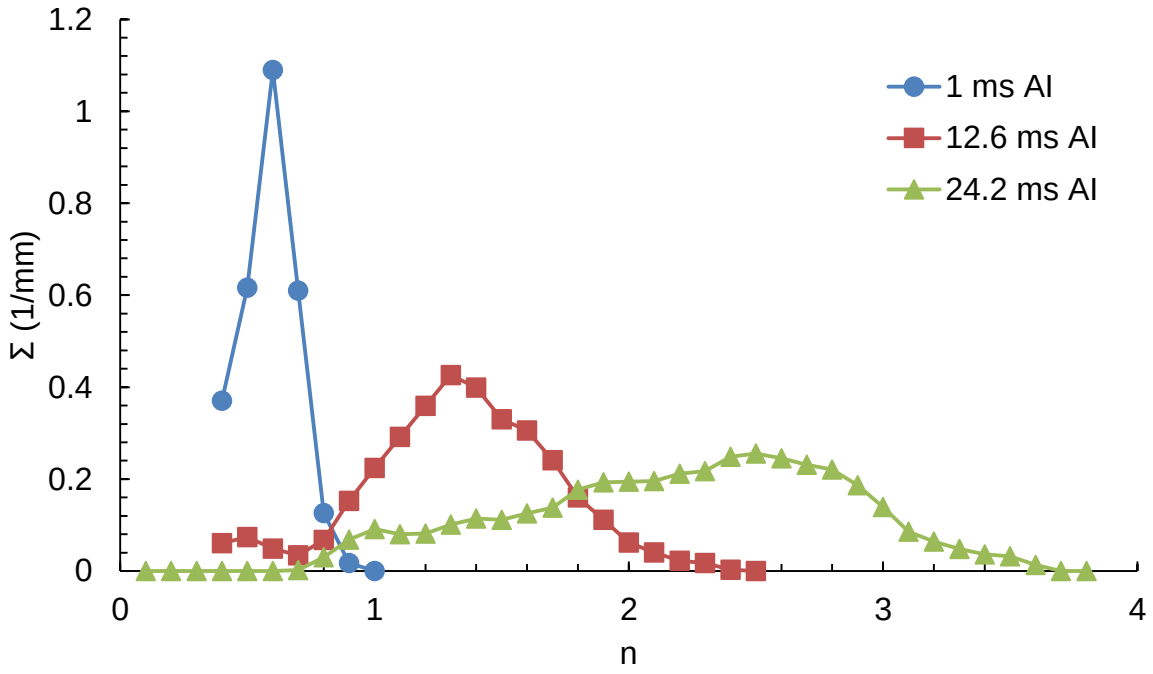

Figure 5.42 Variation of flame surface density with *n* for methane/air at 298K, 0.1 MPa and φ = 0.6, u'/u_l = 4.2

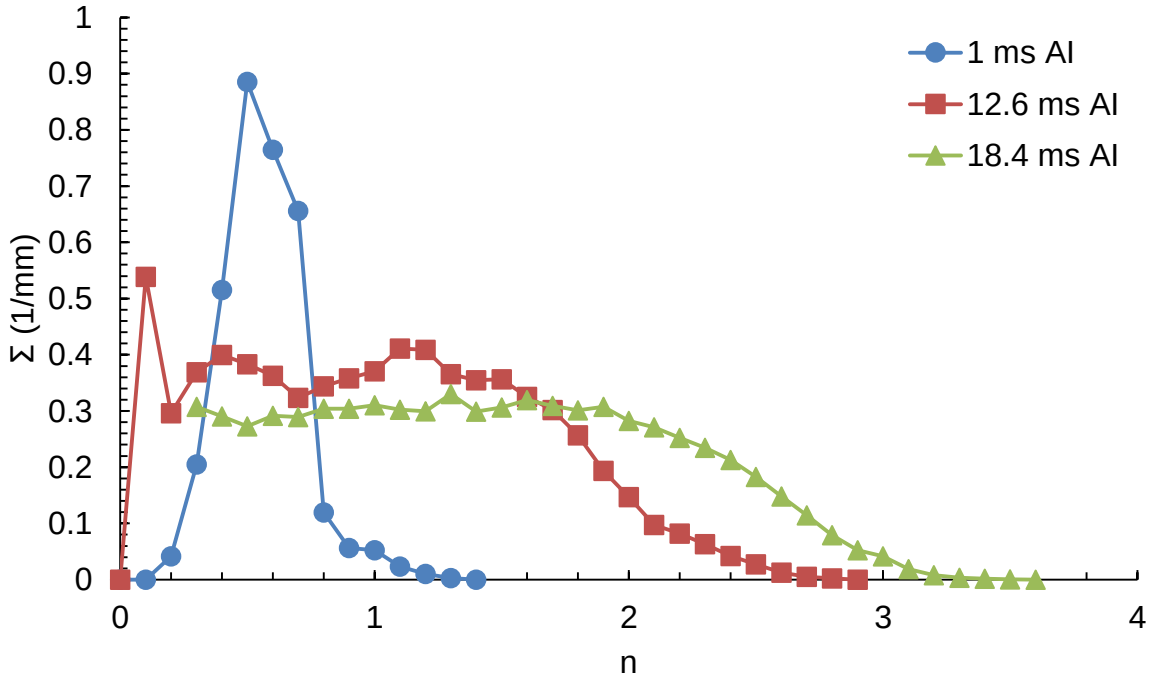

Figure 5.43 Variation of flame surface density with *n* for methane/air at 298K, 0.1 MPa and φ = 0.6, u'/u_l = 12.7

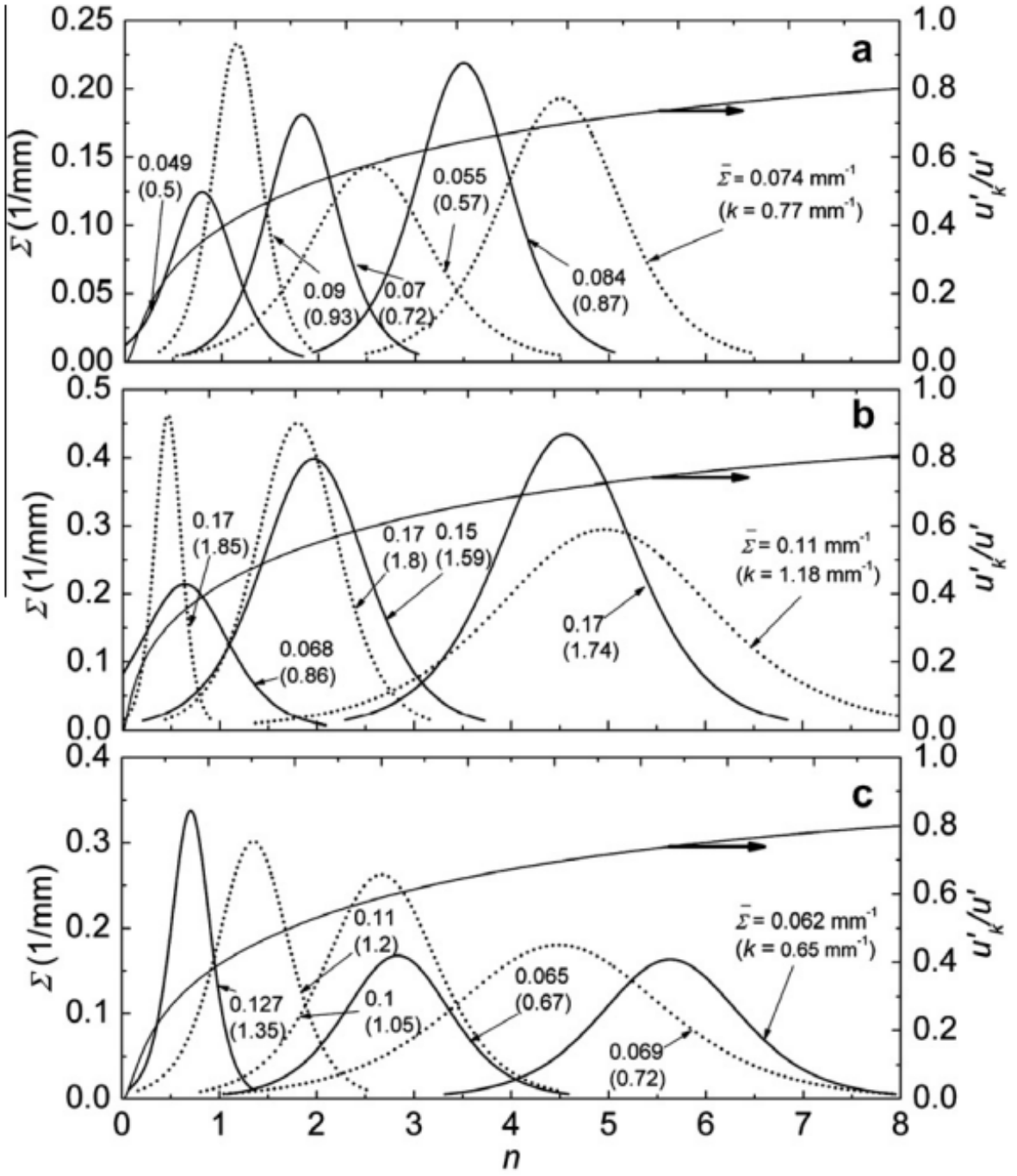

Figure 5.44 Flame surface density variation with normalised radius for propane/air at 300K, solid line $\varphi = 1$, broken line $\varphi = 0.8$ for (a) 0.1 MPa, $u'/u_l = 3.57$ (b) 0.1 MPa, $u'/u_l = 10.7$, (c) 0.5 MPa, $u'/u_l = 5.88$. Reproduced from Bradley et al. (2009)

5.5 Effect of Seeding Particles on the Laminar Burning Velocity

As it is known that the presence of small particles in a combustible mixture can accelerate the burning rate (e.g. Kylafis 2016), experiments were performed to ascertain if this would be the case for the Mie scattering technique employed in this study.

Firstly, the presence of the olive oil seed droplets serves to slightly increase the equivalence ratio. This effect may be calculated as

$$0.6CH_4 + 2(O_2 + 3.76N_2) \rightarrow 0.6CO_2 + 1.2H_2O + 0.8O_2 + 7.52N_2 \quad (5.2)$$

Thus, the total number of moles on the left hand side (LHS) of 5.6.1 is 10.12. The mole fraction of methane is therefore 0.059. With the bomb volume of 30.575 dm^3, this corresponds to a total of 0.073 moles of methane, with a mass of 1.17 g. With an olive oil seed particle concentration of 1.3 x 10^6 per cm^3 of seeded air (Kylafis 2016) at a partial pressure of 0.015 MPa in the bomb and with a modal average particle diameter of 900 nm (PIVTech 2014), this corresponds to approximately 2 mg of olive oil per explosion. This is insufficient to alter the equivalence ratio.

To exclude any other effects arising from the presence of the seed particles, laminar burning velocities and flame speeds were measured with and without seed particles using the technique described in Section 2.2. It was found that the stretched flame speed remained constant at around 0.5 m/s regardless of the presence of seed particles.

5.6 Estimation of Experimental Errors

Since both the flame surface area ratio and flame surface density measurements rely on common flame surface area measurements, error bars have only been included in Fig. 5.7 and are taken to be representative of all surface area errors in the present work. The error bars show a high degree of variability in the experimental results, which is also seen in the turbulent burning velocity results presented by Bradley et al. (2011) et seq. This is to be expected due to the stochastic nature of turbulence. Other sources of error include attainment of the correct equivalence ratio during mixture preparation and starting temperature and pressure prior to ignition. Mumby (2016) investigated the fidelity of laminar burning velocity results, which allowed these latter errors to be quantified in the absence of turbulent. In this case, a typical maximum 2 % error was observed between results obtained at given starting conditions, so these sources of error should be similarly diminutive in the present work.

Chapter 6 – Conclusions and Recommendations for Future Work

6.1 Conclusions

The development of a multiple laser sheet 3D flame imaging technique has been presented, which has allowed the study of flames at engine-like conditions of turbulence. This has revealed further information on flame surface structure in three dimensions, as well as the structure of the burned gas volume. The following subsections outline the findings of the present work.

6.1.1 Analysis of Turbulent Burning Velocities

The technique described in the present work has, for the first time, allowed for the direct measurement of the turbulent burning velocity by means of surface area ratios without the requirement for the assumptions made when analysing 2D data. Thus, the results obtained in the present work allowed the assumptions made in the previous works of Bradley et al. (2003, 2009, 2011 and 2013) and Bagdanavicius et al. (2015) to be validated.

The turbulent burning velocity measurements taken in the present work show excellent agreement with the correlations made with previous 2D experimental measurements at low to moderate RMS turbulence intensities (u'), with a slight deviation at the highest value of u' used in the present study. This deviation may be explained by the propensity of flames to drift in high intensity turbulence, such that when employing i.e. 2D, fixed position laser sheet imaging, it cannot be ascertained if the laser sheets are intersecting the centre of the flame. This affects the analysis of the burning rate based on the progression of the flame front through the mixture, where an extra, third dimension of the velocity vector is present but cannot be ascertained. Additionally, at high u' and thus Karlovitz number, K, the flame edge revealed in Mie scattering images becomes increasingly ambiguous leading to a loss of small flame surface details.

6.1.2 Analysis of the Bending Effect

The surface area ratios measured in the present work indicate the onset of turbulent burning velocity bending at high Karlovitz numbers. As effects of stretch, through the Markstein number, have not been included this indicates that the bending effect exists largely or solely due to a diminishing return on flame surface wrinkling at high values of *K*.

The DNS results presented in Nivarti and Cant (2017) also show bending of the surface area ratio at similar values of *K* as in the present work. These Authors found a propensity toward the generation of negative flame surface curvatures at increasing values of *K*, though this could not be measured in the present work.

The exact mechanism behind the bending effect is yet to be ascertained, though the results of the present work and of Nivarti and Cant (2017) point to surface area destruction being a cause.

6.1.3 Analysis of Reaction Progress Variable Measurements

Reaction progress variable was measured as a function of radius for both the 3D reconstructions and their constitutive 2D binarised laser sheet images. In the latter case, for each batch of 2D images representing a flame at an instant in time, either a sheet at a fixed position in space in the bomb was analysed or the central sheet was defined as that possessing the largest cross sectional area of burned gas.

Where the 2D sheet with the greatest cross sectional area of burned gas was analysed, the flame brush thickness (defined as the distance between the root and tip radius of the flame) was similar to that observed for the 3D reconstruction. The profiles of the *c* versus radius graphs were also visibly very similar.

However, if sheet images at a fixed position in the bomb were assumed to intersect the centre of the flame, significant differences in flame brush thickness and the *c* versus radius profile were observed compared to those seen for the relevant 3D reconstructions at higher values of *K*. Less of a disparity was observed for the lower *K* values employed in the present work.

This implies that at higher *u'*, images of 2D laser sheets passing through the centre of the bomb do not traverse the centre of the flame due to drifting of the flame in the early stages of growth. This is particular relevance if such techniques as PIV are to be used to measure turbulent burning velocities, where a fixed sheet location is used, as it would be necessary to factor in the third dimensional velocity vector to ensure accurate measurement of velocity in 2D.

6.1.4 Comparisons of Flame Surface Density Measurements

Flame surface density measurements were obtained for the 3D reconstructions at a variety of *u'* values. Where flame surface density was plotted as a function of radius from the centroid of the flame, it could be seen that with increasing time from ignition and thus with increasing u'_k, the resulting curves broadened. This was a result of increasing thickness of the flame brush leading to a broader distribution of the increasing flame surface area. Where plotted as a function of the reaction progress variable, the height of the resulting parabola-like profiles increased with increasing u'_k. For highly turbulent flames at long times from ignition, uncharacteristically high peaks of Σ were apparent at *c* values close to unity. On examination of the reconstructions where this was evident, it could be seen that a high concentration of flame surface wrinkling was present near to the flame centroid, typically where the flame had become highly distorted and indented. This provides novel insight into quantified flame surface structure at high *K*.

On direct comparison with the results of Nivarti and Cant (2017), it can be seen that the experimental flames displayed lower flame surface densities at all values of the reaction progress variable for a given u'/u_l, despite the same flames possessing higher values of *A/a*. Investigations into the reasons for this are ongoing at the time of writing.

6.1.5 Comparison of Experimental Surface Area Ratios with DNS

Experimentally derived *A/a* have been compared to those obtained by Nivarti and Cant (2017) at a variety of u'/u_l. The two datasets illustrate the bending effect at higher *u'* and the DNS results illustrate slightly lower overall *A/a* values, but well within an order of magnitude of difference. This might be explained by the highly stretched and distorted nature of the experimental flames, where this could increase the maximum possible flame surface area compared to a flame developing in the duct simulated by the DNS study.

As the DNS is tuneable, this offers an additional explanation. It is unlikely that the reaction progress variable isovalue (c = 0.8) chosen to represent the DNS flame surface is responsible as the maximum level of surface wrinkling was observed at this isosurface of c.

6.1.6 Potential Impacts of the Present Work

For the first time, it has been possible to directly compare 3D experimentally-derived data with simulation studies employing very similar conditions. Where the results obtained were comparable, this demonstrates the validity of the simulations. Where these simulations are ultimately employed in the design of combustion machinery, the present work facilitates verification of the reliability of such simulations. The bending effect is also practically relevant as it represents a limit for the rate of turbulent burning, where maximising the rate of burning is important for simultaneously increasing power output and efficiency of engines whilst reducing emissions of undesirable substances. As the present work has set the scene for analysing this experimentally, the present work could thus be of practical importance for engine design.

6.2 Recommendations for future work

The present work was carried out using a single, very lean methane/air mixture at a fixed starting temperature, pressure, and equivalence ratio, where only u' was varied. This led to a variety of K values, whereas Ma_{sr} was kept constant. To further test the validity of previous correlations of turbulent burning velocities from 2D measurements, Ma_{sr} and u_l could also be varied. Further recommendations are as follows.

1) At the higher u' employed in the present work, the flame surface became wispy and difficult to consistently define. Using seed particles with a higher boiling point may prevent premature evaporation of the seed particles by turbulent mixing of fresh reactants with burned gas, increasing flame edge definition. Using a variety of seed particles may enable different isosurfaces of reaction progress variable to be viewed, to validate the findings of Nivarti and Cant (201) with regards to the level of wrinkling observed at different isosurfaces of c.
2) Only very slowly burning mixtures could be employed here to minimise flame growth during each sweep. Increasing the mirror rotation rate would reduce the time required for each sweep, at the expense of resolution in the z-direction. Using a higher frequency

laser and framing rate camera would allow a lower sweep time for a given z-direction resolution.

3) Combining the presently described technique with simultaneous PIV in three dimensions would allow for a much better understanding of the turbulence/flame interaction in three dimensions. It is the Author's view that this would not be particularly difficult to implement in itself, but capturing double pulses at each sheet position in the bomb would require a very short double-pulse width, which may not allow sufficient time for seed particle movement between images. The angles of the sheets with respect to the camera would also need to be taken into account.
4) Although the presently described technique has been used to capture images and videos of quenching, it has not been possible to analyse these in the present work. Again, high melting point seed particles would aid this analysis.
5) Applying simultaneous schlieren and 3D laser sheet imaging would allow a direct comparison of these two techniques should it be possible to implement this.

6) Reliable surface curvature measurements of the 3D reconstructions have not been made in the present work, where this could give a better insight into the bending effect and would help to verify the findings of Nivarti and Cant (2017) with regards to the formation of negative curvatures at high u'/u_l.

Chapter 7 References

Abdel-Gayed, R.; Bradley, D. and Lawes, M. (1987): "Turbulent burning velocities: a general correlation in terms of straining rates", Proceedings of the Royal Society, London, 414, 389-413

Aleiferis, P.; Taylor, A.; Ishii, K. and Urata, Y. (2004): "The nature of early flame development in a lean-burn stratified-charge spark-ignition engine", Combustion and Flame, 136, 283–302

Al-Shahrany, A.S., Bradley, D., Lawes, M., Woolley, R. (2005): "Measurement of unstable burning velocities of iso-octane–air mixtures at high pressure and the derivation of laminar burning velocities", Proceedings of the Combustion Institute, 30, 225-232

Bagdanavicius, A., Bowen, P., Bradley, D., Lawes, M. and Mansour, M. (2015): "Stretch rate effects and flame surface densities in premixed turbulent combustion up to 1.25 MPa, Combustion and Flame, 162, 4158–4166

Bradley (2016), private communication

Bradley, D. (1992): "How Fast Can We Burn?", Twenty-Fourth Symposium (International) on Combustion/The Combustion Institute, 247-262

Bradley, D., Gaskell, P. and Gu, X. (1996): "Burning Velocities, Markstein Lengths, and Flame Quenching for Spherical Methane-Air Flames: A Computational Study", Combustion and Flame, 104, 176-198

Bradley, D.; Haq, M.; Hicks, R.; Kitagawa, T.; Lawes, M.; Sheppard, C. and Woolley, R. (2003): "Turbulent burning velocity, burned gas distribution, and associated flame surface definition", Combustion and Flame, 133, 415–430

Bradley, D. and Harper, C. (1994): "The Development of Instabilities in Laminar Explosion Flames", Combustion and Flame, 99, 562-572

Bradley, D.; Hicks, R.; Lawes, M.; Sheppard, C. and Woolley, R. (1998): “The Measurement of Laminar Burning Velocities and Markstein Numbers for Iso-octane–Air and Iso-octane–n-Heptane–Air Mixtures at Elevated Temperatures and Pressures in an Explosion Bomb”, Combustion and Flame, 115, 126-144

Bradley, D.; Lawes, M.; Liu, K, Mansour, M. (2013): “Measurements and correlations of turbulent burning velocities over wide ranges of fuels and elevated pressures”, Proceedings of the Combustion Institute, 34, 1519–1526

Bradley, D.; Lawes, M.; Mansour, M. (2009): “Flame surface densities during spherical turbulent flame explosions”, Proceedings of the Combustion Institute, 32, 1587–1593

Bradley, D.; Lawes, M. and Mansour, M. (2011): “Correlation of turbulent burning velocities of ethanol–air, measured in a fan-stirred bomb up to 1.2 MPa”, Combustion and Flame, 158, 123–138

Bradley, D.; Sheppard, C.; Suardjaja, I. and Woolley, R. (2004): “Fundamentals of high-energy spark ignition with lasers” Combustion and Flame, 138, 55–77

Bradley, D.; Sheppard, C.; Woolley, R.; Greenhalgh, D. and Lockett, R. (2000): “The Development and Structure of Flame Instabilities and Cellularity at Low Markstein Numbers in Explosions” Combustion and Flame, 122, 195-209

Bray, K., Domingo, P. and Vervisch, L. (2005): “Role of the progress variable in models for partially premixed turbulent combustion”, Combustion and Flame, 141, 431–437

Broustail, G., Seers, P., Halter, F., Moréac, G. and Mounaim-Rousselle, C. (2011): “Experimental determination of laminar burning velocity for butanol and ethanol iso-octane blends”, Fuel, 90, 1-6

Chakraborty, N. and Cant, R. (2011): “Effects of Lewis number on flame surface density transport in turbulent premixed combustion” Combustion and Flame, 158, 1768–1787

Chakraborty, N. and Cant, R. (2013): "Turbulent Reynolds number dependence of flame surface density transport in the context of Reynolds averaged Navier–Stokes simulations" Proceedings of the Combustion Institute, 34, 1347–1356

Damköhler, G. (1940), Zeitschrift für Elektrochemie und angewandte physikalische Chemie ,46, 11, 601–652 .

Dixon-Lewis, G. (1990): Twenty-Third Symposium (International) on Combustion, The Combustion Institute, 305-324

Gillespie, L; Lawes, M.; Sheppard, C. and Woolley, R. (2000): "Aspects of laminar and turbulent burning velocity relevant to SI engines", SAE Paper Number 2000-01-0192

Gupta, R. B. (2009): "Hydrogen Fuel, Production Storage and Transport"1st edition, Boca Raton NW, U. S., CRC Press

Gu, X.; Haq, M.; Lawes, M. and Woolley, R. (2000): "Laminar Burning Velocity and Markstein Lengths of Methane–Air Mixtures" Combustion and Flame, 121, 41-58

Halter, F., Chauveau, C., Gökalp, I. and Veynante, D. (2009): "Analysis of flame surface density measurements in turbulent premixed Combustion", Combustion and Flame, 156, 657–664

Harker, M. (2009): "Experimental Study of Turbulent Flame Structure", PhD Thesis, Department of Mechanical Engineering, University of Leeds, Leeds U.K.

Harker, M.; Hattrell, T.; Lawes, M.; Sheppard, C.; Tripathi, N. and Wolley, R. (2012): "Measurement of the three-dimensional structure of flames at low turbulence", Combustion Science Technology, 184, 1818-37

Hecht, E (1989): "Optics", Addison-Wesley, 2nd Edition

Hu, E., Huang, Z., He, J., Jin, C. and Zheng, J. (2009): "Experimental and numerical study on laminar burning characteristics of premixed methane–hydrogen–air flames", International Journal of Hydrogen Energy, 34, 4876-4888

Hult, J.; Omrane, A.; Nygren, J.; Kaminski, C.; Axelsson, B.; Collin, R.; Begtsson, P. and Alden, M. (2002): "Quantitative three-dimensional imaging of soot volume fraction in turbulent non-premixed flames" Experiments in Fluids, 33, 265–269

Hult, J.; Gashi, S.; Chakraborty, N; Klein, M.; Jenkins, K.; Cant, S. and Kaminski, C. (2007): "Measurement of flame surface density for turbulent premixed flames using PLIF and DNS" Proceedings of the Combustion Institute, 31, 1319–1326

Jerzembeck, S., Peters, N., Pepiot-Desjardins, P. and Pitsch, H. (2009): "Laminar burning velocities at high pressure for primary reference fuels and gasoline: Experimental and numerical investigation", Combustion and Flame, 156, 292-301

Kondo, T., Lio, S. and Hiruma, M. (1997): "A Study on The Mechanism of Backfire in External Mixture Formation Hydrogen Engines –About Backfire Occurred by Cause of the Spark Plug", SAE Paper no. 971704

Kylafis, G. (2016): "The Explosion and Dispersion Potential of Engineered Nanoparticles", PhD thesis, University of Leeds, Leeds, U.K.

Kroon, D. (2016) c/o The Mathworks File Exchange, Surface Mesh Voxelisation Matlab .m File

Laser Lines, Technical Data Supplied with DM60 Nd:YAG Laser (2016)

Lipatnikov, A. and Chomiak, J. (2004): "A study of the effects of pressure-driven transport on developing turbulent flame structure and propagation" Combust. Theory Modelling, 8, 211–225

Mumby, D. (2016): “Experimental Characterisation of Fuel Blends”, PhD Thesis, Department of Mechanical Engineering, University of Leeds, Leeds U.K.

Nivarti, G. and Cant, R. S. (2017): “Direct Numerical Simulation of the bending effect in turbulent premixed flames”, Proceedings of the Combustion Institute, 36, 1903-1910

Nygren, J.; Hult, J.; Richter, M.; Alden, M.; Christensen, M.; Hultqvist, A. and Johansson, B. (2002): “Three dimensional laser induced fluorescence of fuel distributions in an HCCI engine”, Proceedings of the Combustion Institute, Volume 29, 679–685

Ormsby, M.P. (2005): “Turbulent flame development in a high-pressure combustion vessel”, PhD Thesis, School of Mechanical Engineering, University of Leeds, Leeds U.K.

Ortiz, M; Gayán, P; de Diego, L; García-Labiano, F; Abad, A; Pans, M and Adánez, J (2011): “Hydrogen production with CO_2 capture by coupling steam reforming of methane and chemical-looping combustion: Use of an iron-based waste product as oxygen carrier burning a PSA tail gas” Journal of Power Sources, 196, 4370–4381

PIVTech (2014) Equipment Datasheet for PIV Part14 Aerosol Generator

Rand, D. A. J. and Dell, R. M. (2008) *Hydrogen Energy: Challenges and Prospects*, 1st edition, Cambridge: RSC Publishing

Sethian, J.A. (1999): “Level set methods and fast marching methods: evolving interfaces in computational geometry, fluid mechanics, computer vision, and materials science”, Cambridge university press

Sharpe, G., (2011), Private Communications, cited in Mumby (2016)

Shukman, D. (2013): “Carbon dioxide passes symbolic mark”, BBC News [Online], 10.05. 2013 [09.09.2014], available from: http://www.bbc.co.uk/news/science-environment-22486153

Steen, W. (1998): “Laser Material Processing”, Springer-Verlag, London, 2nd edition, pp84-87

A Matlab code by “Sven” (2015), URL:
https://uk.mathworks.com/matlabcentral/fileexchange/20922-stlwrite-filename--varargin-
Accessed: 17.06.2017

Taubin, G. (1995): “A Signal Processing Approach to Fair Surface Design”, Proceedings of the Fifth International Conference on Computer Vision, 852, Washington DC, USA, IEEE Computer Society, ISBN0-8186-7042-8

The Mathworks (Inc.), 2014, Matlab Helpdesk, “Using Matlab Graphics – Visualising MRI Data” [online], [Accessed 20.09.2014], available from: http://dali.feld.cvut.cz/ucebna/matlab/techdoc/umg/chvolvi3.html

Thorlabs (2015), Technical Specifications of BK7 Lenses

Tripathi, N. (2012): “Dynamics of Confined Premixed Laminar Explosion Flames”, PhD Thesis, Department of Mechanical Engineering, University of Leeds, Leeds U.K.

Turns, S. R. (2006) An Introduction to Combustion: Concepts and Applications, 2nd edition, Asia: McGraw-Hill

Upton, T., Verhoeven, D. and Hudgins, D. (2011): “High-resolution computed tomography of a turbulent reacting Flow”, Exp. Fluids, 50, 125–134

Wenger, D.; Gerecke, A.; Heeb, N.; Hueglin, C.; Seiler, C.; Haag, R.; Naegeli, H. and Renato Zenobi, R. (2009): “Aryl hydrocarbon receptor-mediated activity of atmospheric particulate matter from an urban and a rural site in Switzerland”, Atmospheric Environment, 43, 3556–3562

Yip, B.; Schmitt, R. and Long, M. (1988): “Instantaneous three-dimensional concentration measurements in turbulent jets and flames” Optics Letters, 13, No.2, 96-98

Yong, Y.; Tian, Q.; Gang, L.; Hossain, M.; Gilabert, G. and Shi, L. (2012): “Recent Advances in Flame Tomography” Chinese Journal of Chemical Engineering, 20, 389-399

Bibliography

Borghi, R. (1985). On the structure and morphology of turbulent premixed flames. In: Casci, C.; Bruno, C. eds. Recent advances in aerospace sciences: in honour of Luigi Crocco on his seventy-fifth birthday. New York: Plenum Press, 117-138

Brookes, S.; Cant, R.; Dupere, I. and Dowling, A. (2001): "Computational Modelling of Self-Excited Combustion Instabilities" Journal of Engineering for Gas Turbines and Power, 123, 322-326

Cant, S. (2002): "High-performance computing in computational fluid dynamics: progress and challenges" Phil. Trans. R. Soc. Lond. A, 360, 1211-1225

Chung, T.; Kim, M. and Sohn, J. (1987): "Finite Element Analysis in Combustion Phenomena", International Journal for Numerical Methods in Fluids, 7, 989-1012

Day, M.; Bell, J.; Grcar, J.; Lijewski, M. and Beckner, V. (2005): "Tools for simulation of laboratory-scale premixed turbulent flames" Journal of Physics: Conference Series, 16, 80–90

Day, M.; Shepherd, I.; Bell, J.; Grcar, J. and Lijewski, M. (2007): "Displacement speeds in turbulent premixed flame simulations", Computational Combustion, ECCOMASS Thermatic Conference, 18-20th July 2007, Delft, The Netherlands

Delhaye, B.; Veynante, D.; Candel, S. and Minh, H. (1994): "Simulation and Modelling of Reactive Shear Layers" Theoretical and Computational Fluid Dynamics, 6, 67-87

Department for Energy and Climate Change, 2014, Minimising Emissions from Spark-ignition Gas Engines [Online], [Accessed 09.09.2014], available from: http://chp.decc.gov.uk/cms/minimising-emissions-from-spark-ignition-gas-engines-3

Hawkes, E. and Cant, R. (2001): "Implications of a Flame Surface Density Approach to Large Eddy Simulation of Premixed Turbulent Combustion", Combustion and Flame, 126, 1617–1629

Jenkins, K. and Cant, R. (2002): "Curvature effects on flame kernels in a turbulent environment", Proceedings of the Combustion Institute, Volume 29, 2023–2029

Kychakoff, G.; Paul, P.; van Cruyningen, I. and Hanson, R. (1987): "Movies and 3-D images of flowfields using planar laser-induced fluorescence" Applied Optics, 26, No. 13, 2498-2500

Lawes, M.; Ormsby, M.; Sheppard, C. and Woolley, R. (2012): "The turbulent burning velocity of iso-octane/air mixtures", Combustion and Flame, 159, 1949–1959

Lee, C. and Cant, R. (2013): "CFD Investigation of Turbulent Premixed Flame Response to Transverse Forcing", Proceedings of ASME Turbo Expo 2013: Turbine Technical Conference and Exposition

Lipatnikov, A. (2013): "Fundamentals of Premixed Turbulent Combustion", CRC Press, Boca Raton

Lipatnikov, A. and Chomiak, J. (2002): "Turbulent flame speed and thickness: phenomenology, evaluation, and application in multi-dimensional simulations", Progress in Energy and Combustion Science, 1-74

Libby, P. and Williams, F. 1994. *Turbulent Reacting Flows*. First edition. London: Academic Press

Minamoto, Y.; Swaminathan, N.; Cant, R. and Leung, T. (2014): "Reaction Zones and Their Structure in MILD Combustion", Combustion Science and Technology, 186:8, 1075-1096

Peters, N. (2000): "Turbulent Combustion", 1st edition, Cambridge University Press, Cambridge, England.

Raffel, M.; Willert, C. and Kompenhans, J. (1998): "Particle Image Velocimetry – A Practical Guide", Springer-Verlag Berlin Heidelbergy, Germany, 1st edition, pp34-37

Robbins, D.; El-Bachir, M.; Gladden, L.; Cant, R. and von Harbou, E. (2012): “CFD Modelling of Single-Phase Flow in a Packed Bed with MRI Validation” AIChE Journal, 58, No. 12, 3904-3915

Samsanov, D.; Elsaesser, A.; Edwards, A.; Thomas, H. and Morfill, G. (2008): “High speed laser tomography system” Review of Scientific Instruments, 79, 035102

Yip, B.; Lam, J.; Winter, M. and Long, M. (1987): “Time-resolved Three-Dimensional Concentration Measurements in a Gas Jet”, Science, 235, 1209-1211

Appendix I – Matlab Image Processing Codes

AI.1 Introduction

This section presents ALL Matlab codes written as part of this work. Explanatory notes are provided within the codes where necessary to illustrate to the user the required inputs etc.. These codes do not work "automatically"; they usually require the user to specify the names and numbers of images to be processed and to change the file directory manually.

2D Mie-scattering image flame edge detector code

```
% A code to read in a sequence of images in a folder and trace the flame
% edge, if present. This process returns a black flame on a white
% background and saves it under a different name in the current directory.

% DOI: 21.03.2016

clear all
close all
clc

% Import a sequence of images and process:

tifFiles = dir('*.tif');
numfiles = length(tifFiles);
mydata = cell(1, numfiles);

for k = 1:numfiles

  mydata{k} = imread(tifFiles(k).name);
  A = mydata{k};
  A = A(:, :, 1);
  A = A(:, :);
  AB = edge(A, 'log');
  AC = imfill(AB, 'holes');
  filename = sprintf('Testpd%d.tif', k);
  imwrite(AC, filename);
end
disp('Finished');
```

All-in-one 3D assembly code

```
% An all-in-one code to read in black/white flame images, assemble them,
% fill the gaps and export an STL file representing the assembled but
% unsmoothed flame.

% This code isn't quite all-in-one - please run Edge_detector.m first!

% DOI: 03.08.2016

% Be the change you wish to see in the world

clear all
close all
clc

% PART I

%--------------------------------------------------------------------------

% Import a sequence of images

firstnum = input('Enter the number of the first image in the sequence');
middlesheet = input('Enter the number of the middle sheet wrt the bomb');
lastnum = input('Enter the number of the last image in the sequence');

% Image resolution, could modify the code to ask future users for these...
resh = 200;
resw = 256;

for m = firstnum:lastnum
C = sprintf('Testpd%d.tif', m);
C = imread(C);
C = imcomplement(C); % ADDED 15.12.2016

for l = 1:resh
    for n = 1:resw
        A(l,n) = C(l,n);
    end
end

for i = 2:resh-1
    for j = 2:resw-1
        AS = A(i+1, j-1)+A(i+1, j)+A(i+1, j+1)+A(i, j-1)+A(i, j+1)+A(i-1,
j-1)+A(i-1, j)+A(i-1, j+1);
        if AS<2
            A(i,j)=0;
        else
        end
    end
end
```

```
for i = 2:resh-1
    for j = 2:resw-1
        AS = A(i+1, j-1)+A(i+1, j)+A(i+1, j+1)+A(i, j-1)+A(i, j+1)+A(i-1,
j-1)+A(i-1, j)+A(i-1, j+1);
        if AS<2
            A(i,j)=0;
        else
        end
    end
end

A = bwareaopen(A, 75);
A = imcomplement(A);
AB = sprintf('Testpp%d.tif', m);
imwrite(A, AB);
end

disp('**************************************************************************
');
disp('!!!Please clean up resulting images as necessary before
proceeding!!!');

pause

% Part II
%--------------------------------------------------------------------------
% NOTE: the first sheet is taken as the sheet closest to the camera!
% i is from top to bottom, j is from left to right!

if (exist('Sheet_ASY_variables.mat')==2)
    load('Sheet_ASY_variables.mat');

else
disp('All images in a sweep must be read in to ensure an accurate
reconstruction!');
disp('This includes flame-less images. This is due to the geometric mirror
offset.');
pause
mirrorwidth = input('Enter the distance between rotating mirror parallel
faces (in mm)');
motorfqcy = input('Enter the frequency input to the rotating mirror motor
(in Hz)');
laserfqcy = input('Enter the laser frequency (in Hz)');
mirrorfaces = input('Enter the number of mirror faces');
longres = input('Enter the longest dimension of the images, in pixels')
pixelsize = input('Enter the pixel size, in mm/pixel');
mirrorbc = input('Enter the mirror face to bomb centre distance, in mm');
resw = input('Enter the length-wise image resolution');
resh = input('Enter the height-wise image resolution');
save('Sheet_ASY_variables');
end

disp('--------------------------------------------------------------------')
```

```
% pre-allocate a matrix into which the sheets may be inserted
a = 384;
A = ones(a,a,a);

angrate = 360*(motorfqcy/8);
angrater = angrate*(180/pi);

for b = firstnum:lastnum

    % Calculate the angle between successive sheets

    sheetnum = 0-(middlesheet-b);
    omega = (1/laserfqcy)*(motorfqcy/8)*2*pi; % radians angle between
succesive sheets based on mirror fqcy
    sheetangle = sheetnum*omega

    AB = sprintf('Testpp%d.tif', b);
    AB = imread(AB);
    AB = imcomplement(AB); % ADDED 15.12.2016

    for i = 1:resh
        for j = 1: resw

         zd = mirrorwidth/2;
         w = sheetangle;
         offset = (zd*tan(w/2)*sin(w))/(sin((45*(pi/180))-w))/pixelsize;

         dista = ((507/pixelsize)-(longres/2)) + j;
         opp = dista*tan(sheetangle);
         k = round((opp+(longres/2))+offset);

            A(i, j, k) = AB(i,j);
        end
    end
end

% Slice the resulting reconstruction along x, yielding y-z slices.
% Save the slices for viewing; only save if black pixels are present

for m = 1:a
    AC(:, :) = A(m, :, :);

    AE = sum(AC(:));
    %if sum(AC(:))<(a^2)
       filename = sprintf('Sliced_II_recon%d.tif', m);
       imwrite(AC, filename);
    %else
    %end
end
```

```
% Part III
% ------------------------------------------------------------------------

clear all
worldsize = 384;

for h = 1:384
imagename = sprintf('Sliced_II_recon%d.tif', h)
A = imread(imagename);
A = imcomplement(A);
SE = strel('square', 3); % formerly "disk", <02.11.2016
A = imdilate(A, SE);
A = imcomplement(A);
       filename = sprintf('Sliced_II_filled%d.tif', h);
       imwrite(A, filename);
end

% Part IV
% ------------------------------------------------------------------------

AP = ones(384,384,384);

for i = 1:384
    A = sprintf('Sliced_II_filled%d.tif', i);
    A = imread(A);

    AP(:, :, i)=A(:, :, 1);

end

fv=isosurface(AP,.5);
stlwrite('Unsmoothed_flame.stl', fv);
```

A function to allow STL files to be read into Matlab

By Johnson, E. (2011). URL: https://uk.mathworks.com/matlabcentral/fileexchange/22409-stl-file-reader, Accessed: 17.06.2017

```
function varargout = stlread(file)
% STLREAD imports geometry from an STL file into MATLAB.
%    FV = STLREAD(FILENAME) imports triangular faces from the ASCII or
binary
%    STL file idicated by FILENAME, and returns the patch struct FV, with
fields
%    'faces' and 'vertices'.
%
%    [F,V] = STLREAD(FILENAME) returns the faces F and vertices V
separately.
%
%    [F,V,N] = STLREAD(FILENAME) also returns the face normal vectors.
%
%    The faces and vertices are arranged in the format used by the PATCH
plot
%    object.

% Copyright 2011 The MathWorks, Inc.

    if ~exist(file,'file')
        error(['File ''%s'' not found. If the file is not on MATLAB''s
path' ...
               ', be sure to specify the full path to the file.'], file);
    end

    fid = fopen(file,'r');
    if ~isempty(ferror(fid))
        error(lasterror); %#ok
    end

    M = fread(fid,inf,'uint8=>uint8');
    fclose(fid);

    [f,v,n] = stlbinary(M);
    %if( isbinary(M) ) % This may not be a reliable test
    %    [f,v,n] = stlbinary(M);
    %else
    %    [f,v,n] = stlascii(M);
    %end

    varargout = cell(1,nargout);
    switch nargout
        case 2
            varargout{1} = f;
            varargout{2} = v;
        case 3
            varargout{1} = f;
            varargout{2} = v;
            varargout{3} = n;
        otherwise
            varargout{1} = struct('faces',f,'vertices',v);
    end
```

```
end


function [F,V,N] = stlbinary(M)

    F = [];
    V = [];
    N = [];

    if length(M) < 84
        error('MATLAB:stlread:incorrectFormat', ...
              'Incomplete header information in binary STL file.');
    end

    % Bytes 81-84 are an unsigned 32-bit integer specifying the number of
faces
    % that follow.
    numFaces = typecast(M(81:84),'uint32');
    %numFaces = double(numFaces);
    if numFaces == 0
        warning('MATLAB:stlread:nodata','No data in STL file.');
        return
    end

    T = M(85:end);
    F = NaN(numFaces,3);
    V = NaN(3*numFaces,3);
    N = NaN(numFaces,3);

    numRead = 0;
    while numRead < numFaces
        % Each facet is 50 bytes
        %  - Three single precision values specifying the face normal
vector
        %  - Three single precision values specifying the first vertex
(XYZ)
        %  - Three single precision values specifying the second vertex
(XYZ)
        %  - Three single precision values specifying the third vertex
(XYZ)
        %  - Two unused bytes
        i1    = 50 * numRead + 1;
        i2    = i1 + 50 - 1;
        facet = T(i1:i2)';

        n  = typecast(facet(1:12),'single');
        v1 = typecast(facet(13:24),'single');
        v2 = typecast(facet(25:36),'single');
        v3 = typecast(facet(37:48),'single');

        n = double(n);
        v = double([v1; v2; v3]);

        % Figure out where to fit these new vertices, and the face, in the
        % larger F and V collections.
        fInd  = numRead + 1;
        vInd1 = 3 * (fInd - 1) + 1;
        vInd2 = vInd1 + 3 - 1;
```

```
        V(vInd1:vInd2,:) = v;
        F(fInd,:)        = vInd1:vInd2;
        N(fInd,:)        = n;

        numRead = numRead + 1;
    end

end


function [F,V,N] = stlascii(M)
    warning('MATLAB:stlread:ascii','ASCII STL files currently not
supported.');
    F = [];
    V = [];
    N = [];
end

% TODO: Change the testing criteria! Some binary STL files still begin with
% 'solid'.
function tf = isbinary(A)
% ISBINARY uses the first line of an STL file to identify its format.
    if isempty(A) || length(A) < 5
        error('MATLAB:stlread:incorrectFormat', ...
              'File does not appear to be an ASCII or binary STL file.');
    end
    if strcmpi('solid',char(A(1:5)'))
        tf = false; % ASCII
    else
        tf = true;  % Binary
    end
end
```

STL Display Code

```
% A code to read in and display an STL reconstruction in Matlab. The graph
axis limits may be altered for scaling purposes.

% You have to look beyond the face to see the person true

clear all
close all
clc

% Set figure properties (axes labels, viewing angle etc.)
%axis equal
view(55, -20)
axis tight
%axis([50 250 50 200 35 200])
title('methane/air flame, phi = 0.6, u=0.75m/s, RTP, 18.4ms AI',
'FontSize', 12, 'FontName', 'arial')
xlabel('X', 'FontSize', 12, 'FontName', 'arial')
ylabel('Y', 'FontSize', 12, 'FontName', 'arial')
zlabel('Z', 'FontSize', 12, 'FontName', 'arial')
lightangle(45,30);
lighting gouraud
hcap.AmbientStrength = 0.6;
hiso.SpecularColorReflectance = 0;
hiso.SpecularExponent = 50;
% Import processed STL file
FV=stlread('Sphere.stl');
Z = patch(FV, 'facecolor', 'r', 'edgecolor', 'none');
ZA = polygon2voxel(Z);
```

```
% RPV_3D

% This code is similar in operation to Rj_calc, but adapted for 3D
% matrices. It reads in "slice_filled" 2D images and assembles these into a
% 3D matrix. Thus, the analysed flames are unsmoothed for greater
% scientific accuracy. The centroid of the flame is first determined. Then,
% the coordinates of each flame voxel are extracted and placed into a
% matrix. These are converted into hypotenuse radii from the centroid of
% the flame and fractions burned determined as per individual comments
% below.

% DOI: 28.04.2017

% TBD

clear all
close all
clc

disp('Please check that the graph axis labels are correct before
continuing!')
pause
% Assemble a 3D matrix from 1:384 re-sliced and filled flame images

A = ones(384,384,384);

for z = 1:384
    Ai = sprintf('Sliced_filled%d.tif', z);
    Ai = imread(Ai);
    Ai = Ai(:, :, 1);
    Ai = Ai(:, :);

    % As they stand, imported images have cell values of zero where black
and
    % 255 where white. This should be changed so that white = 1
    % Walk through matrix and change values accordingly

    for i=1:200
      for j=1:256
            if Ai(i,j)==255
               Ai(i,j)=1;
            else
            end
      end
    end

    A(:, :, z) = Ai;

end

% This section of code returns the Cartesian coordinates of all of the
% black (i.e. flame) pixels in the image and then converts them to polar
% coordinates
Y = [0 0 0];
```

```
for i = 1:size(A(:, 1))
    i
    for j = 1:size(A(:, 2))
        for k = 1:size(A(:, 3))
        if A(i,j,k)==0
            %if exist('Y')==0
                %Y = [i, j, k];
            %else Y = [Y; i, j, k];
            %end
        Y = [Y; i, j, k];
        else
        end
    end
    end
end

% Convert the resulting matrix Y into polar coordinates, after splitting Y
% into x, y and z 1D vectors
xY = Y(:,1);
yY = Y(:,2);
zY = Y(:,3);

mxY = round(mean(xY));
myY = round(mean(yY));
mzY = round(mean(zY));

disp('The centroid is located at:')
[mxY, myY, mzY]


 xYRtC = [0];
for x = 1:size(xY)
    xYRtC = [xYRtC; xY(x)-mxY];
end
disp('xYRtC')
 yYRtC = [0];
for x = 1:size(yY)
    yYRtC = [yYRtC; yY(x)-myY];
end
disp('yYRtC')
 zYRtC = [0];
for x = 1:size(zY)
    zYRtC = [zYRtC; zY(x)-mzY];
end
disp('zYRtC')
[TY, RY, ZY] = cart2pol(xYRtC, yYRtC, zYRtC);

 HYP = [0];
for x = 2:size(TY)
    HYP = [HYP; ((RY(x).^2)+(ZY(x).^2)).^0.5];
end
disp('HYP')
% At lots of decimal places, there are tiny differences between otherwise
% similar numbers. "Unique" fails to recognise these as being different,
% which causes problems. Round HYP accordingly.
HYPR = round(HYP, 2);
load('3D_RPV_var.mat'); % This contains a variable called 'ans', + things
% Calculate the hypotenuse from Rho and Z for each voxel. Find number of
% voxels with each hypotenuse value and use same method as for 2D. Numbers
% of elements should probs. start 1 8 6 ... etc.
```

```
% Hypotenuse is sqrt(Rho^2 + Z^2)! We know Z and Matlab calculates Rho.
% Then proceed as before.

% This bit finds how many elements in the matrix possess a certain value
% First, create a matrix containing only ONE of each value present in the
% matrix HYP:
HYPRU = unique(ans);
% Then, "count" the number of occurences of each individual number in the
% matrix. Generate a matrix showing the individual numbers in the frist
% column and the frequency of each number in the second column
out = [HYPRU,histc(HYPR(:),HYPRU)];
outr = out(:, 1);
outb = out(:, 2);
disp('Getting ready to plot graph')
% Reduce the number of data points in the plot
ans10 = [];
for zv = 1:10:length(ans)
    ans10 = [ans10; ans(zv)];
end
% This bit calculates fraction burned at each radius value and plots a
% graph of RPV v's radius. It also gives the flame brush thickness.
fracb = [];
for zx = 1:10:length(out)
    fracb = [fracb; outb(zx)./BZ(zx)];
end
scatter(ans10, fracb, 'filled')
title('3D RPV vs. flame radius from centre, 0.25i SW3', 'FontName',
'arial', 'FontSize', 14)
xlabel('Radius (mm)', 'FontName', 'arial', 'FontSize', 12)
xlim([0 90]);
ylabel('3D RPV', 'FontName', 'arial', 'FontSize', 12)

%reminder
% Also write code to give flame brush thickness!

% NOTE: If there are no occurences of a certain hypotenuse value in the
% matrix processed here, it will NOT be apparent in the "out" matrix. Hence
% HYPRI is loaded at line 107 ish, as this contains all possible hypotenuse
% values. Otherwise, the frequencies and HYPRU values would mismatch in
% Excel.

% Run this code for a completely black 3D matrix and for one containing a
% flame. The hypotenuse values in any 3D matrix will be identical (assuming
% no scale is used, only Cartesian grid coordinates). It's only the
% frequencies of each value which differ. Comparing frequencies gives the
% fraction burned at each hypotenuse value and thus the Reaction Progress
% Variable at each Hypotenuse value. The frequencies are contained in the
% variable "out". Double-click this variable in the Workspace and copy the
% valeus into Excel, alongside solic black grid frequencies. Please see
% sheet 3D_RPV for details

% Link for determining centre of mass of a collection of 3D points:
% https://www.mathworks.com/matlabcentral/newsreader/view_thread/53873
% See last comment in thread. Accessed: 28.04.2017
```

3D Reaction Progress Variable code, Second Half

```
% A very similar code to FSD_Excel_3D, allowing RPV to be plotted against
% FSD. Please copy the colmn of rounded radius and RPV into blankvariablef
% and then follow the instructions given.

% Before running the code, please type the following into the command
% window: blankvariablef = [];

% ... and the sloths and the carp and the anchovies and
% orangutans and breakfast cereals and fruit bats and large...

close all
clc

% Cut and paste a bit of code from my last masterpiece!
blankvariablei = blankvariablef(:, 1);
blankvariableii = blankvariablef(:, 2);

A = [0];
for i = 2:length(blankvariablei)
    if blankvariablei(i) > blankvariablei(i-1)
        A = [A; i];
    else
    end
end

radius = [0];
sumA = [0];
for j = 2: length(A)-1
    numcells = A(j+1)-A(j);
    sumA = [sumA; (sum(blankvariableii((A(j):A(j+1)-1))))/numcells]
    radius = [radius; blankvariablei(A(j))];
end

output = [radius, sumA];
disp('Now copy "output" to Excel. This contains surface area only, this
must be converted to FSD in Excel!')
```

3D Flame Surface Density Code

```
% FSD_3D

% A variation on Rj_calc and 3D_RPV, where the neighbours of each zero
"flame" cell are
% also analysed to give the flame surface area t ovolme ratio of each
% pixel. The average FSD across each pixel at a given radius is then
% calculated.

% You're trying to read this code, too late it's finished. Goodnight!

clear all
close all
clc

disp('Please ensure that the file "3D_RPV_var.mat" is in the current
folder!')

% Read all images into a pre-allocated matrix

A = ones(384,384,384);

for z = 1:384
    Ai = sprintf('Sliced_filled%d.tif', z);
    Ai = imread(Ai);
    Ai = Ai(:, :, 1);
    Ai = Ai(:, :);

    % As they stand, imported images have cell values of zero where black
and
    % 255 where white. This should be changed so that white = 1
    % Walk through matrix and change values accordingly

    A(:, :, z) = Ai;

end

 for i=1:384
      for j=1:384
          for k = 1:384
            if A(i,j,k)==255
               A(i,j,k)=1;
            else
            end
      end
      end
    end

% This section of code returns the Cartesian coordinates of all of the
% black (i.e. flame) pixels in the image and then converts them to polar
% coordinates
Y = [0 0 0 0];
for i = 1:size(A(:, 1))
    i
    for j = 1:size(A(:, 2))
        for k = 1:size(A(:, 3))
        if A(i,j,k)==0
```

```
        % Determine the exposed surface area of each pixel to unburned
        % mixture
        sumneigh = A(i,j,k-1)+A(i,j,k+1)+A(i+1,j,k)+A(i-1,j,k)+A(i,j-
1,k)+A(i,j+1,k);

        SA = 0.416667*0.416667*sumneigh;
        FSD = SA; %/(0.416667*0.416667*0.416667); this green bit was
wrong...

        Y = [Y; i, j, k, FSD];
        else
        end
    end
    end
end

% Convert the resulting matrix Y into polar coordinates, after splitting Y
% into x, y and z 1D vectors. For this code, this is purely to obtain the
% location of the flame centroid.
xY = Y(:,1);
yY = Y(:,2);
zY = Y(:,3);
fsdY = Y(:, 4);
mxY = round(mean(xY));
myY = round(mean(yY));
mzY = round(mean(zY));

disp('The centroid is located at:')
[mxY, myY, mzY]

 xYRtC = [0];
for x = 1:size(xY)
    xYRtC = [xYRtC; xY(x)-mxY];
end
disp('xYRtC')

 yYRtC = [0];
for x = 1:size(yY)
    yYRtC = [yYRtC; yY(x)-myY];
end
disp('yYRtC')

 zYRtC = [0];
for x = 1:size(zY)
    zYRtC = [zYRtC; zY(x)-mzY];
end
disp('zYRtC')


fsdYRtC = [0]; % This bit just adds a zero to start of fsdy so vectors
match up
for x = 1:size(fsdY)
    fsdYRtC = [fsdYRtC; fsdY(x)];
end
disp('fsdYRtC')

[TY, RY, ZY] = cart2pol(xYRtC, yYRtC, zYRtC);

 HYP = [0, 0];
```

```
for x = 2:size(TY)
    HYP = [HYP; (((RY(x).^2)+(ZY(x).^2)).^0.5), fsdYRtC(x)];
end
disp('HYP')

HYPR = round(HYP, 0);
HYPR = sortrows(HYPR, 1);
load handel, sound(y,1/2*Fs)

% Cut and paste a bit of code from my last masterpiece!
blankvariablei = HYPR(:, 1);
blankvariableii = HYPR(:, 2);

A = [0];
for i = 2:length(blankvariablei)
    if blankvariablei(i) > blankvariablei(i-1)
        A = [A; i];
    else
    end
end

radius = [0];
sumA = [0];
for j = 2: length(A)-1
    numcells = A(j)-A(j-1);
    sumA = [sumA; sum(blankvariableii((A(j):A(j+1))))]
    radius = [radius; blankvariablei(A(j))];
end

output = [radius, sumA];
disp('Now copy "output" to Excel. This contains surface area only, this
must be converted to FSD in Excel!')
```

R_j Calculator Code, for 2D Sheets

```
% A code to read in 2D binary, traced flame images and determine
% burning-velocity characterising radii by conversion of the images to
% polar coordinates
%
% Use Largest_flame_slice code first to obtain the "largest" flame slice
% image number for insertion below
%
% NOTE: This code will not work properly if there are disconnected flame
% parts present. The code fails at the regionprops(centroid) line.
% Imcomplement isn't working well here. See manual alternative. For third
% line of this, A(i,j) == 1 or 255. Will return [128.5 100.5] for centroid
% if wrong pixel value selected!
%
% DOI: 31.12.2016

% You've "gotta" hate something, change something, make something better...

clear all
close all
clc

% Read in image
for i = 33
A = sprintf('Testpp%d.tif', i);
A = imread(A);
A = A(:, :, 1);
A = A(:, :);
% imcomplement still isn't working properly so do it manually instead
for i = 1:200
    for j = 1:256
        if A(i, j) == 1
            A(i,j) = 0;
        else A(i, j) = 1;
        end
    end
end
%A = imcomplement(A);

AS = sum(A(:))
figure, imshow(A)
MC = regionprops(A, 'Centroid') % NOTE: It looks like this will also give
                                % the centre of mass of a cluster of flame
                                % parts in a single image see doc
                                % regionprops

MCXY = input('Please round the centroid coordinates and re-enter them (as
e.g. [2 76] INCLUDING BRACKETS!): ');
MCX = MCXY(:, 1);
MCY = MCXY(:, 2);
[TC, RC] = cart2pol(MCX, MCY)
BTBC = [TC RC]

% As they stand, imported images have cell values of zero where black and
% 255 where white. This should be changed so that white = 1
% Walk through matrix and change values accordingly
figure, imshow(A)
for i=1:200
    for j=1:256
```

```
        if A(i,j)==255
           A(i,j)=1;
        else
        end
    end
end

figure, imshow(A)

% Walk through each cell in the matrix and analyse the cell value. The
% first cell to be analysed is at i,j = 1, or x,y = 1. The code then walks
% through each value of y at a given x, so bottom to top, left to right.
% When it finds a cell value of 1 (i.e. the flame edge) the coordinates of
% this point will be returned. These coordinates are then passed to
% bwtraceboundary, which will march along the flame boundary, returning the
% coordinates of each boundary cell. The nested lollops are inefficient and
% should be replaced with something more elegant, if possible.
% Note: i is "top to bottom", j is "left to right"

if (exist('B')==0)
    for i=200:-1:1
        if (exist('B')==0)
            for j=256:-1:1
               if (exist('B')==0)
                   if A(i,j)==1

                       B=[i,j]
                   else
                   end
               else
               end
            end
        else
        end
    end
else
end

impixelinfo
BTB = bwtraceboundary(A,B,'SE')
clear B

% Convert the resulting matrix BTB into polar coordinates
x = BTB(:,1);
y = BTB(:,2);
[T, R] = cart2pol(x, y);

% Produce a complement to the image. NOTE: imcomplement does NOT always
% work here, possible due to extra dimensions added in Paint!

for i = 1:200
    for j = 1:256
        if A(i, j) == 1
            A(i,j) = 0;
        else A(i, j) = 1;
        end
    end
end
%A = imcomplement(A);
```

```
% This section of code returns the Cartesian coordinates of all of the
% black (i.e. flame) pixels in the image and then converts them to polar
% coordinates

for i = 1:200
    for j = 1:256
        if A(i,j)==0
            if exist('Y')==0
                Y = [i-MCY, j-MCX]; % This bit makes coords relative to
centroid
            else Y = [Y; i-MCY, j-MCX];
            end
        end
    end
end
Y

% Convert the resulting matrix Y into polar coordinates, after splitting Y
% into x and y 1D vectors
xY = Y(:,1);
yY = Y(:,2);
[TY, RY] = cart2pol(xY, yY);

end

[TY RY]

RYU = unique(RY);
out = [RYU,histc(RY(:),RYU)];
for i = 1:length(yY)
    if yY(i) == 0
        display('YES!')
        i
    else
    end
end
```

Voxelisation Code

A code by Kroon, D. (2012), URL: https://uk.mathworks.com/matlabcentral/fileexchange/24086-polygon2voxel Accessed: 17.06.2017

```
function Volume=polygon2voxel(FV,VolumeSize,mode,Yxz)
% This function POLYGON2VOXEL will convert a Triangulated Mesh into a
% Voxel Volume which will contain the discretized mesh. Discretization of a
% polygon is done by splitting/refining the face, until the longest edge
% is smaller than 0.5 voxels. Followed by setting the voxel beneath the
vertice
% coordinates of that small triangle to one.
%
% Volume=polygon2voxel(FV,VolumeSize,Mode,Yxz);
%
% Inputs,
%   FV : A struct containing FV.faces with a facelist Nx3 and FV.vertices
%        with a Nx3 vertice list. Such a structure is created by Matlab
%        Patch function
%   VolumeSize : The size of the output volume, example [100 100 100]
%   Mode : (optional) if set to:
%               'none', The vertices data is directly used as coordinates
%                       in the voxel volume.
%               'wrap', The vertices data is directly used as coordinates
%                       in the voxel volume, coordinates outside are
%                       circular wrapped to the inside.
%               'auto', The vertices data is translated and
%                       scaled with a scalar to fit inside the new volume.
%               'center', coordinate 0,0,0 is set as the center of the
volume
%                       instead of the corner of the voxel volume.
%               'clamp', The vertices data is directly used as coordinates
%                       in the voxel volume, coordinates outside are
%                       clamped to the inside.
%   (Optional)
%   Yxz : If true (default) use Matlab convention 1th dimension Y,
%         2th dimension X, and last dimension Z. Otherwise 1th
%         dimension is X, 2th Y and last Z.
%
%
% Outputs,
%   Volume : The 3D logical volume, with all voxels part of the discretized
%            mesh one, and all other voxels zero.
%
% Example,
%   % Compile the c-coded function
%   mex polygon2voxel_double.c -v
%
%   % Load a triangulated mesh of a sphere
%   load sphere;
%
%   % Show the mesh
%   figure, patch(FV,'FaceColor',[1 0 0]); axis square;
%
%   % Convert the mesh to a voxelvolume
%   Volume=polygon2voxel(FV,[50 50 50],'auto');
%
%   % Show x,y,z slices
%   figure,
```

```
%   subplot(1,3,1), imshow(squeeze(Volume(25,:,:)));
%   subplot(1,3,2), imshow(squeeze(Volume(:,25,:)));
%   subplot(1,3,3), imshow(squeeze(Volume(:,:,25)));
%
%   %  Show iso surface of result
%   figure, patch(isosurface(Volume,0.1), 'Facecolor', [1 0 0]);
%
% Example2,
%   % Compile the c-coded function
%   mex polygon2voxel_double.c -v
%
%   % Make A Volume with a few blocks
%   I = false(120,120,120);
%   I(40:60,50:70,60:80)=1; I(60:90,45:75,60:90)=1;
%   I(20:60,40:80,20:60)=1; I(60:110,35:85,10:60)=1;
%
%   % Convert the volume to a triangulated mesh
%   FV = isosurface(I,0.8);
%
%   % Convert the triangulated mesh back to a surface in a volume
%   J = polygon2voxel(FV,[120, 120, 120],'none');
%   % Fill the volume
%   J=imfill(J,'holes');
%
%   % Differences between original and reconstructed
%   VD = abs(J-I);
%
%   % Show the original Mesh and Mesh of new volume
%   figure,
%   subplot(1,3,1),  title('original')
%     patch(FV,'facecolor',[1 0 0],'edgecolor','none'), camlight;view(3);
%   subplot(1,3,2), title('converted');
%     patch(isosurface(J,0.8),'facecolor',[0 0 1],'edgecolor','none'),
camlight;view(3);
%   subplot(1,3,3), title('difference');
%     patch(isosurface(VD,0.8),'facecolor',[0 0 1],'edgecolor','none'),
camlight;view(3);
%
% Function is written by D.Kroon University of Twente (May 2009)

if(nargin<4), Yxz=true; end

% Check VolumeSize size
if(length(VolumeSize)==1)
    VolumeSize=[VolumeSize VolumeSize VolumeSize];
end
if(length(VolumeSize)~=3)
    error('polygon2voxel:inputs','VolumeSize must be a array of 3 elements
')
end

% Volume Size must always be an integer value
VolumeSize=round(VolumeSize);

sizev=size(FV.vertices);
% Check size of vertice array
if((sizev(2)~=3)||(length(sizev)~=2))
    error('polygon2voxel:inputs','The vertice list is not a m x 3 array')
end
```

```
sizef=size(FV.faces);
% Check size of vertice array
if((sizef(2)~=3)||(length(sizef)~=2))
    error('polygon2voxel:inputs','The vertice list is not a m x 3 array')
end

% Check if vertice indices exist
if(max(FV.faces(:))>size(FV.vertices,1))
    error('polygon2voxel:inputs','The face list contains an undefined
vertex index')
end

% Check if vertice indices exist
if(min(FV.faces(:))<1)
    error('polygon2voxel:inputs','The face list contains an vertex index
smaller then 1')
end

% Matlab dimension convention YXZ
if(Yxz)
    FV.vertices=FV.vertices(:,[2 1 3]);
end

switch(lower(mode(1:2)))
    case {'au'} % auto
        % Make all vertices-coordinates positive
        FV.vertices=FV.vertices-min(FV.vertices(:));
        scaling=min((VolumeSize-1)./(max(FV.vertices(:))));
        % Make the vertices-coordinates to range from 0 to 100
        FV.vertices=FV.vertices*scaling+1;
        Wrap=0;
    case {'ce'} % center
        % Center the vertices

FV.vertices=FV.vertices+repmat((VolumeSize/2),size(FV.vertices,1),1);
        Wrap=0;
    case {'wr'} %wrap
        Wrap=1;
    case{'cl'} % clamp
        Wrap=2;
    otherwise
        Wrap=0;
end

% Separate the columns;
FacesA=double(FV.faces(:,1));
FacesB=double(FV.faces(:,2));
FacesC=double(FV.faces(:,3));
VerticesX=double(FV.vertices(:,1));
VerticesY=double(FV.vertices(:,2));
VerticesZ=double(FV.vertices(:,3));

% Volume size to double
VolumeSize=double(VolumeSize);

% Call the mex function
Volume=polygon2voxel_double(FacesA,FacesB,FacesC,VerticesX,VerticesY,Vertic
esZ,VolumeSize,Wrap);
```

Central Flame Sheet Detector Code

```
% Flame size code

% This code reads in a sequence of 2D images and calculates the flame area
% in each. The biggest flame in a sequence may then be selected for further
% processing

clear all
close all
clc

% Read in a sequence of images
firstnum = input('Enter first image number');
lastnum = input('Enter last image number');

C = [0, 0];
for i = firstnum:lastnum
A = sprintf('Testpp%d.tif', i);
A = imread(A);
A = A(:, :, 1);
A = A(:, :);
A = logical(A);
A = imcomplement(A);
B = sum(A(:));
% if B > C(1)
    C = [C; B, i];

end
    CMAX = max(C(:, 1))
    C
```

```
% A code to read in smoothed 3D flame images (as STL files) and determine
the
% surface area (A), equivalent surface area (a) and thus A/a. These values
% may then be compared with ut/ul

% NOTE: THIS CODE OBTAINS BOTH THE SURFACE AREA AND VOLUME FOR THE
% VOXELISED VERSION OF THE RECONSTRUCTION. THIS AVOIDS THE POSSIILITY OF
% SUB-UNITY A/a WITH SOME SMALL, EARLY STAGE FLAMES.

% Whip your hair back and forth

clear all
close all
clc
% Request some data from the user

Masr = 1.4; %input('Enter the strain-rate Markstein number');
up = 1 %input('Enter the rms turbulence velocity');
ul = 0.119; %input('Enter the laminar burning velocity');

% Set figure properties (axes labels, viewing angle etc.)
axis equal
view(55, -20)
title('Smoothed flame as imported', 'FontSize', 14, 'FontName', 'arial')
xlabel('X', 'FontSize', 12, 'FontName', 'arial')
ylabel('Y', 'FontSize', 12, 'FontName', 'arial')
zlabel('Z', 'FontSize', 12, 'FontName', 'arial')

% Import processed STL file
FVi=stlread('Spherex2.stl');
FV = patch(FVi, 'facecolor', 'red', 'edgecolor', 'none');

% Voxelise the flame, i.e. fill the flame with small cubes of a known
% volume, the addition of which gives a reasonable estimate of the voume.

voxel = polygon2voxel(FVi, 400, 'center', true);

% This results in a hollow flame, with the flame edge now being made of
% voxels rather than triangles. Slice the flame and fill in the slices so
% that they take on actual volumes

for i = 1: 400
    A = voxel(:, :, i);
    A = imfill(A, 'holes');
    B(:, :, i) = A(:, :);
end

% Set figure properties (axes labels, viewing angle etc.)
axis equal
view(55, -20)
title('Voxelised flame', 'FontSize', 14, 'FontName', 'arial')
xlabel('X', 'FontSize', 12, 'FontName', 'arial')
ylabel('Y', 'FontSize', 12, 'FontName', 'arial')
zlabel('Z', 'FontSize', 12, 'FontName', 'arial')
```

```
% Display the voxelised flame by means of an isosurface
fv = isosurface(B, 0.5);
fv = patch(fv, 'facecolor', 'red');

% Calculate the volume of the flame by counting the number of voxels and
% multiplying by the volume of each voxel
Array_Sum = (0.4167*0.4167*0.4167*(sum(sum(sum(B)))))/1000;

% Display the volume to the user
fprintf('\nThe flame volume is (cm3)%f\n\n', Array_Sum);

% Calculate the equivalent spherical flame radius from the volume and
% use this to calculate the value of a

eqradius = (Array_Sum./(4*pi/3))^(1/3);
eqarea_a = (4*pi*(eqradius.^2));

fprintf('\nThe value of a is %f\n\n', eqarea_a);

% Calculate and display surface area
verts = get(FV, 'Vertices');
faces = get(FV, 'Faces');
a = verts(faces(:, 2), :)*0.41666667 - verts(faces(:, 1), :)*0.416666667;
b = verts(faces(:, 3), :)*0.41666667 - verts(faces(:, 1), :)*0.416666667;
c = cross(a, b, 2);
area = (1/2 * sum(sqrt(sum(c.^2, 2))))/100;
fprintf('\nThe surface area is (cm2)%f\n\n', area);

Aa = area./eqarea_a;
fprintf('\nA/a =  %f\n\n', Aa);

% Calculate ut/ul using the Derekvation

l = 0.02;
v = 0.0000162;
a = 0.023.*(30-Masr);
K = 0.25.*((up/ul)^2).*(((up.*l)./v)^-0.5);
b = 0.0103.*(Masr-30);
U = a.*(K^b);
upul = up./ul;
utul_D = U.*upul

utul_C13 = U.*((4*K.*((ul.*l)./v)^0.5))^(2/3)
```

2D Flame Slice Curvature Code

```
% A code, authored by P. Shaik, to determine curvatures in 2D black and
% white images. The flame edge must have been traced in these images.

% DOI (revised form): 10.11.2016

% Re-light my fire

clear all;
close all;
clc;

% Read in the BW image

A = imread('Testpp46.tif');
B = bwboundaries(A, 8);
[A,~] = bwboundaries(A, 8);
A = A{1};

% Create separate matrices for x and y
x = A(:,2);
y = A(:,1);

% Create Fourier transforms of the vectors x and y
xf = fft(x);
yf = fft(y);

% Do something else with numbers
nx = length(xf); % Size of transform-ed matrix
hx = ceil(nx/2)-1; % Round each element "up" to next highest +ve integer
value
ftdiff = (2i*pi/nx)*(0:hx); % No idea...
ftdiff(nx:-1:nx-hx+1) = -ftdiff(2:hx+1);
ftddiff = (-(2i*pi/nx)^2)*(0:hx);
ftddiff(nx:-1:nx-hx+1) = ftddiff(2:hx+1);

% Set certain values of each vector to equal zero. Obviously.
xf(25:end-24) = 0;
yf(25:end-24) = 0;

% Get rid of the imaginary bits. Probably.
dx = real(ifft(xf.*ftdiff'));
dy = real(ifft(yf.*ftdiff'));
ddx = real(ifft(xf.*ftddiff'));
ddy = real(ifft(yf.*ftddiff'));

% Generate k. What's k?
k = sqrt((ddy.*dx - ddx.*dy).^2) ./ ((dx.^2 + dy.^2).^(3/2));
```

Schlieren Edge Detection Code

```
% Quick schlieren code

% A code to process schlieren images containing a spark plug, where Prof.
% Sharpe's codes won't work due to very poor image quality. Some manual
% processing is required. This also seems to work very nicely for
% laser-ignited flames. Again, Manuel processing is required.

% DOI: 20.03.2017

% We gotta get out of this place, if it's the last thing we ever do...
% Man there's a better life, for me and you

clear all
close all
clc

% Process some nasty images

bmpFiles = dir('*.bmp');
numfiles = length(bmpFiles);
mydata = cell(1, numfiles);

for k = 1:numfiles

mydata{k} = imread(bmpFiles(k).name);
AB = mydata{k};
A = imread('0.bmp');
A = im2bw(A, 0.2);
% figure, imshow(A)
AB = im2bw(AB, 0.2);
% figure, imshow(AB)
AAB = A==AB;
% figure, imshow(AAB)
AAB = imcomplement(AAB);
  for i = 2:767
    for j = 2:767
        AS = AAB(i+1, j-1)+AAB(i+1, j)+AAB(i+1, j+1)+AAB(i, j-1)+AAB(i,
j+1)+AAB(i-1, j-1)+AAB(i-1, j)+AAB(i-1, j+1);
        if AS<4
            AAB(i,j)=0;
        else
        end
    end
end
AAB = bwareaopen(AAB, 4);
% figure, imshow(AAB)
AAB = imcomplement(AAB);
filename = sprintf('Testpd%d.tif', k);
imwrite(AAB, filename);
end
```

Laser-Ignited Schlieren Image Processing Code

```
% Schlieren code

% A code to process laser ignitied schlieren images and determine the
% equivalent circular radius (for laminar flames)

% Um diddle diddle diddle diddle diddle-I

clear all
close all
clc

% Read in a the background image

A0 = imread('0.bmp');

% Read in each subsequent imagea nd process

bmpFiles = dir('*.bmp');
numfiles = length(bmpFiles);
mydata = cell(1, numfiles);

for k = 1:5:numfiles

  mydata{k} = imread(bmpFiles(k).name);
  A = mydata{k};
  A = edge(A, 'canny');
  A = imfill(A, 'holes');

  for i = 2:767
    for j = 2:767
        AS = A(i+1, j-1)+A(i+1, j)+A(i+1, j+1)+A(i, j-1)+A(i, j+1)+A(i-1,
j-1)+A(i-1, j)+A(i-1, j+1);
        if AS<4
            A(i,j)=0;
        else
        end
    end
end

%figure, imshow(A)

for i = 2:767
    for j = 2:767
        AS = A(i+1, j-1)+A(i+1, j)+A(i+1, j+1)+A(i, j-1)+A(i, j+1)+A(i-1,
j-1)+A(i-1, j)+A(i-1, j+1);
        if AS<4
            A(i,j)=0;
        else
        end
    end
end

A = bwareaopen(A, 800);
A = imcomplement(A);
```

```
imshow(A)

filename = sprintf('Testpd%d.tif', k);
imwrite(A, filename);
end
```

STL Writing Code

A code by “Sven” (2015), URL: https://uk.mathworks.com/matlabcentral/fileexchange/20922-stlwrite-filename--varargin- Accessed: 17.06.2017

```
function stlwrite(filename, varargin)
%STLWRITE   Write STL file from patch or surface data.
%
%   STLWRITE(FILE, FV) writes a stereolithography (STL) file to FILE for a
%   triangulated patch defined by FV (a structure with fields 'vertices'
%   and 'faces').
%
%   STLWRITE(FILE, FACES, VERTICES) takes faces and vertices separately,
%   rather than in an FV struct
%
%   STLWRITE(FILE, X, Y, Z) creates an STL file from surface data in X, Y,
%   and Z. STLWRITE triangulates this gridded data into a triangulated
%   surface using triangulation options specified below. X, Y and Z can be
%   two-dimensional arrays with the same size. If X and Y are vectors with
%   length equal to SIZE(Z,2) and SIZE(Z,1), respectively, they are passed
%   through MESHGRID to create gridded data. If X or Y are scalar values,
%   they are used to specify the X and Y spacing between grid points.
%
%   STLWRITE(...,'PropertyName',VALUE,'PropertyName',VALUE,...) writes an
%   STL file using the following property values:
%
%   MODE          - File is written using 'binary' (default) or 'ascii'.
%
%   TITLE         - Header text (max 80 chars) written to the STL file.
%
%   TRIANGULATION - When used with gridded data, TRIANGULATION is either:
%                       'delaunay'  - (default) Delaunay triangulation of
X, Y
%                       'f'         - Forward slash division of grid quads
%                       'b'         - Back slash division of quadrilaterals
%                       'x'         - Cross division of quadrilaterals
%                   Note that 'f', 'b', or 't' triangulations now use an
%                   inbuilt version of FEX entry 28327, "mesh2tri".
%
%   FACECOLOR     - Single colour (1-by-3) or one-colour-per-face (N-by-3)
%                   vector of RGB colours, for face/vertex input. RGB range
%                   is 5 bits (0:31), stored in VisCAM/SolidView format
%
(http://en.wikipedia.org/wiki/STL_(file_format)#Color_in_binary_STL)
%
%   Example 1:
%     % Write binary STL from face/vertex data
%     tmpvol = false(20,20,20);      % Empty voxel volume
%     tmpvol(8:12,8:12,5:15) = 1;    % Turn some voxels on
%     fv = isosurface(~tmpvol, 0.5); % Make patch w. faces "out"
%     stlwrite('test.stl',fv)        % Save to binary .stl
```

```
%
%   Example 2:
%     % Write ascii STL from gridded data
%     [X,Y] = deal(1:40);             % Create grid reference
%     Z = peaks(40);                  % Create grid height
%     stlwrite('test.stl',X,Y,Z,'mode','ascii')
%
%   Example 3:
%     % Write binary STL with coloured faces
%     cVals = fv.vertices(fv.faces(:,1),3); % Colour by Z height.
%     cLims = [min(cVals) max(cVals)];      % Transform height values
%     nCols = 255;  cMap = jet(nCols);      % onto an 8-bit colour map
%     fColsDbl = interp1(linspace(cLims(1),cLims(2),nCols),cMap,cVals);
%     fCols8bit = fColsDbl*255; % Pass cols in 8bit (0-255) RGB triplets
%     stlwrite('testCol.stl',fv,'FaceColor',fCols8bit)

%   Original idea adapted from surf2stl by Bill McDonald. Huge speed
%   improvements implemented by Oliver Woodford. Non-Delaunay triangulation
%   of quadrilateral surface courtesy of Kevin Moerman. FaceColor
%   implementation by Grant Lohsen.
%
%   Author: Sven Holcombe, 11-24-11


% Check valid filename path
path = fileparts(filename);
if ~isempty(path) && ~exist(path,'dir')
    error('Directory "%s" does not exist.',path);
end

% Get faces, vertices, and user-defined options for writing
[faces, vertices, options] = parseInputs(varargin{:});
asciiMode = strcmp( options.mode ,'ascii');

% Create the facets
facets = single(vertices');
facets = reshape(facets(:,faces'), 3, 3, []);

% Compute their normals
V1 = squeeze(facets(:,2,:) - facets(:,1,:));
V2 = squeeze(facets(:,3,:) - facets(:,1,:));
normals = V1([2 3 1],:) .* V2([3 1 2],:) - V2([2 3 1],:) .* V1([3 1 2],:);
clear V1 V2
normals = bsxfun(@times, normals, 1 ./ sqrt(sum(normals .* normals, 1)));
facets = cat(2, reshape(normals, 3, 1, []), facets);
clear normals

% Open the file for writing
permissions = {'w','wb+'};
fid = fopen(filename, permissions{asciiMode+1});
if (fid == -1)
    error('stlwrite:cannotWriteFile', 'Unable to write to %s', filename);
end

% Write the file contents
if asciiMode
    % Write HEADER
    fprintf(fid,'solid %s\r\n',options.title);
    % Write DATA
    fprintf(fid,[...
```

```
        'facet normal %.7E %.7E %.7E\r\n' ...
        'outer loop\r\n' ...
        'vertex %.7E %.7E %.7E\r\n' ...
        'vertex %.7E %.7E %.7E\r\n' ...
        'vertex %.7E %.7E %.7E\r\n' ...
        'endloop\r\n' ...
        'endfacet\r\n'], facets);
    % Write FOOTER
    fprintf(fid,'endsolid %s\r\n',options.title);

else % BINARY
    % Write HEADER
    fprintf(fid, '%-80s', options.title);             % Title
    fwrite(fid, size(facets, 3), 'uint32');           % Number of facets
    % Write DATA
    % Add one uint16(0) to the end of each facet using a typecasting trick
    facets = reshape(typecast(facets(:), 'uint16'), 12*2, []);
    % Set the last bit to 0 (default) or supplied RGB
    facets(end+1,:) = options.facecolor;
    fwrite(fid, facets, 'uint16');
end

% Close the file
fclose(fid);
fprintf('Wrote %d facets\n',size(facets, 2));



%% Input handling subfunctions
function [faces, vertices, options] = parseInputs(varargin)
% Determine input type
if isstruct(varargin{1}) % stlwrite('file', FVstruct, ...)
    if ~all(isfield(varargin{1},{'vertices','faces'}))
        error( 'Variable p must be a faces/vertices structure' );
    end
    faces = varargin{1}.faces;
    vertices = varargin{1}.vertices;
    options = parseOptions(varargin{2:end});

elseif isnumeric(varargin{1})
    firstNumInput = cellfun(@isnumeric,varargin);
    firstNumInput(find(~firstNumInput,1):end) = 0; % Only consider
numerical input PRIOR to the first non-numeric
    numericInputCnt = nnz(firstNumInput);

    options = parseOptions(varargin{numericInputCnt+1:end});
    switch numericInputCnt
        case 3 % stlwrite('file', X, Y, Z, ...)
            % Extract the matrix Z
            Z = varargin{3};

            % Convert scalar XY to vectors
            ZsizeXY = fliplr(size(Z));
            for i = 1:2
                if isscalar(varargin{i})
                    varargin{i} = (0:ZsizeXY(i)-1) * varargin{i};
                end
            end

            % Extract X and Y
            if isequal(size(Z), size(varargin{1}), size(varargin{2}))
```

```
                % X,Y,Z were all provided as matrices
                [X,Y] = varargin{1:2};
            elseif numel(varargin{1})==ZsizeXY(1) &&
numel(varargin{2})==ZsizeXY(2)
                % Convert vector XY to meshgrid
                [X,Y] = meshgrid(varargin{1}, varargin{2});
            else
                error('stlwrite:badinput', 'Unable to resolve X and Y
variables');
            end

            % Convert to faces/vertices
            if strcmp(options.triangulation,'delaunay')
                faces = delaunay(X,Y);
                vertices = [X(:) Y(:) Z(:)];
            else
                if ~exist('mesh2tri','file')
                    error('stlwrite:missing', '"mesh2tri" is required to
convert X,Y,Z matrices to STL. It can be downloaded from:\n%s\n',...

'http://www.mathworks.com/matlabcentral/fileexchange/28327')
                end
                [faces, vertices] = mesh2tri(X, Y, Z,
options.triangulation);
            end

        case 2 % stlwrite('file', FACES, VERTICES, ...)
            faces = varargin{1};
            vertices = varargin{2};

        otherwise
            error('stlwrite:badinput', 'Unable to resolve input types.');
    end
end

if ~isempty(options.facecolor) % Handle colour preparation
    facecolor = uint16(options.facecolor);
    %Set the Valid Color bit (bit 15)
    c0 = bitshift(ones(size(faces,1),1,'uint16'),15);
    %Red color (10:15), Blue color (5:9), Green color (0:4)
    c0 = bitor(bitshift(bitand(2^6-1, facecolor(:,1)),10),c0);
    c0 = bitor(bitshift(bitand(2^11-1, facecolor(:,2)),5),c0);
    c0 = bitor(bitand(2^6-1, facecolor(:,3)),c0);
    options.facecolor = c0;
else
    options.facecolor = 0;
end

function options = parseOptions(varargin)
IP = inputParser;
IP.addParamValue('mode', 'binary', @ischar)
IP.addParamValue('title', sprintf('Created by stlwrite.m %s',datestr(now)),
@ischar);
IP.addParamValue('triangulation', 'delaunay', @ischar);
IP.addParamValue('facecolor',[], @isnumeric)
IP.addParamValue('facecolour',[], @isnumeric)
IP.parse(varargin{:});
options = IP.Results;
if ~isempty(options.facecolour)
    options.facecolor = options.facecolour;
```

```
end

function [F,V]=mesh2tri(X,Y,Z,tri_type)
% function [F,V]=mesh2tri(X,Y,Z,tri_type)
%
% Available from http://www.mathworks.com/matlabcentral/fileexchange/28327
% Included here for convenience. Many thanks to Kevin Mattheus Moerman
% kevinmoerman@hotmail.com
% 15/07/2010
%--------------------------------------------------------------------------

[J,I]=meshgrid(1:1:size(X,2)-1,1:1:size(X,1)-1);

switch tri_type
    case 'f'%Forward slash
        TRI_I=[I(:),I(:)+1,I(:)+1;  I(:),I(:),I(:)+1];
        TRI_J=[J(:),J(:)+1,J(:);   J(:),J(:)+1,J(:)+1];
        F = sub2ind(size(X),TRI_I,TRI_J);
    case 'b'%Back slash
        TRI_I=[I(:),I(:)+1,I(:);  I(:)+1,I(:)+1,I(:)];
        TRI_J=[J(:)+1,J(:),J(:);   J(:)+1,J(:),J(:)+1];
        F = sub2ind(size(X),TRI_I,TRI_J);
    case 'x'%Cross
        TRI_I=[I(:)+1,I(:);  I(:)+1,I(:)+1;  I(:),I(:)+1;    I(:),I(:)];
        TRI_J=[J(:),J(:);    J(:)+1,J(:);    J(:)+1,J(:)+1;  J(:),J(:)+1];
        IND=((numel(X)+1):numel(X)+prod(size(X)-1))';
        F = sub2ind(size(X),TRI_I,TRI_J);
        F(:,3)=repmat(IND,[4,1]);
        Fe_I=[I(:),I(:)+1,I(:)+1,I(:)]; Fe_J=[J(:),J(:),J(:)+1,J(:)+1];
        Fe = sub2ind(size(X),Fe_I,Fe_J);
        Xe=mean(X(Fe),2); Ye=mean(Y(Fe),2);  Ze=mean(Z(Fe),2);
        X=[X(:);Xe(:)]; Y=[Y(:);Ye(:)]; Z=[Z(:);Ze(:)];
end

V=[X(:),Y(:),Z(:)];
```